Explaining Morphological and Electrical Features of Boron-doped Zinc Oxide to Tailor New Electrodes for Photovoltaics

EPFL

ÉCOLE POLYTECHNIQUE
FÉDÉRALE DE LAUSANNE

Suisse
2016

The most exciting phrase to hear in science,
the one that heralds new discoveries,
is not 'Eureka!', but 'That's funny...'
— Isaac Asimov

Abstract

Photovoltaic modules, flat-panel displays and electrochromic windows are some of the many rapidly developing technologies exploiting the unique features of transparent conductive oxide materials (TCOs). TCOs are a particular class of metal oxides that combine transparency to visible light, a property of glass, with electrical conductivity, a property of metals. Because the two properties are not independent, each TCO is characterized by the trade-off between transparency and conductivity and can be more or less appropriate for a particular application. TCOs are normally synthesized as thin films (0.1-1 μm) on top of an underlying substrate (e.g. glass, silicon wafer, plastic). The application sets the constraints not only on the TCO properties but also on the deposition techniques, which are incompatible with some substrates (e.g. high-temperature deposition is incompatible with plastic substrates).

This thesis is dedicated to the in-depth investigation of one widely used TCO material: boron-doped zinc oxide (ZnO:B) deposited by low-pressure chemical vapor deposition (LP- MOCVD). The main distinction of this polycrystalline material is its low absorptance which allows for thick films (ensuring high conductivity and surface roughness) while maintaining high transparency. This characteristic makes ZnO films deposited by LP-MOCVD ideal as transparent electrodes in thin-film solar cells, which require light-trapping schemes to efficiently absorb all the components of the light spectrum. Although ZnO:B properties have previously been optimized for application in thin-film solar cells, the exact processes behind the film formation depend on a number of deposition parameters and have not been fully described. This thesis substantially clarifies the processes of the film nucleation and growth evolution, and the mechanisms of incorporation of the B atoms into the ZnO.

First, for non-intentionally doped ZnO we establish that the three main deposition parameters influencing the film properties are the deposition temperature, the gas precursor ratio and the total gas flow. We experimented with these three parameters across a wide range of parameter values. We obtained, in particular, a rough film usually applied to thin-film cells that can be deposited at 120 °C, well below the usual deposition temperature of 180 °C. All the films deposited with different parameters were characterized at different stages of their growth using atomic force microscopy, X-ray diffraction and automated crystallographic orientation mapping. These data reveal the dependence of the film preferential orientation on the deposition conditions. We propose a model based on the adsorbed atom mean free path to explain this dependence. Using deposition parameters learnt from this model, we can control the preferential orientation during film growth to increase the grain size and conductivity.

Second, we extend our analysis of conductivity to B-doped ZnO films. To decrease the resistiv-

ity, impurity atoms (boron) were introduced into the film by adding a gas in the deposition chamber. Boron atoms act as electron donors in ZnO, increasing the electrical conductivity and decreasing the transparency. This work quantifies how the impurity concentration and spatial distribution affect the film conductivity. Quantification of the B atoms incorporated in the film was performed using nuclear reaction analysis. In particular we found that a high level of O precursor gas favors B incorporation in the film. The dopant spatial distribution was investigated specifically on the type of film applied in thin-film solar cells. Combining nano secondary ion mass spectroscopy at nanometric scale and Kelvin probe force microscopy we demonstrate that the dopant atoms incorporate in only one of the two sides of each grain. This is a new and surprising observation because dopant atoms are commonly assumed to be uniformly distributed in the film.

The transparency and electrical conductivity of ZnO depend not only on the concentration of the carriers but also on their mobility. Increasing the carrier mobility is beneficial both for transparency and conductivity. Understanding the mechanisms limiting the carrier mobility is fundamental to designing the most suitable film. The sources of carrier scattering are investigated for different intrinsic (i.e. O vacancies and Zn interstitials) and extrinsic (B atoms) impurity concentrations. We observed that for the same B concentration the source of electron scattering depends on the concentration of intrinsic defects: for films with a lower concentration of intrinsic defects, the main source of scattering is the grain boundaries; for films with a higher concentration of intrinsic defects, the main sources are the mechanisms happening in the crystalline region.

Finally, ZnO:B films deposited by LP-MOCVD were optimized using the characterization results and successfully applied in four different types of solar cells: tandem amorphous/microcrystalline silicon, amorphous silicon, copper indium gallium selenide and silicon heterojunction. The advantages of the developed films to these four cells included the simplification of the fabrication process, the reduction of reflectance and parasitic absorption, and a better understanding of carrier transport mechanisms through the device.

This thesis presents new findings on the film growth mechanism under different deposition conditions and on the mechanisms of B incorporation in ZnO. Importantly, it proves the applicability of thin-film characterization techniques that were not used previously on ZnO films. This thesis is a step forward in understanding and improving the properties of polycrystalline ZnO:B films, and the techniques explored here can be further applied to the broader class of polycrystalline thin films.

Key words: transparent conductive oxide, thin film, photovoltaics, transparent electrodes, parasitic absorption, zinc oxide, low-pressure chemical vapor deposition, electrical properties, optical properties, carrier mobility, film preferential orientation, dopant concentration, dopant distribution, grain boundary, electron scattering mechanisms, diethylzinc, water, boron, nano secondary ion spectroscopy, Kelvin probe microscopy, nuclear reaction analysis, Kanaya-Okayama method.

Riassunto

Moduli fotovoltaici, schermi piatti e vetri elettrocromici sono solo alcune delle tecnologie che traggono vantaggio dalle caratteristiche uniche fornite dagli ossidi trasparenti e conduttivi (OTC). Gli OTC sono una famiglia particolare di ossidi metallici che combinano trasparenza alla luce, tipica del vetro, e conduttività elettrica, tipica dei metalli. L'interdipendenza di queste due proprietà si traduce in un compromesso che rende ogni tipo di OTC più o meno adatto per una determinata applicazione. Gli OTC sono normalmente sintetizzati sotto forma di pellicole sottili (0.1 - 1 μm) su differenti tipi di substrati (vetro, wafer di silicio, plastica). Il tipo di applicazione determina non solo le proprietà dell'OTC ma anche i vincoli relativi alla tecnica di deposizione (ad esempio trattamenti ad alta temperatura sono incompatibili con substrati come la plastica).

Questa tesi è dedicata allo studio di uno degli OTC tra i più utilizzati: l'ossido di zinco drogato boro (ZnO:B) depositato per deposizione chimica da vapore a bassa pressione (LP-CVD). La principale caratteristica di questo materiale policristallino è il basso assorbimento ottico che permette di crescere pellicole spesse (che favoriscono alta conduttività e rugosità superficiale) mantenendo allo stesso tempo un'altra trasparenza. Queste caratteristiche rendono lo ZnO depositato per LP-CVD ideale come elettrodo trasparente per celle solari sottili, celle che necessitano sistemi di intrappolamento della luce per assorbire tutte le componenti dello spettro solare. Sebbene le proprietà degli strati in ZnO:B siano state precedentemente ottimizzate per applicazioni in celle solari, l'esatto processo di crescita della pellicola dipende da differenti parametri di deposizione il cui effetto non é stato completamente spiegato. Questa tesi chiarisce i processi di crescita della pellicola (nucleazione e successiva evoluzione) e di incorporazione degli atomi di boro nell'ossido di zinco.

Inizialmente, abbiamo stabilito quali siano i parametri di deposizione che influenzano maggiormente le proprietà delle pellicole di ZnO non drogate: la temperatura di deposizione, il rapporto in fase gassosa tra i precursori molecolari e il flusso totale di gas. Variando questi tre parametri abbiamo dimostrato che le pellicole a pronunciata rugosità tipicamente utilizzati in celle solari possono essere depositati a 120 °C, temperatura molto inferiore dei 180 °C utilizzati in precedenza. Tutti gli strati ottenuti variando questi tre parametri sono stati caratterizzati a stadi successivi della loro crescita. Queste analisi hanno mostrato il legame dell'orientazione preferenziale della pellicola dalle condizioni di deposizione. Abbiamo giustificato questo legame tramite un modello basato sul cammino libero medio degli atomi adsorbiti sulla superficie della pellicola. Regolando opportunamente i parametri di deposizione, secondo questo modello, siamo stati in grado di controllare l'orientazione preferenziale della pellicola durante

ii

la crescita ottenendo di conseguenza un aumento nella dimensione dei grani.

In seguito, abbiamo analizzato la conduttività delle pellicole di ossido di zinco drogato boro. Per diminuire la resistività, atomi estranei al reticolo cristallino di ZnO (boro) sono introdotti nella pellicola aggiungendo un precursore molecolare del boro in fase gassosa. Gli atomi di boro agiscono come donatori di elettroni nel reticolo di ZnO, aumentando la conduttività elettrica e diminuendo la trasparenza. Questo lavoro quantifica come la concentrazione e la distribuzione degli atomi di boro influiscono sulla conduttività della pellicola. La quantificazione degli atomi di boro incorporati nel film è stata eseguita attraverso l'analisi da reazione nucleare (NRA). In particolare, abbiamo osservato che alte concentrazioni del gas precursore dell'ossigeno favoriscono l'incorporazione del boro nel film. Attraverso la combinazione della spettroscopia di massa degli ioni secondari a scala nanometrica (nanoSIMS) e della misura del voltaggio di contatto mediante microscopia KPF, abbiamo dimostrato che gli atomi di boro vengono incorporati solamente in uno dei due lati di ciascun grano. Questa osservazione contraddice il modello più accettato secondo il quale la distribuzione degli atomi del drogante nel film è ritenuta essere uniforme.

Trasparenza e conduttività elettrica delle pellicole di ZnO non dipendono solamente dalla concentrazione dei portatori di carica ma anche dalla loro mobilità. L'aumento della mobilità dei portatori favorisce sia la trasparenza che la conduttività. La comprensione dei meccanismi fisici che limitano la mobilità dei portatori è essenziale per progettare i film più adatti alle varie applicazioni. Le cause che limitano la mobilità dei portatori sono state investigate per differenti concentrazioni di difetti intrinseci e atomi di boro. Abbiamo osservato che per la stessa concentrazione di boro, la fonte principale di dispersione degli elettroni dipende dalla concentrazione di difetti intrinseci: per pellicole con basse concentrazioni di difetti intrinseci la fonte principale sono i bordi di grano, per pellicole con concentrazioni più elevate la fonte principale sono i processi che si producono nella regione cristallina.

Infine, le pellicole in ZnO:B ottenute per LP-CVD sono state applicate come contatti trasparenti in quattro tipi differenti di celle solari: silicio amorfo/silicio microcristallino, silicio amorfo, rame indio gallio selenio (CIGS) e eterogiunzioni a base di silicio. I vantaggi delle pellicole ottimizzate per queste quattro celle solari riguardano la semplificazioni del processo di fabbricazione, la riduzione della riflettanza e degli assorbimenti parassiti e una migliore comprensione dei meccanismi di trasporto delle cariche attraverso il dispositivo.

Questa tesi presenta nuove scoperte riguardo all'influenza dei parametri di deposizione sui processi di crescita e di incorporazione del boro delle pellicole di ossido di zinco. Inoltre, dimostra l'applicabilità di tecniche di caratterizzazione che non erano state precedentemente utilizzate per pellicole di ossido di zinco. Questa tesi rappresenta un passo in avanti verso la comprensione e il miglioramento delle proprietà delle pellicole di ZnO:B.

Parole chiave: ossido conduttivo trasparente, pellicola sottile, fotovoltaico, contatto trasparente, ossido di zinco, deposizione chimica in fase vapore, proprietà elettriche, proprietà ottiche, mobilità dei portatori di carica, orientazione preferenziale della pellicola, concentrazione del drogante, distribuzione del drogante, bordo di grano, processi di sparpagliamento degli elettroni, dietilzinco, acqua, boro, nanoSIMS.

Acknowledgements

Acknowledgements

List of Abbreviations and Symbols

A	absorptance
ACOM	automated crystal orientation mapping
AFM	atomic force microscopy
a-Si:H	hydrogenated amorphous silicon
E_b	height of potential barrier at grain boundary
EQE	external quantum efficiency
ϕ	total gas flow
FF	fill factor
FTIR	Fourier transform infrared spectroscopy
$FWHM$	full width at half maximum
H_2O/DEZ	water to diethylzinc gas flow ratio
J_{sc}	short-circuit current density
KPFM	Kelvin probe force microscope
m^*	electron effective mass
μ_{opt}	optical mobility
N_e	free-carrier density
N_t	planar density of electron-traps at grain boundaries
nanoSIMS	secondary ion mass spectroscopy at nanometric scale
nid	non-intentionally doped
NRA	nuclear reaction analysis
R_{sh}	sheet resistance
ρ	resistivity
ρ_c	contact resistivity
TR	total reflectance
TT	total transmittance
T_{hp}	hot-plate temperature
V_{oc}	open-circuit voltage
WF	workfunction
$\langle x \rangle$	mean free path of adsorbed atom
x_{seg}	dopant segregation level
ZnO:Al	aluminum-doped zinc oxide
ZnO:B	boron-doped zinc oxide

Contents

Contents

List of Figures

List of Tables

1 Introduction

This thesis investigates the structural and optoelectronic properties of non-intentionally doped and boron-doped zinc oxide (ZnO and ZnO:B) films deposited by low-pressure chemical vapor deposition (LP-MOCVD). The general goal of this work is to control the film properties through the deposition process and to tailor films for new applications in photovoltaics.

This chapter describes the general scientific context and the research field in which this thesis was conducted. In Section 1.1, we state the requirements that a material should fulfill to be classified as a transparent conductive oxide (TCO). By going through the historical development of TCOs we present the characteristic properties of this unique class of materials. TCOs have growing importance in our everyday life, and they need to be synthesized from abundant, and possibly non-toxic, elements to satisfy the high demand in future years.

A commonly used TCO that complies with both of these requirements is zinc oxide (ZnO). ZnO is an n-type semiconductor material whose unit cell lacks inversion symmetry, leading to peculiar crystallographic and optoelectronic properties. The structural and optoelectronic properties of ZnO are presented in Section 1.2.

Among the various techniques used to deposit ZnO, we chose LP-MOCVD, a technique already used for ZnO deposition 30 years ago. The advantages and the main open questions related to ZnO films deposited by LP-MOCVD are presented in Section 1.3. The present thesis addresses some of these open questions, with a special focus on the structural development of the film and on the incorporation of the dopant in the film.

The goals and the outline of the thesis are presented in Section 1.4.

Finally, the main contributions of this thesis are highlighted in Section 1.5.

1.1 Optical Transmittance and Electrical Conductivity: TCO Mixed Blessing

As the name suggests, a transparent conductive oxide is a metal oxide that simultaneously features high optical transmittance in the visible region (generally higher than 80%), and high electrical conductivity (10^3 S/cm or larger). To be transparent in the range of visible light (390 and 700 nm), the oxide needs to have a band gap of at least 3.2 eV. (A smaller band gap can be used, relying upon the Burstein-Moss shift with doping to increase to the effective optical gap [Ingram et al., 2004]). Similar band gaps are typical for oxides formed with metals such as tin, cadmium, zinc and indium. Note that these are all ionic compounds. The electrical conductivity σ is provided by charge carriers that can move (quasi-) freely within the material:

$$\sigma = eN_e\mu_d,$$

(1.1)

where e is the elementary charge, N_e the carrier concentration and μ_d is the drift carrier mobility. When perfectly stoichiometric, these TCOs have no free charge carriers and therefore are dielectrics. Free carriers are commonly introduced in these oxides by modifying their stoichiometry or by incorporating appropriate extrinsic dopant atoms into the lattice.

TCOs are usually thin films grown in conditions of thermodynamic non-equilibrium featuring an intrinsic non-stoichiometry. The majority of them are O deficient and thus n-type materials [Klein, 2012]. In some cases the intrinsic carrier concentration can reach values up to $1 \cdot 10^{20}$ cm^{-3} [Minami, 2000], but generally it is lower and not sufficient to provide the conductivity required by the applications. The maximum carrier concentration achieved by adding extrinsic dopant atoms depends on the dopant solubility in the oxide [Minami, 2000] and can reach values up to $4 \cdot 10^{21}$ cm^{-3} [Ellmer, 2012]. In TCOs the increase in free-charge-carrier concentration is not always desired because above a certain value of N_e it reduces the optical transmittance. When an electromagnetic wave passes through a material containing free charge carriers, it can trigger collective oscillation of the carriers and be partially or totally absorbed. The extent of the interaction depends on the wavelength of the electromagnetic wave and on the concentration of the charge carriers. The maximum of absorptance happens at the so-called plasma wavelength λ_p:

$$\lambda_p = 2\pi c \sqrt{\frac{\epsilon_\infty m^*}{4\pi N_e e^2}},$$

(1.2)

where ϵ_∞ is the high-frequency permittivity and m^* is the carrier effective mass. Below this wavelength the electromagnetic wave is not absorbed by the free charge carriers and the material is transparent. The requirements set by Equation 1.1 for conductivity and by Equation 1.2 for transparency set the main trade-off for TCOs. On the one hand, the increase in free charge carriers is beneficial for the conductivity, but, on the other hand, it shifts the

plasma wavelength towards the visible region, reducing the transparency of the material. That is why, to increase the conductivity without reducing the transmittance, it is preferable to improve the carrier mobility.

1.1.1 Historical Development

The following historical survey of TCOs is based mainly on the detailed reviews of Bright and Ingram [Bright, 2007, Ingram et al., 2004].

The history of TCO materials starts more than 100 years ago. The first TCO to be synthesized was cadmium oxide (CdO). In 1907 Bädeker obtained a thin film of CdO by thermally oxidizing in air a film of sputtered cadmium [Bright, 2007]. Bädeker, considered the father of TCOs, studied the electrical properties of various compounds (CdO, CuI, Cu_2O, Ag_2Se) [Grundmann, 2015] that today we know as semiconductors. Although his characterization and deposition tools were far more primitive than ours (e.g. film thickness was assessed using the specific weight of the compound and by weighing the sample before and after etching the film), he was able to obtain a resistivity for CdO film as low as $1.2 \cdot 10^{-3}$ Ω cm [Grundmann, 2015]. Today CdO is not widely used due to its toxicity but it remains theoretically interesting because of its impressive electron mobility: 200 cm^2/Vs at a carrier concentration around $1 \cdot 10^{20}$ cm^{-3} (using single-crystal Mg as the substrate) [Wang et al., 2006].
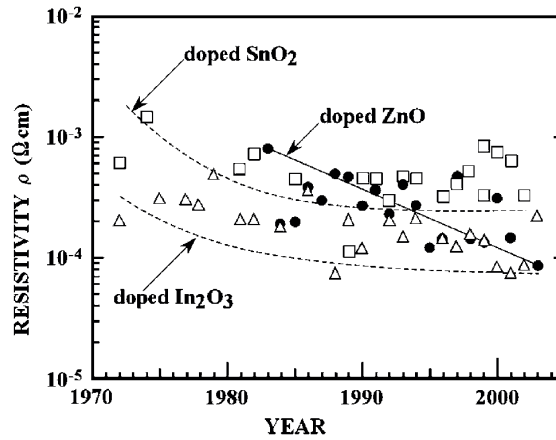
Figure 1.1: Chronological evolution of the resistivities of three of the most common TCO materials: SnO_2 ($\square$), In_2O_3 ($\triangle$) and ZnO ($\bullet$) [Minami, 2005].

Post-deposition oxidation of metal films was also the first method to produce tin oxide (SnO_2) in 1932 [Littleton, 1938]. SnO_2 thin films were the first TCOs to be used in an application. Deposited on glass, these films were employed as aircraft windshield de-icers in World War II [Gordon, 2000].

Afterwards, indium oxide (In_2O_3)-based TCOs were developed, and the fabrication process of indium-tin oxide (ITO) by chemical deposition (pyrolysis) from $InCl_4$ was patented in 1950 [Zunick, 1950]. The post-deposition oxidation of metal was an approach not easy to control,

and therefore researches started working on sintering powders of metal oxides to be used as sputtering targets to deposit TCO films. In the 1970s, using this technique, Vossen found the optimum In_2O_3/SnO_2 target ratio to be 80/20 mole% for ITO; however, he indicated that due to preferential re-sputtering, the material composition of the film was not the same as the one of the target [Vossen, 1976]. In 1972, Fraser and Cook using partially oxidized ITO targets (DC conductive for sputtering) obtained a thin film with a resistivity of $1.8 \cdot 10^{-4}$ Ωcm and visible transmittance close to 85%. [Fraser and Cook, 1972]

In the same years ZnO-based TCOs were developed. In 1971, both the first Al-doped ZnO (ZnO:Al) film [Wasa and Hayakawa, 1971] and the first ZnO-based varistor [Matsuoka, 1971] were reported. Since then, investigations of various possible dopants were performed, and deposited films have been continuously improved (cf. Figure 1.1) reaching typical conductivities on the order of $5 \cdot 10^{-4}$ Ωcm for SnO_2 and $1 \cdot 10^{-4}$ Ωcm for both ITO and ZnO [Minami, 2000].

Table 1.1: Overview of the performances of the main TCO films deposited on glass at a maximum temperature of 200°C.

film	deposition technique	T °C	N_e $10^{20} cm^{-3}$	μ cm^2/Vs	ρ $m\Omega cm$	d nm	R_{sh} Ω_{sq}	T_{vis} %	Reference
ZnO	LP-MOCVD	180, 200*	0.3	58	3.6	2000	18	90	[Ding et al., 2013]
ZnO:B	LP-MOCVD	180	1.2	45	1.2	2000	6	87	[Ding et al., 2013]
ZnO:Ga	RF-MS	200	7.5	19	0.45	600	7	85	[Wang et al., 1996]
ZnO:Al	RF-MS	RT	1.5	45	0.93	200	46	85	[Nanto et al., 1984]
IZO	RF-MS	60, 200**	2.3	60	0.45	100	45	80	[Morales-Masis et al., 2015]
IO:H	ALD	130	1.7	138	0.27	75	36	84	[Macco et al., 2014]
ITO	DC-MS	200	6.0	40	0.26	70	37	80	[Tuna et al., 2010]
IMO	DC-MS	RT	5.2	20.2	0.60	130	46	80	[Miao et al., 2006]

RF-MS: radio frequency magnetron sputtering;
ALD: atomic layer deposition;
DC-MS: direct current magnetron sputtering;
RT: room temperature;
* 20' annealing in hydrogen plasma;
** 20' annealing in air.

The successes of binary compounds fostered interest in multicomponent compounds. During the 1980s, TCOs like $ZnSnO_3$, $MgIn_2O_4$, $GaInO_3$ and $Zn_2In_2O_5$ were developed [Freeman et al., 2000]. In the 1990s, some of the binary combinations were thoroughly investigated, in particular the ZnO-In_2O_3 (IZO) system demonstrated excellent optoelectronic properties [Minami et al., 1995]. In 2005 Furubayashi *et al.* demonstrated Nb- or Ta-doped TiO_2 as a viable TCO: epitaxially grown films feature resistivities as low as $5 \cdot 10^{-4}$ Ω cm [Furubayashi et al., 2005].

$CuAlO_2$, the first p-type TCO with useful conductivity, was reported in 1997 [Kawazoe et al., 1997]. This development opened the route to the fabrication of a transparent *p-n* junction, which was demonstrated with the structure n^+-ZnO/n-ZnO/p-SrCu$_2$O$_2$/ITO. The diode, deposited on glass, had a transparency around 70% in the visible region [Kudo et al., 1999].

Flexible electronics is another topic of recent interest. The need for flexibility led researchers to consider the mechanical properties of TCO thin films. In this pursuit, the development of ionic amorphous oxide semiconductors (IAOS) such as CdO–PbO_2, $AgSbO_3$ and $InGaZnO_3$ [Hosono et al., 1996, Yasukawa et al., 1995, Orita et al., 2001] is of the main importance since the electrical properties of these amorphous materials are less affected by mechanical stress applied to the device. Other remarkable properties of IAOS are high-temperature stability and the potential for depositing films at low substrate temperatures (< 200°C) [Ellmer, 2012].
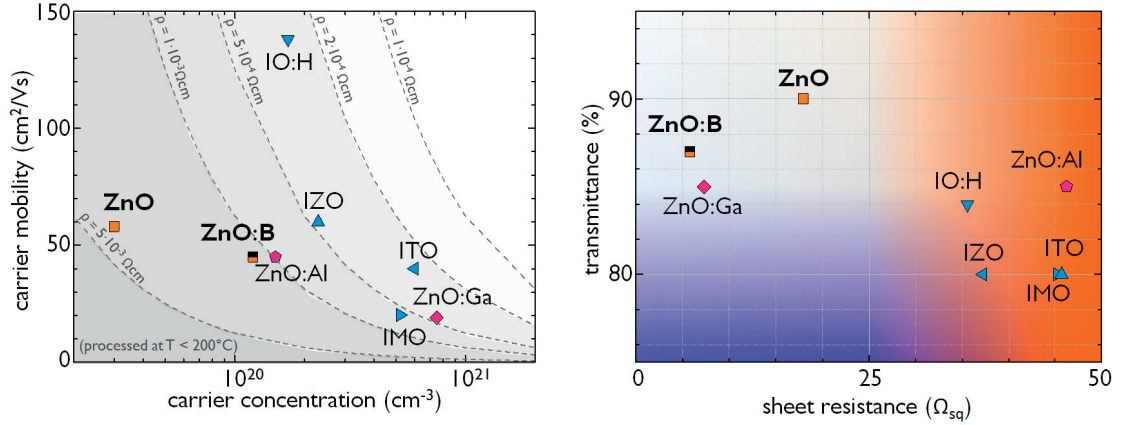
*Figure 1.2: Overview of the performances of several TCO films presented in Table 1.1: **(a)** Carrier mobility vs. carrier concentration; **(b)** Transmittance vs. sheet resistance. ZnO and ZnO:B (in bold) are the films investigated during this thesis.*

1.1.2 TCO Applications

Transparent conductive oxides play a major role in optoelectronics. In the last 50 years, to support the incessant progress of the electronic industry, the possibility of TCO applications have increased to such an extent that now we can find TCOs almost everywhere: from the supermarket iceboxes to smart phones and from photovoltaic modules to OLED television screens. In applications such as lighting, displays and solar cells, the optoelectronic properties of TCOs are instrumental for high-efficiency performance of devices [Kumar and Zhou, 2010, Ellmer, 2012, Holman et al., 2012, Frijnts et al., 2015].

In the following we describe some of the main applications in which TCOs are employed.

Low-Emissivity Windows. The goal of a window is to let the visible light pass through while screening (either by absorbing or reflecting) the heat transfer. The two parameters used to quantify these window properties are the visible transmittance (*VT*) and the solar heat-gain coefficient (*SHGC*). A low-emissivity windows combines high *VT* with low *SHGC*, by exploiting a TCO layer coated on its surface. In this passive application, good electrical conductivity is sacrificed for IR reflectivity and high transparency in the visible regime. The high IR reflectance of TCOs is used to improve the energy efficiency of building windows. In hot climates, TCO-coated glass reflects the infrared portion of the incident sunlight off the buildings. In cold

climates, infrared radiation is reflected back into the buildings. It was estimated that low-emissivity glazing can contribute up to 32% of the European Union's 2020 target of 300 MT/y CO^2 reduction in the building sector [Schreuder, 2014].

Electrochromic Windows. Also known as "smart windows", these windows are able to change their reflectance and transmittance when an electric field is applied (electrochromism). The TCOs are used as transparent electrodes in order to provide the electric field to the electrochromic stack. The switching time between the reflective mode and transparent mode depends on the surface of the windows. At the moment they are applied in windows of vehicles, for example on the Boeing 787 Dreamliner aircraft.

Defrosting Windows. The TCO deposited on the window is heated by passing a current through it (Joule effect) allowing it to defrost the windows of vehicles such as cars and aircrafts. Tin oxide is an ideal candidate due to its low cost and high durability.

Electromagnetic Shields. Electromagnetic shielding is often used to limit external electromagnetic interferences, for example to limit electromagnetic emission of display screens. TCOs are particularly suitable in cases when an electromagnetic shield needs to be transparent. The TCO free charge carriers interact with the applied electromagnetic field (reflecting or absorbing it) preventing the field from crossing the shield.

Flat-Panel Displays. Currently one of the main applications of TCOs is as front electrodes in flat-panel displays, for which high conductivity and transparency are needed. Flat-panel displays are constituted by thermally sensitive layers and therefore the low deposition temperature is another main factor for the choice of the appropriate TCO.

Photovoltaic Modules. TCO thin films are often employed to extract the charge carriers generated within the photovoltaic absorber of silicon heterojunction, cadmium telluride and copper indium gallium selenide solar cells. The main requirements for this application are high transparency, high conductivity, large-area capability, low deposition temperature and long durability (resistant to moisture ingression and light exposure).

Transparent Electronics. Thin-film transistors, OLEDs and touch screens are only some of the recent applications in which TCOs play an essential role. The development of a reliable p-type TCO is the sine qua non to produce a fully transparent active electronic element to further develop this field.

1.1.3 Needs for Durable and Long-Lasting TCO Supply

ITO is, so far, the most used TCO owing its success to a combination of factors like etchability, low deposition temperature and low resistivity. Flat-panel displays are the leading application for indium consuming more than 50% of the world primary output of indium [Matos, 2006]. In the last years, photovoltaic cells and other competing uses are further increasing demand for indium.

Increasing the indium supply to comply with the industrial demand is not straightforward since most of the world primary indium supply originates as a by-product of processing zinc ores mined in China, Peru and Australia, and to a lesser extent as a by-product of copper, lead, tin and precious metals. Considering historical prices, it would be unlikely that production of the primary products would increase in order to produce more of indium metal [Bleiwas, 2010].

Currently the indium supply is finely matched to industry demand. Although new supplies from mining are available, they are not economically viable. This can result in potential price volatility as sharp moves in demand create short-term price escalations. These factors make it unlikely that ITO can readily become the commodity product that device manufacturers require.

Alternative TCOs based on less-costly raw materials, such as tin, zinc and titanium already exist but can match the performance offered by In-based TCOs only in some cases. The improvement of TCOs based on these materials is the path to ensure a robust development for all the technologies requiring the unique properties of this class of materials.

Table 1.2: Abundance (atom fraction) of the chemical elements in Earth's continental crust and price (2013, U.S. market) of the metals composing the most common TCOs. Silver and gold are listed for comparison [McNutt, 2013, Haxel et al., 2005].

Element	Abundance 10^6 Si atoms	World Production t	Price $\$/kg$
Ti*	$8 \cdot 10^3$	$1.0 \cdot 10^{7*}$	$1.1 \cdot 10^1$
Zn	$1 \cdot 10^2$	$1.3 \cdot 10^7$	$2.2 \cdot 10^0$
Ga	$2 \cdot 10^1$	$5.7 \cdot 10^2$	$6.0 \cdot 10^2$
Sn	$3 \cdot 10^0$	$3.2 \cdot 10^5$	$2.7 \cdot 10^1$
Cd	$8 \cdot 10^{-2}$	$2.2 \cdot 10^4$	$4.0 \cdot 10^0$
In	$5 \cdot 10^{-2}$	$8.0 \cdot 10^2$	$5.7 \cdot 10^2$
Ag	$4 \cdot 10^{-2}$	$2.6 \cdot 10^4$	$7.7 \cdot 10^2$
Au	$1 \cdot 10^{-3}$	$2.8 \cdot 10^3$	$4.0 \cdot 10^4$

* For Ti the world production value is given for the concentrated mineral, i.e. the sum of titaniferous slag, rutile, ilmenite and leucoxene.

1.2 General Properties of Zinc Oxide

Zinc compounds were probably used by early humans as a paint or medicinal ointment. Zinc oxide ointment is already mentioned in 1st century A.D. as a preferred treatment for a variety of skin conditions by the Greek physician Dioscorides [Oleson, 2008] and in 11th century A.D. by Avicenna [Harding, 2006].

Zinc oxide is an inorganic compound composed by one atom of oxygen (O) and one of zinc

(Zn). It is present in the Earth's crust as the mineral zincite, but most of the ZnO used in industry is produced synthetically [Völz, 2006]. ZnO is not toxic and, due to its reflective properties, is often used in sunblock creams. It is also used as an additive in numerous products including rubbers, plastics, ceramics, glass, cement, adhesives, sealants, lubricants, paints, ointments, pigments, foods, batteries, fire retardants and first-aid tapes.

1.2.1 Wurtzite: A Non-Centrosymmetric Structure

Zinc oxide crystallizes in two main forms: hexagonal wurtzite, shown in Figure 1.3, and cubic zincblende. In both cases, the zinc and oxide centers are tetrahedral. The bonding in ZnO is largely ionic (Zn^{2+}-O^{2-}) with the corresponding radii of 0.074 nm for Zn^{2+} and 0.140 nm for O^{2-} [Klingshirn et al., 2010]. The face-centered cubic (FCC) zincblende form can be stabilized by growing ZnO on substrates with a cubic lattice structure.
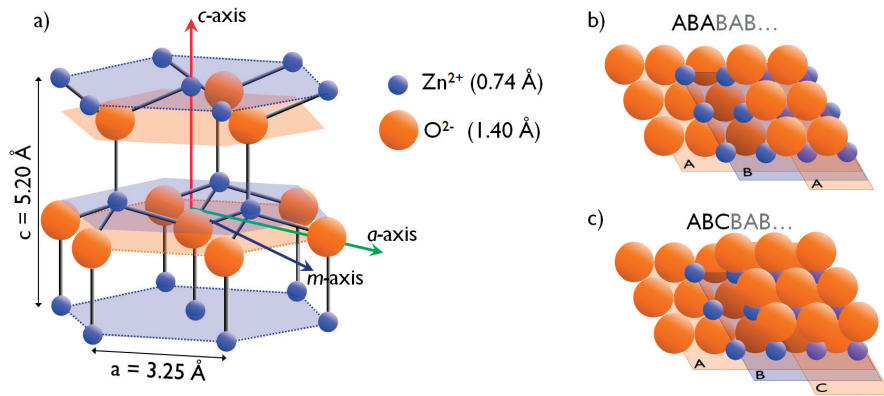
*Figure 1.3: **(a)** Wurtzite structure showing the alternation of O and Zn planes perpendicular to the c-axis. **(b)** Atom stacking sequence of regular wurtzite (ABABAB...) and **(c)** basal stacking fault in the wurtzite configuration (ABCBAB...).*

The wurtzite structure is part of the hexagonal closed-packed (HCP) system and consists of tetrahedrally coordinated atoms. Atoms are packed in bilayer planes of oxygen and zinc along the *c*-axis in an ABABAB pattern, as presented in Figure 1.3. The lattice constants are $a = 0.325$ nm and $c = 0.52$ nm; their ratio $c/a \approx 1.60$. The main directions within the wurtzite structure are the *c*-axis (perpendicular to the hexagonal basal plane), the *a*-axis and the *m*-axis (both lying in the basal plane). The wurtzite is a non-centrosymmetric structure. It possesses an electrical dipole along the *c*-axis whose polarity depends on the relative position of O and Zn atoms in the bond parallel to the *c*-axis: Zn-polar if the Zn atom is below (as in Figure 1.3), O-polar if the O atom is below [Morkoç and Özgür, 2009].

Due to the high electronegativity of O, the Zn-O bond is ionic and therefore the electrons forming the bond are displaced from to the Zn nuclei to the O nuclei. Along the *c*-axis, planes composed only by Zn atoms alternate with the ones composed only by O atoms. Combined with the non-centro-symmetric structure of wurtzitic cell, this creates electric dipoles oriented
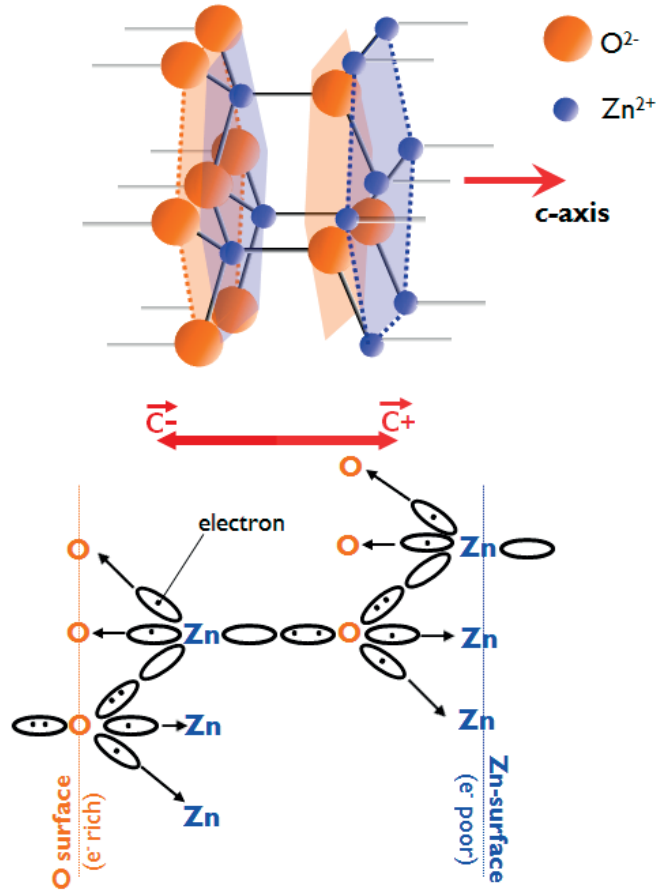
Figure 1.4: Difference in electron concentration between Zn- and O-terminated surfaces, adapted from [Mariano and Hanneman, 1963].

along the axis.

As shown in Figure 1.4, the atoms belonging to a plane are bound to three atoms in one direction and one atom in the other direction. Due to energy minimization, surfaces are formed at the plane that exposes only one dangling bond per atom. The two directions of the *c*-axis are not equivalent: along the *c*+ direction the single dangling bond is formed from a Zn to an O atom, while along the *c*- direction the single dangling bond is formed from an O to a Zn atom. Therefore, grains growing along *c*+ will be Zn-terminated, while the ones growing along the *c*- will be O terminated. As demonstrated by Tasker [Tasker, 1979] Both types of termination have unbalanced charges at surface and undergo reconstruction [Kunat et al., 2002, Kresse et al., 2003, Meyer, 2004]. In particular, due to the ionic nature of the bond, O-terminated planes have higher concentration of electrons than Zn-terminated ones.

The higher electron concentration makes the O-terminated surfaces more chemically reactive under reducing environment, and cause their faster etching rate [Mariano and Hanneman, 1963, Jo et al., 2005]. The higher electron concentration at O surfaces is exploited for gas

sensing applications due to the higher sensitivity to certain gases [Adachi et al., 2015].

1.2.2 Basal Stacking Faults

One of the most common defects in ZnO is the stacking fault on the hexagonal basal plane [Sagalowicz and Fox, 1999, Gerthsen et al., 2002]. As discussed, the normal stacking sequence of the wurtzite structure is ABABAB. A fault is the substitution of the wurtzite stack with the zincblende (atoms bind on the FCC hollow site – C – instead of HCP site –A): ABCBAB (cf. Figure 1.3). It has been calculated that in ZnO this fault has low formation energy [Yan et al., 2004, Blackwell et al., 2013]. In ZnO, the *c*-axis is a polar axis and the stacking fault should create a discontinuity in the polarization vector that could induce a compensating building up potential [Yamada et al., 2007, Konar et al., 2011]. This potential could then interact with the carriers modifying the transport properties along the *c*-axis (perpendicular to the basal plane). However, so far no electrical anisotropy due to stacking faults has been reported for polycrystalline ZnO.

1.2.3 Semiconducting Properties

ZnO has a direct and wide band gap of 3.4 eV [Mang et al., 1995, Reynolds et al., 1999]. In reality, because of the frequent impurity defects which introduce tail states close to the conduction band, the band gap of the intrinsic material varies typically between 3.2 and 3.4 eV at room temperature. This translates into the onset of light absorption at $\approx$ 360–390 nm [Ellmer et al., 2008]. Furthermore the band gap ZnO can be engineered, for example by alloying MgO (down to 2.3 eV) or CdO (up to 4.0 eV) [Ohtomo et al., 1998, Makino et al., 2001].

Non-intentionally doped (nid) ZnO is usually n-type due to the presence of intrinsic defects, such as zinc interstitials (Zn_i) and oxygen vacancies (O_v). The electron concentration of nid samples can be as high as $1 \cdot 10^{20}$ cm^{-3} [Minami, 2000]. Although it has been proposed for long time that the sources of free electrons are O_v and Zn_i [Harrison, 1954, Hagemark, 1976], their actual source is currently debated. It has been shown that O_v are deep donors and cannot directly contribute to the n-type character of ZnO [Janotti and Van de Walle, 2005]. Recently, it has been suggested that hydrogen (H), which is present in almost all growth environments, can substitute for O and act as a shallow donor [Van de Walle, 2000, Janotti and Van de Walle, 2009]. The H substitution of O would explain the stability of the n-type character with temperature and its dependence on reducing/oxidizing environments. Although the question is still not resolved, the researchers agree on the fact that the presence of O_v is a necessary but not sufficient condition to the n-type character of ZnO.

Another experimental observation that contradicts the hypothesis that O_v is a direct source of electrons in nid ZnO comes from the calculated charge Z of the ionized impurities. O_v should create an ionized center with a double negative charge ($Z = 2$). Bikowski *et al.* analyzed the dependence of carrier mobility on carrier concentration over a large collection of data for
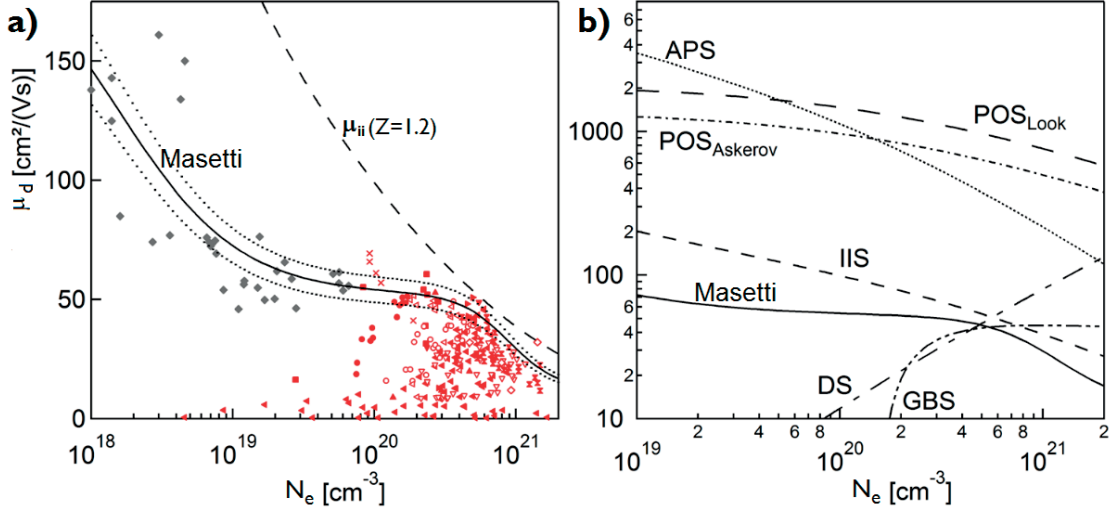
Figure 1.5: **(a)** *Drift mobility (μ_d) of ZnO samples as a function of free-carrier concentration (N_e). The markers show experimental data for single-crystalline (grey markers) and polycrystalline ZnO (red markers), while the solid line represents the Masetti semi-empirical curve for single crystal ZnO [Masetti et al., 1983]. The dotted lines mark 10% of the Masetti curve and the dashed line shows the theoretical values for the electron scattering by ionized impurities assuming $Z = 1.2$ [Bikowski and Ellmer, 2014].* **(b)** *The main mechanisms of electron scattering calculated for ZnO thin films: acoustical phonons (APS), polar-optical phonons (POS), grain boundaries (GBS), and dislocations (DS) and ionized impurities (IIS), [Bikowski and Ellmer, 2014].*

polycrystalline ZnO thin films (presented in Figure 1.5). They found the best fit for values of ionized impurity charge close to $Z = 1.2$, which can be explained only by assuming that the majority of ionized scattering centers are singly ionized [Bikowski and Ellmer, 2014].

Ionized impurities are supposed to be the main source of electron scattering at high doping levels ($N_e > 1 \cdot 10^{20}$ cm^{-3}) but there are other scattering mechanisms too. The other main sources of electron scattering in ZnO films are listed below.

Neutral Impurities. Lattice defects that are electrically neutral.

Optical Phonons. Polar-optical phonons appear in material having at least partially ionic bonding. Thermal oscillation in anti-phase of the atoms generates an electric dipole momentum which strongly interacts with electromagnetic waves.

Acoustical Phonons. Acoustical phonons are caused by thermal oscillations of the atom in the lattice corresponding to pressure waves (i.e. in-phase oscillation of the atoms).

Grain Boundaries. In polycrystalline materials the boundaries of the grains are atomically disordered regions. Additionally they are supposed to collect amphoteric impurities that trap charge carriers.

Dislocations. Other defects, e.g. screw and edge dislocations, within a crystal structure are

very often present in polycrystalline films.

The sources of electron scattering relevant for LP-MOCVD ZnO films will be investigated in detail in Chapter 4.

1.3   LP-MOCVD ZnO:B, Known Properties and Open Questions

In this thesis, we used the low pressure metalorganic chemical vapour deposition (LP-MOCVD) to obtain ZnO films. For many applications and for solar cells in particular, deposition temperatures below 200 °C are required if we want to avoid to modify the properties of the other layers of the cells on which the TCO is deposited [Shah et al., 1999, De Wolf et al., 2012, Hagendorfer et al., 2014]. This constraint limits the choice in terms of material and deposition techniques. LP-MOCVD is one of the techniques which allow depositions below 200 °C (cf. Table 1.1).

Another important reason we chose this technique is because LP-MOCVD ZnO films combine high transmittance and low sheet resistance. Figure 1.2 and Table 1.1 show the performance of some of the most commonly used TCOs. When comparing the resistivity of the different TCOs (Figure 1.2a) ZnO and ZnO:B films are among the more resistive. However, for the applications, the parameter that determines the ohmic losses is not the resistivity ρ but the sheet resistance R_{sh}, that can be decreased by increasing the film thickness d:

$$R_{sh} = \frac{\rho}{d} \tag{1.3}$$

On the one hand, the low resistivity of LP-MOCVD ZnO and ZnO:B prevents these layers to be used in the applications where they are required to be very thin (e.g. in flexible devices). On the other hand, for applications where the thickness is not an issue, ZnO and ZnO:B films provide the highest transmittance at low R_{sh} (cf. Figure 1.2a).

In addition, two advantages of the LP-MOCVD technique are the practical simplicity of deposition and the fast film growth rate. LP-MOCVD produces polycrystalline ZnO films with optoelectronic properties particularly suited for thin-film solar cells. The use of ZnO in solar cells is widespread and dates back at least 30 years, and has resulted in the in-depth investigation of optimization of the films for this particular task. Despite being a widely used and researched material, there remain some fundamental questions about the properties of ZnO, limiting the potential of this material for photovoltaic and other applications.

ZnO films have been deposited by the oxidation of diethylzinc (DEZ: $Zn(C_2H_5)_2$) since the beginning of the 1980s [Ghandhi et al., 1980, Shealy et al., 1981]. Although different gas precursors for O have been tried [Lau et al., 1980], the films showing the best optoelectronic properties are deposited using water vapor to oxide the DEZ.

During *chemical vapor deposition* (CVD) the film is formed by chemical reactions happening between two (or more) gas species on a heated substrate. The structural and optoelectronic properties of the films deposited by CVD are highly sensitive to the substrate temperature. Therefore, uniform heating is essential in order to deposit a film with uniform properties. Working at *low pressures* (0.1–1 mbar) ensures larger diffusivity of the gas species with respect to the atmospheric pressure, which in turn favors larger uniformity of deposition, improved conformal coverage and lower contamination and minimizes the reactions in the gas phase [Ohring, 2002b]. Using a *metalorganic* precursor for the metallic species allows us to deposit films with good uniformity at low temperatures. This is because the weak bond between the metal and the organic groups allows for an easy dissociation of the molecule, providing a uniform and constant supply of metal over the whole substrate surface.

The overall reaction responsible for the formation of ZnO films from H_2O and DEZ gas precursors is [Lau et al., 1980]:

$$Zn(C_2H_5)_{2(g)} + H_2O_{(g)} \rightarrow ZnO_{(s)} + 2C_2H_{6(g)} \tag{1.4}$$
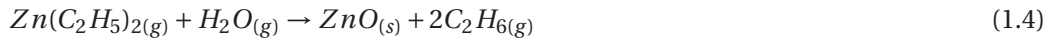
The actual exact reaction chain varies with the deposition conditions [Smith and Schlegel, 2003].

In order to reduce the resistivity, boron atoms are incorporated into ZnO films. Diborane (B_2H_6) gas is added as a B precursor in the gas phase. Boron atoms substitute Zn atoms in the ZnO lattice and act as donors. The consequent increase in the free-carrier concentration leads to an increase of the conductivity but at the same time to an increase of the absorptance in the IR (cf. Figure1.6).

Historically, LP-MOCVD ZnO:B films have been applied mainly as front electrodes in photovoltaic cells because of their transparency, the pronounced surface roughness and the low deposition temperature (< 200 °C). The higher transparency reduces parasitic absorption and the surface roughness increases the collection probability of the photon within the absorber [Frijnts et al., 2015], making ZnO:B layers ideal for application in thin-film solar cells (where light-management schemes are essential for high-performance devices). The properties of ZnO:B layers that are relevant for solar cell efficiency, such as absorptance and conductivity, are well-known and have been optimized significantly [Wenas et al., 1991b, Tabuchi et al., 1993, Faÿ et al., 2005, Nicolay et al., 2012]. Nevertheless, the mechanisms behind the film growth and dopant incorporation as well as the influence of the intrinsic and extrinsic defects on the electron scattering have not been fully clarified.

In the following we review the state of the art in ZnO:B films used as the front contact in thin-film solar cells and point out the main open questions.
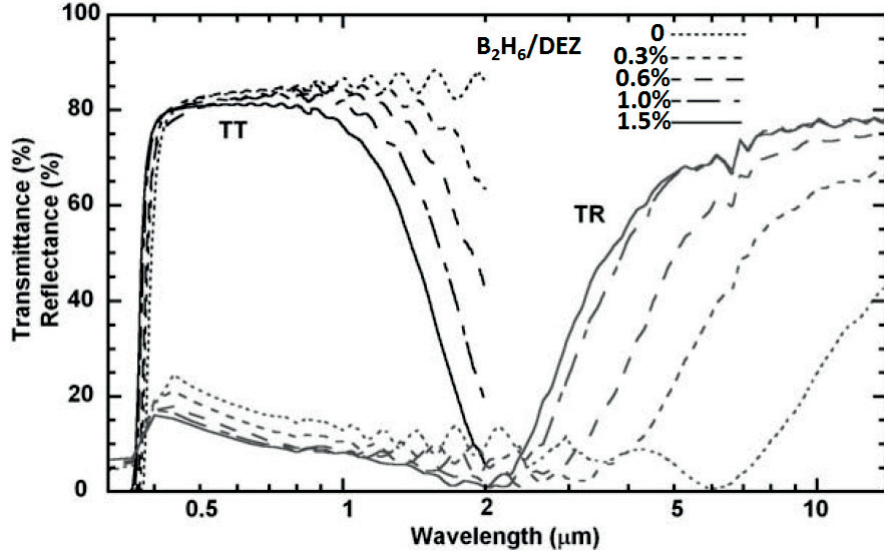
Figure 1.6: Total transmittance TT and total reflectance TR for 2-µm-thick ZnO films, for which the gas phase doping ratio B_2H_6/DEZ used during the deposition was varied from 0 (non-intentionally doped) to 1.5% (highly doped), [Steinhauser, 2008].

1.3.1 Layer Optimization for Thin-Film Si-Based Solar Cells

In terms of light-trapping ability when applied in thin-film solar cells, the ideal film morphology is the one provided by the *a*-textured films as demonstrated by Battaglia *et al.*[Battaglia et al., 2012]. Moreover, the *a*-textured films show also the lowest resistivity among samples deposited at low deposition temperatures: in 1991 Wenas *et al.* already obtained $2.5 \cdot 10^{-3}$ Ωcm [Wenas et al., 1991b], decreased to $1.0 \cdot 10^{-3}$ Ω cm by Faÿ [Faÿ, 2003].

Further improvements of the light-trapping and electronic properties seem unlikely within a one-step deposition. Attempts to reduce the absorptance, modify the surface roughness and reduce the resistivity have been done by means of a two-step deposition; i.e. varying the deposition conditions during film growth [Ding et al., 2012, Hongsingthong et al., 2013, Chen et al., 2015] or by means of post-deposition treatments [Ding et al., 2014].

The investigation of the space of the deposition parameters has been rarely performed [Faÿ, 2003] and the deposition temperature is the only parameter thoroughly investigated in terms of its effect on optoelectronic properties [Wenas et al., 1991a, Faÿ et al., 2005, Maejima et al., 2014] and on film growth mechanisms [Nicolay et al., 2009]. Only recently the H_2O/DEZ ratio has been manipulated to tailor the film morphology and preferential orientation in order to increase cell performance [Nicolay et al., 2012, Hongsingthong et al., 2013].

A detailed investigation of the simultaneous effect of the main controllable deposition parameters, namely deposition temperature, precursor gas ratio and total gas flow, could shed light on the film growth mechanisms and possibly increase the range of deposition conditions for

the different types of films. Moreover, the development of layers with new morphologies and useful optoelectronic properties could widen the possible applications of ZnO:B films.

1.3.2 Electron Scattering Sources: from Grain Boundaries to Ionized Impurities

Electrons moving in thin films experience scattering due to different sources. In LP-MOCVD ZnO:B films, the contribution of each scattering source has been assessed in a semi-quantitative way only for a-textured films [Myong et al., 2007, Steinhauser et al., 2007]. It was demonstrated that the carrier mobility is limited at low doping concentrations by the scattering from grain boundaries and at high doping concentrations by the scattering from ionized impurities. Therefore, in order to achieve lower resistivities, it would be necessary to reduce the detrimental influence of the ionized impurities.

A limitation of LP-MOCVD ZnO:B is represented by the low maximum achievable carrier concentration($N_e \approx 3 \cdot 10^{20}$ cm^{-3}) [Faÿ, 2003, Nomoto et al., 2011]. The main consequences are the moderate minimum resistivity (preventing ZnO:B from being used in flexible devices, where thin TCOs are required), and higher sensitivity to water ingression. The maximum achievable carrier concentration is usually related to the solubility limit of the dopant atoms in the crystalline lattice of the host material. Thus, the higher maximum carrier concentration of ZnO:Al ($1.5 \cdot 10^{21}$ cm^{-3}) is attributed to the solubility limit of Al in ZnO ($\approx 4\%$ [Ellmer, 2001]), which is four times larger than that of B ($\approx 1\%$ [Pawar et al., 2005]). Minami *et al.* compared the properties obtained by doping sputtered ZnO with different impurities from group III (B, Al, Ga, In) finding that the best performances are obtained using Al as impurity [Minami et al., 1985]. Maejima *et al.* reported a carrier concentration of $6.1 \cdot 10^{20}$ cm^{-3} for ZnO:B films deposited by RF magnetron sputtering, i.e. two times larger than the one obtained with LP-MOCVD [Maejima et al., 2014]. This suggests that the solubility limit of B in ZnO deposited by LP-MOCVD is currently not the main limitation towards a lower resistivity.

A detailed investigation on the mechanism of dopant incorporation in the film and its dependence on the deposition condition can reveal the constraints on the carrier mobility (scattering mechanisms) and on carrier concentration (dopant incorporation).

1.3.3 Characterization Techniques

Previous work characterized mainly optical, electrical and some structural properties of LP-MOCVD ZnO:B films. The optical characterization has been usually performed using UV-VIS-NIR spectrophotometer [Wenas et al., 1991b, Faÿ et al., 2005] and Fourier transform infrared spectroscopy [Prunici et al., 2013, Steinhauser et al., 2007]. These two techniques allow to measure transmittance and reflectance and to calculate related parameters such as absorptance and some electronic properties (e.g. optical carrier mobility).

The electrical properties of ZnO:B films have been investigated using four-probe measurements [Boccard et al., 2012] and Hall effect setup [Ding et al., 2012, Koida et al., 2016] which

give access to the film resistivity, carrier concentration and carrier mobility.

Structural and morphological characterization have been performed using scanning electron microscopy [Tabuchi et al., 1993, Biron et al., 2013, Hänni et al., 2013], X-ray Diffraction [Wenas et al., 1991a, Nicolay et al., 2009] and transmission electron microscopy [Faÿ, 2003], mainly to investigate the morphology of the film surface.

On the one hand, all these techniques provide information useful for the optimization of the film properties in application such as solar cells. On the other hand, this set of information is not sufficient for the comprehension of the mechanisms responsible for the film evolution. This limits our ability to control the film properties by tuning the deposition parameters.

Within this thesis we used several characterization techniques to get spatially resolved information and perform elemental analyses. These techniques, rarely used to characterize TCO films, allowed us to move forward in the comprehension of the film formation and the incorporation of the dopant atoms in the film. We will describe the technical properties of these techniques in Chapter 2; here we highlight the benefits of these techniques for our analysis.

- *Automated crystal orientation mapping (ACOM)*. ZnO:B is a polycrystalline material in which the grain size depends on the film thickness. The films usually applied in solar cells have a film thickness of $\approx$ 1-2 μm and a grain size between 100-250 nm [Faÿ et al., 2005]. The knowledge of the preferential orientation of the grains composing the film (and analyze their evolution during the growth) is useful to understand which are the mechanisms governing the different stages of growth (nucleation, thickening and final stage). The analysis of the preferential orientation of the grains in the film is normally done using the electron backscattered diffraction technique (EBSD) whose spatial resolution is in the order of several hundreds of nanometer [Humphreys, 2001] and therefore not sufficient for our samples. The spatial resolution of ACOM, in the order of some tens of nanometers [Rauch and Dupuy, 2005], allows to perform an analysis of the preferential orientation of the grains in very thin films.

- *Secondary ion mass spectroscopy resolved at the nanometric scale (NanoSIMS)*. The distribution of impurity atoms in polycrystalline film is of high interest to understand how the doping process modifies the film optoelectrical properties. In ZnO:B the dopant is boron, a light element not easy to detect by energy dispersive x-ray due to its low x-ray atomic scattering factor [Birajdar et al., 2007]. SIMS measurements resolved at the nanometric scale are the ideal way to investigate the boron spatial distribution even at low concentrations ($\approx$ 1% atomic).

- *Kelvin probe force microscopy (KPFM)*. Local modifications of the electronic properties can be obtained using the KPFM. This investigation tool proved to be sensitive for example to local variation of the carrier concentration in ZnO thin film [Maragliano

et al., 2014]. This setup can bring useful information especially to understand the possible local modifications of the workfunctions in doped films.

- *Nuclear reaction analysis (NRA).* The concentration of boron atoms that are actually incorporated in the ZnO:B films has rarely been measured in previous work [Kobayashi and Nakada, 2014] and its dependence on the deposition parameters was never investigated. A detailed investigation of the deposition parameters influence on the boron concentration requires a technique sensitive to light elements in small concentrations. NRA is a technique suitable to detect a small concentration (down to 0.05%) of impurities in a host material and it is sensitive to light elements such as Li, B, C, N and F [Gavrilov et al., 2003]. It is, therefore, suitable to estimate the concentration of concentration of boron in ZnO films even at very low doping levels.

1.3.4 Application in Solar Cells
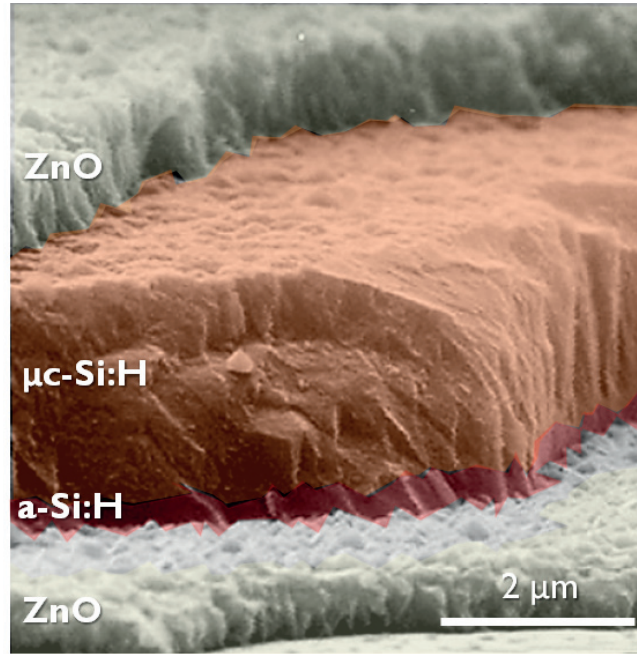
Figure 1.7: Example of application of LP-MOCVD ZnO as transparent electrode in tandem amorphous/microcrystalline silicon-based thin-film solar cells, [Shah et al., 1999].

Until recently, LP-MOCVD ZnO:B has been used mainly as transparent electrode in silicon-based thin-film solar cells [Tabuchi et al., 1993, Dominé et al., 2008, Schuttauf et al., 2014], as shown in Figure 1.7. The fine optimization of light-trapping capability together with low absorptance and low sheet resistance of the ZnO:B layer allowed for the fabrication of high-efficiency thin-film photovoltaic modules with industrial equipment. The efficiency of 1.4-m^2 tandem amorphous/microcrystalline-silicon (micromorph) modules has reached 10% in the production line [Stannowski et al., 2013] and up to 12.3% in the pilot line [TELSolar, 2014, Green et al., 2015]. Currently, the interest in this technology has decreased mainly due

to the dramatic drop in the cost of (mono- and poly-) crystalline silicon. Nonetheless, the characteristics of LP-MOCVD ZnO:B (low absorptance, low deposition temperatures and "soft" deposition conditions, i.e. no ion bombardment and no light emission) are appealing also for solar cells based on different absorbers. Recently, LP-MOCVD ZnO:B has been applied as an electrode in various types of solar cells, such as copper indium gallium selenide (CIGS) [Koida et al., 2016], silicon heterojunction (SHJ) [Favier et al., 2011], dye sensitized (DSSC) [Mahmood and Park, 2013] and inverted polymer based (IPSC) [Hu et al., 2013]. In general, the cells featuring ZnO:B films as the front contact gain in short-circuit current but have higher omhic losses with respect to the baseline TCO.

1.4   Aim and Outline of the Thesis

Despite the increasing importance of ZnO in semiconductor devices, the mechanisms of thin-film growth have not been investigated in depth. While, it is possible to find several studies dealing with the basic processes behind the growth of polycrystalline materials, very few consider specificities inherent to the deposition of materials with a peculiar crystallographic orientation such as ZnO in its wurtzite form or deposition regimes far from the thermodynamic equilibrium such as LP-MOCVD. The few studies addressing wurtzite ZnO refer mainly to the sputtering deposition process [Kluth et al., 2003, Kajikawa, 2006]. A detailed analysis of the growth mechanisms of LP-MOCVD ZnO is an important problem as it is the key to control the film growth. Such analysis will allow us to increase the range of deposition conditions and to develop new film morphologies, while maintaining useful optoelectronic properties that will better comply with the requirements of the various types of photovoltaic cells.

1.4.1   Goals of this Work

The purpose of this thesis is to:

- Define the properties of the film at nucleation, coalescence and "final" stage, in relation to the different LP-MOCVD deposition conditions.

- Investigate the mechanisms of dopant incorporation and their influence on the opto-electronic properties.

- Develop a growth model that is able to describe the film growth and dopant incorporation and that allows us to control the film evolution in order to tailor its properties.

- Improve the efficiency of various types of PV cells by applying the developed films with novel (morphological, electrical, optical) properties.

1.4.2   Outline

The thesis is structured as follows:

Chapter 2. We describe the preparation techniques (deposition and post-deposition) and characterization methods that were used during this work.

Chapter 3. We investigate the influence of the deposition parameters, namely temperature, precursor gas ratio and total gas flow, on the ZnO film properties at the different stages of film growth. By means of X-ray diffraction, atomic force microscope and automated crystal orientation mapping we analyse preferential orientation, structure and crystallinity for different types of films. We propose a model explaining the film evolution in terms of ad-atom mobility and the survival-of-the-fastest theory. We verify the main predictions of the developed model by means of simulations. We obtain a fine control over the film morphology (e.g. increased grain sizes) through control over the film preferential orientation.

Chapter 4. We show that by tuning the precursor gas ratio it is possible to control the concentration of the intrinsic defects and, consequently, the absorptance and the carrier concentration of a ZnO:B film. Using nuclear reaction analysis, we assess the dependence of the dopant incorporation on the precursor gas ratio (i.e. H_2O content in the gas phase). The interplay between intrinsic and extrinsic defects is further analyzed with respect to their combined effect on the electron scattering. Fourier transformed infrared spectroscopy and temperature-dependent Hall effect measurements define the main sources of scattering and quantify their relative contributions.

Chapter 5. By means of nano secondary ion mass spectroscopy (nanoSIMS) we determine that in ZnO:B films the dopant atoms segregate non-uniformly and incorporate only in one side of each grain (bimodal segregation). Using Kelvin probe force microscopy, we investigate the relation between dopant segregation and local electronic properties. The effect of the non-uniform distribution in the film of the dopant atoms on the charge transport properties and optical absorptance are described with the aid of simulations. Finally, we propose a model which attributes the bimodal dopant segregation to the polar surfaces of ZnO films.

Chapter 6. We applied a selection of films discussed in Chapter 3 to four different types of photovoltaic cells. A bilayer composed of *a*- and *c*- textured films is used to simplify the state of the art fabrication of tandem micromorph cells. The low density and low refractive index of porous films are assessed and used to demonstrate a reduced reflectance in amorphous silicon solar cells. The *a*-textured rough films are applied to reduce the parasitic losses in copper indium gallium selenide cells; the low deposition temperature demonstrated in Chapter 3 is shown to be beneficial for cell performance. The effect of the carrier concentration on the electronic band alignment in silicon heterojunction solar cells is explained combining carrier lifetime and photoemission spectroscopy measurements with simulations.

1.4.3 Experimental Approach

The previous literature addressed the performance optimization of mainly one type of ZnO:B films (*a*-texture rough films), which were characterized with standard techniques such as Hall

effect, FTIR spectroscopy, UV-VIS-NIR spectroscopy and scanning electron microscopy measurements. This thesis focuses on the deeper understanding of the film properties rather than on the performance optimization for a specific device. We followed a two-fold approach to draw in-depth conclusions about the mechanisms of film evolution and dopant incorporation.

First, we systematically explore a broad three-dimensional range of deposition parameters in order to understand their combined effect. Secondly, we exploit new characterization techniques, such as automated crystallographic orientation mapping (ACOM), secondary ion mass spectroscopy at nanometric scale (SIMS), Kelvin probe force micrscopy (KPFM), nuclear reaction analysis (NRA), energy dispersive spectroscopy (EDS) and monochromatic x-ray photoemission spectroscopy (XPS), to measure various film properties at consecutive stages of film growth.

To perform these specialized measurements, during this thesis, we set collaborations with various experts in laboratories spread all over Europe. In particular, the tight collaboration with the Interdisciplinary Center for Electron Microscopy (CIME) of EPFL helped to define and the achieve the goals of the present work.

1.5 Contributions of this Work to the Research Field

The main contributions of this thesis can be summarized as follows:

- We demonstrate that the main deposition parameters controlling the film properties are temperature, gas precursor ratio and total gas flow. The useful range of a single parameter (e.g. temperature) can be extended by setting appropriately the two other parameters (e.g. precursor gas ratio and total gas flow). We use this finding to relax the constraints on the deposition conditions (e.g. lower the deposition temperature).

- We explain the development of the preferential orientation, from nucleation to a late-stage film, in terms of adsorbed atom mobility. The proposed model correctly describes the influence of deposition parameters and has demonstrated its usefulness in controlling the film structural properties. This model can be generalized in future to control other CVD processes such as atomic layer deposition or plasma-enhanced chemical vapour deposition.

- We quantify the B-concentration incorporated into the film and demonstrate that it depends on the H_2O/DEZ ratio. We take into account the interplay of the intrinsic and extrinsic defects on the electron-scattering mechanisms and demonstrate that the doping level is not the only parameter which affects the carrier mobility. Importantly, we show that the concentration of intrinsic defects also plays a role in defining the limiting carrier mobility mechanism.

- Contrary to the common assumption of uniform dopant distribution, we found that for LP-MOCVD ZnO:B, dopant atoms segregate in a bimodal distribution: they incorporate

only in one side of each grain. We attribute the reason of this segregation to the ZnO polar surfaces. We further quantify the effect of the bimodal dopant distribution on the charge transport mechanisms though a set of simulations and show that it improves the conductivity compared to the case of uniform dopant distribution.

- We estimate the density of a thin film using a non-destructive method based on EDS and confirm the correctness of the results using simulations and optical measurements. We demonstrate that this non-destructive measure can be successfully used to assess the density of porous films.

- We propose an explanation for the beneficial effect of the TCO carrier concentration on the charge transport mechanisms at the p-type contact of the SHJ solar cells in terms of lower depletion region at the tunnelling recombination interface between p-doped hydrogenated amorphous silicon and n-type ZnO:B film.

To summarize, within this thesis we made extensive use of special characterization techniques to obtain insightful observations about structural, compositional and optoelectronic properties of the ZnO:B films. These novel sets of data were used to propose a model describing the mechanisms of film formation and of dopant incorporation. Importantly, the characterization techniques and the developed model can be applied in future to polycrystalline materials other than ZnO to study their properties.

This work led to several first-authored [Fanni et al., 2014, Fanni et al., 2015b, Fanni et al., 2015a] and co-authored [Moulin et al., 2013, Ding et al., 2014, Tomasi et al., 2016] publications.

2 Preparation and Characterization Methods

The present chapter describes the techniques used to prepare LP-MOCVD ZnO:B thin films and the characterization methods used to analyze their *structural*, *elemental* and *optoelectronic* properties. Measurements and analysis of the physical properties of the film such as thickness, resistivity, carrier mobility, carrier concentration, absorptance, plasma frequency, structure and film preferential orientation, were performed by the author at PVLAB and at other EPFL laboratories. More specialized investigation techniques such as determination of the boron and hydrogen concentrations, boron spatial distribution, contact potential difference, work-function and automated crystal orientation mapping were performed in collaboration with various laboratories within Europe.

2.1 Preparation Techniques

2.1.1 Low-Pressure Metalorganic Chemical Vapor Deposition

All the ZnO:B thin films characterized within this thesis were deposited by low-pressure metalorganic chemical vapor deposition (LP-MOCVD), Figure 2.1 presents a schematic diagram of the deposition system. Two precursor gases: water vapor (H_2O) and diethylzinc (DEZ) are used as sources of respectively oxygen (O) and zinc (Zn) and are introduced into the deposition chamber by simple evaporation; their flow is controlled by a mass flow controller. The injection in the chamber is realized through a cooled showerhead. Inside the chamber, the gases are mixed and react on the surface of the heated substrate (0.5-mm-thick borosilicate glass SCHOTT AF45 or 200-μm-polished n-type silicon wafer). During this thesis, we will refer to the deposition temperature as the one measured by means of thermocouple inside the aluminum hotplate. The feedback control loop is referred to this temperature, which is larger than the actual one at the substrate surface (where the ZnO-forming reactions take place). The difference between the hotplate temperature and the substrate temperature depends on the thickness of the ZnO already deposited on the hotplate, and it increases with temperature as shown in Table 2.1 for a clean hotplate, i.e. no ZnO layer on the hotplate surface.

Table 2.1: *Temperatures measured within the hotplate T_{hp} and at the upper surface of a 0.5-mm-thick borosilicate glass T_g. The measurement were made without any ZnO layer deposited on the hotplate surface.*

T_{hp}	T_g
°C	°C
100	90
180	165
250	215

Diborane (B_2H_6), diluted at 2% in argon, is added as n-type dopant in order to tune the film carrier concentration [Wenas et al., 1991b]. In the following non-intentionally doped (nid) samples will refer to ZnO film deposited without the addition of diborane in the gas phase. The doping level is indicated by means of the B_2H_6/DEZ ratio in the gas phase, e.g. a flow of 200 sccm of B_2H_6/Ar and 100 sccm of DEZ in the gas phase will be indicated as a doping level of 1% (=(100 x 0.02)/200). Two pumps (a primary and a root vacuum pump) evacuate the exhaust gases. A pressure gauge combined with a butterfly valve allows us to control the chamber pressure during the deposition. The range of deposition parameters investigated within this thesis is presented in Table 2.2.
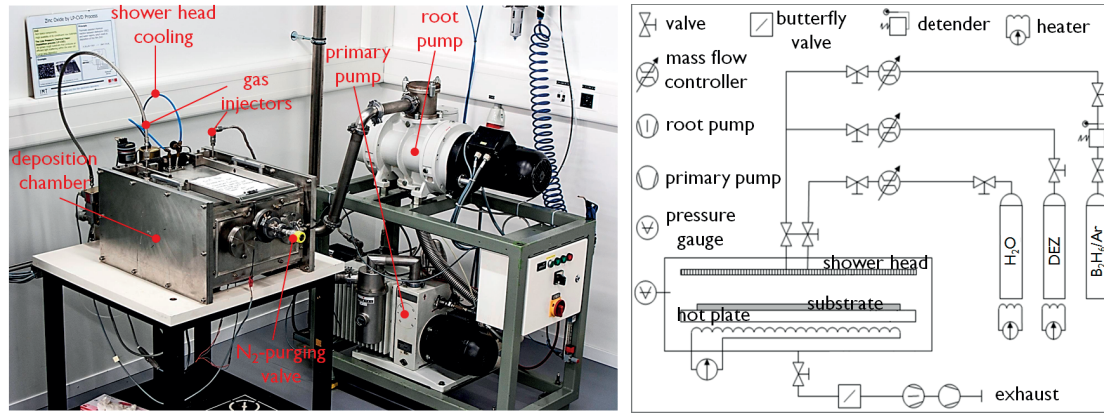
Figure 2.1: *Picture and schematic of the LP-MOCVD system used during this thesis to deposit ZnO:B films [Steinhauser, 2008].*

Table 2.2: Space of parameters investigated within this thesis

parameter	range
temperature	50 - 250 *°C*
pressure	0.1 -1 *mbar*
gas flow	75 - 450 *sccm*
H_2O/DEZ	0.25 - 8
B_2H_6/DEZ	0 - 0.08

2.1.2 Chemical Mechanical Polishing System

For certain measurements (e.g. nano secondary ion mass spectroscopy, Kelvin probe force microscopy), the film roughness can produce artifacts due to non uniform emission of secondary atoms during sputtering or modification of the local potential due to morphology-related interaction with the tip. In order to reduce the roughness of the ZnO surfaces before these analysis, the film surface was polished with the mechano-chemical procedure shown in Figure 2.2 and developed by Cuony [Cuony, 2011]. The polishing is obtained by combining mechanical (felt disc in a solution of colloidal silica particles, 40 nm in diameter) and chemical (silica particles chemically interact with the ZnO surface partially etching it) processes.
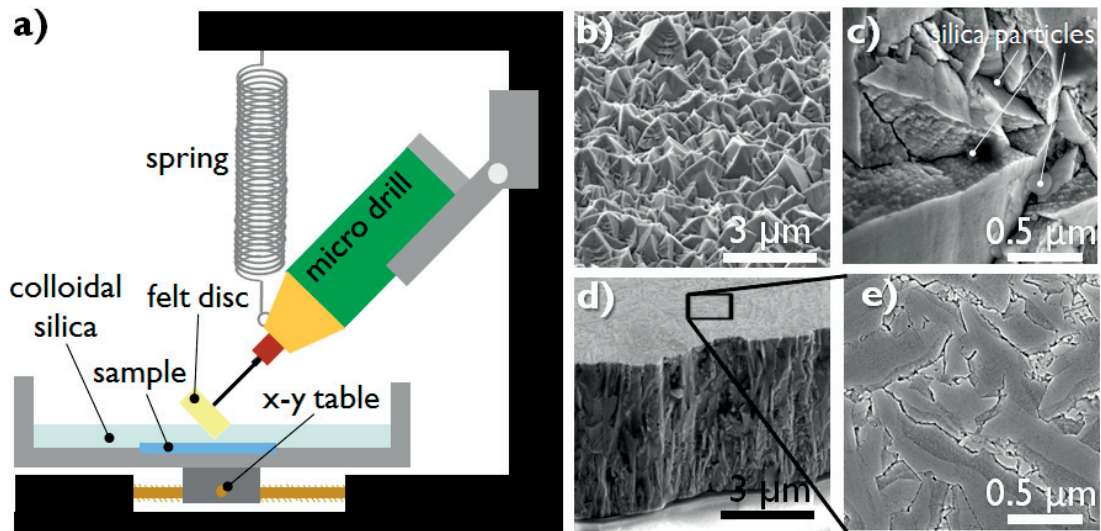
*Figure 2.2: **(a)** Schematic diagram of the mechano-chemical polishing system used to flatten the surfaces of ZnO films [Cuony, 2011]. Scanning electron microscopy micrographs of 7-µm-thick ZnO films **(b)** as deposited; **(c)** chemically etched by colloidal silica (the round feature is a silica particle); and chemically and mechanically polished **(d)** in tilt view and **(e)** top view.*

2.2   Characterization Techniques

The present section lists the main characterization techniques used to assess the structural, elemental, optical and electronic properties of the ZnO films.

2.2.1   Structural Properties

Stylus Profilometer

An Ambios XP-2 stylus profilometer was used to assess the film thickness. The system registers the height of a stylus that scans the surface of the sample. A step in the film is obtained by ink lift-off in acetone. The film thickness is measured by scanning the stylus across the patterned step.

Scanning Electron Microscope

A JEOL JSM-7500 TFE thermal field emission scanning electron microscope (SEM) was used to acquire information regarding the morphology of the film. Quantitative information regarding grain size was extracted from top view and cross section micrographs using the *stereologic method* based on proportionality constant equal to 1 [Han and Kim, 1995]. The measurements were performed by the author at the Optics Group of EPFL.

Kanaya-Okayama method
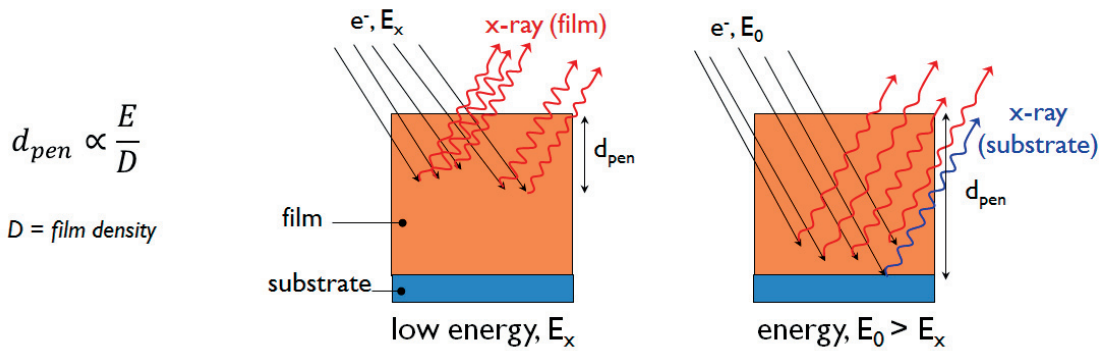
Figure 2.3: The Kanaya-Okayama method is based on the dependence of the electron beam penetration depth (d_{pen}) on film density (D) and beam energy (E). At a specific energy (E_0) x-ray emitted by elements present only in the substrate are detected, by measuring film thickness (at E = E_0, $d_{pen} = d_{film}$) and the beam energy (E_0) it is possible to estimate the relative film density (D).

Energy-dispersive X-ray spectroscopy (EDS) was used to determine the density of films having different porosity according to the Kanaya-Okayama equation [Kanaya and Okayama, 1972]. The technique relies on the relationship between the electron beam energy, interaction volume

and material density, as sketched in Figure 2.3. The interaction volume of a porous layer depends on its thickness and density, since the voids inside a material do not interact with the electrons. Electrons that have to cross a thick and dense film will need a larger energy compared to those going through a thin and porous layer. The corresponding energy is assessed by EDS as the minimal energy E_0 at which it is possible to observe the X-ray signal coming from elements characteristic of the glass substrate. Knowing the thickness d, and supposing that electrons are absorbed exclusively by ZnO (atomic number $Z_{ZnO} = 38$, and atomic mass $A_{ZnO} = 81.4$), the density ρ (in arbitrary units) of the inhomogeneous film can be found according to [Kanaya and Okayama, 1972]:

$$\rho = \frac{2.76 \cdot 10^{-2} \cdot A \cdot E_0^{1.67}}{d \cdot Z^{0.89}} \tag{2.1}$$

The EDS measures were performed by Yonat Milstein from B-nano Ltd.(Rehovot, Israel).

Transmission Electron Microscope

A JEOL JEM-2200F transmission electron microscope (TEM) was used to acquire information regarding the structural and crystallographic preferential orientation of the films. The instrument was operated in the bright field, selected area diffraction and scanning modes. The measurements were performed by A. Brian Aebersold and Dr. Duncan T.L. Alexander at the Interdisciplinary Center for Electron Microscopy of EPFL (Lausanne, Switzerland). A very effective way to investigate the texture evolution of the film was developed within the ZONEM project by A. Brian Aebersold. Automated crystal orientation mapping (ACOM; NanoMegas ASTAR [Rauch et al., 2008]) of cross-sectional samples was carried out. The microscope was operated at 200 kV in nanobeam diffraction mode, and the beam was scanned in a raster across the specimen with steps of 5 nm. Further details on sample preparation and microscope settings are described elsewhere [Aebersold et al., 2015]. The TEM cross-sectional samples for ACOM were prepared by Ar$^+$-ionbeam milling (Gatan Inc. PIPS) according to the *double-wedge method* described by Dieterle *et al.* [Dieterle et al., 2011]. The combination of double wedge preparation and ACOM analysis, described in Figure 2.4, drastically reduces the sample preparation time and allows for statistically significant structural quantification as explained in [Aebersold et al., 2015].
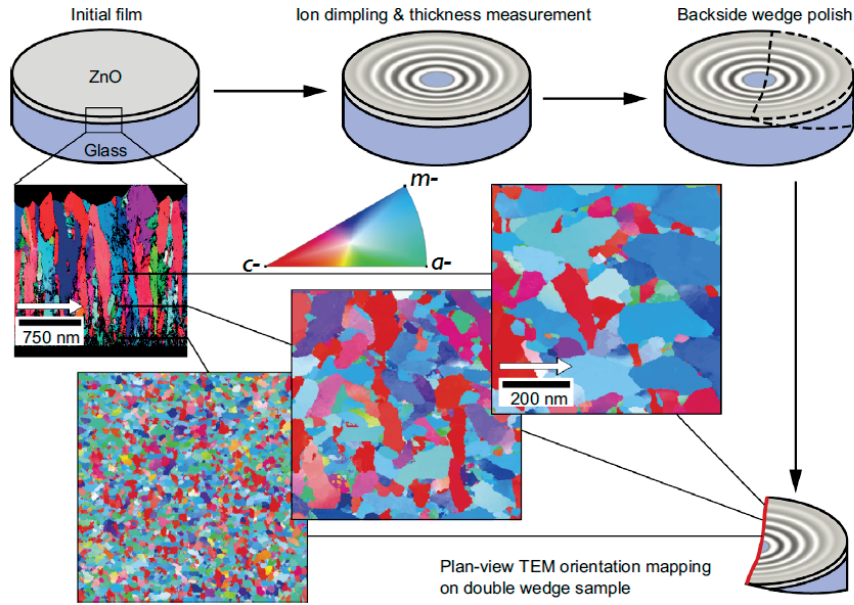
Figure 2.4: Double-wedge method for plan-view ACOM at defined heights in polycrystalline films. The inverse pole figure maps are given with respect to the white arrows and the color map shown [Aebersold et al., 2015].

X-Ray Diffraction

A Bruker D8 Discover tool was used to acquire the X-ray diffraction (XRD) pattern of the thin ZnO films deposited on glass. From these patterns, information regarding film texture and crystalline quality (grain size, local strain/defects) was extracted. The instrument was operated in the ω-2θ and grazing incidence configuration. The X-ray source was a Cu-Kα radiation (λ = 0.1542 nm). The measurements were performed by the author in the Institute of Condensed Matter Physics of EPFL (Lausanne, Switzerland).

Atomic Force Microscope

A Bruker Dimension Icon atomic force microscope (AFM) was used to obtain quantitative information about the film surface. The instrument was operated in the tapping and peak force tapping modes. The data were analyzed either with the Bruker dedicated software (Nanoscope Analysis) or with the freeware Gwyddion software [Nečas and Klapetek, 2012]. The measurements were performed by the author at the Microscopy and Nanoscopy facility of the Centre Suisse d'Electronique et Microtechnique (Neuchâtel, Switzerland).

2.2.2 Elemental Analysis

Nuclear Reaction Analysis

Nuclear reaction analysis (NRA) is used to measure *low-atomic-number* elements such as C, N, O, and B in thin films. In order to determine B concentration in the ZnO:B films, the following nuclear reaction was used [Ligeon and Bontemps, 1972]:

$$^{11}B + p \longrightarrow \, ^{8}Be + \alpha_0$$
$$\searrow \, ^{8}Be^* + \alpha_1$$
$$\searrow \alpha_{11} + \alpha_{12}$$
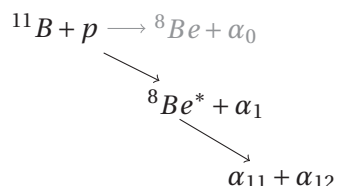
A proton beam accelerated at 660 MeV is directed at the film. The proton breaks the B atom into one beryllium (Be) atom and one α particle. In turn the metastable Be^* decomposes into two α particles; hence for each B atom three α particles are collected. This reaction offers a powerful method for the detection of trace quantities of boron due to boron's large cross section [Liu et al., 2002]. These measurements were performed at Centro Nacional de Aceleradores, (Sevilla, Spain) by Dr. Francisco Javier Ferrer Fernández, on 500 nm ZnO:B samples deposited on Si wafers. In order to obtain quantitative measurements, a reference sample with a known amount of B was measured. The sample was produced by ion-implantation on a nid ZnO. The ion implantation was performed at CNR-IMM (Bologna, Italy) by Dr. Marica Canino.

Elastic Recoil Detection Analysis

Hydrogen content in the samples was measured by Elastic Recoil Detection Analysis (ERDA) using a 3.0 MeV $^{4}He^{2+}$ beam [Avasthi et al., 1995]. In this technique an α-particle beam is sent on the sample with an energy sufficient to knock-out lighter atoms, e.g. H atoms. The recoiled H-atoms are detected. A filter (13 um Mylar foil) was put in front of the surface barrier detector (at 35°) in order to stop the scattered α-particle. These measurements were performed at Centro Nacional de Aceleradores (Sevilla, Spain) by Dr. Francisco Javier Ferrer Fernández

NanoSIMS

A Cameca NanoSIMS 50L was used to perform secondary ion mass spectroscopy with nano-metric resolution (NanoSIMS). A highly focused primary beam (Cs^+) is shot across the sample surface allowing secondary ion images to be produced with a spatial resolution that can clearly resolve structures larger than a few hundred nanometers in linear dimension. The instrument, sketched in Figure 2.5, is equipped with a multi-collector system that allows for simultaneous collection of up to seven different isotopes. For this thesis: C^-, CN^-, BO^-, BO_2^-, $_{64}ZnO^-$, $_{66}ZnO^-$, O^- were collected. The Cs^+ beam is easy to focus, and therefore it is used to sputter a very small surface region. When using a positively charged primary beam, it is
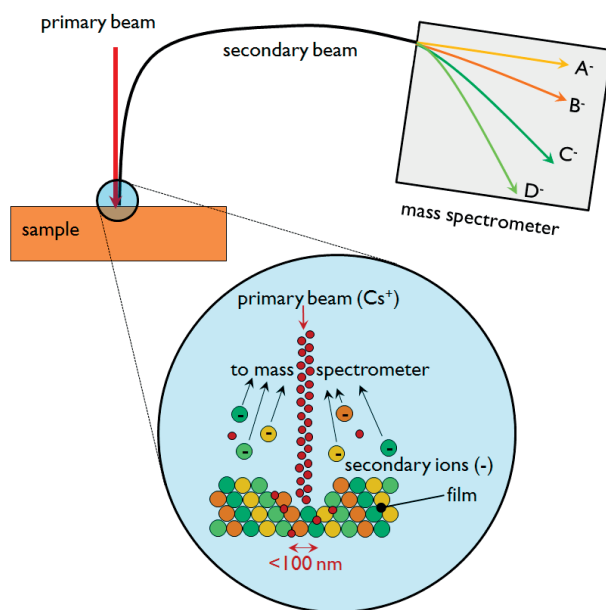
Figure 2.5: Schematic of the NanoSIMS sputtering process. The well-focused positive primary beam (Cs^+) ejects atoms in the film, generating the negative secondary beam directed to the mass spectrometer, where the atoms are separated according to their mass/charge ratio.

possible to collect only negatively charged secondary ions. This fact represents a challenge when detecting species that are difficult to ionize negatively such as boron. Therefore, in order to increase the emission of secondary ions, we decided to detect BO^- and $BO_2^{\ -}$ instead of B^- [Kontis et al., 2016]. The measurements were performed at the Laboratory for Biological Geochemistry of EPFL (Lausanne, Switzerland) by Dr. Stéphane Escrig.

2.2.3 Optoelectronic Properties

UV-VIS-NIR Spectrophotometer

A Perkin Elmer Lambda 950 was used to measure total transmittance TT, diffuse transmittance DT, total reflectance TR and diffuse reflectance DR in the spectral range 320 - 2500 nm. This instrument belongs to the category of the *dispersive* photometer because the spectrum of the light is dispersed before the light crosses the sample, and only a part of it is allowed to continue his way towards the sample. A moving slit just after the monochromator allows us to vary the chosen component of the light. By repeating the procedure over the whole spectrum, the curve (either transmittance or reflectance) is acquired; thus the final curve (transmittance or reflectance) is composed by as many data points as the components the light is divided into. The main parts of the spectrophotometer are: the *light source* (a deuterium lamp for the UV and a tungsten lamp for the VIS-NIR); the *monochromator* which, combined with a moving slit, allows us to select a defined component of the spectrum (wavelength width: 1 - 10 nm); and the *detector* (Si-based for the UV-VIS and InGaAs-based for the NIR). The spectrophotometer
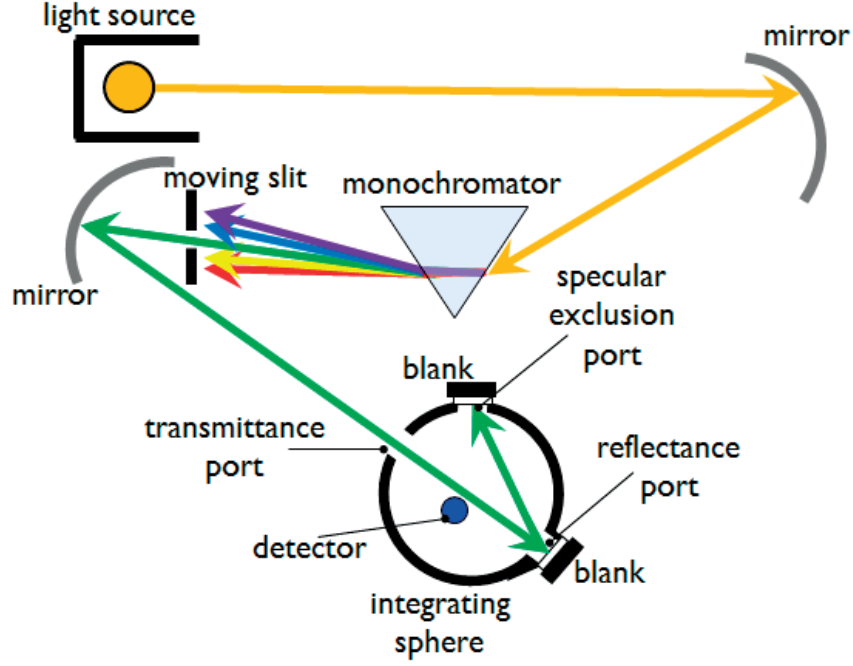
Figure 2.6: Schematic representation of the UV-VIS-NIR spectrophotometer. The main components are the light source, the monochromator and the detector. Our setup is equipped with an integrating sphere allowing us to collect both direct and diffuse signals.

is equipped with an integrating sphere necessary to collect the light transmitted through films that scatter light (e.g. rough films). The sphere is internally coated with Spectralon^{TM} (sintered teflon), a highly reflective material (reflectance higher than 98% in the UV-VIS-NIR spectral range). The sphere has three ports (transmittance, reflectance, specular exclusion). By properly locating the sample and the blanks at the different ports, it is possible to measure TT, DT, TR, DR. From TT, DT and TR measurements we calculate the film absorptance:

$$A = 1 - TT - TR \tag{2.2}$$

and the film haze factor:

$$H = \frac{DT}{TT} \tag{2.3}$$

since the optical properties of the film depend on the type of substrate, within this thesis the values of the optical parameters refer to the sample "film + substrate" and they are measured with the light beam impinging first on the film (cf. Figure 2.6).

It is known that the transmittance measurements on rough films, having surface features
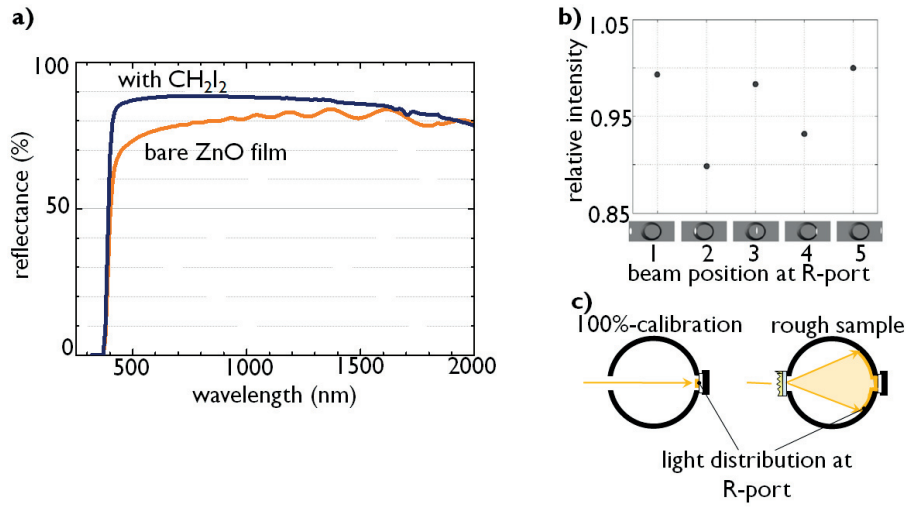
Figure 2.7: Measurement artifact on the total transmission curve induced by a rough sample. (a) Transmittance curve measured on the same sample without (orange line) and with (blue line) refractive index matching liquid (CH_2I_2). (b) Detected light intensities, normalized to the highest intensity, for different positions of the light spot on the reflectance port (R-port), [Nilsson et al., 2011]. (c) Light distribution (yellow region) at the R-port during collection of 100%-calibration curve and measurement of rough sample.

comparable with the wavelength of the light [Llopis and Tobías, 2005], are affected by artefacts leading to the underestimation of the transmittance [Nilsson et al., 2011]. Figure 2.7a shows that for a 2.5-μm-thick non-intentionally doped sample the transmittance underestimation in the visible can reach values up to 10%. Nilsson *et al.* [Nilsson et al., 2011] demonstrated that the effect is due to the non-uniformity of sensitivity to the incoming light in region of the reflectance port (R-port). They measured the light collected by the detector when directing the beam in five different positions spanning from the inner integrating sphere on the right of the R-port up to the left of the R-port. They observed that when the light hits the frame of the blank sample (position 2 and 4) the collected light is 10% lower than in position 1,3 and 5 (cf. Figure 2.7b). They attributed this effect to light leakage through the frame between the blank and integrating sphere. This loss plays a role during the measurement of rough samples. As shown in Figure 2.7c, the distribution of the light at the R-port during the baseline is limited to the blank area. At first bounce no light hits the frame of the blank, while during the measurement of a rough sample the light is distributed on a wider region that includes the whole frame of the blank, leading to light losses. To get rid of this artefact, transmittance (and reflectance) measurements were performed by applying diiodomethane (CH_2I_2), a liquid matching the ZnO refractive index (n = 1.9), to the front surface of the film as described in [Steinhauser, 2008].

Fourier Transform Infrared Spectrometer

A Bruker Vertex 80 Fourier transform infrared (FTIR) spectrometer was used to measure the reflectance TR and transmittance TT in the infrared region (1 - 25 μm). Although an FTIR spectrometer measures the same physical parameters as a dispersive spectrometer, the way in which the information is collected is quite different. In particular, the light spectrum is not split according to wavelength using a monochromator. Rather it is "encoded" before interacting with the sample by using an interferometer. Afterwards the signal is "decoded" by applying a Fourier transform as shown in Figure 2.8a. The interferometer consists of a beam splitter, a stationary mirror, and a moving mirror (typical difference in optical path d_x is in the range of some cm). The main element of the interferometer is the beamsplitter. In distance $d_s t$ a stationary mirror is set perpendicular to the incoming beam. A second mirror is placed on a moving stage in distance $d_0 + d_x$ along the incoming beam. The typical path of the moving mirror d_x is in the range of some centimeter. Radiation coming from the source strikes the beam splitter and separates into two beams. One beam is transmitted through the beam splitter to the moving mirror, and the second is reflected to the stationary mirror. The fixed and moving mirrors reflect the radiation back to the beam splitter where the two beams interfere and half of the recombined beam passes to the sample. As shown in Figure 2.8b, the intensity of the recombined beam depends on the difference in optical path between the two mirrors, achieving a maximum value when the two paths are equal $d_0 + d_x = d_{st}$. This is the only position with constructive interference for the whole spectrum. At any other position only a single wavelength interfere constructively. In this way, each mirror position is related to the wavelength that interferes constructively for that specific optical path difference (encoding). A straightforward consequence is that the instrument resolution increases with the available difference in optical path. A single curve is composed by recombined intensity measures at each mirror position. The encoded signal is sent to the sample where the light is absorbed only at specific wavelengths, and by means of the Fourier transform is converted into the frequency domain where the sample's effect on the different wavelengths is easily recognizable, cf. Figure 2.8c (decoding). The advantages of this instrument over a dispersive one are several: greater radiant power to the detector (higher S/N ratio), higher resolution and faster spectral acquisition [Oriel, 2000].

In the IR range, it is not possible to collect the transmittance of films deposited on borosilicate glass due to the absorption of these substrates for wavelengths larger than 2800 nm (vibrational excitation of OH-groups) [SchottGlass, 2012]. Thus we measured the reflectance of the film using a specular reflectance accessory.

The reflectance curve of a typical TCO film can be described combining the Drude model of electron conductivity (reproducing the features due to free carriers) with the Lorentz model of dipole oscillators (reproducing the intra band transition of the electrons). In this approxima-
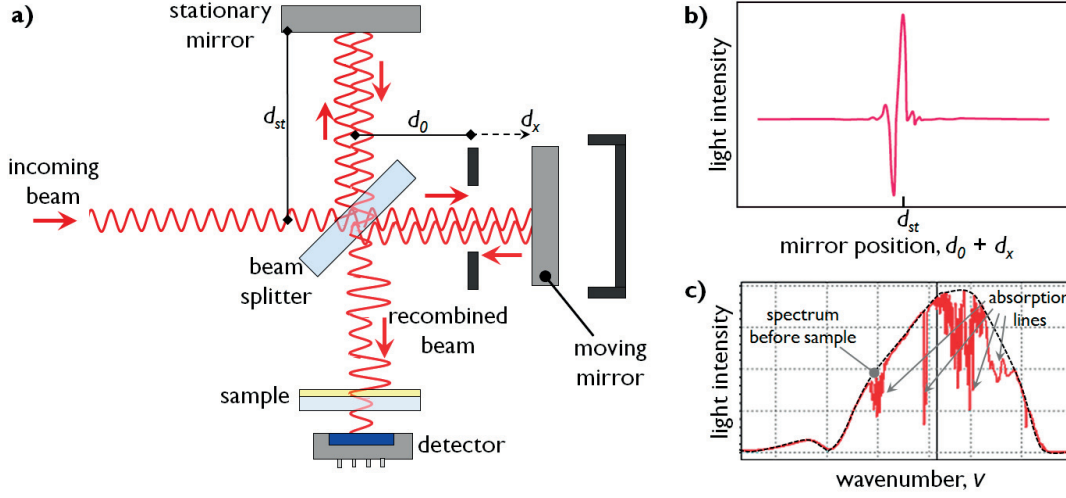
Figure 2.8: **(a)** *Schematic of the FTIR spectrometer based on the interferometer that is composed of a beam splitter, a stationary mirror and a moving mirror.* **(b)** *The interferogram (space domain) is how the signal looks just after the recombination at the beam splitter.* **(c)** *After the Fourier transform (frequency domain), the spectrum shows absorption lines at defined frequencies that depend on the sample properties.*

tion, the dielectric constant ϵ_r of the film can be written as [Fox, 2010]:

$$\epsilon_r(\omega) = 1 - \frac{\omega_p^2}{(\omega + i\gamma\omega)} \tag{2.4}$$

where γ is the damping factor (reducing the momentum of the electrons) and ω_p is the frequency at which the collective resonant oscillation of the electrons takes place, known as plasma frequency. As shown in Figure 2.9 for wavelengths larger than ω_p, the free electrons present in the film start reflecting the electromagnetic wave. The plasma frequency is defined as:

$$\omega_p = \sqrt{\frac{N_e e^2}{\epsilon_{opt}\epsilon_0 m^*}} \tag{2.5}$$

where ϵ_{opt} is the dielectric constant measured in the transparent spectral region ($\kappa = 0$), ϵ_0 is the vacuum permittivity and m^* is the electron effective mass. This model allow us to derive

the free-carrier concentration (cf. equation 2.5) and the carrier optical mobility μ_{opt}:

$$\mu_{opt} = \frac{e}{m^*\gamma} \tag{2.6}$$

by fitting the film reflectance curve obtained by FTIR [Fujiwara and Kondo, 2005]. As shown in Figure 2.9, the wavelength at which the minimum of the reflectance curve appears λ_0 does not exactly correspond with the wavelength related to the plasma frequency λ_p. The relation between these two parameters is given by [Fox, 2010]:

$$\lambda_p = \sqrt{\frac{\epsilon_{opt}}{\epsilon_{opt} - 1}}\lambda_0 \tag{2.7}$$

and it should be taken into account when calculating ω_p, and all the derived parameters (e.g. N_e and m^*) from reflectance curves.
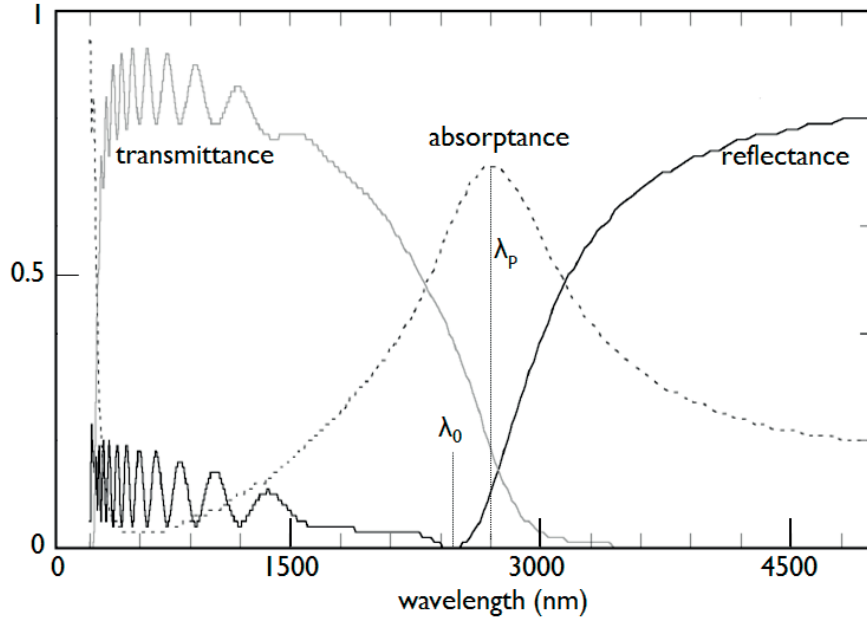
Figure 2.9: Transmittance, absorptance and reflectance curves for a typical degenerated TCO film ($\epsilon_{opt} = 3.8$, $\omega_p = 7000\ cm^{-1}$, $\Gamma = 475\ cm^{-1}$, $d = 2\ \mu m$). λ_p is the wavelength related to the plasma frequency and λ_0 is the wavelength where the minimum in reflectance occurs. Adapted from [Steinhauser, 2008].

Hall Effect Setup

An Ecopia HMS 5000 Hall effect setup was used to determine resistivity ρ, bulk carrier concentration N_e and drift carrier mobility μ_d in the film. Our setup, schematically presented in Figure 2.10, exploits the van der Pauw configuration that requires square samples (0.5 - 2 cm, side dimension) on which four metallic contacts are applied at corners A,B,C,D. ρ is assessed by applying a current I_{AB} (intensity range: 1 nA to 15 mA) between corner A and B, measuring the voltage V_{DC} between D and C. The same is done for I_{BC} and V_{AD}. In this way the resistances R_1 and R_2 can be calculated:

$$R_1 = \frac{V_{DC}}{I_{AB}} \qquad\qquad R_2 = \frac{V_{AD}}{I_{BC}} \tag{2.8}$$

and the film sheet resistance R_{sh} is obtained by solving the following equation [van der Pauw, 1958]:

$$e^{-\frac{\pi R_1}{R_{sh}}} + e^{-\frac{\pi R_2}{R_{sh}}} = 1 \tag{2.9}$$

and finally ρ can be calculated:

$$\rho = R_{sh}d \tag{2.10}$$
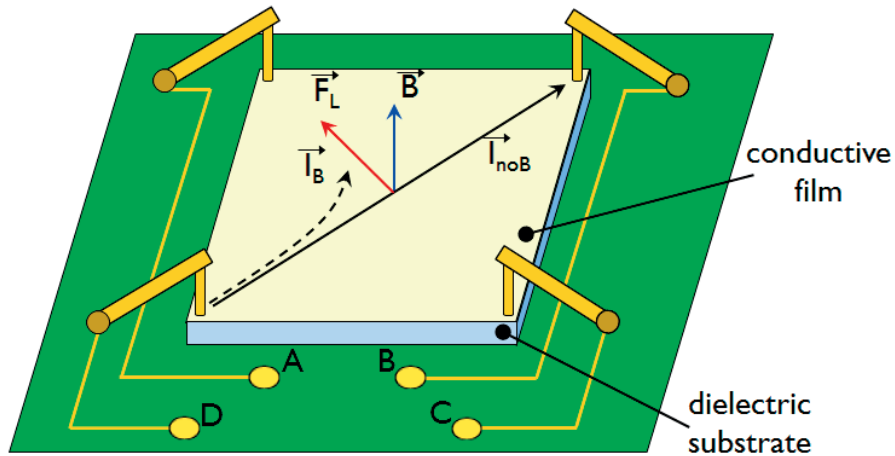
Figure 2.10: Schematic diagram of the Van der Pauw configuration used within our Hall effect setup.

A magnetic field (0.56 T) is used to determine the values μ_H and N_e. The working principle is the Lorentz force $\vec{F}_L$ that acts on charge carriers moving in a magnetic field $\vec{B}$ as shown in Figure 2.10. A current I_{BD} is applied between the contacts B and D and the voltage VAC between A and C is measured; the same measurement is repeated with the magnetic field applied obtaining $V_{AC,field}$. The Hall coefficient R_H is obtained:

$$R_H = \frac{d}{B} \cdot \frac{V_{AC,field} - V_{AC}}{I_{BD}} \tag{2.11}$$

and the Hall mobility μ_H and the carrier concentration N_e can be calculated:

$$\mu_H = \frac{R_H}{\rho} \qquad\qquad N_e = \frac{1}{e\rho\mu_H} \tag{2.12}$$

Notice that a scattering factor r, taking into account the energy spread of the carriers involved in the conduction, is sometimes used to correct the value of μ_H. The corrected value is referred as drift mobility μ_d:

$$\mu_d = \frac{\mu_H}{r} \tag{2.13}$$

The value of r varies between 0.6 and 2 [Blood and Orton, 1992]. Within this thesis we will use the value of 1 that is the value normally used for degenerated polycrystalline films [Orton and Powell, 1980, Anno et al., 1998, Preissler et al., 2013].

Additionally, in polycrystalline films, due to the presence of carrier traps at grain boundaries a part of the grain can be depleted of carriers [Seto, 1975]. When the depletion region extends only partially through the grain, the Hall effect measures N_e (carrier concentration in the bulk of the grain). However when the grain is fully depleted, the measured carrier concentration could be much lower than the bulk doping level. In this particular case the measured electron concentration corresponds to electrons capable of moving between the grains [Orton and Powell, 1980]. This is usually the case for films characterized by small grains, as for example thin films where the volume occupied by the depletion regions is comparable with that of the non-depleted regions. An equation was proposed by Look *et al.* to correct for this apparent thickness-dependent effect [Look et al., 2013].

Temperature-dependent Hall effect measurements were made using a dedicated sample-holder that cools the film to the boiling point of nitrogen (77 K), and heat it up progressively until 350 K.

Kelvin Probe Force Microscopy

A Bruker Dimension Icon scanning electron microscope in Kelvin probe force microscope (KPFM) configuration was used to measure the contact potential difference (CPD) between the film surface and tip [Nonnenmacher et al., 1991]. As shown in Figure 2.11, the electrostatic potential V_{CPD} between the film and the tip is quantified by compensating it with an external bias V_{DC}. The V_{CPD} is proportional to the workfunction difference between the sample surface ϕ_f and the tip ϕ_t:

$$V_{CPD} = \frac{\phi_s - \phi_t}{e} \qquad (2.14)$$

where e is the elementary positive charge. In KPFM topography and contact potential difference are simultaneously measured using the same AFM tip. The method to separate the two signals exploits the several resonance peaks which a mechanically vibrated cantilever generally has. In amplitude-modulation mode, topography is measured by the oscillation at the first resonance frequency, and contact potential difference is measured by the amplitude of the oscillation at the second resonance frequency [Melitz et al., 2011]. The measurements were performed at the Institute of Physics of the Czech Academy for Sciences (Prague, Czech Republic) by Dr. Aliaksei Vetushka and Dr. Martin Ledinský.
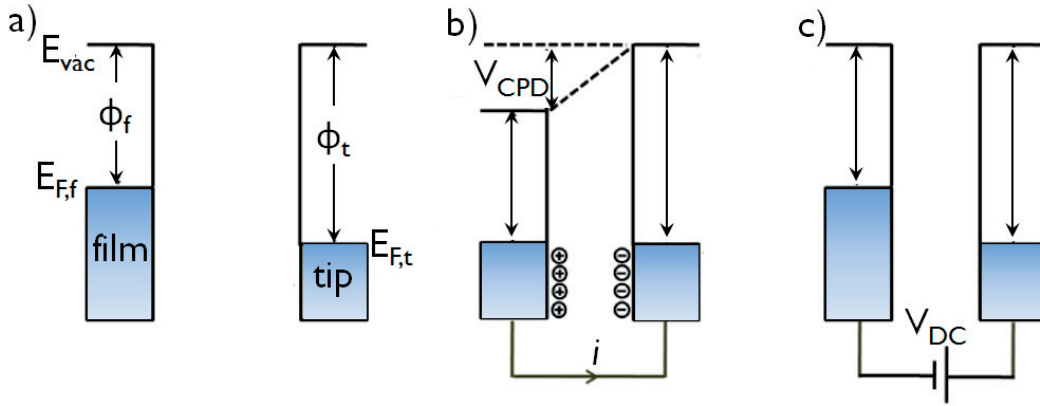
Figure 2.11: KPFM measurement principle. Compensation of the electrostatic potential build up between the sample and tip due to the difference in workfunction. Electronic energy level for three different cases: (a) tip and sample do not interact electrically (b) the tip and the sample are close enough to electrically interact, and (c) the applied external bias V_{DC} compensates for the built up potential.
E_{vac} = energy of vacuum level, $E_{F,f}$ = film Fermi energy, $E_{F,t}$ = tip Fermi energy, ϕ_f = film workfunction, ϕ_t = tip workfunction, [Melitz et al., 2011].

X-ray Photoelectron Spectroscopy and Ultraviolet Photoelectron Spectroscopy

Information regarding the electronic energy states and bands in ZnO and Si were acquired respectively by X-ray and ultraviolet photoelectron spectroscopy (XPS and UPS). Due to its high excitation energy (E_{ex}=1256.6 eV for Mg-source), XPS is well-suited to investigate the energy of material core levels. In contrast, UPS exploits a lower excitation energy source (E_{ex}=21.1 eV for He-I line) and is therefore ideal to investigate energy levels closer to the vacuum energy, giving access to properties such as workfunction and ionization potential. The secondary electrons in XPS are more energetic than those in UPS and therefore can run a longer mean free path before being absorbed by the sample. This fact allows XPS analysis to be less sensitive than UPS to the pollutant species adsorbed at the surface. XPS and UPS measurements were performed at CISSY laboratory of Helmholtz Zentrum Berlin (Germany), partially by myself as visiting researcher (within the transnational access provided by the European SOPHIA project) and partially by Prof. Christian Pettenkofer and Andreas Popp.

3 Control of ZnO Film Growth Modes

Understanding the mechanisms responsible for the development of the film preferential orientation is crucial to tailor the film properties for various applications. In this chapter, we show that by tuning hotplate temperature (T_{hp}), H$_2$O/DEZ ratio and gas flow (ϕ) it is possible to relax the constraints on the substrate. For example, we demonstrate that rough a-textured film can be deposited down to 120 °C, well below the 180 °C usually reported in the literature [Wenas et al., 1991b, Faÿ et al., 2005].

Systematic investigation of deposition parameters allows us to find several options for depositing films with a desired structure.

First, we systematically investigate the influence of deposition parameters on the film preferential orientation (Section 3.3). The deposition parameters we consider are T_{hp}, H$_2$O/DEZ ratio and ϕ. We monitor the deposition process from the nucleation to the final stage and show that the modification of these three deposition parameters results in two different main textures, namely a- and c- texture. We explain the observed variation of preferential orientation in terms of adatom mean free path $\langle x \rangle$.

We characterize the main structural differences between two types of films, and we observed the crack formation in the c-textured films, but not on the a-textured films (Section 3.4). We further find that the formation of cracks depends on the thermal expansion coefficient between the glass substrate and the film. We therefore were able to prevent the crack formation in c-textured films by using glass substrate with an appropriate thermal coefficient.

In the last part of this chapter (Section 3.5), we show how the deposition parameters that we have investigated can be manipulated during the deposition process to obtain the films with 25% larger grain sizes. The procedure we propose consists in controlling the preferential orientation, switching it from c- to a- texture just after the nucleation stage. Finally, we use a film growth simulation analysis to explain the effects of the proposed process in terms of *survival of the fastest* principle.

Part of these results were published in [Fanni et al., 2014, Fanni et al., 2015a].

3.1 Motivation and State of the Art

As discussed in Chapter 1, ZnO in its hexagonal wurtzite phase presents a non-centrosymmetric unit cell, leading to strongly anisotropic properties and growth along different crystallographic axes. The prismatic *c*-axis is polar, while the *m*- and *a*-axes (lying on the basal plane, cf. Figure 1.3) are not. As a result, mechanical and electrical properties can differ significantly depending on the axis orientation associated with the film texture and on grain morphology [Ellmer et al., 1996, Pung et al., 2008]. For these reasons, the film preferential orientation is a key parameter to tailor ZnO film properties.

The current models regarding thin-film growth and texture evolution consider as driving forces the minimization of surface energy and film strain energy. These models were explained in a detailed review paper by Thompson [Thompson, 2000]. In this paper, the author separates the growth into three distinct stages: *nucleation*, *coalescence* and *thickening*. At nucleation, the driving force is the surface energy minimization and therefore the faster-growing directions are the ones perpendicular to the minimum surface planes. During coalescence and thickening, if no other driving force overcomes the surface energy minimization, then epitaxial growth takes place on the already-formed grains, preserving the initial film texture as reported by Verghese and Singh [Verghese and Clarke, 1999, Singh et al., 2008]. Minimization of the surface energy combined with limited diffusion of adsorbed atom (adatom) can lead to a texture transition during the film thickening as proposed by Kajikawa *et al.*[Kajikawa et al., 2003].

Another force that can play a role in film texture development is strain energy minimization. Strain formation and accumulation depends on various processes, a main one being the way in which the film nucleates. Film nucleation in different clusters is prone to strain generation during the coalescence stage: when two clusters impinge on each other, they form a grain boundary. The formation of the boundary can happen without diffusive processes through elastic distortion of the cluster [Thompson, 2000, Seel et al., 2000, Spaepen, 2000]. During the following grain growth of grains, more and more stress will be accumulated at this boundary. Materials characterized by a high melting point (as SnO_2 and ZnO) show low adatom diffusion coefficients. For these materials the minimization of the energy stored due to strain can easily become thermodynamically more favorable than the surface energy minimization, leading to the appearance of a different crystallographic orientation as shown by Consonni *et al.* for sputtered SnO_2 [Consonni et al., 2012].

In addition, energy and strain minimization can be biased by the environment in the deposition chamber. Batzill *et al.* showed that the energy of a surface should be considered with respect to its surrounding environment; indeed, a surface rich in oxygen atoms can be stable in an oxidizing atmosphere but unstable in a reducing atmosphere and therefore undergoes reconstruction [Batzill et al., 2005]. This explanation was used by Körber *et al.* to unravel the texture dependence of sputtered SnO_2 on the oxygen content of the plasma [Körber et al., 2010].

In CVD, films grow through chemical reactions mainly happening at the substrate/film surface
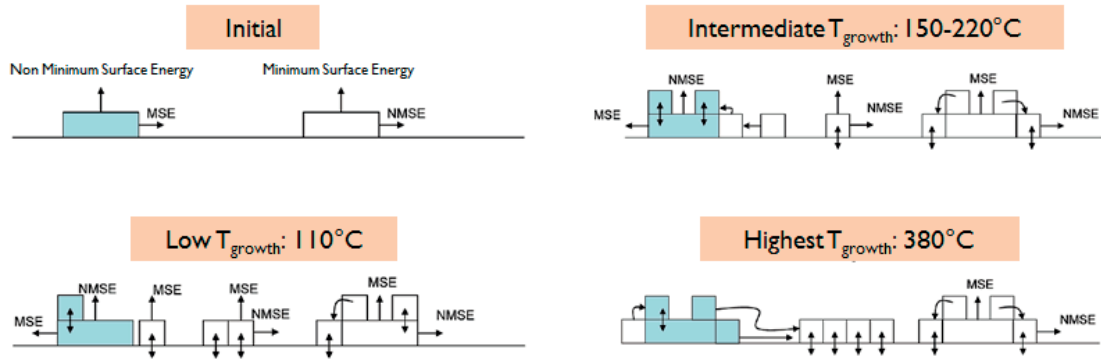
Figure 3.1: Schematic of the temperature influence on the preferential orientation selection mechanisms for LP-MOCVD ZnO [Nicolay et al., 2009].

rather than in the gas phase [Roth, 1981, Oda et al., 1985, Pan et al., 2006]. These reactions, and hence film growth, are influenced by controllable parameters such as substrate temperature and gas precursor flows [Wenas et al., 1991a, Faÿ et al., 2005]. The current growth model for polycrystalline LP-MOCVD ZnO was proposed by Nicolay *et al.* [Nicolay et al., 2009]. The model, sketched in Figure 3.1, is based on the observation of the dependence of texture formation on growth temperature: at temperatures lower than 150 °C the preferential orientation is with the *c*-axis perpendicular to the substrate. At intermediate temperatures (150 - 220 °C) the film preferential orientation, with the *a*-axis perpendicular to the substrate. At high temperatures (380 °C) the preferential orientation is again the *c*-axis. The explanation is based on the work of Kajikawa where the surfaces are divided into minimum surface energy (MSE, *c*-planes for ZnO [Fujimura et al., 1993]); and non-minimum surface energy (NMSE, e.g. *a*-planes) [Kajikawa et al., 2003].

At the nucleation stage the nuclei exposing the MSE planes parallel to the substrate grow faster and soon tend to occupy a larger surface than the NMSE [Thompson, 2000]. At *low temperature* the adatom diffusion is almost negligible and the adatoms stick very close to the place where they land on the surface, therefore the thickening of the film develops epitaxially on the thin coalesced layer and the MSE texture is preserved. At *intermediate temperatures* the adatom diffusion is increased allowing the diffusion between different facets but not between different grains. Adatoms diffusing on MSE can easily migrate on NMSE while adatoms travelling on NMSE are hindered by the higher dangling-bond density and most of them will then get stuck on NMSE. Therefore during thickening the texture is changed from MSE to NMSE. *High temperature* allows for the diffusion between grains. Grains grow minimizing the surface energy, therefore exposing the MSE plane. The application of Kajikawa's model was widened to explain the texture dependence on the variation of the ratio of the precursor gases (H_2O/DEZ) [Nicolay et al., 2012]. This model sets the basis for a more comprehensive theory that is able to include all the other deposition parameters of LP-MOCVD (as for example gas flow and pressure).
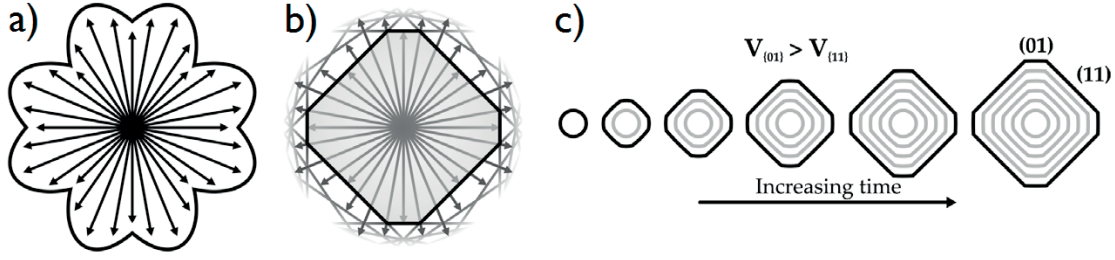
*Figure 3.2: **(a)** Plot of growth velocity versus orientation. **(b)** Kinetic Wulff construction following from the growth velocity plot shown in (a). **(c)** Initial circular grain evolving into equilibrium Wulff shape; $V_{[11]}$ is the slower growing direction and therefore it will asymptotically dominate the surface of the polyhedron [Ophus et al., 2009].*

The simulation of film growth is a useful tool to predict which growth conditions favor a required film property. A common approach to simulate thin-film growth exploits the hypothesis that polycrystalline films start the growth from a series of unconnected crystalline clusters having a certain orientation with respect to the substrate normal. The clusters grow according to the fastest crystalline growing direction that is set by the deposition conditions as shown in Figure 3.2.

A useful way to mathematically define the evolution of the grain shape is by using the *Wulff thoerem* which identifies the equilibrium shape of a polyhedron as the one which minimizes the value $\sum_i \gamma_i A_i$ where γ_i and A_i are respectively the surface energy and area of the i_{th} plane [Wulff, 1895]. Often in the simulations, the surface energy vectors are replaced with the growth velocity vectors as sketched in Figure 3.2. Initially the crystalline clusters are not in mutual contact and develops according to the Wulff theorem. At coalescence, the clusters impinge on each other and the competition between the different grains starts. Geometric considerations dictate that a grain will be deleted only by a grain having a more favorable orientation. This theory, known as *survival of the fastest*, forecasts that the grains having the most favorable orientations will dominate the film surface at the final stage [Kolmogorov, 1937, van der Drift, 1967].

The first 3D simulations that followed this approach were performed by Thijssen *et al.*[Thijssen et al., 1992]. Smereka *et al.* refined the model by applying a level set methodology [Smereka et al., 2005]. Although providing valuable outcomes, this algorithm keeps track of more information than required to describe the surface [Norris and Watson, 2007], thus Ophus *et al.* reduced the amount of information required by storing only the data relative to the film surface, defined as the highest point reached by grains at each point of a 2D grid [Ophus et al., 2009]. They further improved the model by implementing the self-shadowing effect, showing that it plays a minor role for evaporation and collimated sputtering techniques while is relevant for LP-MOCVD [Ophus et al., 2010a]. In the present work, in order to simulate the deposition of LP-MOCVD ZnO the Ophus model described in [Ophus et al., 2010a] was adapted.

3.2 Experimental Details

Different series of films with thickness varying from some nm to 2 μm were deposited on glass substrates, except the two nucleation series under a-textured and c-textured conditions which were deposited on n-type Si wafers (d = 200 μm, ρ = 1 Ωcm) in order to be observed with SEM. To investigate the effect of T_{hp}, H_2O/DEZ and ϕ, a wide range of parameters was considered, respectively: 100 - 250 °C, 0.25 - 4 and 75 - 435 sccm. Unless differently stated, the center of the space of parameters (reference conditions) was set to be 170 °C, 1, 150 sccm, which are the conditions that lead to the a-textured rough film commonly used as an electrode in photovoltaic cells [Faÿ et al., 2005, Koida et al., 2016].

The deposition rate was calculated as the ratio between the film thickness (measured with a profilometer) and deposition time (measured with a stopwatch). The film morphology was investigated by SEM (tilted and plan view) and the film preferential orientation by means of XRD (ω-2θ) and ACOM-TEM (done by A. Brian Aebersold). The nucleus size and concentration were derived by 0.5 x 0.5 μm^2 AFM images using the watershed function for grain identification. The film crystallinity was assessed by fitting the peak relative to a-planes (($11\bar{2}0$)-peak) of the XRD pattern with a Gaussian function and extracting the full width at half maximum (FWHM). The structural defects were imaged by means of STEM and SADP-TEM (done by A. Brian Aebersold, CIME-EPFL). Stress in the film was semi-quantitatively determined by depositing on 200 μm-thick Si wafer and measuring the bending of the wafer with a profilometer (done by J. Persoz and F. Dauzou, PVLAB). The cracks in the film were observed by means of SEM and a confocal microscope.

The simulations dealing with preferential orientations and growth velocities along the different directions were performed by A.Brian Aebersold within the frame of the ZONEM projects. The code was adapted from one developed by Ophus *et al.* [Ophus et al., 2010a]. We used hexagonal grains instead of conical ones in order to more accurately describe the wurtzitic unit cell of ZnO.

3.3 Influence of Deposition Parameters

After showing which regimes govern the film growth of LP-MOCVD ZnO, this section presents the investigations that allowed us to define the influence of the deposition parameters on the film structural properties. The effects of T_{hp}, H_2O/DEZ and ϕ on nucleation and film thickening are investigated by following the evolution of structural parameters such as film morphology and preferential orientation. The crystallinity and structural properties of the various film textures are also discussed.

3.3.1 Considerations on Growth Regimes

Chemical vapor deposition processes can be classified according to the process limiting the growth rate of the film: either *surface reactions* or *mass transport* [Ingle et al., 1996, Ohring, 2002b]. The two regimes can be easily distinguished in the Arrhenius plot of Figure 3.3, which shows the dependence of the deposition rate (R) on T_{hp} and total gas flow ϕ. At low T_{hp}, all the curves are characterized by an exponential increase of R according to the following relation [Morosanu, 1990]:

$$R = Ae^{-\frac{E_a}{kT_{hp}}} \tag{3.1}$$

where A is a constant, E_a is the activation energy for the reactions happening at the surface and k is the Boltzmann constant. This dependence shows that at low T_{hp} the growth is limited by surface reactions. This is the regime in which R increases with T_{hp}. At a certain T_{hp}, R stops increasing, meaning that the film growth is now limited by the mass transport from the gas phase. These two regimes are indicated in Figure 3.3. Note that the T_{hp} at which the transition between the two regimes occurs increases with increasing ϕ. Indeed, at constant chamber pressure, a higher gas flow increases the gas velocity in the chamber, shifting the transition temperature to a higher value [Carlsson and Martin, 2010]. Indeed, at high ϕ the flow of molecules that reaches the substrate is higher and over compensates the lower time that each molecule spend on the surface. The results is that at high ϕ more molecules are involved in the film-forming reactions extending the surface-reaction-limited regime to higher T_{hp}. This hypothesis is verified by the fact that, within the surface-reactions-limited regime, the DEZ consumption rate [Faÿ, 2003] increases with increasing ϕ. In terms of deposition rate and process control, the ideal conditions are in the surface-reactions-limited regime, but at the cusp of the transition to the mass-transport-limited regime. Such conditions allow for high deposition rates and fine control over the process throughout the T_{hp} range, once the ϕ is set.
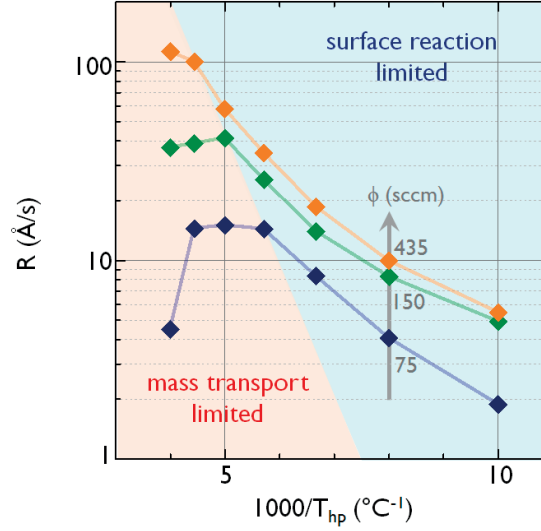
Figure 3.3: Arrhenius plot of the ZnO deposition rate for various gas flows. The combination of temperature (T_{hp}) and gas flow (ϕ) set the limiting growth regime: either surface reactions limited (light-blue-colored region) or mass transport limited (pink-colored region).

3.3.2 Parameters Influence on the Final Stage of the Film

The combination of T_{hp} and ϕ influences not only the deposition rate but also the surface morphology and preferential orientation, as shown in Figure 3.4, for films in their *final stage* (we define the *final stage* to be when the film achieves a thickness of 2 μm). Wenas *et al.* showed that a transition from *c*- to *a*- textured film is obtained by increasing T [Wenas et al., 1991b]. Nicolay *et al.* already pointed out that the same texture transition can be obtained by decreasing the H_2O/DEZ [Nicolay et al., 2012]. To have a more comprehensive view regarding the texture transition we investigated also the effect of the total gas flow. Figure 3.4 shows the different surface morphologies (observed by SEM) obtained at different T_{hp} and ϕ. These parameters influence the material growth velocity along the different crystalline orientations, resulting in the distinct surface morphologies [Wang et al., 2003, Wang et al., 2015].

The small *c*-textured grains (top-left images) are formed when the growth-velocity along the *c*-axis is larger than along the *m*- or *a*-axis, whereas the hexagonal flakes characterizing the bottom-right images are due to a higher growth velocity along the basal plane (*m*- and *a*-) when compared to the *c*-axis. At intermediate T_{hp} between these two cases, *a*-textured grains characterized by surface structures of wedges or three-sided pyramids are obtained. Moreover Figure 3.5 clearly shows that the transition in texture can be obtained by varying only one parameter among T_{hp}, H_2O and ϕ. In order to show that, we chose a common reference point for the three series: *c*-textured film close to the texture transition (T_{hp} = 155 °C; H_2O/DEZ = 1; total flow = 200 sccm). To trace the texture switch we observed the ratio between the XRD-intensity of the *a*-peak and *c*-peak. Additionally, since *c*-textured films are characterized by small surface features that do not scatter light in the visible range, we control the texture transition by calculating the diffuse transmittance at λ = 550 nm (DT_{550nm}). We set DT_{550nm}=

5% as the transition threshold between the two textures.

We observed the texture transition either by increasing the T_{hp}, by increasing H_2O/DEZ or by decreasing the ϕ. The possibility of varying the film texture by means of three parameters allow us to deposit films having similar properties under very different conditions. Note that the rough a-textured films optimized for the Si thin-film solar cells can be deposited either at 160 °C as usually reported [Faÿ et al., 2005, Hongsingthong et al., 2013, Koida et al., 2016], or at 120 °C if H_2O/DEZ and the ϕ are opportunely adjusted. This allows us, for example, to deposit the rough film on plastic substrates.
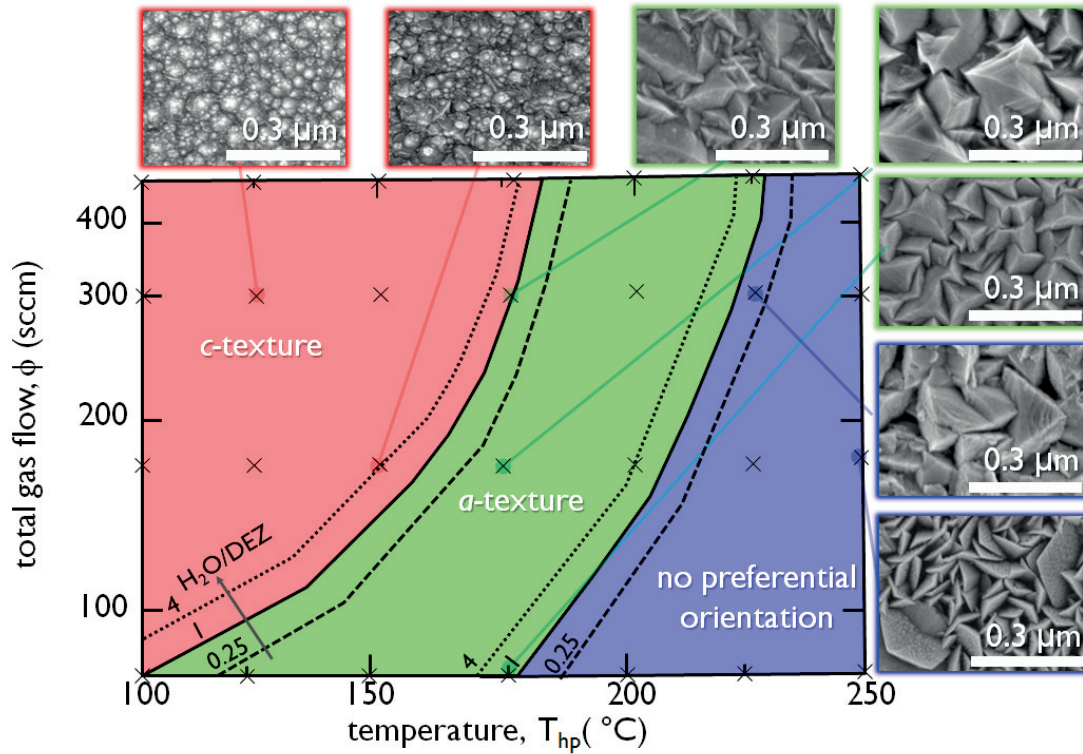
Figure 3.4: Combined effect of temperature (T_{hp}) and gas flow (ϕ) on film preferential orientation (derived from XRD patterns) and surface morphology (observed by SEM). Film thickness 2 μm.
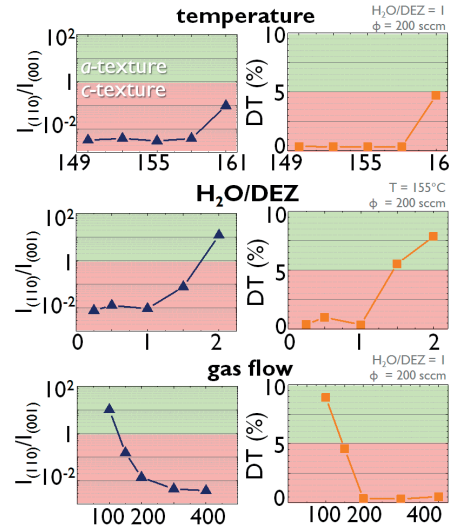
Figure 3.5: c- to a- texture switch obtained by independently varying a single deposition parameter, either temperature, H_2O/DEZ or gas flow. Film thickness 2µm.

3.3.3 Parameters Influence on Nucleation and Film Thickening

In this section, we consider how the deposition parameters affect the nucleation and the thickening of the film. Baji *et al.* showed that for atomic-layer-deposited ZnO the properties of the nucleating clusters can be tuned by adjusting the deposition parameters [Baji et al., 2012]. Here we deposited ZnO on Si wafers for only a few seconds in order to observe the very first stages of the nucleation with SEM (cf. Figure 3.6). We investigated the nucleation of *a*-textured and *c*-textured films. Both film types exhibit island-like nucleation. The difference between the two film types is noticeable already after 3": the nucleation of the *a*-textured film is characterized by a lower concentration of large nuclei than that of the *c*-textured film. At coalescence the clusters of the *a*-textured film appear to be larger than the *c*-textured ones.
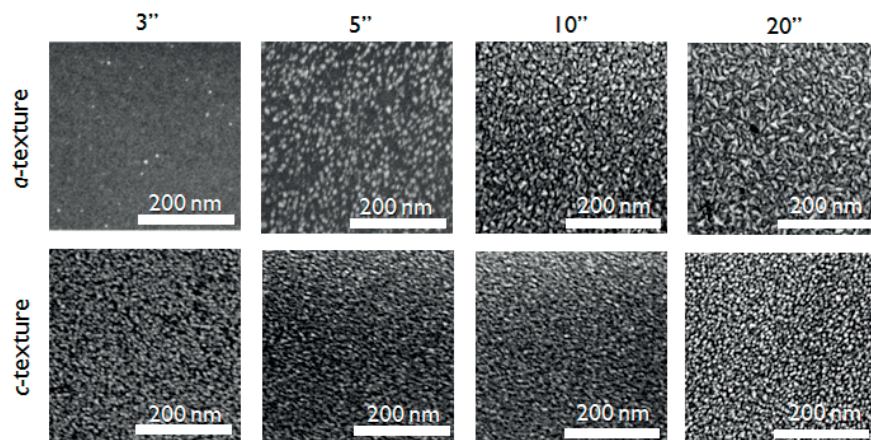
Figure 3.6: SEM micrographs of the nucleation stage for a- and c-textured films.

49

In order to quantify the effect of T_{hp}, H_2O/DEZ and ϕ at nucleation stage, we acquired AFM images of three series of samples in which we changed the parameters one by one. We assessed the influence of the growth parameters by means of two indicators: nuclei density (ρ_N) and average nuclei height (h_N, both derived from AFM images). Figure 3.7 shows the effect of T_{hp}, H_2O/DEZ and ϕ on the film features at nucleation. An increase in temperature leads to increased h_N while slightly decreasing ρ_N. An increase in H_2O/DEZ, at a constant ϕ, increases the h_N and dramatically ρ_N. An increase in ϕ, at a constant H_2O/DEZ, decreases the h_N and strongly increases the ρ_N.
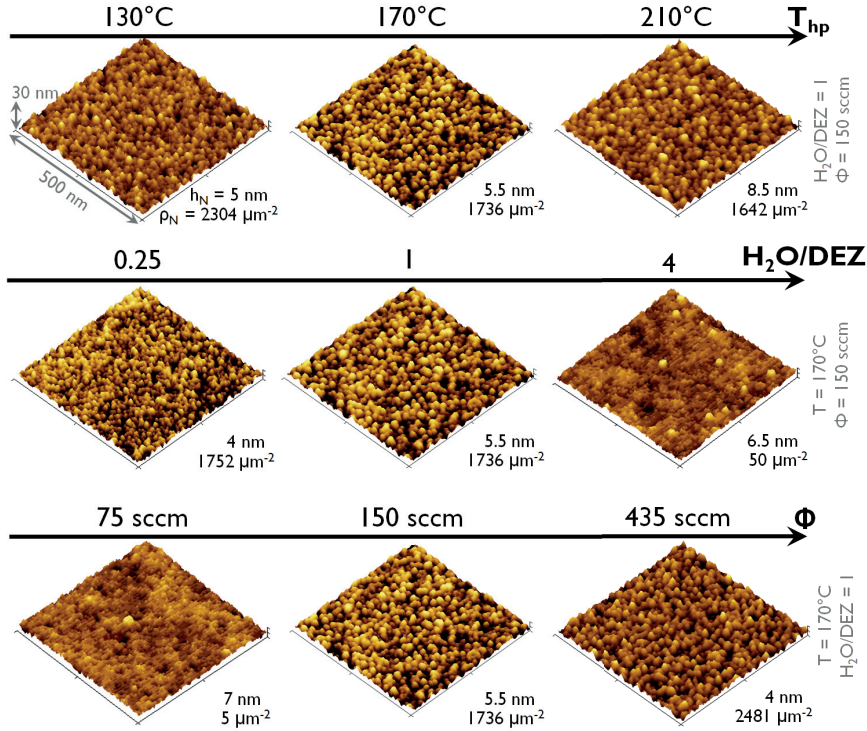
Figure 3.7: Effect of temperature (T), H_2O/DEZ and gas flow (ϕ) on the film nucleation. For each condition, the surface morphology, average nuclei height (h_N) and density (ρ_N) are reported. Derived from AFM measurements. Film thickness between 5 and 10 nm.

To assess the texture development during film thickening, we used the texture coefficients (*TC*) as indicators [Harris, 1952, Moutinho, 1995]. These indicators are derived from the XRD pattern and represent the relative intensity of a particular orientation *(abcd)* with respect to the others for a given film thickness. They are defined as follows:

$$TC(abcd) = \frac{I(abcd)/I_{ICSD}(abcd)}{\frac{1}{N}\sum_{hkil=1}^{N} I(hkil)/I_{ICSD}(hkil)} \tag{3.2}$$

where *I(abcd)* is the measured intensity of the *(abcd)*-peak; I_{ICSD} is the intensity for ZnO

powders reported in the Inorganic Crystal Structure Database (ICSD, for ZnO data from [Kihara and Donnay, 1985]); and N is the number of XRD peaks considered, in our case N = 3: $(10\bar{1}0)$, (0001), $(11\bar{2}0)$ respectively related to the m-, c- and a-orientations. From Equation 3.2 it is possible to show that for randomly distributed powders the TC value for all peaks is 1; while in the case of textured film, the TC of the preferential orientation increases reaching a maximum value of N only when no other peaks are present in the XRD pattern.

Figure 3.8 shows the effect of each deposition parameter on the evolution of the texture coefficients during film thickening. At low T_{hp} the c-texture is present from nucleation and is maintained until the final stage; with increasing T_{hp} the m- and a-orientations are more and more favored already at nucleation, and at the final stage the a-texture always becomes the preferential orientation. The H_2O/DEZ ratio shows an effect similar to the one induced by temperature, except that, for low values, the c-texture (PO at nucleation) is overtaken by the a-texture during growth. An increase in ϕ shows the opposite trend, at low gas flow the a-texture is preferential and by increasing the ϕ the c-texture takes over (already since the nucleation stage).
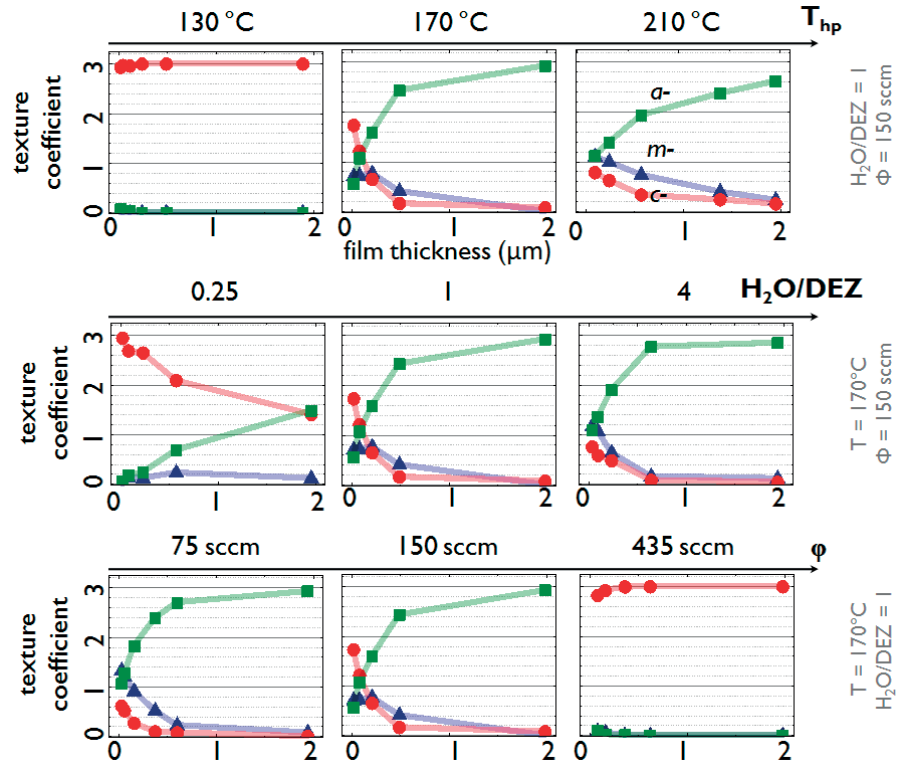
Figure 3.8: Effect of temperature (T), H_2O/DEZ and gas flow (φ) on the film preferential orientation with respect to film thickening. Green, blue and red curves represent respectively a-, m- and c- orientation. Texture coefficients are derived from XRD pattern.

A confirmation of the evolution of the preferential film orientation comes from TEM observations. The *double wedge* sample preparation (cf. Section 2.2) combined with the ACOM allows

us to follow the evolution of the preferential orientation by analyzing just one sample for each deposition condition as shown in Figure 3.9. The film deposited at 150 °C shows that *c*-texture starts in the first tens of nm and is conserved during the growth. The film deposited at 170 °C does not show any defined preferential orientation at nucleation; at around 300 nm the *a*-oriented grains start to overtake the *c*-oriented ones becoming the dominant ones during the following film thickening.
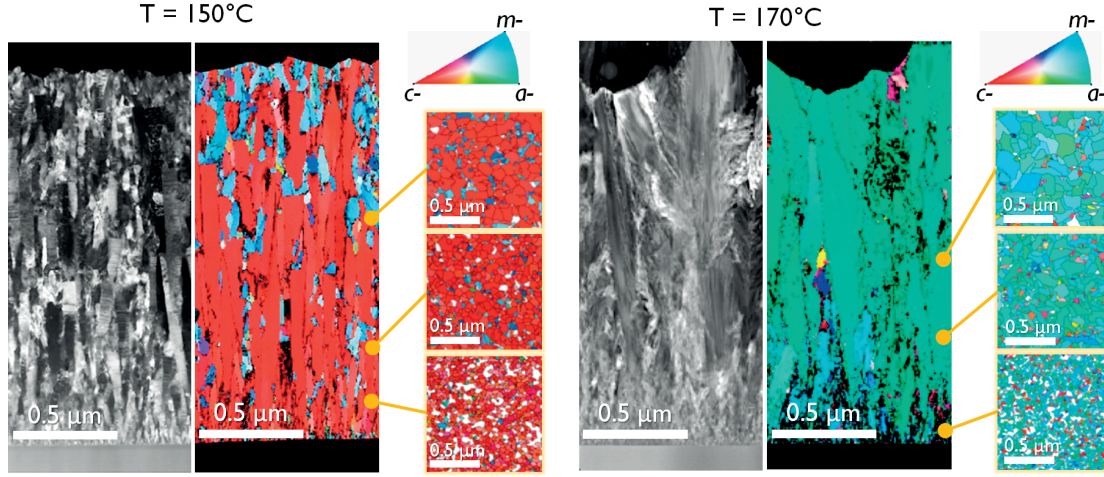
*Figure 3.9: Dark-field STEM and TEM-ACOM images of ZnO films deposited at: **(a)** 150 °C and **(b)** 170 °C. The colors, represented in the inverse pole figure, refer to the grain orientation along the substrate normal. Courtesy of A.B. Aebersold*

3.3.4 Adatom Mobility and Film Crystallinity

The observed dependency of the film structural properties on the deposition parameters can be explained in terms of adatom mobility. It is known that the formation of an ordered lattice requires that adatoms coming from the gas phase can travel long enough to find a good attachment site. Hence, when the adatom mean free path is too short to find a low-energy lattice site, the film will likely be amorphous [Ohring, 2002a]. Conversely the degree of well-ordered crystalline material improves as the adatom mean free path increases. At the low temperatures studied here (< 250 °C), adatom desorption is negligible (cf. Figure 3.3 where no *desorption regime* is observed). Consequently, the adatom motion on the film surface can be modeled as Brownian [Mirica et al., 2004]. If D is the adatom diffusion coefficient and τ the time before the adatom motion is stopped by the arrival of subsequent adatoms from the gas phase, the adatom mean free path $\langle x \rangle$ can be expressed as:

$$\langle x \rangle = \sqrt{2D \cdot \tau} \tag{3.3}$$

Moreover it is possible to show that τ is related to the adatom flow from the gas phase ϕ_{ad} and

to the lattice interatomic distance d_0 by [Lewis and Anderson, 1979, Reichelt, 1988]:

$$\tau = \frac{1}{\phi_{ad} \cdot d_0^2} \tag{3.4}$$

Substituting Equation 3.4 into Equation 4.5, and considering that, in a first approximation, the adatom flow is proportional to the gas flow $\phi_{ad} \propto \phi$, the adatom mean path can be written as:

$$\langle x \rangle = \sqrt{\frac{2}{d_0^2} \cdot \frac{D}{\phi_{ad}}} \propto \sqrt{D/\phi} \tag{3.5}$$
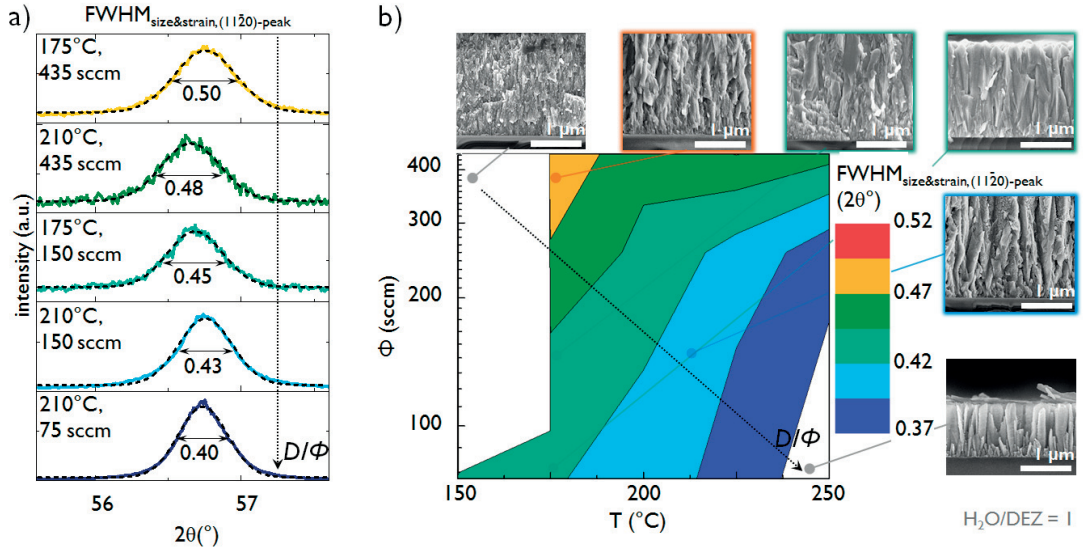
Figure 3.10: Effect of temperature and gas flow on the film crystallinity. (a) Narrowing of the FHWM with increasing D/ϕ ratio. (b) Combined effect of temperature (T) and gas flow (Φ) on the crystalline quality of the film. SEM cross-sectional images referred to some T,ϕ combinations.

Seeing that the adatom mean free path is proportional to $\sqrt{D/\Phi}$, this ratio must therefore be maximized to achieve high-quality crystalline material. It is noted that Brune *et al.* proposed a similar parameter (with deposition rate instead of gas flow) for the diffusion of silver atoms on platinum [Brune et al., 1999]. The effect of the deposition parameters on film texture previously reported can therefore be described in terms of the variation of $\langle x \rangle$. As shown by [Reichelt, 1988], the adatom mean free path increases monotonically with temperature leading to a more crystalline film. Inversely an increase in gas flow reduces $\langle x \rangle$ leading to less crystalline film. The effect of H_2O/DEZ is less straightforward. It was reported that in CVD the organic by-products released by the dissociation of the DEZ molecule (cf. Equation 1.4) tend

to remain on the film surface [Mar et al., 1995] reducing the adatom mobility. An increase of H_2O content in the gas phase could favor the desorption of by-products [Koch et al., 1997] and in turn increases the adatom mobility.

We assessed the relative quality of the crystalline material by comparing the broadening of the XRD peaks as shown in Figure 3.9. Note that TEM observations show that the films contain no detectable volume fraction of amorphous phase, other than the thin (sub-nm thick) disordered material along incoherent grain boundaries. Supposing that no composition gradient is present through the film, we attribute deviations from high crystalline material to: non uniform distribution of grain sizes (affecting the disordered grain boundary volume fraction) and from non-uniform local strain, microstrain (associated with an increase in the density of intragranular defects such as dislocations). Both effects translate into an increase in the measured full width at maximum height $FWHM_{meas}$ of each XRD peak, whose broadening can depend on contributions of crystallite size $FWHM_{size}$, microstrain $FWHM_{strain}$, and from instrumental setup $FWHM_{instr}$. For a Gaussian fitting peak, the following expression holds [Bish and Post, 1989, Karen and Woodward, 1998]:

$$FWHM_{meas}^2 = FWHM_{size}^2 + FWHM_{strain}^2 + FWHM_{instr}^2 \qquad (3.6)$$

Following from this, it is clear that, by removing the $FWHM_{instr}$, the resulting XRD peak width provides a comparative indication of the *crystalline quality*, here defined as increased grain size or lower microstrain/defect population, so corresponding to better overall material ordering [Patterson, 1939, Cullity, 2001] In Figure 3.10, the crystalline quality is assessed by comparing the width of Gaussian functions fitted to the $(11\bar{2}0)$-peak, of different films with instrumental broadening removed. Despite the large differences between the $(11\bar{2}0)$-peak intensities at various deposition conditions, the Gaussian functions fit the peaks well and are all characterized by a standard errors on *FWHM* values below 2%, confirming the fairness of the comparison. The peak width narrows, and hence crystalline quality improves, as T_{hp} increases and Φ decreases. This verifies the dependencies stated by Equation 3.5 that crystalline quality is directly related to the adatom mean free path $\langle x \rangle$. A similar trend was observed for ZnO films synthesized by combustion chemical vapor deposition [Polley and Carter, 2001]. Additional observations from SEM cross sections of cleaved ZnO films (Figure 3.10) point in the same direction. When D/Φ increases, the fracture surfaces exhibit more clearly defined grains and grain boundaries. This is similar to reports for metallic thin films by Thornton and Barna *et al.* [Thornton, 1977, Barna and Adamik, 1998], and could correlate both with an increase in crystallite size, and with a decrease in microstrain and crystalline defects that leads to cleaner inter-granular cleavage.
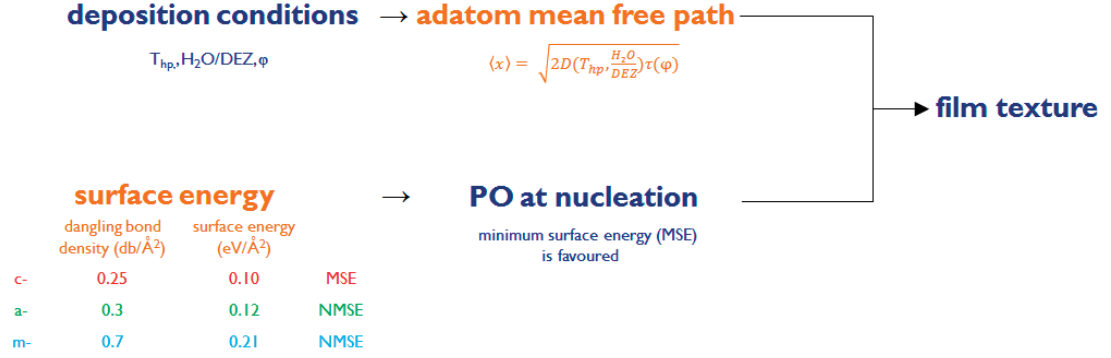
Figure 3.11: Schematics showing underling the dependence of film texture on both adatom mobility and the preferential orientation at nucleation. The values of surface energy for the different orientations are taken from [Fujimura et al., 1993].

3.4 Structural Defects

Two main film textures were observed in the deposition parameter space considered in Section 3.3: *c*- and *a*-texture. These two textures are characterized by some differences in structural defects. To better differentiate the two films we define the selection layer as the initial region of growth that precedes the establishment of a clear preferential crystallographic film orientation. As shown in Figure 3.9 and 3.12, the *a*-textured film shows a thick selection layer of poorly defined microstructure corresponding to the classical competitive overgrowth that leads to dominant V-shaped grains, while the *c*-texture film shows a very thin selection layer ($\approx$50 nm) and a high density of columnar grains. A further confirmation of the difference in the evolution of the texture comes from the selected-area diffraction pattern images of Figure 3.12 that are taken from the first 0.2 μm of the layers (see inset). These show that the *a*-textured film does not have a well-defined preferential orientation (full rings for the (0001) and (10$\bar{1}$0) planes, and large arcs for the (11$\bar{2}$0)) while the *c*-textured does (the two arcs of intensity from (0001) planes perpendicular to the substrate), this observation is also confirmed by Figure 3.9. The selection layer contains a high concentration of grain boundaries that affects the film electrical properties. The thicker selection layer of *a*-textured films reduces the film resistivity of the first hundreds of nanometers with respect to the *c*-textured film. We will show in chapter 6 that when the film is used as front electrode in copper indium gallium selenide (CIGS) photovoltaic cells, the presence of a relatively thick and resistive selection layer can be beneficial.

The second microstructural difference relates to the presence of basal stacking faults, clearly visible by TEM observations. Basal stacking faults are often reported in ZnO thin films [Sagalowicz and Fox, 1999] and their presence is likely due to their low formation energy, calculated to be smaller than 0.05 eV [Blackwell et al., 2013]. Basal stacking faults are approximately parallel to the substrate in the *c*-textured films (hence visible only in cross section, Figure 3.12) and approximately perpendicular to the substrate in the *a*-textured films (hence better visible in plan view, Figure 3.12d). It is known that linear and plane defects can influence the way in which the film develops [Germain et al., 2003, Fang et al., 2005], in Chapter 5 we will explain
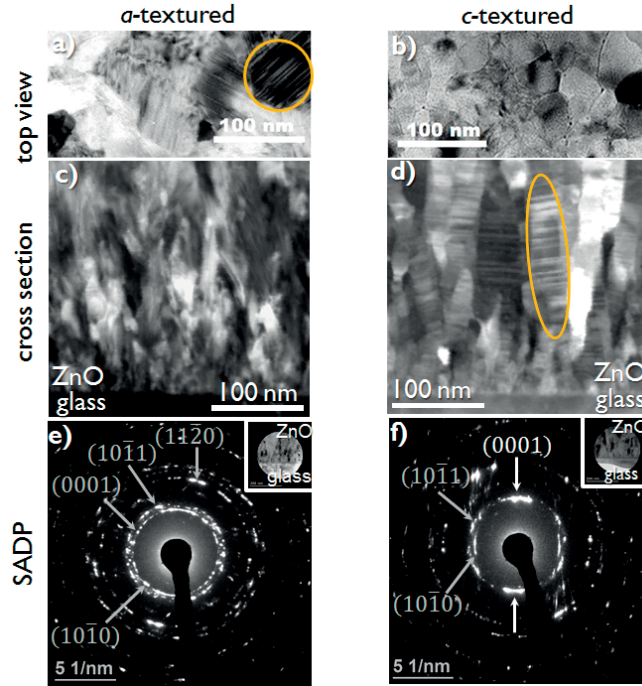
Figure 3.12: Observation of the microstructure of a- and c-textured films. **(a)** *and* **(b)** *TEM plan view of 1.5-µm-thick films.* **(c)** *and* **(d)** *dark field STEM of the cross section of the first 0.3 µm of the films. The orange rings underline some of the grains containing stacking faults.* **(e)** *and* **(f)** *Selected area diffraction pattern of the first 0.2 µm of the film (region of interest shown in the insets). Courtesy of A.B. Aebersold.*

that this is true also for *a*-textured ZnO films.

There is an additional structural difference between *c*- and *a*-textured films: *c*-textured films deposited on the glass commonly used in our laboratory (AF32, Schott, 0.5 mm) are prone to crack formation while *a*-textured films are not. Cracks appear for *c*-textured films thicker than 1.2 - 1.4 μm. As shown in Figure 3.13a, 3.13b, 3.13c the width of the crack increases with the film thickness. Plan view and cross-sectional SEM images revealed that in 3-μm-thick films some cracks propagate along the whole ZnO layer reducing the conductivity of the sample to around 10-20%. The detrimental effect becomes more important when the samples are exposed to moisture, likely due to the ease with which water vapor can enter the films through the cracks. Tests performed in damp heat conditions (relative humidity 85% and temperature 85°C) for 500 h showed that the sheet resistance of *c*-textured films with cracks increases by several orders of magnitude (up to the GΩ_{sq}) with respect to the 600-700Ω_{sq} of the crack-free films.

It is known that cracks in thin film can be induced by tensile stress [Thompson and Carel, 1996, Addonizio and Diletto, 2008]. By depositing the films on 200μm Si-wafer and measuring the amplitude of the bending, we verified that both *a*- and *c*-textured films accumulate tensile stress, and that the stress accumulated by the *c*-textured films is three times larger than that

of the *a*-textured films as shown in Figure 3.13. The causes of stress formation could be either local deformation of the crystal, known as *intrinsic* stress, or the difference in thermal expansion coefficients between the film and the substrate, known as *thermal* stress [Morosanu, 1990]. We hypothesised that crack formation in *c*-texture is induced by thermal stress after observing that most of the cracks appeared on the film during the cooling period just after the deposition. As shown in Table 3.1, the thermal expansion coefficient at 450 K (the deposition temperature is about 425 K) of *c*-textured film [Hanada, 2009] is larger than the one of the AF32 Schott glass [Glass, 2013a] while the *a*-textured film has a thermal expansion coefficient [Hanada, 2009] comparable with that of the glass. As shown in Figure 3.13e, 3.13f we eliminate the cracks in *c*-textured films by depositing on Schott DF263 (0.5 mm), a glass with a thermal expansion coefficient larger than *c*-textured film [Glass, 2013b].

Table 3.1: Thermal expansion coefficients at T = 450 K for a- and c- textured ZnO [Hanada, 2009], crystalline silicon [Watanabe et al., 2004] and two types of Schott glass AF32 [Glass, 2013a] and D263 [Glass, 2013b]

material	α_{450K} (10^{-6} K^{-1})
a-textured ZnO	3.15
Schott AF32	3.2
c-Si	3.3
c-textured ZnO	5.5
Schott D263	7.2
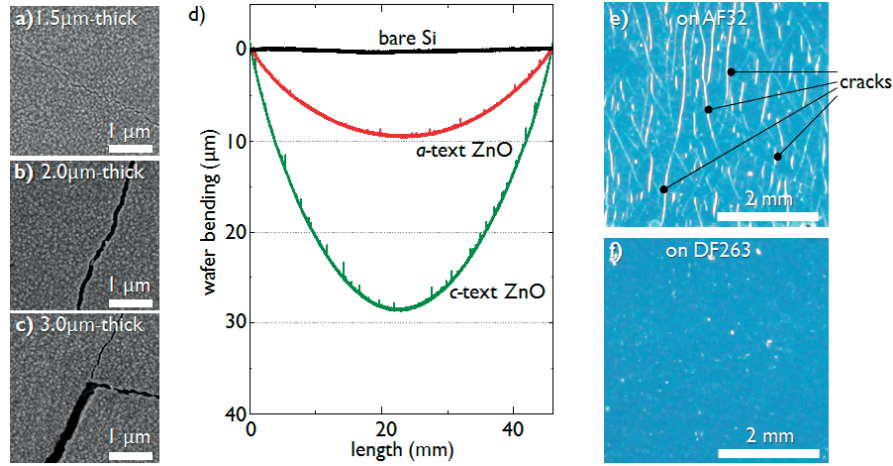
Figure 3.13: SEM images of the cracks induced by the tensile stress on c-textured film deposited on Schott AF32 glass for a film thickness of (a) 1.5 μm, (b) 2.0μm and (c) 3.0 μm. (d). Bending of the Si wafer due to the tensile stress induced by a- and c-textured films. Confocal microscope images of a 3-μm-thick film c-textured film deposited (e) on Schott AF32 glass, cracks visbile, and (f) Schott D263 glass. Courtesy of J. Persoz.

3.5   Control of the Film Preferential Orientation

3.5.1   Simulations

So far we obtained different films showing a large variety of properties at their final stage. Actually, these films were "naturally grown" i.e. without any modification of the deposition parameters during the growth. Now we want to understand how to tune the film preferential orientation during growth in order to further customize film properties. To do that we ran simulations showing how the structural properties of the film (mainly grain size) are influenced by a variation of the film preferential orientation during film growth.

The implementation of the code followed the approach proposed by Ophus *et al.* [Ophus et al., 2009]. In this approach, polycrystalline film starts from nuclei randomly distributed on the substrate surface. The nuclei orientation can be chosen to be randomly distributed or preferentially distributed along a particular direction. The nuclei are forced to be at a minimum distance between each other. As more material is deposited each crystallite expands until it meets a neighbour forming a grain boundary. Once formed, grain boundaries are stationary. As growth continues, the faster growing grains subsume these slower neighbours. The growth velocity of a crystal facet depends only on its crystallographic orientation and the Wulff construction is implemented by plotting from each nucleation point the growth velocity vectors for all face orientations. Planes are placed perpendicular to these vectors at a distance from the origin proportional to their growth velocity. The surface of a grain is defined by all the surfaces of the planes closest to the origin. The point on the surface furthest from the origin corresponds to the fastest growth direction. If the vector from the nucleation point of the grain to the farthest grain point is perpendicular to the substrate then this grain will grow at least as fast as any other grain. Most real crystal systems have various equivalent directions (symmetries) and therefore multiple equivalent fastest growth directions.

To simulate the wurtzite structure we chose the hexagonal bi-pyramid shown in Figure 3.14 (in grey). This shape has six equivalent directions corresponding to the *a*-axis and two equivalent corresponding to the *c*-axis. The growth velocity along a certain direction direction is defined by setting the distance between the origin of the bi-pyramid and its apex along that direction. We performed the simulations by combining three preferential orientations at nucleation (*a*-axis, none or *c*-axis) and three deposition condition (fastest *a*-, fastest *c*- and same growth velocity), ending up with nine possible combinations. Figure 3.14 shows that for random oriented grains at nucleation the grain size does not change noticeably with respect to the particular fastest grow direction. When considering *c-(a-)* as the preferential orientation at nucleation, we see that at final stage the grains are small when *c-(a-)* is the fastest growing direction. They become larger when the growth velocity of the *c-(a-)*orientation is decreased with respect to *a-(c-)*. Our findings are in agreement with the ones of Ophus *et al.* for conical grains [Ophus et al., 2010b]. They showed that when the preferential orientation at nucleation is *biased towards* the fastest growing direction many grains have a favourable orientation and the strong competition between them produces films composed by many, but narrow, grains.
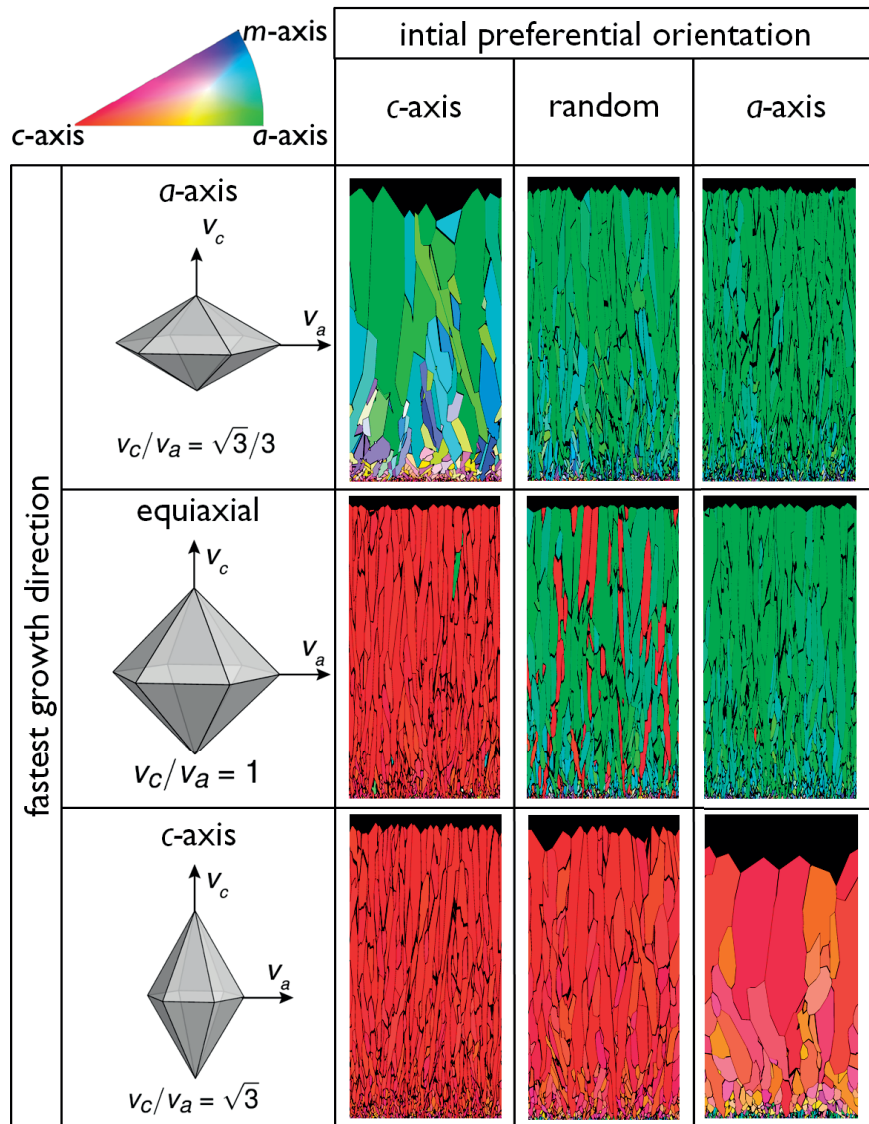
Figure 3.14: Simulation outcomes of structural film evolution, cross-sectional view, combining different relative growth rates (rows) and preferential orientations at nucleation (columns). Data courtesy of A.B. Aebersold.

On the other hand when the preferential orientation is *biased away* from the fastest growing direction, there are very few grains having the favourable orientation that in the long run will dominate the surface. The few surviving grains that compose the film at finale stage will be wider.

3.5.2   Increasing Grain Size

Simulations showed that a nucleation layer characterized by a low fraction of grains oriented along the fastest-growth orientation should develop larger grains than a layer having a large fraction of grains oriented along the fastest orientation. Figure 3.15 schematically shows the experiment we set up according to the simulation prediction in order to obtain larger grains.
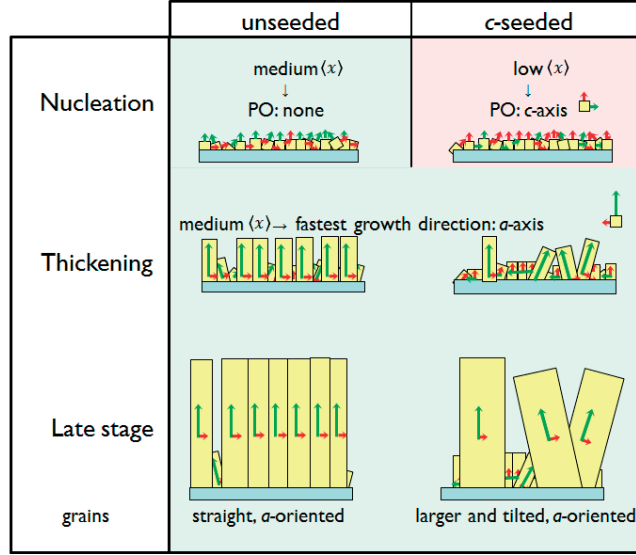
Figure 3.15: Schematic of the preferential orientation evolution for unseeded and c-seeded a-textured films.

As the stage we chose the conditions close to the ones optimized for the application as electrodes in solar cells (medium $\langle x \rangle$ ratio, 180 °C, 1.3, 150 sccm) which leads to the *a*-axis being the fastest-growth direction. In order to minimize the fraction of *a*-oriented grains at nucleation, we deposited a seed layer (50 nm thick) with the *c*-axis as the preferential orientation (low $\langle x \rangle$ conditions, 150 °C, 0.7, 250 sccm). After having deposited the *c*-seed layer, we increased the $\langle x \rangle$ ratio, such that the *a*-axis was now the fastest-growth direction. We compared this *c*-seeded layer with an unseeded layer in which we kept the medium $\langle x \rangle$ conditions constant during the whole deposition. The impact of the *c*-seeded layer on the grain size during growth is shown in Figure 3.16, which compares the ACOM results of two cross sections (unseeded, *c*-seeded) with the simulation outcomes for the same configuration ($v_a > v_c$ on unseeded and *c*-seeded layer). Both orientation maps were overlaid with a greyscale reliability index, as defined by Rauch and Dupuy [Rauch et al., 2008]. The dark vertical lines can be considered as boundaries separating different grains, with each grain being colored according to its crystallographic orientation according to the inverse pole figure (IPF) map shown in the figure. Green grains are the ones growing with their *a*-plane parallel to the surface, while red grains and the blue grains have respectively their *c*-plane and *m*-plane parallel to the surface. The *c*-seeded layer is evident as red-colored grains in the first 100 nm of film at the film-substrate interface. This *c*-seeded layer has a marked influence on the subsequent average grain size. The difference in average size between the two films is less than 5 nm at

a film thickness of 0.5 μm, but increases as the film thickens until reaching a 23% difference at a film thickness of 2 μm (129 *vs.* 105 nm, for *c*-seeded and unseeded films, respectively). A similar difference in grain size between the two samples (26 ± 6 %) was independently derived from SEM top-view images, thus confirming the statistical significance of the grain size difference. On average, grains of the *c*-seeded film are tilted away from the direction perpendicular to the substrate surface by a larger angle when compared to the unseeded film, which qualitatively agrees with numerical simulations [Ophus et al., 2010b].
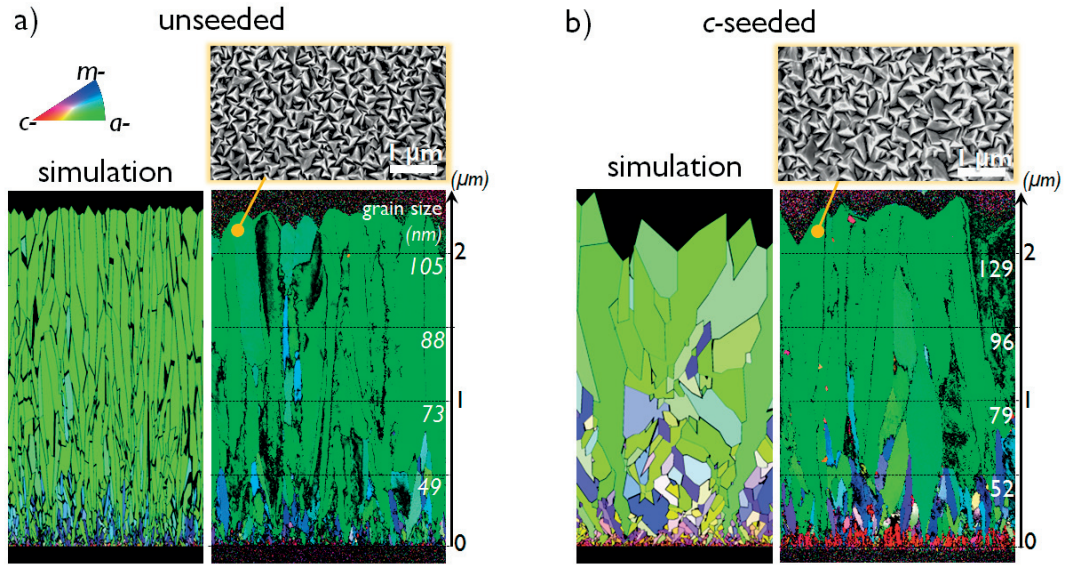
Figure 3.16: Plan view SEM micrographs, simulation outcomes and ACOM TEM measured cross section of (a) an unseeded film and (b) a c-seeded film. The inverse pole figure orientation maps show the grain orientation perpendicular to the substrate; a-orientation (green), c-orientation (red) and m-orientation (blue). Data courtesy of A.B. Aebersold.

3.6 Summary and Conclusions

In this chapter, the general theories describing thin-film growth were put into perspective with respect to LP-MOCVD ZnO thin films. We presented a detailed investigation of the main deposition parameters affecting the growth of ZnO films at different growth stages. By combining the acquired knowledge with the above mentioned theories we comprehensively explain the observed dependencies of film structure on the different deposition parameters. An explanation, based on the dependency of the adatom mean free path on the deposition parameters, allowed us to control the preferential orientation of the film at different stages of its evolution. The simulations based on the survival-of-the-fastest principle showed that, one way to obtain a larger grain one approach si to use a seed layer having a preferential orientation biased away from the one at late stage. Experiments proved the prediction to be correct.

The main outcomes are:

- **Deposition of *a*-textured film at temperatures well below** the previous reported ones (120°C vs. 160°C)

- Proof of the **different stacking faults orientation** and selection layer thickness between *a*- and *c*-textured films

- Deposition of **crack-free** thick *c*-textured films

- **Control of film preferential orientation** at the different growth stages allowing us to deposit film with an increased grain size of about 25% with respect to the reference

- Definition of the **influence of the deposition parameters** (temperature T_{hp}, H$_2$O/DEZ, gas flow ϕ) on growth regimes and film parameters

	increase T_{hp}	increase H$_2$O/DEZ	increase ϕ
deposition regime	→ mass transport	→ mass transport	→ surface reactions
adatom mean free path	increase	increase	decrease
nucleation	bigger nuclei	lower density	higher density
preferential orientation	→*a*-axis	→*a*-axis	→*c*-axis

4 Interplay of Intrinsic and Extrinsic Defects on Dopant Incorporation and Electron Scattering Sources

The charge carriers moving through a film experience scattering, which limits their mobility. For polycrystalline films the main sources of scattering are: grain boundaries, ionized impurities and phonons. The investigation of the relative contribution of each of these mechanisms aims to assess and reduce the main limitation to carrier mobility. For LP-MOCVD ZnO this analysis was previously performed only for films with a-texture and rough surface. In this chapter, we extend this investigation by experimenting with a wider range of gas precursor ratios and doping levels to analyze the interplay between intrinsic and extrinsic defects and their contributions to electron scattering.

Intrinsic defects in ZnO are oxygen vacancies and zinc interstitials, while extrinsic defects are the incorporated B atoms. Using Hall effect and optical measurements, we estimate the concentration of intrinsic defects for different H_2O/DEZ ratios of deposition. To measure the concentration of extrinsic defects, we use nuclear reaction analysis, which shows that H_2O/DEZ ratio also affects the incorporation of B atoms. More precisely, films deposited in a H_2O-rich atmosphere (high H_2O/DEZ ratio) incorporate more B atoms and obtain higher carrier concentrations up to $3.0 \cdot 10^{20}$ cm^{-3}, combined with the minimal resistivity of $1.0 \cdot 10^{-3}$ Ωcm.

Using Hall effect measurements at variable temperature and FTIR measurements, we show that the presence of intrinsic defects changes the limiting scattering mechanism. We distinguish between two regimes: when the H_2O/DEZ ratio is low (<1, high concentration of intrinsic defects) and when the H_2O/DEZ ratio is high (>1, low concentration of intrinsic defects). In the first regime, the grain boundary scattering is reduced but ionized defect scattering is increased, even if carrier concentration is low (e.g. in nid films). In the second regime, the carrier mobility of films is limited by scattering at grain boundaries, even if carrier concentration is high (e.g. up to $\approx$ 1-2$\cdot 10^{20}$ cm^{-3}). We combine these observations to demonstrate that the main limitation to carrier mobility depends not only on the doping level (as is often reported) but also on the interplay between intrinsic and extrinsic defects.

We show that scattering by phonons plays a minor role and is observable only for films with a

high concentration of intrinsic defects and a high doping level.

4.1 Motivation and State of the Art

ZnO films can have various sources of free electrons such as intrinsic defects (e.g. O_v and Zn_i), extrinsic defects (mainly atoms from group III such as B, Al, Ga, In) and combination of the previous two (e.g. H atoms filling an O_v). In this section, we review the effects that these defects induce on the N_e and μ_d of ZnO films previously reported in the literature.

Intrinsic defects are known to play an important role in determining the optical and electrical properties of ZnO. Small variations in stoichiometry significantly impact the electron concentration and the absorptance of the material. Zinc excess as low as 0.07% induces an observable yellowing of the material [Earnshaw and Greenwood, 1997, Wiberg and Holleman, 2001]. It was shown that the yellow color of ZnO thin film is the result of the creation of energy levels in the band gap related to the presence of O_v or Zn_i [Li et al., 2000, Rodnyi and Khodyuk, 2011, Wang et al., 2012].

Regarding the addition of extrinsic dopant atoms, the LP-MOCVD technique allows higher flexibility compared to physical vapor deposition (PVD) systems. In an LP-MOCVD system, the doping level can be directly controlled by adjusting the gas flow of the dopant precursor, while in PVD systems the doping level is determined by the impurity concentration inside target. For PVD it is known that, when using doped target (e.g. ZnO:Al), the N_e can be tuned by varying the O-partial pressure inside the chamber. Lower O-partial pressure generates higher film N_e [Kim et al., 2000, Singh et al., 2001].

For LP-MOCVD ZnO, the doping level is often quantified as B_2H_6/DEZ ratio in the gas phase [Steinhauser et al., 2007, Faÿ et al., 2007, Addonizio and Diletto, 2008], but the effect of the gas precursors ratio on N_e and on the dopant atoms incorporated in the ZnO:B films was rarely investigated. The quantification of the B concentration was performed only on a-textured films commonly used for thin-film solar cells ($N_e \approx 1 \cdot 10^{20}$) resulting in the concentration value of $\approx 1\%$ [Martin De Nicolas, 2012, Kobayashi and Nakada, 2014]. To our knowledge, the possible effects on the film carrier concentration of the oxidant or the reduction of the atmosphere at the gas phase have not been investigated, and it could provide useful insight on the mechanisms of B incorporation. It is reasonable to assume that during the film formation there is an interplay between intrinsic and extrinsic defects, for example, Mao *et al.* showed that B incorporation induces O_v and Zn_i [Mao et al., 2016].

LP-MOCVD ZnO films contain H in concentrations up to some percents [Steinhauser, 2008, Ding, 2013]. It is not surprising to find H atoms in the film since each of the precursor gases (H_2O, DEZ and B_2H_6) contains it. Substitutional H atom on O sites was proposed as shallow donor in ZnO [Janotti and Van de Walle, 2005]. This mechanism could play a role in the high intrinsic N_e of LP-MOCVD ZnO films. Furthermore, it was reported that H-plasma treatments increase the μ_d and the N_e of ZnO films [Ding, 2013].

Both intrinsic and extrinsic defects create ionized and neutral impurities that scatter electrons and reduce their mobility. These and other scattering mechanisms have been extensively investigated since the 1950's because of the growing importance of polycrystalline silicon for the semiconductor industry [Volger, 1950]. This previous work aimed to understand the intrinsic limitations of the polycrystalline material compared to the monocrystalline material and, in particular, it addressed the mechanisms governing carrier transport through the grain boundaries. Petritz was the first to demonstrate that, in polycrystalline films, μ_d is thermally activated due to the presence of a potential barrier E_b at the grain boundaries [Petritz, 1956]:

$$\mu_d = \mu_0 e^{-\frac{eE_b}{kT}},$$
(4.1)

where μ_0 is the carrier mobility within the crystalline regions. Equation 4.1 implies that all free carriers contribute to the conduction but with reduced mobility. Although the detrimental effect of the grain boundaries was demonstrated and quantified, the physical process leading to a decrease in μ_d was still not clarified. Additionally, the reason why N_e was lower than the dopant concentration (N_d) at low doping level was still debated (doping efficiency < 1). During the 1970's, by generalizing the observation of Petritz, Seto developed a model that convincingly solved both issues [Seto, 1975]. In a polycrystalline film, at low doping levels, some of the electrons released by the extrinsic dopants are trapped at the grain boundaries generating the observed potential barrier E_b that reduces μ_d. By assuming a certain trap density N_t at the grain boundary, Seto derived the height of the barrier potential and differentiated two regimes with respect to the grain size L and the ionized dopant concentration N_d (cf. Figure 4.1):

I. totally depleted grains

$$\text{for } LN_d < N_t \qquad\qquad E_b = \frac{e^2 L^2 N_d}{8\epsilon}$$
(4.2)

II. partially depleted grains

$$\text{for } LN_d > N_t \qquad\qquad E_b = \frac{e^2 N_t^2}{8\epsilon N_d}$$
(4.3)

where ϵ is the dielectric permittivity of the film, and N_t is expressed as an interfacial density [cm^{-2}] since grain boundaries are bi-dimensional. The two regimes are represented in Figure 4.1. In the first regime, the number of free carriers provided by the dopant atoms is less than the number of traps at the grain boundaries. Therefore, only some of the traps are filled and the grains are completely depleted of carriers. The barrier height, which depends on the number of filled traps (LN_d in I, N_t in II), increases when dopant atoms are added until it reaches its maximum value when all the traps are filled by free carriers $LN_d = N_t$. In the

second regime, when dopant atoms are added, the number of filled traps N_t remains constant but the barrier height decreases as the depletion region within the grain becomes smaller. The model makes use of the dipole approximation to calculate the barrier height, with the strength of the dipole depending on the distance between the barycenter of the positive and negative charges. The barycenters of the two types of charges do not correspond because the regions around the barrier are depleted from the electrons that were trapped. The width of the depletion region W is defined by the ratio between the planar concentration of filled traps and the carrier concentration [Seto, 1975]:

$$W = \frac{N_t}{N_e} \tag{4.4}$$

Electrons can cross the potential barrier either by thermionic emission [Petritz, 1956, Seto, 1975], or by tunnelling [Martinez and Piqueras, 1979]. The thermionic process depends on the barrier, while the probability of tunnelling through the barrier increases exponentially with the decrease of the depletion region around the boundary [Simmons, 1963]. Therefore, the transport through the barrier is dominated at low doping level by the thermionic emission and at high doping level by the tunnelling process. Although within the Seto model N_d refers only to the ionized extrinsic dopant concentration, its use can be generalized to also account for ionized impurities linked to intrinsic dopants in degenerated semiconductors such as ZnO.

The conductivity of semiconductor devices is generally increased by increasing the dopant concentration, which leads to unwanted effects such as Auger recombination [Dziewior and Schmid, 1977, Tyagi and Van Overstraeten, 1983] and light parasitic free-carrier absorption [Fujiwara and Kondo, 2005]. The Seto model is important because it allows us to predict simultaneously the variation in N_e and μ_d. As a result, the resistivity can be estimated from the dopant concentration.

Seto's original model has been refined several times. Martinez and Piqueras showed that, for highly doped films, it is necessary to add a tunnelling contribution to the thermionic emission as another transport mechanism [Martinez and Piqueras, 1979]. Baccarani *et al.* pointed out the existence of a third regime not considered by Seto: partially filled traps and partially depleted grains [Baccarani et al., 1978]. Bruneaux *et al.* demonstrated the necessity of weighting the barrier height over the density of filled states just below the Fermi level [Bruneaux et al., 1991]. More recently, Kajikawa further generalized the model implementing barrier height fluctuations [Kajikawa, 2012].

The Seto model is also used to describe transport properties in TCOs [Major et al., 1986, Bruneaux et al., 1991, Zhang and Ma, 1996]. For degenerated polycrystalline ZnO thin films, the main sources of electron scattering are known to be *grain boundaries, ionized impurities* and *phonons* [Bikowski and Ellmer, 2014]. Two measurement techniques are commonly used to separate the contribution of each source. As already discussed, the Hall effect setup provides
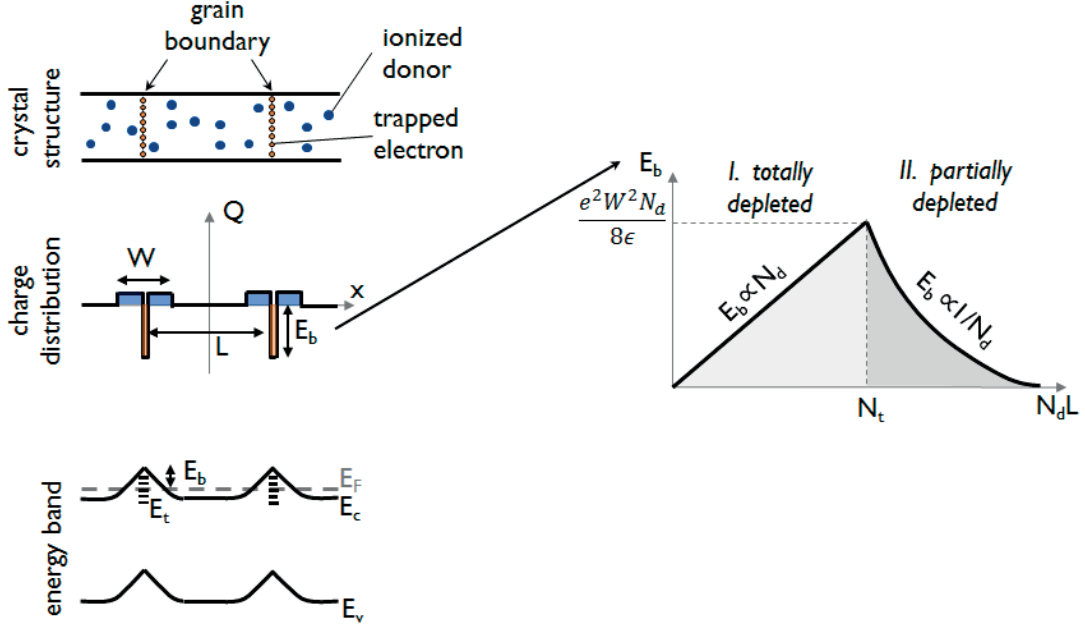
Figure 4.1: *(a)* Crystal structure, charge distribution and energy band as described in the Seto model. *(b)* Dependence of the potential barrier E_b on the product of donor concentration N_d and grain size L. W = depletion region width, Q = electric charge, N_t = sheet concentration of trap states, E_t = energy of trap states. Adapted from [Seto, 1975]
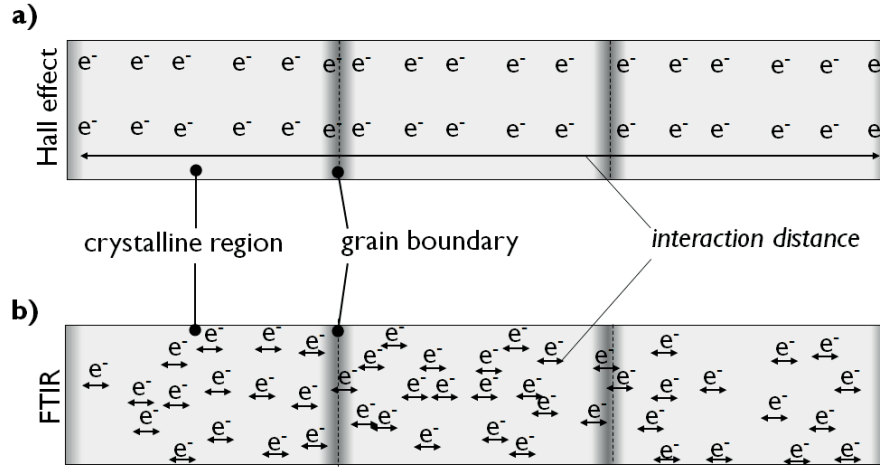
Figure 4.2: *Schematic representation of the different electron interaction distances during Hall effect and FTIR measurements. **(a)** In Hall effect measurements, the electrons are forced by the electric field to cross the whole sample interacting with the crystalline region and the grain boundaries. **(b)** When excited by infrared radiation (as in FTIR) the mean free path of electrons is on the order of tens of nm. The larger the grains, the smaller the share of electrons that interact with a grain boundary.*

μ_d, which includes the contributions of all the scattering mechanisms. By varying temperature, it is possible not only to estimate the order of magnitude of the barrier at the grain boundaries [Seto, 1975, Bruneaux et al., 1991], but also to assess the possible influence of phonons [Zhang and Ma, 1996]. The second technique commonly used is FTIR (or equivalently ellipsometric spectroscopy). FTIR provides access to free-carrier optical mobility, the carrier mobility in absence of grain boundary scattering [Brehme et al., 1999, Steinhauser et al., 2007, Prunici et al., 2013]. As shown in Figure 4.2, the film region probed during FTIR measurement depends on the ratio between the grain size and the interaction distance. The larger this ratio is, the lower the share of electrons interacting with a grain boundary will be, and therefore the probed region will be essentially the crystalline one [Knoops et al., 2015]. By measuring the carrier mobility with these two techniques on the same series of samples, it is possible to understand whether scattering of the carriers occurs predominantly within the grain boundary or within the grain.

4.2   Experimental Details

The ZnO films were deposited on 0.5-mm-thick borosilicate glass, at a hotplate temperature of 180°C and a chamber pressure of 0.35 mbar. The H_2O/DEZ series was deposited by keeping the (H_2O + DEZ) gas flow constant, i.e. by varying the flow of both gases together for each sample of the series as listed in Table 4.1.

Table 4.1: Real gas flows of water H_2O, diethylzinc DEZ and diborane B_2H_6 (2% in argon) for the three doping series analyzed in the present chapter.

H_2O/DEZ = 0.5			H_2O/DEZ = 1.0		
H_2O	**DEZ**	**B_2H_6/Ar**	**H_2O**	**DEZ**	**B_2H_6/Ar**
sccm	*sccm*	*sccm*	*sccm*	*sccm*	*sccm*
50	100	0	75	75	0
50	100	10	75	75	5
50	100	20	75	75	20
50	100	50	75	75	50
50	100	100	75	75	70
50	100	130	75	75	100

H_2O/DEZ = 1.5		
H_2O	**DEZ**	**B_2H_6/Ar**
sccm	*sccm*	*sccm*
90	60	0
90	60	5
90	60	10
90	60	50
90	60	80

For nuclear reaction analysis (NRA) and electron recoil detection analysis (ERDA), the samples were around 500 nm thick and deposited on 200-μm-thick c-Si(n) wafer. Calibration of the B concentration for NRA was done by implanting a known amount of B ions in a non-intentionally-doped ZnO film also deposited on c-Si(n) wafer. The NRA measurements were performed by Javier Ferrer at Centro Nacionales des Acceleradores (Sevilla, ESP). The B-ion implantation was done by Marica Canino at the Institute for Microelectronics and Microsystems (Bologna, Italy).

All the other measurements were performed on $\approx$ 2.5-μm-thick films to increase the FTIR reflectance signal (related to the collective oscillation of electrons, plasma frequency). The film absorptance was obtained by measuring transmittance and reflectance in the 320 - 2000 nm range using a UV-VIS-NIR spectrophotometer and applying a refractive index matching liquid (CH_2I_2) at the front surface of the ZnO in order to reduce artifacts induced by film roughness. The carrier concentration and carrier mobility were measured using the Hall effect setup both at room temperature and variable temperature (80-350 K). The optical mobility was obtained by fitting the reflectance curves with the Drude model. The sample depositions and Hall effect and FTIR measurements were performed by David Frédéric Schmidt at PVLAB EPFL.

4.3 Intrinsic Dopants

In LP-MOCVD ZnO, the variation of the H_2O/DEZ ratio not only induces a texture change, as seen in section 3.3, but also affects the electrical and optical properties.

The first observable effect when decreasing the H_2O/DEZ ratio is a change in the film color. At high H_2O/DEZ the film appears white; decreasing this ratio results in a yellowish film. The effect is clearly observed in the absorptance curves (Figure 4.3a). A decrease in the H_2O/DEZ ratio reveals a kink near the band gap onset, which leads to an increased absorptance in the 400 - 550 nm range. This change can be attributed to the creation of defect-related energy levels as tail states of one of the two energy bands (i.e. valence or conduction). Note that a single ionized oxygen vacancy — responsible for the color transition from white to pale yellow — was reported for hydrothermally grown ZnO and measured to be 0.24 eV below the bottom of the conduction band, which is in agreement with the film absorptance increase for wavelengths around 400 nm [Simpson and Cordaro, 1988].

The curves of Figure 4.3a also show the second effect: a decrease in free-carrier absorptance in IR with increasing H_2O/DEZ. This observation is confirmed by the measurement of N_e shown in Figure 4.3b: when increasing the H_2O/DEZ ratio, a decrease in N_e is observed. This decrease in N_e allows us to locate the energy of the defect states related to non stoichiometry close to the conduction band (due to the n-type character of nid ZnO).

Noteworthy, the films deposited at H_2O/DEZ = 1.5 show an extremely low absorptance, constantly below 2% in the wavelength range 500 - 2000 nm. In LP-MOCVD ZnO films, such low film absorptance was previously reported only for films that underwent air annealing [Ding,

2013].
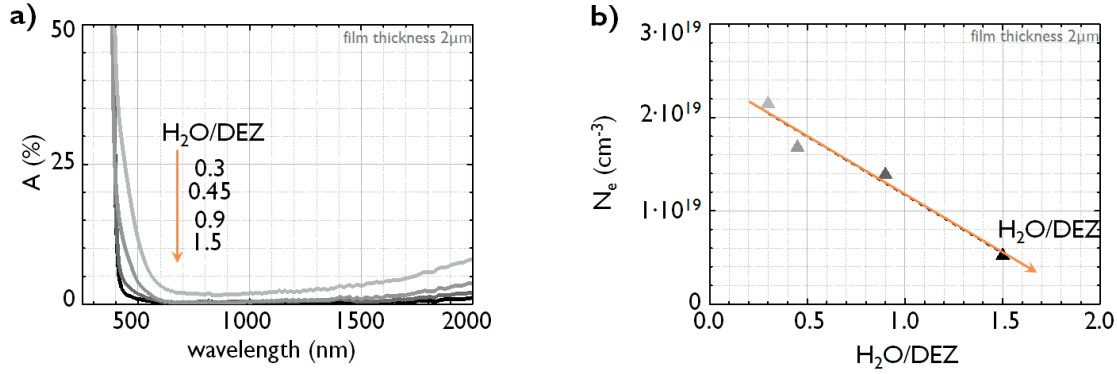
*Figure 4.3: Effect of H_2O/DEZ ratio variation on **(a)** absorptance (A) and **(b)** carrier concentration (N_e) of the film. Film thickness 2 μm.*

4.4   B incorporation and Doping Efficiency

As shown in Figure 4.3b, N_e of as-deposited intrinsic ZnO films varies between 0.5 and $2 \cdot 10^{19}$ cm^{-3}. Due to the moderate μ_d, these values are too low to yield the conductivity required by many applications. To further increase the conductivity of the film, an extrinsic dopant is added, which for LP-MOCVD ZnO is mainly done by adding B atoms to the gas phase in the form of B_2H_6. Although it is known that N_e depends on the B_2H_6/DEZ ratio [Wenas et al., 1991b] and that it saturates at values between $2\text{-}3 \cdot 10^{20}$ cm^{-3} [Faÿ, 2003], few studies have assessed the joint influence of the gas precursor flow ratios on B incorporation and doping efficiency (defined as N_e/N_B, where N_B is the boron concentration).

To investigate the influence of the precursor flows on doping efficiency, we deposited three doping series with the same B_2H_6/DEZ ratio but different H_2O/DEZ, namely 0.5, 1.0, 1.5. Figure 4.4a shows that the B incorporation increases roughly linearly with the B_2H_6/DEZ ratio of the gas phase. Interestingly, for the same B_2H_6/DEZ ratio, N_B increases with the H_2O/DEZ ratio, reaching the maximum value close to $1 \cdot 10^{21}$ cm^{-3} which is in agreement with SIMS measurements on a highly doped film [Martin De Nicolas, 2012, Kobayashi and Nakada, 2014]. A possible reason for the increase of N_B with H_2O/DEZ would be that an excess of water in the gas phase favors the decomposition of the B_2H_6 molecule [Weiss and Shapiro, 1953] leading to a more effective incorporation of B into the film. In order to assess which species are formed during the deposition, and possibly verify this hypothesis, FTIR measurements should be used to analyze the gas phase at different H_2O/DEZ ratio.

The dependence of N_e on B_2H_6/DEZ, shown in Figure 4.4b, is similar but with two noticeable differences: at high B_2H_6/DEZ, the N_e starts reaching saturation, and the relative difference between the three curves is less pronounced than for the B incorporation. Indeed, the N_e/N_B (cf. Figure 4.4c) decreases with increasing H_2O/DEZ as well as with increasing B_2H_6/DEZ. Similar values of doping efficiency were reported for RF-sputtered ZnO doped with different
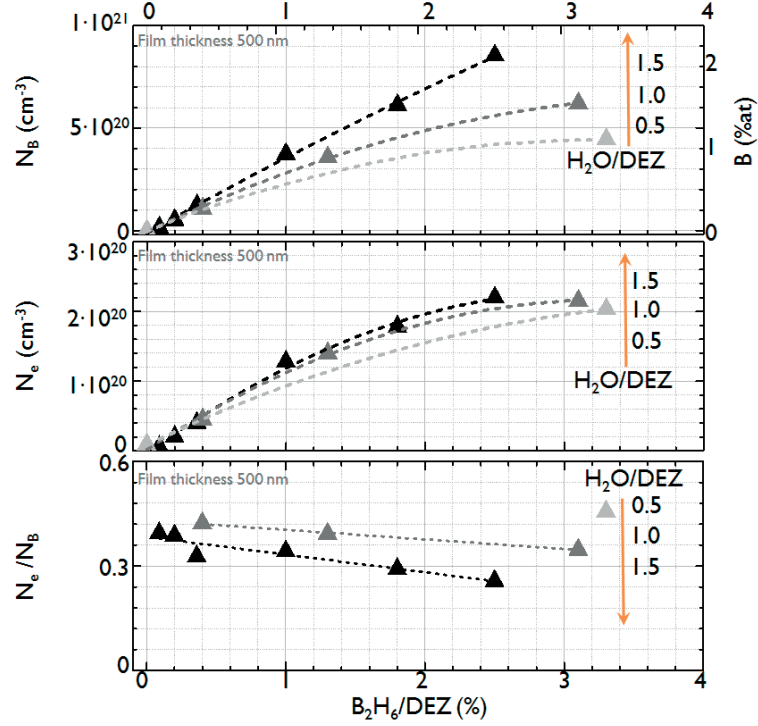
Figure 4.4: Effect of H_2O/DEZ ratio on **(a)** boron incorporation in the film (N_B, boron concentration), **(b)** carrier concentration N_e and **(c)** doping efficiency N_B/N_e. Values obtained using nuclear reaction analysis and Hall effect measurements in 500 nm-thick films. The lines are guides for the eyes.

impurities (Al, Ga, In, Ge) [Wang et al., 1996]. The decrease in doping efficiency with H_2O/DEZ could be related to the increased dissociation efficiency of the B_2H_6 molecule due to the presence of H_2O. Indeed, at high H_2O/DEZ, more B is incorporated into the film but a part of it remains bonded with the O coming from water, creating BO_x complexes which do not release free carriers. Overall, the lower N_e/N_B ratio is completely compensated for by the higher N_B, which provides a larger N_e in the film deposited with higher H_2O/DEZ.

Note that the cumulative N_e range achievable at low H_2O/DEZ is smaller (2 - $15 \cdot 10^{19}$ cm^{-3}) than the range achievable at high H_2O/DEZ (0.5 - $30 \cdot 10^{19}$ cm^{-3}) as shown in Table 4.2.

Table 4.2: Ranges of carrier concentration N_e achievable at different H_2O/DEZ ratios for a film thickness of 2 µm.

H_2O/DEZ	N_e nid $10^{19} cm^{-3}$	N_e heavily doped $10^{19} cm^{-3}$
0.5	2.0	15
1.0	1.0	25
1.5	0.3	30

71

4.4.1 Diborane Flux and Hydrogen Concentration in the Film

With the goal to distinguish the effect of B and H on the carrier concentration at increasing doping level, we performed ERDA and NRA measurements on a doping series of samples and on a B-implanted nid film. The results, summarized in Table 4.3, show a weak correlation between the H concentration (N_H) and N_e. The N_e/N_H ratio varies between 0.1 and 2.8% but it is 30 times lower than the N_e/N_B ratio. Interestingly, after the B-ion implantation the carrier concentration of the nid film increases significantly. Since the difference between as-deposited and B-ion implanted film is only the addition of B-atoms we directly attribute this effect to the B-atoms.

These results are not sufficient to exclude the effect of H atoms on the N_e of ZnO films. Macco *et al.* found high N_H of $\approx 4.2\%$ in indium oxide deposited by atomic layer deposition for films with the carrier concentration of $1 \cdot 10^{20}$ cm^{-3} [Macco et al., 2015]. Despite the low doping efficiency ($< 4\%$) they attributed the carrier concentration to the presence of H-atoms. Our results are not conclusive but they clearly show that for ZnO:B films the effect of B atoms on N_e is stronger than the one of H atoms.

Table 4.3: Comparison between carriers, hydrogen and boron concentrations (N_e, N_H, N_B) in the film at increasing doping levels (B_2H_6/DEZ in the gas phase) and constant H_2O/DEZ ratio of 1. Measurements performed using electron recoil detection analysis (ERDA). Film thickness 500 nm.

	B_2H_6/DEZ	N_e	N_H	N_e/N_H	N_B	N_e/N_B
	%	$10^{19}cm^{-3}$	$10^{19}cm^{-3}$	%	$10^{19}cm^{-3}$	%
nid	0	3.0	340	0.1	0	-
nid, B-implanted	0	6.0	330	1.8	10	60
moderately doped	0.4	4.5	380	1.2	10	45
highly doped	1.3	14	500	2.8	35	40

4.5 Dependence of Drift and Optical Mobility on the H_2O/DEZ Ratio

The optical mobility, obtained from FTIR measurements, is commonly used to quantify the scattering contribution of the crystalline regions of the film. Unlike Hall effect measurements, in which all the scattering contributions are probed, an electron excited by an IR electromagnetic wave will scatter mainly within the grains. As a consequence, in a polycrystalline film, we should expect $\mu_{opt} \geq \mu_d$. If an electron absorbs all the energy from the incoming photon $\hbar\omega_p$, its mean free path l_e can be calculated as [Knoops et al., 2015]:

$$l_e = v_e \tau = \sqrt{\frac{2\hbar\omega_p m^* \mu^2}{e^2}} \tag{4.5}$$

where v_e is the kinetic energy transferred from the photon to the electron and τ is the time between two scattering events. Therefore, for ZnO with a carrier concentration between 1–$30 \cdot 10^{19}$ (i.e. m* = 0.15 – 0.30, cf. Figure 4.5), an electron excited by IR waves with a wavelength between 1 and 20 μm (IR range used here) has an l_e between 5 and 25 nm. Note that, by using the Fermi velocity ($v_e = v_F = \hbar(3\pi^2 N_e)^{1/3}/m^*$) the calculated l_e is very similar [Knoops et al., 2015]. This means that during FTIR measurements the majority of the excited electrons do not cross a grain boundary (L$\approx$ 200 nm for 2.5-μm-thick film). That is why μ_{opt} is limited by the scattering mechanisms within in the crystalline region.

In order to assess which scattering contribution is dominant when varying the doping and the gas precursor ratio, we measured μ_{opt} and μ_d on three doping series, each characterized by a different H_2O/DEZ ratio, namely 0.5, 1.0 and 1.5.
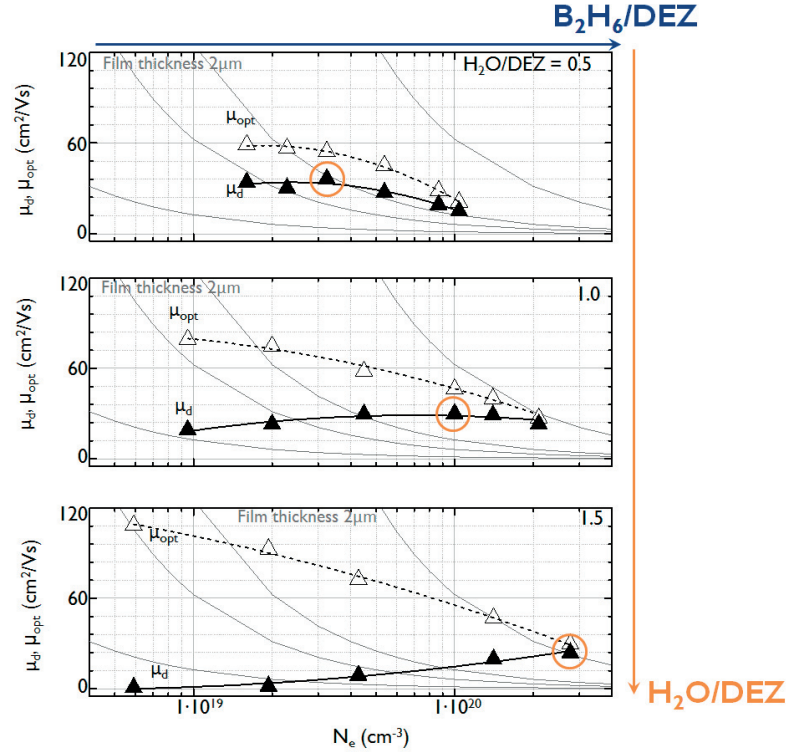
Figure 4.5: Optical mobility μ_{opt} ($\triangle$, measured with FTIR) and drift mobility μ_d ($\blacktriangle$, measured with Hall effect) for three doping series at different H_2O/DEZ ratios: 0.5, 1.0, 1.5. The orange circles indicate the highest μ_d value of each series. The continuous light-grey lines on the background indicate regions with the same resistivity. The solid and dashed black lines are guides for the eyes.

Figure 4.5 shows different trends. First, at low N_e, μ_{opt} is higher than μ_d for the three H_2O/DEZ ratios. By increasing N_e, μ_{opt} decreases until it reaches the value of μ_d. This effect, already reported for different polycrystalline TCOs [Fujiwara and Kondo, 2005, Steinhauser et al., 2007, Rey et al., 2013], is attributed to the increase in ionized impurities within the grain, which we probed by FTIR.

Second, μ_{opt} increases with increasing H_2O/DEZ. The effect is noticeable especially for the nid samples with low N_e. For the nid sample at $H_2O/DEZ = 1.5$, we calculated the μ_{opt} value of 120 cm^2/Vs for $N_e = 0.6\cdot10^{19}$ cm^{-3}, which is larger than the value predicted by the semi-empirical Masetti formula and suggested by Bikowski and Ellmer as the maximum achievable for polycrystalline films [Bikowski and Ellmer, 2014]. Nevertheless, the value is well below the limitation due to ionized impurity scattering ($Z = 1.2$) calculated by the same authors. In addition, this value of 120 cm^2/Vs is comparable with μ_d measured for the same N_e on single-crystal ZnO [Ellmer, 2001].

Third, N_e at which the maximum of μ_d is achieved increases with increasing the H_2O/DEZ ratio: $3\cdot10^{19}$ cm^{-3} at 0.5, $1.8\cdot10^{20}$ cm^{-3} at 1.0 and $3.0\cdot10^{20}$ cm^{-3} at 1.5 (presumed maximum, since $\mu_{opt} = \mu_d$). This shift of the maximum μ_d towards higher N_e yields the lowest resistivity ($1\cdot10^{-3}$ Ωcm) for the H_2O/DEZ ratio of 1.5.

4.6   Considerations on Effective Mass

As discussed, in polycrystalline film, μ_d is governed by N_e which screens the barrier potential at grain boundary reducing its detrimental effect on μ_d. On the contrary, we observed that keeping constant N_e, μ_d still varies when we increase the H_2O/DEZ ratio. We attribute this unexpected variation of μ_d to a variation of N_t. It is known that in an oxidizing environment, oxygen species chemisorb at grain boundaries and trap electrons [Orton and Powell, 1980] resulting in an increase in the potential barrier height. Similarly, under H_2O-rich conditions the O concentration is larger in the whole film and in particular in the surroundings of the grain boundaries resulting in a larger N_t and a reduction of μ_d. The films deposited at high H_2O/DEZ, are very transparent (cf. 4.3) and show large μ_{opt}. By reducing the barrier potential at grain boundaries, for example using a post-deposition hydrogen plasma treatment [Oh et al., 2007, Chang et al., 2010], these films could combine high conductivity with a very low absorptance.

We measured the reflectance curves using FTIR spectroscopy. We then obtained the values of μ_{opt} by fitting these curves to the Drude model. We used N_e measured by Hall effect and m^* as a fit parameter. Thus, additional information provided by the FTIR measurement is the variation of m^* with respect to N_e. In Figure 4.6, the stars indicate all the combinations of m^* and N_e obtained for the three series presented in Figure 4.5. The other symbols represent m^* values for various ZnO materials (single and polcrystalline; In-, Ga-, and Al-doped) obtained with various characterization techniques such as ellipsometry [Fujiwara and Kondo, 2005, Yamada et al., 2010], Seeback coefficient [Young et al., 2000, Wang et al., 2014], Faraday rotation [Baer, 1967] and four coefficients method [Kim et al., 2008]. Interestingly, all the m^* values follow the same trend with respect to N_e. The dependence of m^* on N_e is due to the non-parabolicity of the conduction band. Although this effect is often omitted in the calculations [Steinhauser et al., 2007, Messerschmidt et al., 2014], it must be taken into account when dealing with the scattering contributions in TCOs as was experimentally shown in 1989 by
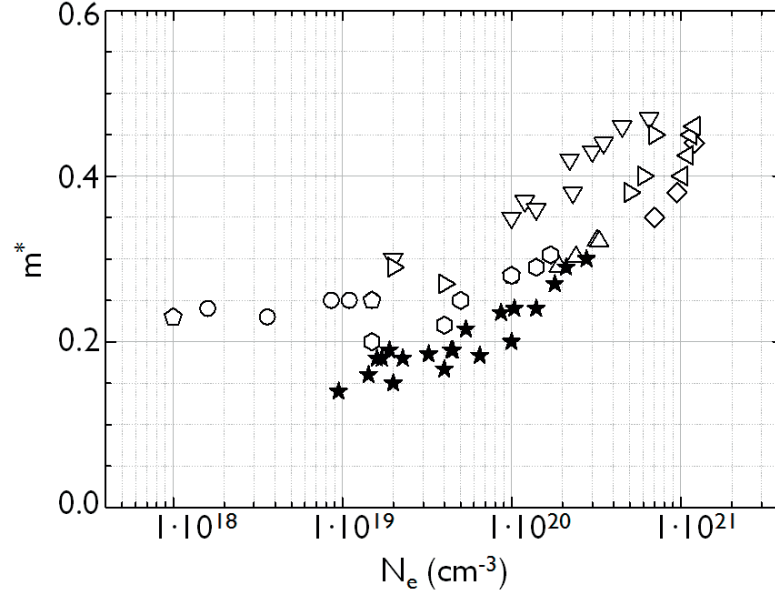
Figure 4.6: Effective mass m^* dependence on carrier concentration N_e. The values obtained within this work ($\bigstar$, from FTIR measurements) are compared with values reported in literature. Data sources: single crystal ZnO $\bigcirc$: [Baer, 1967]; and polycrystalline ZnO $\triangle$: [Wang et al., 2014]; $\triangledown$: [Kim et al., 2008]; $\diamondsuit$: [Fujiwara and Kondo, 2005]; $\triangleleft$:[Yamada et al., 2010]; $\triangleright$: [Young et al., 2000]; $\varhexagon$:[Prunici et al., 2013]; $\varhexagon$:[Ding, 2013].

Pisarkiewicz *et al.* for SnO_2 [Pisarkiewicz et al., 1989].

4.7   Scattering Contributions

When various independent scattering contributions limit the carrier mobility μ_i, the μ_d is obtained by combining them according to Matthiessen's rule [Matthiessen and Vogt, 1864]:

$$\frac{1}{\mu_d} = \sum_i \frac{1}{\mu_i} \tag{4.6}$$

Since we measured the μ_d related to two different interaction distances, nm-scale for FTIR (μ_{opt}) and cm-scale for Hall effect setup (μ_d, cf. Figure 4.2), it is possible to distinguish two contributions to electron scattering. Assuming that the scattering due to grain boundaries is the only relevant mechanism that differentiates μ_d from μ_{opt}, Equation 4.6 allows us to calculate the limitation to the carrier mobility due to the grain boundary μ_{gb}:

$$\mu_{gb} = \frac{\mu_d \mu_{opt}}{\mu_d - \mu_{opt}} \tag{4.7}$$

Figure 4.7 shows the dependence of μ_d on H_2O/DEZ and B_2H_6/DEZ ratio. The trends are clear: μ_{gb} dominates at low N_e and high H_2O/DEZ while it plays a minor role at high N_e and low

H_2O/DEZ. We can explain these observations by referring to the increased defect density (and hence N_e) at low H_2O/DEZ (cf. Figure 4.3). Indeed, the intrinsic defect concentration within the crystal lattice (O_v, Zn_i) is high and hinders the carrier mobility within the crystalline region. Moreover, the carrier concentration is high and effectively screens the potential barrier formed at the grain boundary. The higher crystallinity of the samples deposited at high H_2O/DEZ (cf. also Figure 3.10) leads to larger μ_{opt} (which approaches that of the single crystal) and lower μ_{gb} due to the lower carrier concentration.
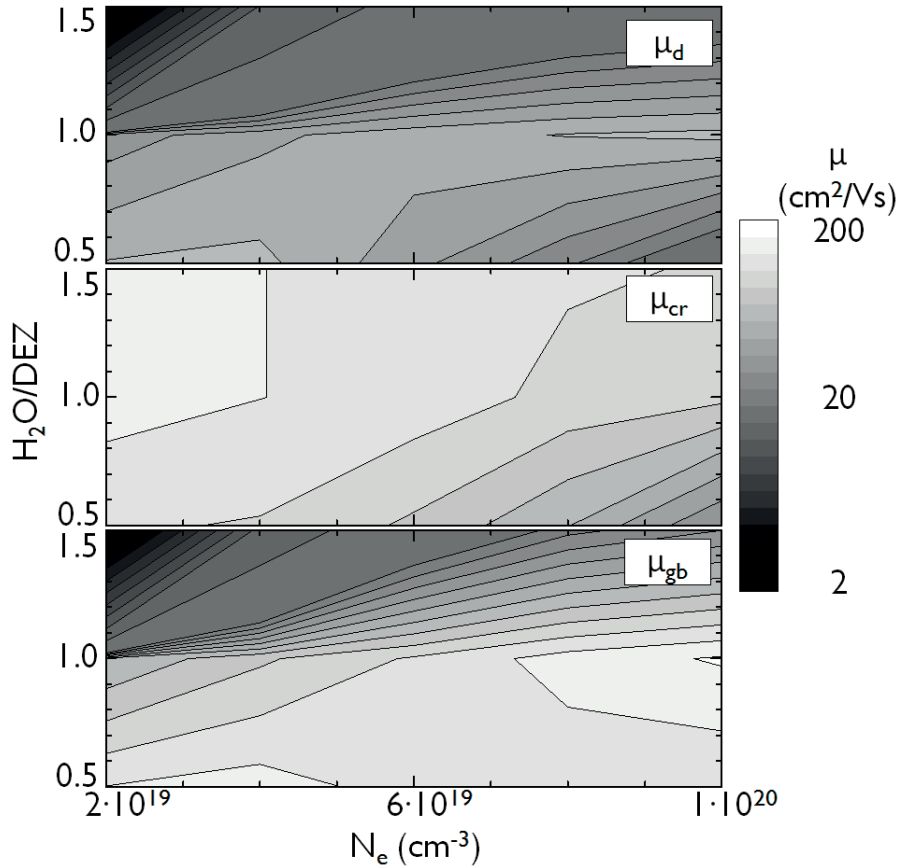
Figure 4.7: Combined effect of the H_2O/DEZ ratio and carrier concentration (N_e) on the drift carrier mobility (μ_d). The effect is separated in the contributions from: the crystalline region (μ_{opt}) and the grain boundary (μ_{gb}).

In order to verify these explanations and qualitatively assess the effect of phonon scattering, we performed Hall effect measurements at variable temperature. Using this technique, it is possible to assess the temperature dependency on the carrier concentration and carrier mobility. We performed these measurements with all the samples analyzed in Figure 4.5. For clarity, in Figure 4.8, we only show the nid and highest doped samples of each H_2O/DEZ series. As the nid sample of the H_2O/DEZ = 1.5 series was too resistive to be measured at temperatures below 200 K (μ_d = 0.3 cm^2/Vs, N_e = 6·10^{18} cm^{-3} at room temperature) we substituted it in the plot with the lowest doped sample of the series (μ_d = 0.5 cm^2/Vs, N_e = 2·10^{19} cm^{-3} at room

temperature).
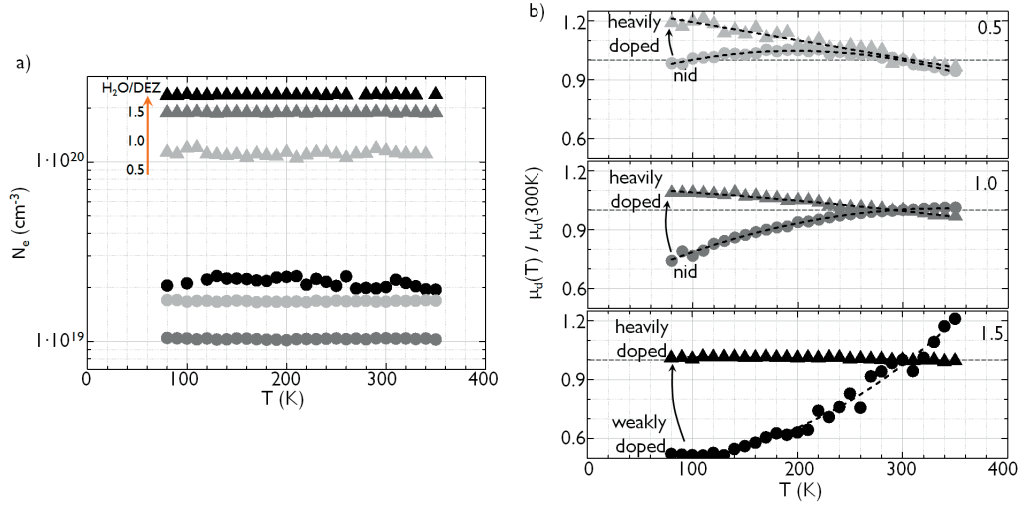
*Figure 4.8: Temperature dependence Hall effect measurements of **(a)** carrier concentration (N_e) and **(b)** drift mobility μ_d (normalized to the value at 300 K) for nid (◯) and doped (△) films deposited at three different H_2O/DEZ ratios: 0.5 (light grey), 1 (grey) and 1.5 (black). The lines are guides for the eyes.*

Figure 4.8a shows that, for all the samples, N_e does not depend on temperature, meaning that the samples are already degenerated at 80 K. This suggests that the donor states (either intrinsic or extrinsic) should be as close as 7 meV (i.e. kT at 80K) from the conduction band. More likely, the tail states due to intrinsic defects extend continuously to the donor states, allowing the electrons to be promoted into the conduction band by a small thermal energy.

Figure 4.8b shows the dependence of μ_d on temperature. To make the comparison between the different curves easier we normalized all the μ_d(T) to μ_d(300 K). At $H_2O/DEZ = 1.5$, the lowest doped sample shows a strong temperature dependence, doubling its μ_d value from 80 K to room temperature. In contrast, the heavily doped sample does not show any dependence on temperature. At $H_2O/DEZ = 1$, the trend is similar but the temperature dependence of the nid sample is lower and the heavily doped sample shows a weak negative temperature dependence (from 1.07 to 1, between 80 K and 300 K). At $H_2O/DEZ = 0.5$ the temperature dependence is weak and characterized by two regimes: up to ≈ 200 K μ_d increases; afterwards it decreases and features at 300 K almost the same μ_d as at 80 K. The heavily doped sample shows a pronounced μ_d decrease with temperature (1.25 to 1 from 80 K to 300 K).

In terms of grain boundary scattering, these results confirm the ones presented in Figure 4.5 since it is clear that the thermal activation of μ_d vanishes with increasing N_e. In terms of other scattering mechanisms, these results provide new information. In degenerated semiconductors, the decrease of μ_d with temperature is often attributed to phonon scattering [Zhang and Ma, 1996, Bikowski and Ellmer, 2014]. Although it has no direct dependence on N_d [Bikowski and Ellmer, 2014], the phonon contribution becomes evident at high N_e as the

grain boundary contribution to the scattering decreases. Indeed, in the three series of samples, the phonon scattering appears when the grain boundary limitation is negligible. Interestingly, the sample with the highest N_e among the three series does not show any μ_d decrease with temperature, and the strongest phonon effects are observed in the sample that has the highest defect density. These results suggest that the effect of the phonon is tied to the presence of intrinsic defects in the film.

4.8   Summary and Conclusions

In this chapter we demonstrated the interplay between intrinsic and extrinsic defects that determines the relative importance of the different charge-scattering mechanisms. In particular we investigated the combined effect of the H_2O/DEZ ratio and the B_2H_6/DEZ ratio on the B concentration in the film and on the optical and drift mobility.

The main results can be summarized as follows:

- In non-intentionally doped samples, decreasing the H_2O/DEZ ratio leads to an increase in absorptance close to the band gap onset, and an increase in carrier concentration. Both effects are explained by an increase in the **intrinsic defect concentration**, which creates states close to the conduction band.

- A high H_2O/DEZ ratio favors **B incorporation** into the films but reduces the number of free electrons released per atom of B in the film (the doping efficiency).

- In the considered deposition range, the **maximum drift mobility** is achieved at a medium H_2O/DEZ ratio and high doping, and at low H_2O/DEZ ratio for non-intentionally doped samples.

- The **effective mass** of ZnO thin films, obtained by fitting film reflectance curves measured by FTIR, increases from 0.15 to 0.30 for films with a carrier concentration between 0.5 and $30 \cdot 10^{19}$ cm^{-3}.

- Within the investigated deposition conditions, the **main scattering mechanisms** which contribute to decrease of the carrier mobility are identified as follows:

Main Source of Electron Scattering

H_2O/DEZ	*nid*	*heavily doped*
low	in-grain (ii, ph)	in-grain (ii, ph)
medium	grain boundary	in-grain (ii, ph)
high	grain boundary	in-grain (ii)

ii: ionized impurities; ph:phonons

5 Bimodal Dopant Segregation in *a*-textured ZnO films

Two fundamental requirements of transparent conductive oxide films are high conductivity and low optical absorptance, two properties which strongly depend on the film's free-carrier concentration. The free-carrier concentration is usually increased by the addition of extrinsic dopants which are commonly assumed to be distributed uniformly in the films as discussed in Section 5.1. In this chapter, we present new evidence against this assumption showing that for LP-MOCVD ZnO:B films boron dopant atoms are not uniformly distributed.

Using secondary ion mass spectroscopy at nanometric scale (nanoSIMS) analysis we show that the growth segregation process favours the incorporation of boron atoms into one side of each ZnO grain (Section 5.3).

In Section 5.4, we present the Kelvin probe force microscopy (KPFM) measurements which confirm that these boron atoms are electrically active, locally increasing the free-carrier concentration in the film.

In addition, we performed optical absorption measurements and numerical simulations of band bending to demonstrate that, when compared to uniform dopant distribution, the bimodal distribution modifies the electron transport mechanisms (Section 5.5) and induces non-linear effects on the film's optical absorptance (Section 5.6).

In Section 5.7, we discuss a possible explanation for the observed differences between the two sides of the grain. These can be attributed to the different polarity of the lateral surfaces of the grain and a preliminary model of boron incorporation is proposed to capture this relation.

5.1 Motivation and State of the Art

Extrinsic impurities are commonly introduced in various materials to customize their properties. Historical examples are the nanoparticles used to color the medieval stained glass [Delgado et al., 2011] and the carbon atoms added to strengthen the Damascus blades [Reibold et al., 2006]. In modern semiconductor materials, the tuning of their electrical properties is

performed by introducing a certain amount of extrinsic impurities — dopants. Impurities can be introduced into the host material either during the material synthesis (e.g. dopant precursor in an CVD-process) or by post-deposition treatments (e.g. ion implantation). In both cases, the material conductivity is defined not only by the concentration of the impurities but also by their spatial distribution.

As discussed in Chapter 4, the influence of N_d on μ_d and N_e is described by the Seto model [Seto, 1975]. The model shows that the height E_b and the width W of the potential barrier at the grain boundary depend on the dopant spatial distribution (electrical dipole approximation). Due to the presence of grain boundaries, the influence of the spatial distribution of the impurities should be stronger in polycrystalline material than in single crystals. Nevertheless, for polycrystalline silicon, Seto assumed a uniform spatial distribution of dopants in the film. Following Seto, most of the previous work on TCOs and polycrystalline semiconductors also assumed homogeneous doping throughout the grains, with possible modifications only at the grain boundary [Kinemuchi et al., 2011, Bikowski et al., 2015]. So far, the influence of the dopant distribution on the film properties has been taken into account only for nanowires [Perea et al., 2009, Koren et al., 2010].

The spatial distribution of dopant atoms is therefore an important factor which can potentially affect electrical properties of polycrystalline TCOs. In addition to electrical properties, the dopant distribution could also impact the optical properties of TCOs as it was reported for ITO nanocrystals [Lounis, 2014].

5.2 Experimental Details

ZnO thin films were deposited by LP-MOCVD on 4×4 cm^2 0.5-mm-thick borosilicate glass substrates at T_{hp} = 180 °C. The thickness of the films was varied between 1 μm and 7 μm, as measured by a stylus-profilometer. Total transmittance *TT* and total reflectance *TR* were measured with an UV-VIS-NIR spectrophotometer and the absorptance *A* was calculated as $A = 1 - TT - TR$. The film morphology was assessed by a scanning electron microscope in secondary electron mode. The relative frequency of the three types of boundaries (Figure 5.8) was calculated by sampling grain boundaries of one 5×5 μm^2 SEM micrograph with the stereological method [Han and Kim, 1995]. N_e and μ_d were assessed with a Hall effect setup. μ_{opt} was derived from Fourier transform infrared reflectance measurements by fitting the curves with the Drude model [Fujiwara and Kondo, 2005, Steinhauser et al., 2007]. The dopant distribution in the film was assessed by NanoSIMS (Cameca, NanoSIMS 50L) using a <100-nm-wide cesium ion beam to sputter the surface. Seven different isotopes were detected: O$^-$, ^{64}ZnO$^-$, ^{66}ZnO$^-$, BO$^-$, BO$_2^-$, C$^-$ and CN$^-$. The contact potential differences were measured at ambient atmosphere with a scanning probe microscope (Bruker Dimension Icon) used in the Kelvin probe force configuration [Nonnenmacher et al., 1991]. Bruker PFQNE-AL probes (silicon pyramidal tip on a silicon nitride cantilever) were used. In order to reduce roughness-related artifacts before nanoSIMS and contact potential measurements, the ZnO film surface

was polished with the chemical mechanical procedure [Cuony, 2011] shown in Figure 2.2a. Simulations of band bending at the grain boundaries were performed using the AFORSHet software developed at Helmholtz Zentrum Berlin [Varache et al., 2015]. The built-up barrier potential at grain boundaries was simulated by introducing a boundary layer (1 nm wide; N_t = $1 \cdot 10^{13}$ cm^{-2}) between two ZnO layers (L = 100 nm wide each); the whole set of parameters used for simulations is listed in the Appendix (cf. Table A.1).

5.3   Bimodal Boron Dioxide Segregation

We performed spatially resolved elemental analysis to estimate the distribution of the dopant boron atoms in a-textured polycrystalline ZnO:B films. The measurements were performed using NanoSIMS which employs a well-focused primary ion beam (Cs$^+$) with a spatial resolution below 100 nm to sputter the film surface [Hoppe et al., 2013].

There are three challenges to address to correctly perform these measurements. First, at a film thickness normally used for application in solar cells (1–2 μm) the grain size of an a-textured film is around 100 nm [Faÿ et al., 2005]. These grain sizes are comparable to the spatial resolution of the instrument, thus it is not possible to spatially resolve the information originated in neighbouring grains. In a-textured films, the grain size increases roughly linearly with the film thickness [Steinhauser, 2008]. Thus, we could exploit NanoSIMS only on a-textured films with a thickness of around 7 μm (average grain size of about 2 μm, cf. Figure 2.2e).

Second, the roughness of the film after deposition (shown in Figure 2.2b) can generate artifacts during SIMS measurements. For this reason the film was polished using a chemical mechanical polishing process[Cuony, 2011] with the system schematically illustrated in Figure 2.2a. After polishing, the surface becomes suitably flat as shown in Figure 2.2b and Figure 2.2c. Figure 2.2c underlines a particular characteristic feature of the a-textured film: each grain is divided into two sides, with one side having a darker imaging contrast and the other a brighter contrast in secondary-electron imaging acquired by SEM.

Third, when using a positively charged primary ion beam (Cs$^+$), it is possible to collect only negatively charged secondary ions. This represents a challenge when detecting species such as boron that are difficult to ionize negatively. In order to increase the secondary ion emission detection, it is preferable to set up the detection for BO$^-$ and BO$_2^-$ [Kontis et al., 2016]. We chose to monitor the O$^-$ signal in order to normalize the BO$^-$ and BO$_2^-$ signal and reduce the artifacts in B concentration potentially arising from the non uniformity of O.

Figure 5.1 shows NanoSIMS emission maps acquired on a polished ZnO film. In the secondary electron image (Figure 5.1a), the bright/dark contrast of each marked grain is readily visible. Figure 5.1b reveals that BO$_2$ segregates to regions of the film corresponding to the bright sides of grains in the SEM micrographs, while the darker sides do not contain any BO$_2$ (or its concentration is below the detection limit of the setup). Moreover, Figure 5.1b shows
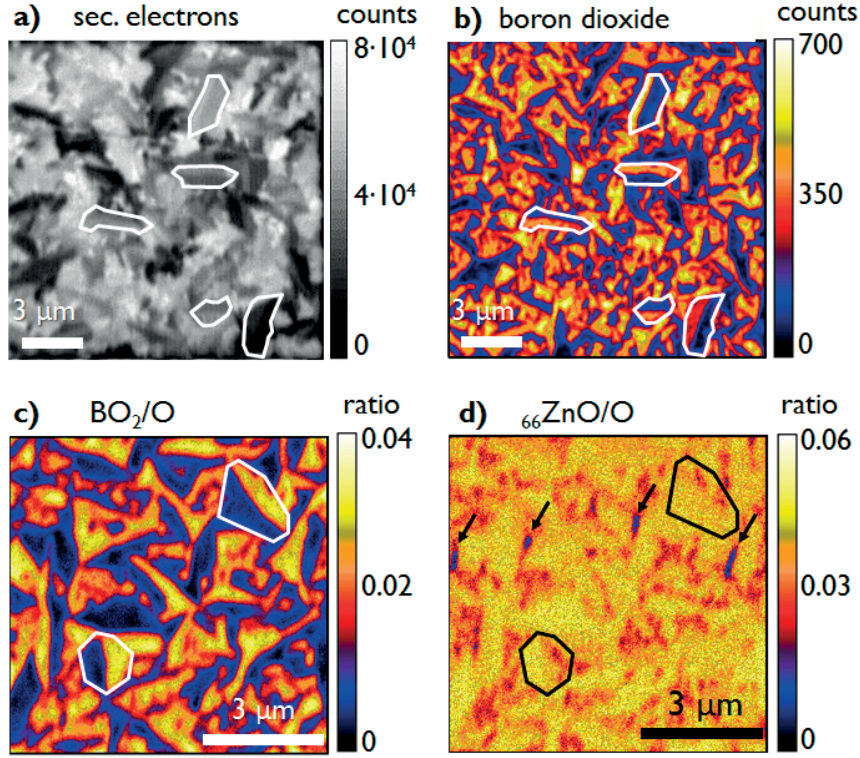
Figure 5.1: NanoSIMS maps of doped a-textured polished ZnO film (a) secondary electrons signal and (b) boron dioxide map of the same surface region. Close-up view of a different region for the ratios: (c) boron dioxide/oxygen (BO$_2$/O) and (d) zinc oxide/oxygen ($_{66}$ZnO/O). The regions at low Zn concentration (indicated by arrows) are likely due to roughness artifacts.

that, within the bright side of the grain, the BO$_2$ concentration is uniform. We can therefore describe the dopant distribution within the film as *bimodal*, since the film is clearly composed of two types of regions: the one characterized by a uniform dopant distribution and the one other without any dopants.

Figure 5.1c and 5.1d show a closer view of a different region of the same samples. The BO$_2$ and ZnO were normalized to the O signal, to get rid of the features characteristic of the O-distribution. The BO$_2$/O ratio map shows features similar to BO$_2$, confirming the bimodal distribution of B. In the ZnO/O map, the distribution is more uniform: the small regions (red areas) presenting lower values likely correlate with the center of the region presenting higher values of BO$_2$/O and therefore are likely due to the substitution of Zn by B atoms. A similar correlation for substitutional dopant was already observed in aluminum doped ZnO analyzed by atom probe tomography [Bikowski et al., 2015] and energy-dispersive X-ray spectroscopy [Kinemuchi et al., 2011]. Figure 5.1d shows four small regions with very low values of the ZnO/O ratio (blue areas, indicated by arrows) that do not correlate with the BO$_2$/O map. We attribute these extremely low values to measurement artifacts related to superficial roughness either due to preferential etching along cracks in the grain or incomplete surface polishing.

5.4 Spatially Resolved Electrical Potential

The previous section presented clear evidence that BO_2 is not uniformly distributed in the ZnO:B film. In this section, we investigate whether the observed peculiar spatial distribution affects the electronic properties of the film. We investigate the ZnO:B films using the Kelvin probe force microscopy (KPFM) technique.

To correlate the dopant spatial distribution with the electronic potential, we measured the contact potential difference V_{CPD} on a polished a-textured film. The energy eV_{CPD} related to the contact potential difference depends on the film and tip workfunctions, respectively ϕ_f and ϕ_t [Melitz et al., 2011]:

$$eV_{CPD} = \phi_f - \phi_t, \tag{5.1}$$

where e is the elementary positive charge. Assuming that the tip workfunction is constant during the scanning, we can derive from Equation 5.1 that V_{CPD} decreases when the difference between the Fermi level and the bottom of the conduction band ($E_F - E_c$) of the film increases [Maragliano et al., 2014]:

$$V_{CPD} = \frac{(\chi_f - (E_F - E_c) - \phi_t)}{e}, \tag{5.2}$$

where χ_f is the electron affinity of the film surface. Equation 5.2 is valid assuming that the film surface is representative of the bulk, and that, e.g., no Fermi level pinning takes place at the surface [Sommerhalter et al., 2000, Melitz et al., 2010]. Assuming further that in degenerately doped semiconductors the value E_F - E_c increases with the carrier concentration of the film N_e [Pisarkiewicz et al., 1989, Hu et al., 2013], Equation 5.2 shows that V_{CPD} decreases when increasing the doping level in the film.

Figure 5.2 illustrates how the contact potential difference is generated in our measurement setup, which is composed of an n-doped Si-tip and a degenerately doped ZnO film. In principle, from Equation 5.2 it should be possible to compute N_e of the film. In reality, due to the non-uniformity of the electric field at the tip surface, the measured values provided by the KPFM setup are influenced by the tip geometry and tip-sample distance [Jacobs et al., 1998, Zerweck et al., 2005]. This generates an undesired additional interaction of the cantilever with the electric field leading to an underestimation of V_{CPD}, which makes quantitative analysis problematic. Therefore, we use the relation stated in Equation 5.2 in a qualitative fashion. Figure 5.3 compares the surface height signal with the V_{CPD} signal. The difference in height, within 5-10 nm, between the two sides of the grain is ascribed to differential etching rates during the chemical mechanical polishing process. It is known that the O-terminated surface of ZnO is more prone to etch than the Zn-terminated surface [Mariano and Hanneman, 1963, Jo et al., 2005]. Hence, it is reasonable to assume that the O-terminated side has been etched faster by the chemical solution used to polish the surface [Cuony, 2011]. This difference in height helps to correlate the side of the grain observed with scanning probe microscope
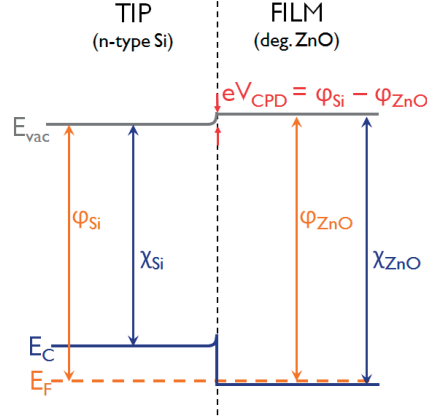
Figure 5.2: Electronic energy band alignment for the electrically connected system tip (n-type Si) and film (degenerately doped ZnO). The contact potential difference V_{CPD} depends on the difference in workfunction between Si and ZnO that decreases linearly with $E_F - E_c$, which in turn depends on the carrier concentration in ZnO. E_{vac} = vacuum energy, χ = electron affinity, φ = workfunction.

(SPM) and with SEM/NanoSIMS. The robustness of the measured potentials is supported by the homogenous local potential distribution over the same side of the grain and by similar V_{CPD} on the bright side of different grains. Additionally, as shown in Figure 5.3, the contact potential difference is not observable in non-intentionally doped films. We can conclude that topographical artifacts play only a very minor role during KPFM measurement. Interestingly, the bright side of the grain in the SEM image, the one containing BO_2, is the higher side of the grain as observed in the height map recorded with SPM (Figure 5.3a). Figure 5.3b shows the map of the contact potential difference of the same region shown in Figure 5.3a, where the side containing BO_2 shows a lower V_{CPD}. According to Equation 5.2, this means that the side of the grain containing BO_2 has a higher N_e than the side without BO_2. This observation proves that the BO_2 non-uniformity can be related to a segregation of ionized boron that is the source of free electrons in B-doped ZnO.
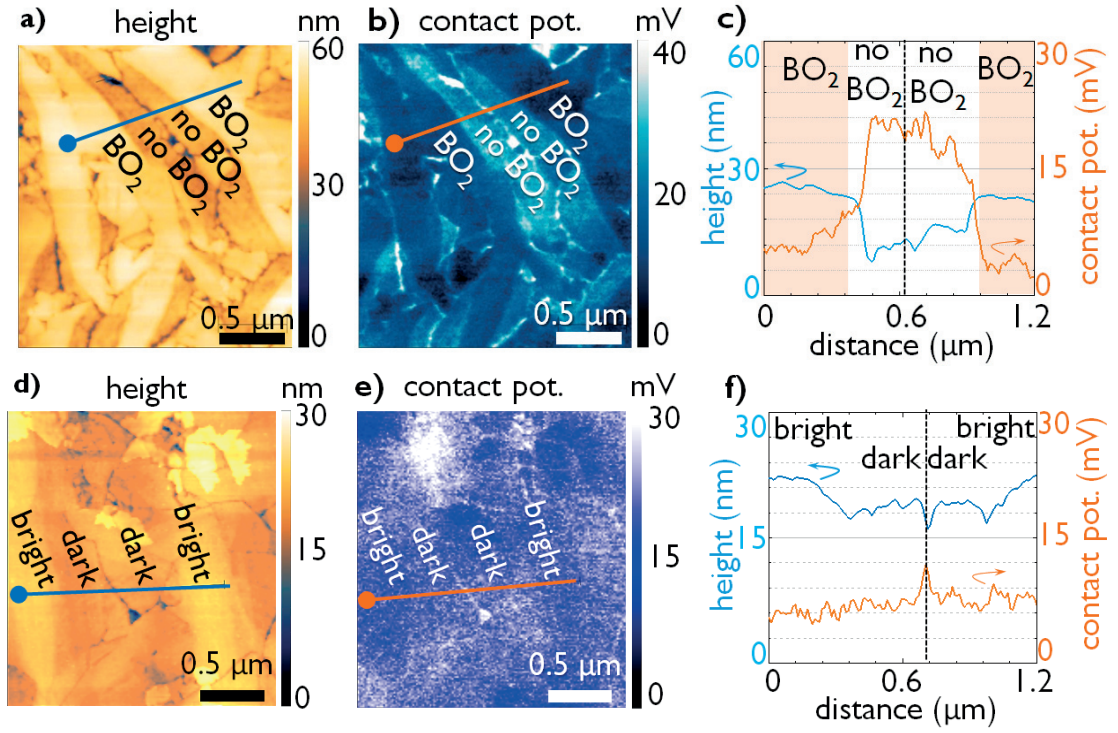
*Figure 5.3: Scanning probe microscopy measurements on a polished doped (a,b,c) and non-intentionally doped (d,e,f) films: **(a)**, **(d)** height map, **(b)**, **(e)** contact potential difference map, and **(c)**, **(f)** line profile extracted from the height map (blue) and contact potential difference map (orange).*

5.5   Influence of Bimodal Dopant Segregation on Electronic Properties

The boron segregation reported in the previous sections is expected to affect lateral conductivity in the film by producing band bending at the different interfaces. A step in the electronic potential should be formed in the doped film between the two sides of the grain, hindering the electrons from entering the side that does not contain boron. This step would increase with the difference in carrier concentration between the two sides of the grain. Based on Seto's model, another effect to consider when assessing the barrier height at grain boundaries is the screening of the negative build-up barrier by the positive fixed charges introduced via doping. As discussed in Section 5.1 an increased dopant concentration N_d reduces the barrier height at a grain boundary E_b and barrier width W according respectively to Equation 4.3 and 4.4.

To calculate the effect of the carrier concentration on the barrier at grain boundary, it is necessary to estimate the N_e in each of the two sides of the grain. For this estimation we assume that N_e measured with Hall effect is the average weighted on the occupied surface, between N_e within each side of the grain. We define a segregation level parameter x_{seg} to take into account the fact that the overall surface of bright sides of the grains does not have the same size as the overall surface of the dark sides (from SEM micrographs we obtained the surface area close to 60% for the bright regions). If x_{dop} is the fraction of surface film containing dopant atoms (e.g. for a uniformly doped film x_{dop} = 100%), we define the segregation level x_{seg} as:

$$x_{seg} = 1 - x_{dop}, \tag{5.3}$$

i.e. the segregation level increases when the regions of film bulk containing dopants become smaller. The carrier concentration of the doped side of the grain $N_{e,dop}$ can be found assuming that the Hall-effect-measured film carrier concentration N_e is the combination of $N_{e,dop}$ and $N_{e,nid}$ weighted on x_{seg}:

$$N_e = x_{seg} N_{e,nid} + (1 - x_{seg}) \cdot N_{e,dop} \tag{5.4}$$

Using this approximation and considering x_{seg} of 40% (i.e. 60% of film surface is constituted by bright regions) we can estimate the N_e in the doped regions of the non-uniform doped samples, as indicated in Table 5.1.

5.5.1   Three Types of Grain Boundaries

E_b does not only depend on N_t but also on the energy position of the trap states (E_t) (cf. Figure 4.1), defined as the energy distance from the valence band maximum. We used the simulation

Table 5.1: Comparison between the N_e for the case of uniform doping and non-uniform doping. The column of non uniform doping represents the doped regions, assuming the same average N_e of the uniform distribution and a $N_e = 1 \cdot 10^{19}$ cm^{-3} for the nid doped regions.

	uniform $x_{seg} = 0$	non-uniform $x_{seg} = 40\%$
doped area %	100	60
$N_{e,nid}$ $10^{19} cm^{-3}$	1	1
$N_{e,mod}$ $10^{19} cm^{-3}$	5	7.7
$N_{e,mod}$ $10^{19} cm^{-3}$	10	16

software AFORS Het to quantify the influence that E_t and N_t have on E_b. The results of the simulations are presented in Figure 5.4.

The plots represent two grains (width 100 nm, of which only 50 nm are shown) divided by a grain boundary. In Figure 5.4a we show the effect of E_t and in Figure 5.4b we show the effect of N_t. In these two figures both grains are non-intentionally doped. Figure 5.4c considers the same N_t variation of Figure 5.4b but one of the two grain is moderately doped. We observe that increasing the energy of the trap state decreases the height of the barrier: the closer the state is to the Fermi energy (which lies above the conduction band bottom), the lower is the probability of occupation of the trap states and hence the barrier will be smaller. Interestingly, there is no difference between E_t at 2.7 eV and 3.0 eV; both levels are deep enough to have all the traps filled. It is clear that increasing N_t leads to an increase in E_b but, as soon as one of the two grains is doped, the screening effect of the positive ionized donors reduces E_b.

For the following simulations we assume the energy level related to trap states to be deep enough in the band gap so that the traps are all filled by electrons already for non-intentionally doped film. This assumption is in agreement with the independence of N_e with respect to temperature [Steinhauser, 2008], indicating that the increased spreading of the electron distribution (Fermi distribution) due to temperature does not change the amount of the trapped electrons.

To quantify the effect of dopant segregation on electron transport and compare it with the uniform distribution case, we simulated the effect of the barrier height on the contact resistivity at grain boundary. To do that we should take into account the fact that not all grain boundaries are equal. Since each grain is composed of two different sides, three types of grain boundaries can be formed (cf. Figure 5.5):

   I. both sides containing BO_2

  II. one side with BO_2 and one without

 III. both sides without BO_2
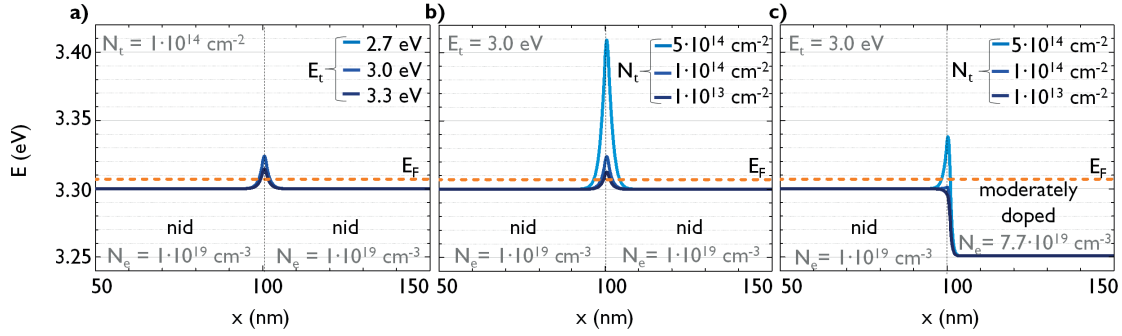
Figure 5.4: AFORS Het simulated potential barrier at grain boundary. The effect of (a) trap energy level (E_t) and (b) trap concentration (N_t) between two nid grains. (c) The effect of N_t between a nid and a moderately doped grain. Values referenced to the valence band maximum.
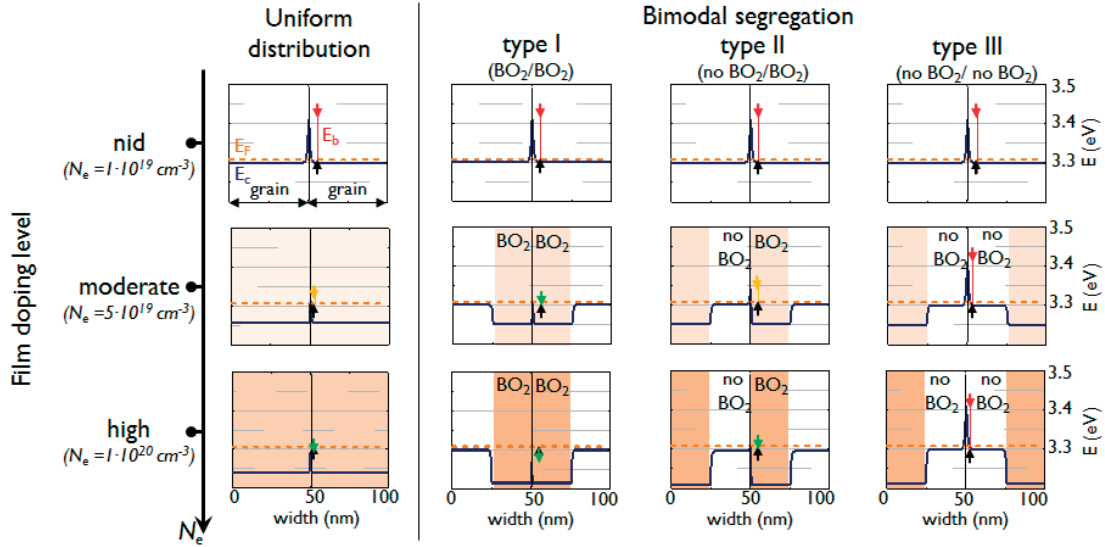
Figure 5.5: Simulations showing the dependence of the potential barrier height E_b on the average film carrier concentration (N_e) for the uniform dopant distribution compared with the three different types of grain boundaries. Red arrows represent barriers larger than 50 meV; orange, barriers between 0 and 50 meV; and green, no barrier. Simulations were performed with AFORS Het; grain size $L = 100\,nm$, grain boundary trap concentration $N_t = 5 \cdot 10^{13}\,cm^{-2}$. The whole set of values used for the simulation is listed in Table A.1.

For non-intentionally doped film N_e on the two sides of the grain is the same, therefore the barrier height is the same for each type of boundary (cf. Equation 4.3). In doped films, N_e inside the two grain sides composing the boundary depends on the type of boundary and therefore the barrier height will be different. We simulated the variation of E_b with respect to the average film N_e for each of the three types of boundaries (the grain structure and parameters used for the simulations can be found in the Appendix, cf. Figure A.1 and Table A.1). Figure 5.5 presents the results of the simulations. For non-intentionally doped films, the barrier height is the same (>100 meV) for the three types of boundaries. As expected, the barrier height evolves differently when the dopant is incorporated into the film. The two sides that constitute the type I boundary incorporate the boron atoms during deposition; and E_b decreases according to Equation 4.3. At N_e of $5 \cdot 10^{19}$ cm^{-3}, there is no barrier for the electrons. At type II boundaries, one side does not incorporate dopants, and is therefore not subject to an increase in N_e; on the other side, however, N_e increases. The negative-charge screening is less effective than for type I, reducing the barrier height below 50 meV at $5 \cdot 10^{19}$ cm^{-3} and totally screening the barrier at $2 \cdot 10^{20}$ cm^{-3}. The two sides of a type III boundary do not incorporate dopant atoms; hence the barrier is not affected, and remains larger than 100 meV even for high doping.

The permanence of the barrier at type III boundaries at high doping levels poses an obstacle to electron transport through the film. In a uniformly doped film, all the grain boundaries are assumed to be characterized by the same E_b, which decreases with increasing N_d [Seto, 1975]. A similar vanishing of the barrier with N_d has in fact been reported for LP-MOCVD a-textured ZnO:B [Steinhauser et al., 2007], an observation that apparently contradicts the permanence of the type III boundary barriers at high N_d that are illustrated in Figure 5.5.

Table 5.2: Variation of contact resitivities ρ_c with doping level for the three types of boundaries (I, II, III) and the uniform distribution. The values calculated from the IV-curves shown in Figure 5.6.

doping level	$\rho_c(I)$ 10^{-4} Ωcm^2	$\rho_c(II)$ 10^{-4} Ωcm^2	$\rho_c(III)$ 10^{-4} Ωcm^2	$\rho_c(U)$ 10^{-4} Ωcm^2
nid	13	13	13	13
moderate	1.5	5.1	13	1.8
high	0.3	3.8	13	0.9

To solve this contradiction we simulated the current-voltage curve for each type of grain boundary and for the uniform dopant case (cf. Figure 5.6). From these curves, we extracted the values of ρ_c (cf. Table 5.2). For nid films, ρ_c is the same for the four types of boundaries. For doped films, ρ_c decreases faster with the increase of doping for type I boundaries than for the film with uniform distribution. For type II boundaries, the decrease is slower and, for the type III boundaries, ρ_c remains unchanged. To obtain an effective $\rho_{c,eff}$ value for the film with a non-uniform dopant distribution we combined $\rho_c(i)$ of each grain boundary with the
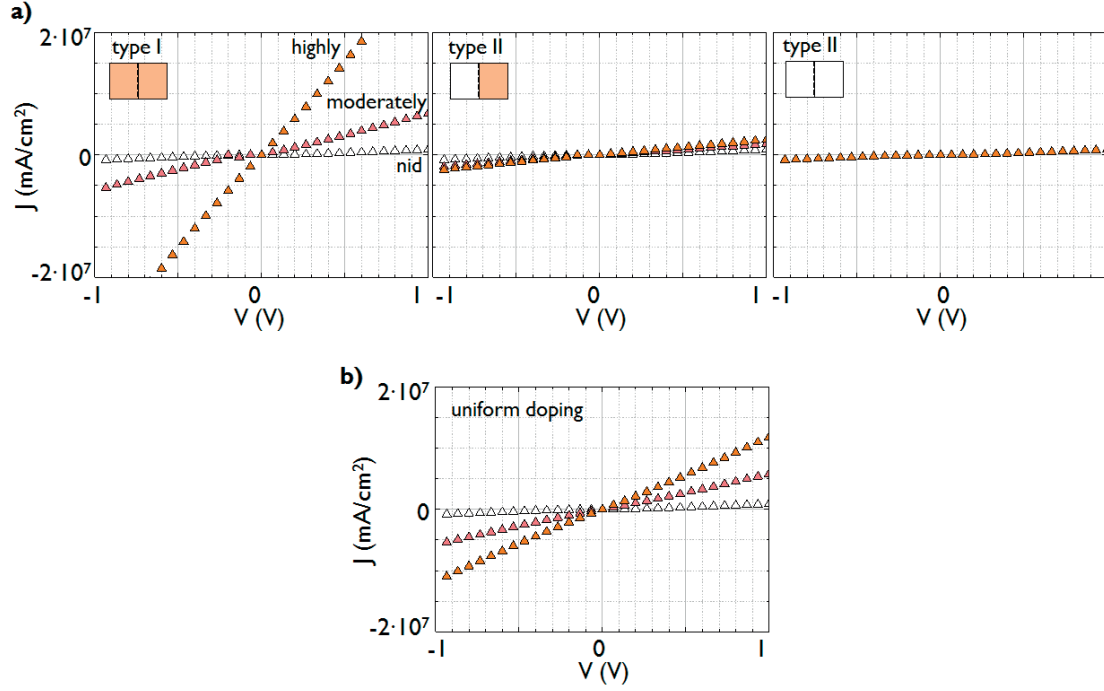
Figure 5.6: Doping dependence of current density (J) vs. voltage (V) curve of the boundary region. The simulated values compared four cases: the three types of grain boundaries (I,II,III) and uniform doping distribution. "nid", "moderatly" and "highly" refer to the doping level.

frequency of the three types of boundaries $f(i)$:

$$\frac{1}{\rho_{c,eff}} = \sum_i \frac{f(i)}{\rho_c(i)} \tag{5.5}$$

Figure 5.7 compares the effective contact resistivity for the non-uniform case $\rho_{c,eff}$ with the effective contact resistivity $\rho_{c,U}$ for the uniform case at different doping levels. As expected, $\rho_{c,eff}$ decreases at high doping level and when the frequency of type I boundary $f(I)$ is increased. Interestingly, the difference between $\rho_{c,eff}$ and $\rho_{c,U}$ depends both on N_e and the frequency distribution $f(i)$. For all the three frequency distributions considered, at high doping level $\rho_{c,eff}$ is lower than $\rho_{c,U}$. We compare these frequency distributions with the empirical distribution in *a*-textured ZnO:B films estimated using the stereological method (on a 5x5 μm^2 area, 150 grain boundary counted in total). Surprisingly, the distribution of the three boundary types is not uniform. Specifically, type I and II boundaries are much more frequent, respectively 40% and 50%, than type III (10%). We attribute this non-uniform frequency to the presence of regions constituted by small grains that preferably appear at the boundary with the dark side and to the observed dependency of the in-plane orientation of the neighbouring grains. By comparing the dopant segregation observed in *a*-textured ZnO:B films with the simulated data we can infer that, at high doping level, the bi-modal spatial distribution of dopants provides higher conductivity than the uniform dopant distribution. Note that the
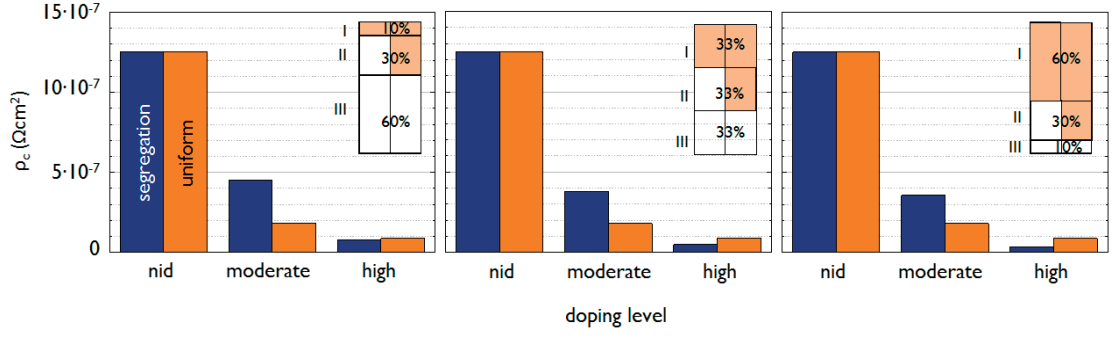
Figure 5.7: Variation of contact resistivity ρ_c at grain boundary with the doping level (nid, high, moderate) for the case of dopant segregation (x_{seg} = 40% and uniform film. The ρ_c at grain boundaries are extracted from the J-V curves of Figure 5.6, for the dopant segregation film the effective ρ_c is obtained by assuming a certain relative frequency of the three types of boundaries. The three plots show three different cases: (a) 10% of type I, 30% of type II and 60% of type III; (b) 33.3% of I, 33.3% of II, 33.3% of III; (c) 60% of I, 30% of II, 10% of III.

negative influence of the barriers at type III boundaries (present also at high doping level) does not affect the overall increase in the conductivity. We attribute this to the existence of electron percolation paths through the type I boundary regions with high dopant concentration, as sketched in Figure 5.8.

boundary type	relative frequency
	%
I	40
II	50
III	10
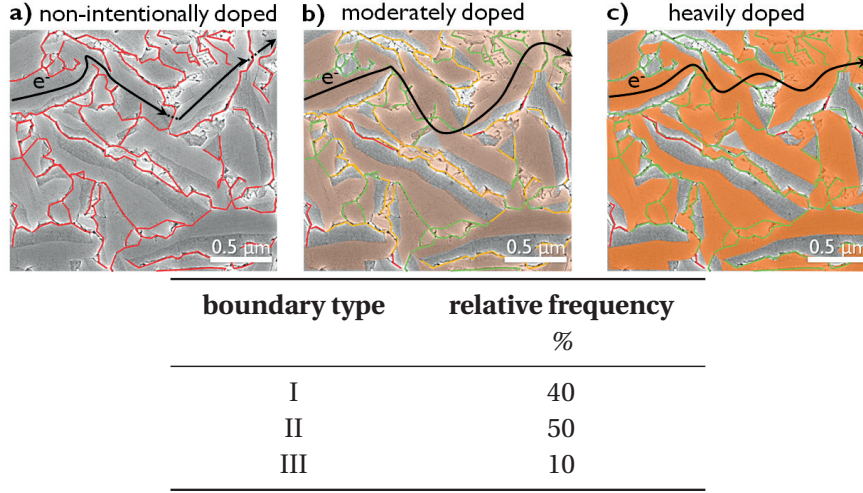
Figure 5.8: SEM micrograph of the polished a-textured film. The image (same for the three cases) is used to illustrate how the paths available to electrons vary with the doping level. The grain boundaries have been marked using the same color code as in Figure 5.5. Three different doping levels have been considered: (a) non-intentionally doped, (b) moderately doped and (c) heavily doped. In (b) the three types are distinguishable: type I (green), type II (orange) and type III (red). The orange shaded regions are drawn according to Figure 5.1 and indicate where the dopant atoms are incorporated: darker orange means higher N_d. The table indicates the relative frequency (estimated through the stereological method) of the three types of boundary.

5.6   Non-Linear Effects on Film Absorptance

The spatial distribution of dopant atoms affects not only the electronic properties but also the optical properties [Park et al., 2011, Lounis et al., 2014], which are another important feature of TCOs. ZnO:B films that have similar electronic properties can be deposited with either *a*- or *c*-texture [Nicolay et al., 2012, Fanni et al., 2014]. The surface of *a*-textured films (Figure 5.9a) is characterized by large wedges and is noticeably different from the small and round grains on the surface of *c*-textured films (Figure 5.9b). Figure 5.9c presents the absorptance A of both *a*- and *c*-textured films having the same thickness d, carrier concentration N_e and optical carrier mobility μ_{opt}. Surprisingly, the *a*-textured film is characterized by an absorptance at 2000 nm that is 3.5% higher than that of the *c*-textured film. According to the Drude model the film absorptance A_{fc} is [Fox, 2010]:

$$A_{fc} = 1 - e^{-\alpha_{fc}d} \tag{5.6}$$

The absorption coefficient α_{fc} mainly depends on d, N_e and μ_{opt} [Chopra et al., 1983]:

$$\alpha_{fc} = \frac{\lambda^2 e^3 N_e}{4\pi^2 \epsilon_0 c^3 n m^{*2} \mu_{opt}}, \tag{5.7}$$
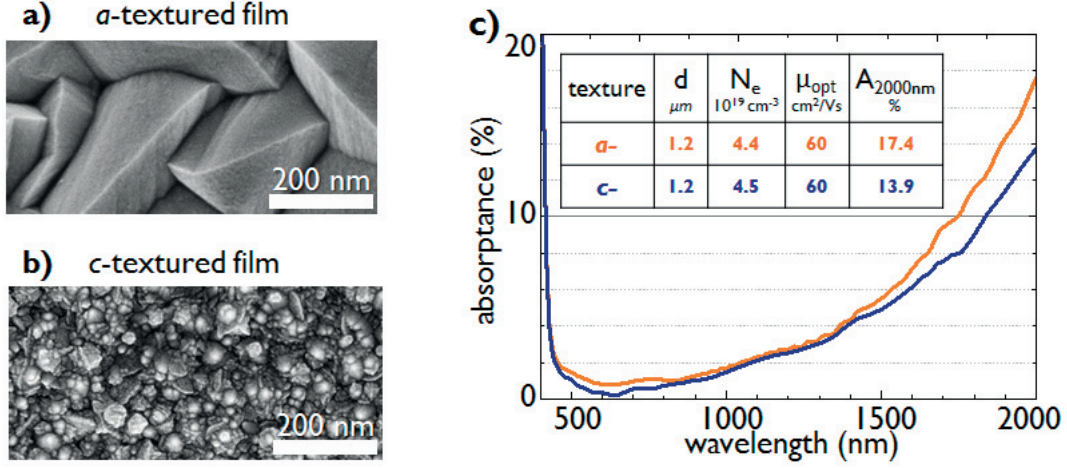
*Figure 5.9: Secondary electron SEM plan view micrographs for **(a)** an a-textured film and **(b)** c-textured film. Film thickness ≈ 2μm. **(c)** Absorptance (A) of a- and c-textured ZnO:B films with nearly identical film thickness (d), carrier concentration (N_e) and optical carrier mobility (μ_{opt}), cf. inset.*

where λ is the wavelength, ϵ_0 is the vacuum permittivity, c is the speed of light in vacuum, n is the refractive index and m^* is the effective mass. Therefore, assuming the same reflectance for the two films, according to Equation 5.6 and 5.7, A_{fc} should also be the same. Knowing that the dopant segregates in a-textured films and assuming a uniform dopant distribution in c-textured films (Figure 5.10c does not show a bipolar grain contrast), we simulated the effect of dopant segregation in order to explain the observed difference in absorptance. Combining Equation 5.4, 5.6 and 5.7 and it is possible to calculate the absorptance of a film characterized by dopant segregation:

$$A_{tot} = x_{seg} \cdot A_{fc,nid} + (1 - x_{seg}) \cdot A_{fc,dop} \tag{5.8}$$

At the first-order approximation (for low A values), based on Equations 5.6, 5.4 and 5.8, A should not depend on the x_{seg} because the increase in N_e in the doped regions should be compensated by the decrease of x_{dop}. However, the simulated curves presented in Figure 5.10a show that the film's absorptance increases with x_{seg}. We attribute this effect to the decrease in μ_{opt} when increasing N_e [Fujiwara and Kondo, 2005, Steinhauser et al., 2007], shown in Figure 5.10b. This decrease in μ_{opt} makes the increase of α_{fc} with respect to N_e (cf. Equation 5.3) faster than a linear proportional relationship. From Equation 5.8, we calculated the absorptance difference at $\lambda = 2000$ nm between a uniformly doped and a dopant segregated film ($x_{seg} = 40\%$) to be about 0.8%. However, this difference is much less than the 3.5% difference measured between a- and c-textured films. This means that the non-linear effect related to the variation in optical carrier mobility can only partially explain the difference
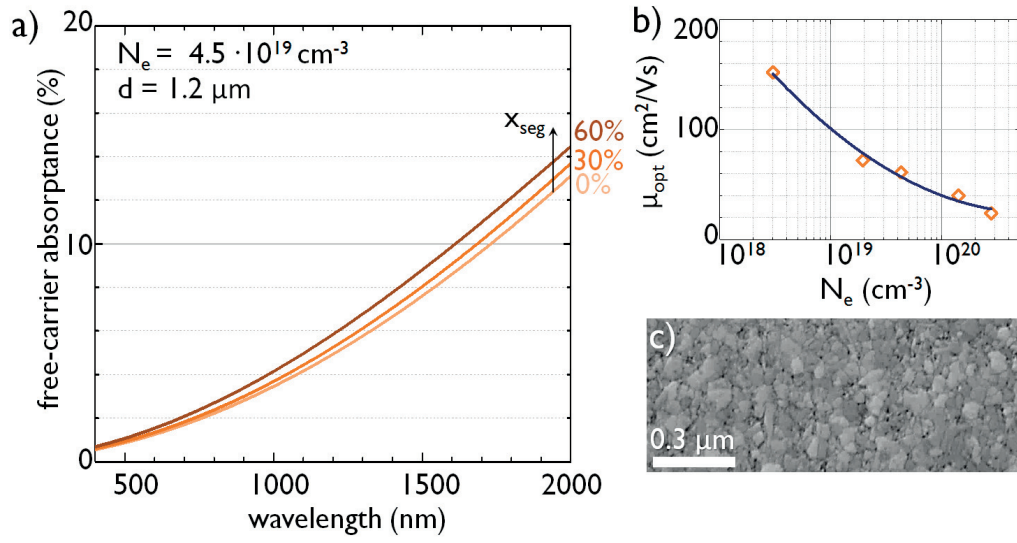
Figure 5.10: ***(a)*** *Increase in free-carrier absorptance (A_{fc}) with segregation level x_{seg} for films with the same measured carrier concentration (N_e). Curves are obtained from Equation 5.8 (with N_e = 4.5·10^{19} cm^{-3}, d = 1.2 µm, n = 1.9, m* = 0.28 and μ_{opt} is derived from (b)).* ***(b)*** *Optical mobility (μ_{opt}) dependence on carrier concentration. Values are derived from FTIR measurements.* ***(c)*** *Plan view SEM micrographs of polished surfaces of c- textured ZnO films, courtesy of F. Landucci.*

observed between a- and c-textured films. We suspect that differences in defect type and defect density between the two textures (presented in Chapter 3) can influence the Hall effect measurements (in particular the scattering factor r) [Orton and Powell, 1980, Preissler et al., 2013] influencing the estimation of N_e and μ_d values.

5.7 Polarity Effect on Film Growth and B Incorporation

In the previous sections, we presented various observations proving the difference in morphological, compositional and electronic properties of the two sides of each grain. An additional difference between the two sides is how easily they are etched.

Figure 5.11 shows the morphological evolution of films dipped in a solution of HCl (dilution 1/2000 in water). The two sides already appear different in as-deposited films, the bright side is characterized by small bumps aligned on the stacking faults (SFs) while the dark side features elongated shapes perpendicular to the stacking faults. Figures 5.11b, 5.11c and 5.11d, show that the etching is faster on the dark side compared to the bright side.

Finally, cross section TEM observations (Figures 5.11e and 5.11f) show that both the sides are characterized by a high concentration of defects (mainly basal stacking faults), and that, in the dark side, the concentration of these defects appears to be even higher and less periodic.

Table 5.3 lists the observed differences between the dark and the bright sides of the grains. In the following, we propose an explanation accounting for the majority of these differences.

Table 5.3: Observed differences between the two sides (bright and dark) of each grain.

technique	bright side	dark side
TEM	less defects	more defects
SEM (as dep)	bumps, clear SF-lines	elongated features
SEM (polished)	wider, concave	narrower, convex
SEM (etched)	harder to etch	easier to etch, spikes formed
NanoSIMS	BO_2	no BO_2
KPFM	lower WF	higher WF

Different etching rates on the different crystallographic planes for the wurtzite structures have been reported already in the 1960's [Gatos and Lavine, 1960, Mariano and Hanneman, 1963]. For monocrystalline ZnO, different etching rates are attributed to the different electron concentration at the surface (cf. Section 1.2). Comparing the etching rate and the particular shapes of the etched surfaces (cf. Figure 5.11) with other polycrystalline ZnO films [Jo et al., 2005] allows to identify the bright (dark) side of the grain with the one exposing the c+ (c-) direction on the lateral surface of the grain as indicated in Figures 5.12a, 5.12b and 5.12c. Furthermore, by considering the average dimensions of the grain in the different crystalline directions we can qualitatively assess the relative growth velocity along the various directions.
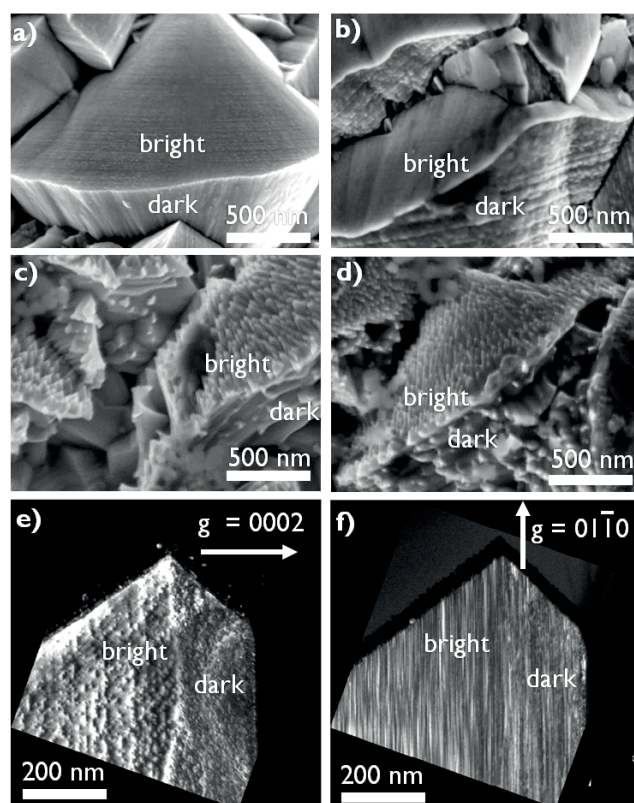
*Figure 5.11: Observed differences between the dark and bright side of the grain. Differential etching of HCl-dipping (dilution 1/2000) plan-view SEM micrographs of **(a)** as deposited, **(b)** after 1", **(c)** after 10" and **(d)** after 20". Cross section dark field TEM micrographs taken under two different zone axis: **(e)** g = 0002 and **(f)** g = 01$\bar{1}$0, courtesy of D.T.L. Alexander.*
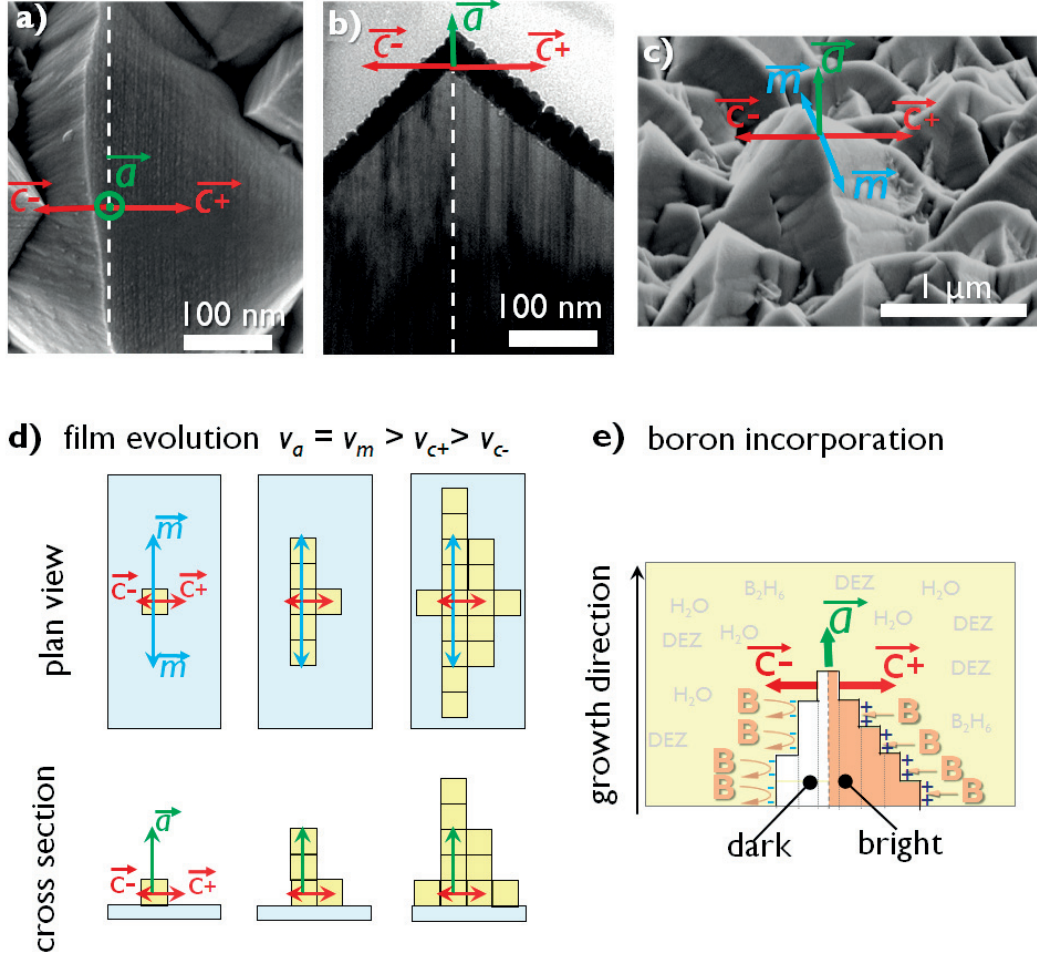
Figure 5.12: Asymmetry of a grain with respect to the crystallographic orientations: a, m, c+ and c-axis. (a) SEM plan view. (b) TEM cross section. (c) SEM tilted view. Proposed models for (d) film evolution and (e) asymmetric boron incorporation.

The grain is elongated in the *m* and *a* directions and the bright side of the grain is wider than the dark one. We propose that the relative growth velocities are ranked as follows:

$$v_a \approx v_m > v_{c+} > v_{c-} \qquad (5.9)$$

Note that a similar ranking was also proposed by Faÿ [Faÿ, 2003].

The grains grow faster in the lateral directions (*m*, *a*) forming wide platelets. The high density of stacking faults suggests that the propagation along the *c*-direction is likely to be mediated by the formation of stacking faults; extended defects are known to influence the film growth [Germain et al., 2003, Fang et al., 2005]. The different growth rates between the *c+* and *c*-directions are attributed to the different superficial charge that attracts or repels various molecules from the gas phase. In films having the wurzite unit cell, polar surfaces were already

reported to induce a different growth rate on the *c*+ and *c*- directions as for example in gallium nitride (GaN) and ZnO [Wang et al., 2003, Garrido et al., 2012].

Similarly, we assume that the sticking coefficient of the B_2H_6 molecule is different on the two lateral surfaces determining whether or not the B-atoms are incorporated into one of the two sides. The incorporation dependency on film polarity was reported for single crystalline GaN [Li et al., 2000, Collazo et al., 2007] and ZnO films [Ogino et al., 2014]. In particular, Mg-doped ZnO by pulsed laser deposition showed higher Mg-concentration on the *c*- oriented than on the *c*+ oriented films [Adachi et al., 2013]. The authors attributed this observation to the difference in sticking coefficient between Zn and Mg atom on the *c*+ and *c*- surfaces [Kato et al., 2004]. Their observations show that the film polarity can play a role in the dopant incorporation but are not directly applicable to the case of polycrystalline LP-MOCVD ZnO. In their case, the concentration of Mg incorporated into the *c*- film was about three times higher the concentration of Mg incorporated in the *c*+ and therefore comparable with the sticking coefficient ratios; while in our case no dopant at all is found in one of the two grains. The polycrystalline nature of the film and the chemical-reaction-based growth mechanisms add complexity to the dopant incorporation mechanisms and would require further investigations to fully clarify this effect.

5.8 Summary and Conclusions

In this chapter, we unveiled a remarkable bi-modal spatial segregation of boron in *a*-textured LP-MOCVD ZnO films. Using direct measurements and simulations we showed the effect of the dopant segregation on the electronic and optical properties of the film.

The main results are:

- In ZnO films **B-atoms incorporate only into one side** of each ZnO grain.

- Using contact potential measurements we related the spatial segregation to **non-uniform local electronic properties**. The regions containing boron show a lower workfunction.

- Simulations based on the band alignment at grain boundary showed that for highly doped samples **the contact resistivity is lower for the bimodal distribution than for the uniform distribution**.

- Various observations demonstrating the difference between the two sides of the grains are summarized. Based on these observations, we explain the bimodal dopant segregation as the result of the **different surface polarity** of the two lateral sides of the grains.

6 Applications in Photovoltaic Cells

In this chapter, we demonstrate the application of controlled LP-MOCVD depositions studied in Chapter 3 to the development of transparent ZnO electrodes in solar cells. We have experimented with four types of layers in four solar cells that use different absorbers: tandem hydrogenated amorphous/microcrystalline (micromorph) silicon, *n-i-p* hydrogenated amorphous silicon (a-Si:H), copper indium gallium selenide (CIGS) and silicon heterojunction (SHJ), and found several advantages of the use of LP-MOCVD ZnO films for each device.

For the thin film *micromorph* cells we developed a two-step deposition process for the front ZnO contacts which allows us to decouple optical properties of the film from its electrical properties. By combining a 2-μm-thick *a*-textured ZnO film with a thinner *c*-textured film we were able to smoothen the film surface, reducing crack formation in the microcrystalline film, while preserving its useful electrical properties. The cells deposited using this procedure had an as-deposited efficiency higher than 12%, comparable with the state-of-the-art cells that require more complex post-deposition steps such as O_2/Ar plasma etching, to smoothen the surface (Section 6.1).

For *n-i-p a-Si:H* solar cells, we developed a ZnO double layer composed of an antireflection coating applied on top of the conductive front electrode (upper layer). The antireflection coating layer consists of detached nanometer-scale pillars, forming films with a high porosity, therefore reducing the refractive index from 1.9 (case of ZnO dense layer) down to 1.65 in the visible range of the spectra. By applying this layer on top of the conductive dense ZnO electrode the reflectance of the a-Si:H cell is reduced on average below 5% in the visible range (Section 6.2) .

In the case of *CIGS* solar cells, we applied the LP-MOCVD ZnO:B electrodes as the front contact of the cells. The motivation of this work, is to demonstrate the clear advantage of the ZnO:B layers with respect to the more commonly used TCOs as aluminium doped ZnO (ZnO:Al), indium tin oxide (ITO) and fluorine-doped tin oxide (FTO), i.e. its lower absorptance, for the same sheet resistance R_{sh}. The performance of the cells is compared to reference devices that use ZnO:Al as the front contact. While the ZnO:B cells consistently present an improvement in

short circuit current J_{SC}, their open circuit voltage V_{OC} and fill factor FF are lower as compared than those if ZnO:Al devices. The possible causes of this will be discussed in detail in Section 6.3.

For *silicon heterojunction* (SHJ) cells, we studied the effect that the application of ZnO:B electrodes with distinct carrier concentrations has on cell performance. Outcomes show that electrically a high N_e is beneficial at both contacts (*ip* and *in*). At the *ip*-contact the beneficial effect is the result of two opposing effects: a narrower inversion layer within the crystalline silicon c-Si layer (detrimental) and the decrease of the depletion region at the a-Si:H(p)/TCO recombination junction (beneficial). By combining direct measurements and simulations of the electronic band structure within the device, we clarified the relative importance of these two effects (Section 6.4).

Part of these results are presented in [Ding et al., 2014, Fanni et al., 2015b, Tomasi et al., 2016].

6.1 Smoothening for Micromorph Cells

6.1.1 Motivation

A micromorph cell is a tandem device composed of an a-Si:H cell on top of an hydrogenated microcrystalline silicon (μc-Si:H) cell, whose typical thicknesses are respectively 250 nm and 1.2 μm. The spectral response of μc-Si:H extends up to 1100 nm but its absorption coefficient is too low to fully absorb the infrared component of the sun spectrum in 1.2 μm of material [Despeisse et al., 2011]. Therefore, light-trapping schemes must be implemented into these cells in order to increase the light path inside the absorber [Krc et al., 2003, Krc et al., 2010]. The fine optimization of the light-trapping capability together with the low absorptance and low R_{sh} of the ZnO:B layer enabled the fabrication of high-efficiency thin-film photovoltaic modules. The efficiency of 1.4-m^2 tandem micromorph modules has reached 10% in production line [Stannowski et al., 2013] and up to 12.3% in the pilot line [TELSolar, 2014, Green et al., 2015].

One approach to increase the light trapped in the absorber consists of using a rough front electrode that will scatter the incoming light, increasing the probability for light absorption, and resulting in an increase of the cell's (J_{SC}). The drawback of this approach is that the amorphous and microcrystalline silicon growing on top of the pyramidally textured electrode tends to form cracks, especially due to the problematic filling of the sharp valleys present on the textured electrodes. The consequences are a reduction of the V_{OC} and FF of the cell [Python et al., 2009, Bugnon et al., 2012]. An Ar/O plasma post-treatment has been widely used to smoothen the sharpest features of the LP-MOCVD front electrode, still maintaining a good light-scattering ability [Addonizio and Antonaia, 2009]. This process is effective but it requires an additional process step and equipment, which is not convenient for production. Here, we present a two-step ZnO deposition process consisting of: rough *a*-textured ZnO electrodes, covered with a smoothening layer of *c-textured* ZnO, all done by a single deposition

producing *as deposited* samples in which the valleys between the features are partially filled.

6.1.2 Experimental Details

Micromorph cells in the *p–i–n* configuration were prepared by plasma-enhanced chemical vapor deposition (PECVD) in a medium-sized industrial KAI reactor from silane, hydrogen, carbon dioxide, phosphine and trimethylboron. Cell depositions were performed by Mathieu Charrière (PVLAB). The top a-Si:H cell was 250 nm thick and the bottom μc-Si:H cell was 1.2 μm thick. A 90 nm-thick silicon oxide n-layer was used as an intermediate reflector between the two cells [Dominé et al., 2008]. The micromorph cells were patterned to an area of 1 cm^2 by sulfur hexafluoride plasma etching. The front contact was composed by a 1.8 - 2.2-μm-thick layer of rough *a*-textured film (H_2O/DEZ = 1, hotplate temperature 180 °C, gas flow 150 sccm) coated with a 0.2-0.5-μm-thick layer of smooth *c*-textured film (H_2O/DEZ = 0.7, hotplate temperature 180 °C, gas flow 150 sccm). The back contact was a 2.4-μm-thick LP-MOCVD ZnO:B layer with a R_{sh} of 25 Ω/sq. A white dielectric was used as the back reflector. Cell performance was assessed by current–voltage (I–V) measurements using an AM1.5 sun simulator under standard test conditions. The J_{SC} of each cell was evaluated from external quantum efficiency (*EQE*) measurements. All solar cell parameters presented are initial values, i.e. not stabilized.

As seen in Section 3.3, the transition between *c*- and *a*-texture is very sensitive to the temperature of the substrate, and a high conductivity is obtained for deposition parameters close to the transition between the two types of films. This means that the temperature should be highly uniform on the hotplate in order to ensure the uniformity of the filled film (high conductivity *a*-textured + high conductivity *c*-textured). We verified the uniformity of film parameters over the whole deposition area by co-depositing on five glass substrates, four placed in the corners of the hotplate and one in the center, as shown in Figure 6.1. The uniformity of the electrical properties of the filled layers is as good as the uniformity on the reference layer, confirming the applicability of this method also on larger deposition areas.

6.1.3 Results

In order to investigate the effect of the *c*-texture filling on the cell performance, we increased the thickness of the filling layer while keeping constant (2.4 μm) the total film thickness. As a reference electrode we chose a 2.4-μm *a*- textured film that underwent 4' of Ar+O_2 plasma etching treatment, i.e. the state of the art of ZnO electrodes for micromorph cells. The morphological and electrical parameters of the analyzed layers are shown respectively in Figure 6.2 and 6.3. The *c*-textured film preferentially grows in the valley between the features, likely due to the ease of nucleating in the valleys rather than on the faces of the pyramids. The filling of the valley should reduce the tendency of amorphous and microcrystalline silicon to form cracks. The variation in *c*-texture filling thickness allows us to tune the haze parameter (i.e. light scattering ability) without impacting the N_e and μ_d. Therefore, this two-step deposition

	2.4	2.1 + 0.3
d	-7%	-5%
R_{sh}	+21%	+21%
H	-7%	-8%

	2.4	2.1 + 0.3
d	-10%	-9%
R_{sh}	+20%	+22%
H	-7%	-7%

	2.4	2.1 + 0.3
d	2.4 µm	2.45 µm
R_{sh}	19.4 Ω_{sq}	17.1 Ω_{sq}
H	59.9%	53.0%

	2.4	2.1 + 0.3
d	-12%	-10%
R_{sh}	+28%	+25%
H	-6%	-7%

	2.4	2.1 + 0.3
d	-13%	-11%
R_{sh}	+30%	+29%
H	-7%	-8%
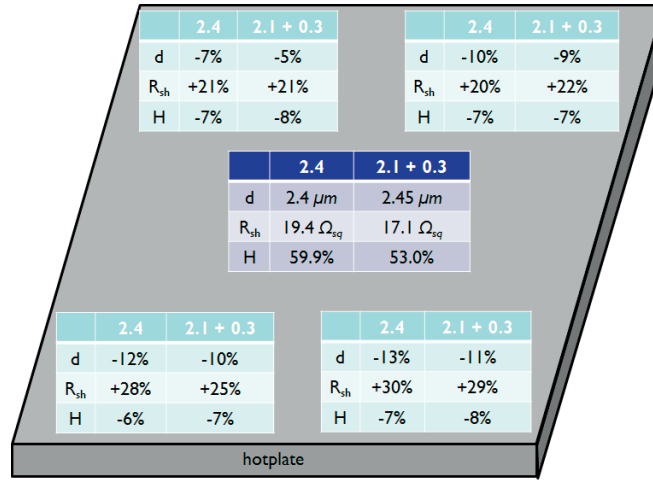
hotplate

Figure 6.1: Relative variation of thickness d, sheet resistance R_{sh} and haze H for films deposited at the four corners of the hotplate (light-blue tables) compared to a film deposited in the center (darker blue table). The comparison shows that the uniformity of film properties over the hotplate surface of the developed layer (2.1 + 0.3 c-filled) is as good as the reference layer (2.4 µm a-textured as deposited).
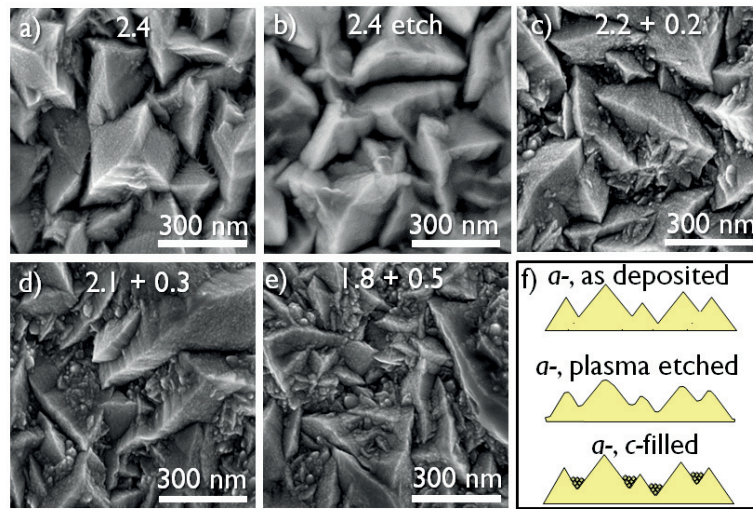
Figure 6.2: SEM micrographs of the various front electrodes investigated within this section (a) 2.4-µm-thick a-textured as-deposited film (b) 2.4-µm-thick a-textured etched film (c) 2.2 µm-thick a-textured film filled with 0.2 µm-thick c-textured film (d) 2.1-µm-thick a-textured film filled with 0.3-µm-thick c-textured film (e) 1.8 µm-thick a-textured filled film with 0.5 µm-thick c-textured film. (f) Schematic draws diagrams of the different electrodes.

allows decoupling the optical properties from the electrical ones increasing the freedom in the optimization of the electrode.

Figure 6.4 shows the impact of the *c*-textured-filled electrodes on the cell performance. V_{OC}
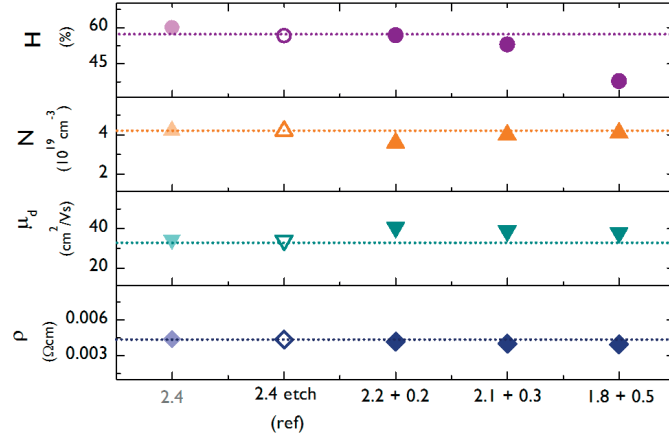
Figure 6.3: Haze (H), carrier concentration (N_e), carrier mobility (μ_d) and resistivity (ρ) for the films presented in Figure 6.2.

and *FF* of the filled samples are higher than the as-deposited 2.4-μm-thick film, and they increase with the thickness of the filling reaching values that are similar or larger than the plasma-treated reference. As expected from the decrease in haze, the increase of the filling thickness reduces the J_{SC}. As clarified by the EQE plot of Figure 6.4b, the bottom cell (microcrystalline) collects less light in the IR likely due to the shorter light path in the cell. The compromise between the V_{OC} and FF increase and the J_{SC} decrease is reached for a filling thickness of 0.3 μm cell reached an efficiency of 12.3%, just slightly lower than that of the reference cell (η = 12.4%).
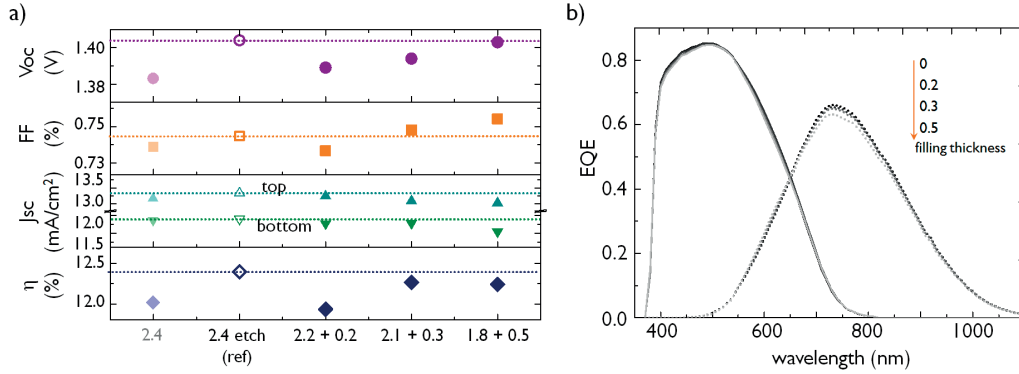
*Figure 6.4: **(a)** Open-circuit voltage (V_{OC}), fill factor (FF), short-circuit current density (J_{SC}) and efficiency (η) of micromorph cells using the electrodes presented in Figure 6.2. **(b)** External quantum efficiency (EQE) for the same series of cells presented in (a).*

We demonstrated a two-step process providing as-deposited films that have properties very similar to those of the state-of-the-art electrodes, therefore simplifying the fabrication process of the film without compromising the performance.

6.2 Porous Film for a-Si:H Cells

6.2.1 Motivation

Porous TCOs are of interest for a wide range of applications. For example, due to the high surface exposed to the surrounding atmosphere they are applied in gas sensing devices [Wan et al., 2004, Jing and Zhan, 2008, Li et al., 2010] and due to their low and graded refractive index they are effective as antireflective layers [Schirone et al., 1997].

The aim of this application is to reduce the reflectance of a *n-i-p* a-Si:H solar cells. To reduce it we apply a porous layer on the front surface of the cell acting as antireflection coating. The knowledge in controlling the film morphology through deposition parameters acquired in Chapter 3 allows us to tune the film porosity. In this section, we demonstrate how to tune it to obtain the refractive index that minimizes the reflection at the interface between standard ZnO:B films and glass.

In order to assess the density of porous layer we use a non-destructive method (Kanaya-Okayama, based on SEM-EDS cf. Chapter 2) [Kanaya and Okayama, 1972]. This method was previously used only for asses the density of compact compound layer composed by different materials. Here we validate the reliability of this method for porous layers with the use of complementary measurements (transmittance and reflectance) and simulations.

The ZnO porous layer with the lowest refractive index is applied on a *n-i-p* a-Si:H solar cells demonstrating a reduction of reflectance (to 5% in the visible range) that results in a simulated gain in J_{SC} of 1%.

6.2.2 Experimental Details

Dense films were obtained with a H_2O/DEZ flow ratio of 1 at a substrate temperature of 180 °C. For the nanopillar ZnO films, the substrate temperature was increased to 250 °C and the H_2O/DEZ flow ratio to 4. The gas flow was kept constant at 150 sccm. The thickness of the films varied between 0.65 and 1.2 μm. A large part of these depositions were performed by Benoît Delaup (PVLAB). a-Si:H layers were deposited in the *n–i–p* configuration by plasma-enhanced chemical vapor deposition (PECVD) while the front electrode was made of either the dense or dense/nanopillar film stacks as shown below. a-Si:H solar cells were deposited by Xavier Niquille (PVLAB). Details on the density assessment based on EDS measurements (Kanaya-Okayama method) performed by Yonat Milstein (B-nano) are explained in section 2.2.

6.2.3 Calculating the Appropriate Refractive Index

We are interested in developing a layer featuring a refractive index between that of glass and that of ZnO film in order to reduce the reflectance of an a-Si:H cell. The Fresnel equations

allow us to quantify the amount of light transmitted and reflected at an interface. Considering a thin film deposited on a substrate and immersed in air, the reflectance of the system at normal incidence is calculated as:

$$R = (\frac{n_{air}\, n_s - n_f^2}{n_{air}\, n_s + n_f^2})^2 \tag{6.1}$$

where n_{air}, n_s and n_f are the refractive index of air, the substrate and the film, respectively. This value of reflectance represents the minimum achieved for the specific wavelengths and the specific film thickness that produce destructive interference, i.e. phase shift of 180° between the beam reflected at the air/film interface and at the film/substrate interface. For this application we are not interested in cancelling the reflectance at a specific wavelength, rather we want to find the value of n_f that decreases the average value of the reflectance over a wide spectral range (i.e. the spectral response of a-Si:H). This can be done by setting R = 0 in Equation 6.1:

$$n_f = \sqrt{n_{air}\, n_s} \tag{6.2}$$

Considering that in real application the solar cell is encapsulated with glass ($n_f = 1.5$), Equation 6.2 shows that the reflectance of the a-Si:H in n-i-p configuration (whose upper layer is the ZnO electrode, $n = 1.9$) is minimized applying an antireflection coating with a refractive index of $n_f = 1.69$.

6.2.4 From Dense to Well-Separated Nanopillar Films

As seen in Section 3.3, typical high-quality LP-MOCVD ZnO electrodes are deposited at a hot-plate temperature of 180 °C and a H_2O/DEZ ratio of 1. These films are dense and characterized by V-shaped grains having a preferential orientation along the a-axis ('dense' in Figure 6.5). The film surface is rough due to pyramid-like features.

Increasing the temperature during deposition leads to increased competition between crystalline orientations, such that the growth rates along different orientations become similar. Therefore the film structure becomes more disordered ('flaked' in Figure 6.5) and without preferential orientation [Faÿ et al., 2005, Nicolay et al., 2009]. In this case, the layer is characterized by flakes expanding in different directions and creating voids in the film. By further increasing the H_2O/DEZ ratio from 1 to 4, the film develops separated nanopillars with an elongated section; the long side measures around 100 nm, and the short side measures around 30 nm ('nanopillars' in Figure 6.5). The change in film structure from dense to nanopillars leads to an
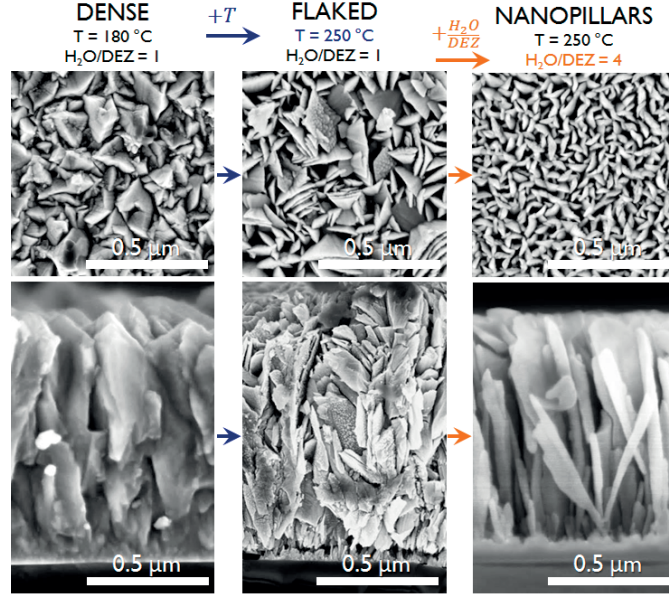
Figure 6.5: SEM micrographs (plan views and cross sections) showing structural variations due to an increase in temperature and a subsequent increase in the H_2O/DEZ ratio.

increase in the void fraction, inhibiting the lateral carrier transport but also increasing transmittance and simultaneously reducing reflectance, as shown in Figure 6.6a. The absorption of the different films is therefore similar.

From measured R and T curves we obtained the film n_{eff} by using the software *RefDex* that is based on the transfer-matrix-method-based [Manley et al., 2014]. Note that, at 550 nm n_{eff} decreases from 1.9 for the dense film to 1.65 for the nanopillars film. This change in n_{eff} can be explained by the effective-medium theory, which links the void fraction with the film's optical properties.

6.2.5 Assessing Film Density and its Influence on the Effective Refractive Index

The *effective-medium theory* is used to estimate the optical properties of an inhomogeneous material by combining the properties of the constituent materials weighted by their volume fractions. Many models exist to derive the optical properties in a mixed film [Levy et al., 1985, Yoldas and Partlow, 1985]. In order to relate the optical properties of the film to its density we calculate n_{eff} of the porous films by assuming that they are composed of a mixture of dense ZnO with refractive index n_{ZnO}, and air ($n = 1$), using the Maxwell-Garnett equation [Levy et al., 1985]:

$$n_{eff}(\lambda) = n_{ZnO}(\lambda) \frac{2(1 - v_f)n_{ZnO}(\lambda) + (1 + 2 \cdot v_f)}{(2 + v_f)n_{ZnO}(\lambda) + (1 - v_f)} \tag{6.3}$$
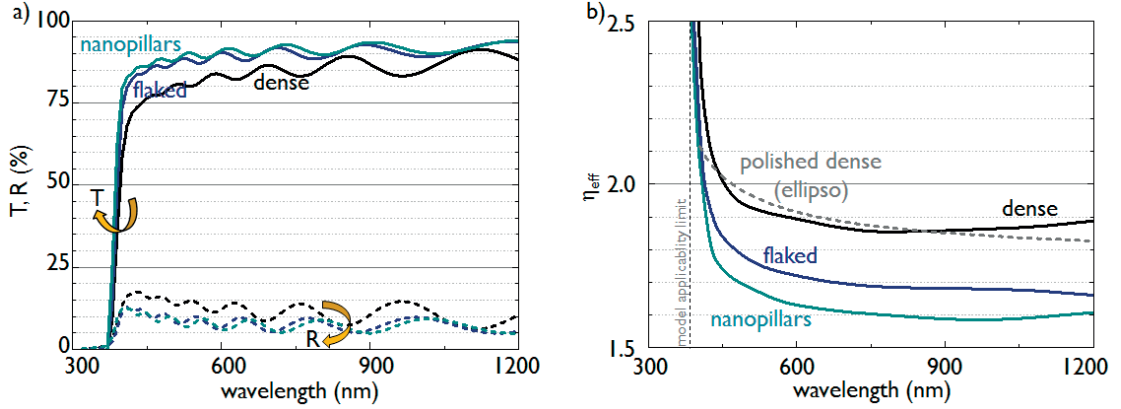
*Figure 6.6: **(a)** Optical transmittance (T) and reflectance (R) of the layers presented in Figure 6.5. **(b)** Effective refractive index (n_{eff}) of the same series of samples. The curves are derived from the transmittance and reflectance spectra shown in (a) using the simulation software RefDex [Manley et al., 2014]. The refractive index of a polished dense film, measured with ellipsometry (dotted grey curve), is shown as a comparison; notice that below 400 nm the strong decrease in transmission prevents estimation of n_{eff} from spectrophotometric measurements.*

with v_f being the void fraction, and n_{ZnO} derived from spectroscopic ellipsometry measurements.[1] The refractive index obtained by ellipsometry from a polished dense layer was in good agreement with the one derived with the *RefDex* software for an unpolished dense layer (cf. Figure 6.6b), validating the reliability of the software outcomes.

In order to determine the density we used the Kanaya-Okayama method based on EDX measurements (explained in Section 2.2). Assuming that the polished dense ZnO film is fully compact, it is useful to define the relative film density as:

$$\rho_{rel} = \rho / \rho_{dense,ZnO} \tag{6.4}$$

Thus, the void fraction v_f can be expressed by:

$$v_f = 1 - \rho_{rel} \tag{6.5}$$

The values of relative density for the different layers obtained with the Kanaya-Okayama method are listed in Table 6.1; the void fraction increases to 13% for the flaked layer and up to 24% for the porous one.

---

[1]Due to the porosity of the film we could obtain reliable values of n_{eff} only for the polished dense film. As previously explained, we obtained n_{eff} for the other films using *RefDex*.

Table 6.1: Assessment of the film density with the Kanaya-Okayama method (cf. Chapter 2). Parameters used: minimal beam energy (E_0) and film thickness (d); and outputs obtained: relative density (ρ_{rel}) and void fraction (v_f) for the dense (polished and as-deposited), flaked, and nanopillar films.

	$\mathbf{E_0}$	**d**	ρ_{rel}	$\mathbf{v}_f$
	keV	*μm*	*%*	*%*
dense	19.0	1.17	97	3
polished dense	13.6	0.65	100	0
flaked	17.9	1.18	87	13
nanopillars	14.9	0.99	76	24

To our knowledge this was the first time that the Kanaya-Okayama method was used to assess the relative density of a porous layer [2] Therefore, in order to verify the results obtained through Equation 2.1, we simulated the interaction volume of the electron beam with the ZnO films using the software CASINO [Drouin et al., 2007]. As defined in section 2.2, E_0 is the minimal beam energy allowing a certain share of the incoming electrons to pass through the ZnO layer and to release from the glass constituents enough X-rays to be detected. Each simulation performed with CASINO was characterized by means of the measured values of E_0, d and ρ_{rel} listed in Table 6.1 and using 5.6 g/cm^3 for $\rho_{dense,ZnO}$ [Morkoç and Özgür, 2009].

Figure 6.7 shows the remaining energy of the beam electrons with respect to their position inside the film. Note that the average energy of the electrons reaching the glass is close to 5% of the initial beam energy for all four samples, even though they each have a unique value of E_0, d, and ρ_{rel}. The fact that the beam energy at the ZnO/glass interface is very close in all four cases is consistent with the outcomes of the Kanaya-Okayama method. We can test the soundness of our approach by comparing these results (v_f, obtained with the Kanaya-Okayama method, and n_{eff}, assessed by $RefDex$) with the predictions of the effective medium theory obtained using Equation 6.3. As shown in Figure 6.8 our results agree well with the Maxwell-Garnett equation validating the applicability of the Kanaya-Okayama method for porous layers.

6.2.6 Reducing a-Si:H Cell Reflectance

In this section we demonstrate the antireflection coating capability of the nanopillar layer by depositing it on a-Si:H solar cells. In an a-Si:H cell in the *n–i–p* configuration, a top layer consisting of a TCO acts as the front electrode (cf. Figure 6.9). In order to have both the excellent optoelectronic properties of the dense layer and the antireflective properties of the nanopillar layer, we deposited them sequentially as presented in Figure 6.9. When the a-Si:H is coated only with the dense ZnO film, the reflectance of the solar cell decreases from 22% to 7% (with respect to the bare a-Si:H) in the spectral range between 400 and 700 nm. When the

---

[2]The method was previously developed to estimate the density of alloys composed of two or more different materials [Kanaya and Okayama, 1972].
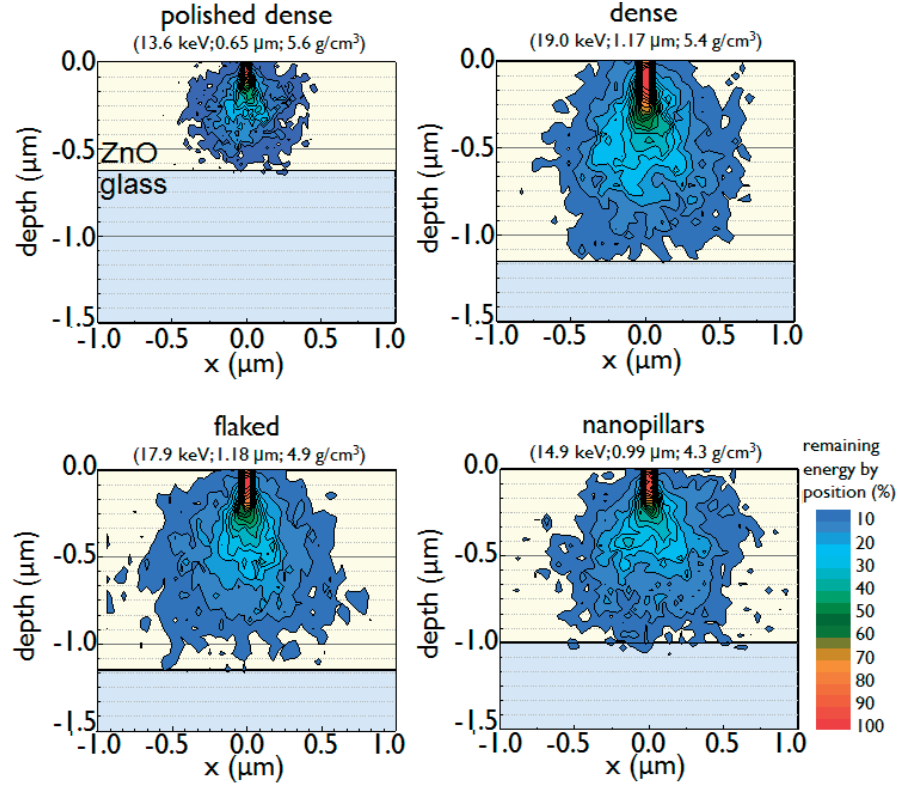
Figure 6.7: Simulated interaction volume (in cross section) between the EDS electron beam and ZnO film on glass for the four films analyzed. The different colored regions represent the remaining electron energy with respect to the initial beam energy.

ZnO nanopillar film is deposited on top of the front ZnO contact, the reflectance decreases further to 5%. This result is explicable in terms of the graded transition introduced by the nanopillar film between the refractive index of air and that of dense ZnO (cf. Equation 6.2). The observed decrease in reflectance results in a calculated J_{SC} increase of $\approx 1.1\%$.

Nanopillars proved to reduce the cell reflectance, but in order to be effective as electrodes they should additionally provide low R_{sh}. The porosity of the ZnO nanopillar layer reduces the carrier lateral mobility, which dramatically increases the film sheet resistance as shown in Table 6.2. However, the combination of nid ZnO nanopillars on top of the dense ZnO:B provides the low sheet resistance (39 Ω_{sq}) required for application as an electrode in a-Si:H solar cells [Boccard et al., 2012]. Note that, the optical analysis was performed on nid films and the necessary R_{sh} is reached only for doped films. Nonetheless the previously presented measurements are still meaningful since the addition of boron changes the film optical properties mainly outside the a-Si:H spectral response, i.e. in the UV ($\lambda < 350$ nm, Burstein–Moss effect) and in the IR ($\lambda > 1000$ nm, free carrier absorption) as reported in the literature [Wenas et al., 1991b, Faÿ et al., 2005].

We developed and characterized a ZnO porous layer, tuning its refractive index to reduce
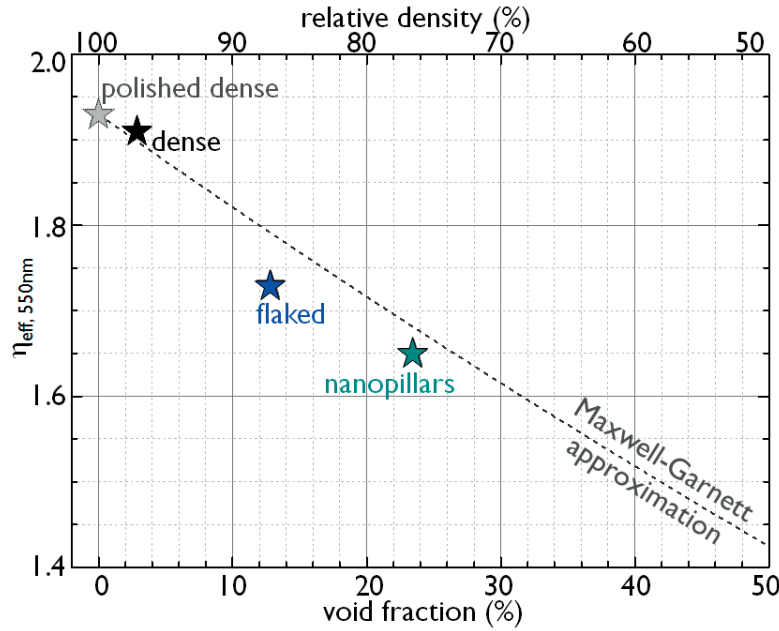
Figure 6.8: Effective refractive index n_{eff} at λ = 550 nm (derived from optical measurements, RefDex) versus void fraction (assessed with the Kanaya-Okayama method) for the polished dense, dense, flaked and nanopillar films. Experimental values (stars) are compared with the effective-medium theory predictions (dotted line, Equation 6.3).
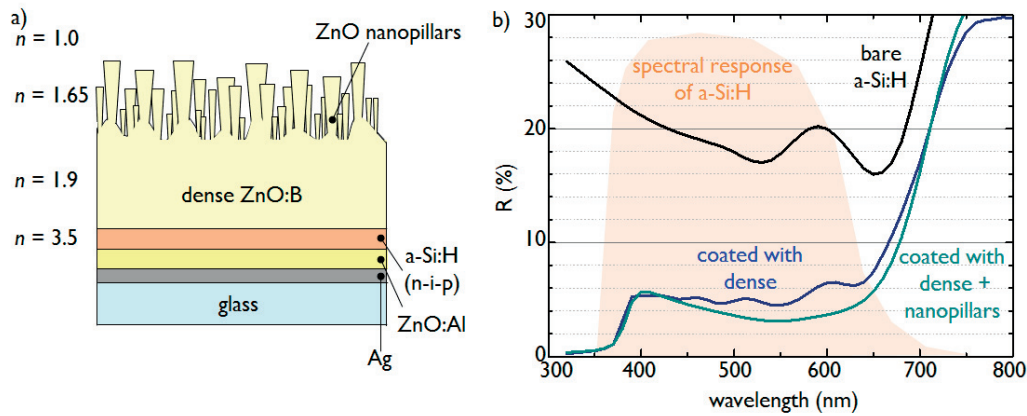
*Figure 6.9: **(a)** Schematic, not to scale, of the n-i-p a-Si:H cells showing the lowest reflectance: the front electrode is composed of an upper ZnO nanopillar layer (antireflective) and a lower ZnO dense layer (providing lateral conductivity). **(b)** Reflectance (R) of different a-Si:H cells: bare, coated with dense film, and with dense film + nanopillar film (as sketched in (a)).*

the light reflectance at the air/dense ZnO film interface. When deposited on top of the front contact of an a-Si solar cell, the porous layer acts as antireflection coating reducing the cell reflectance below 5% in the visible range. The gain in J_{SC} is calculated to be ≈ 1.1%.

Table 6.2: Electrical properties of the dense, nanopillar and dense + nanopillar films without and with extrinsic doping.

	non-intentionally doped		doped	
	d μm	R_{sh} Ω_{sq}	d μm	R_{sh} Ω_{sq}
dense	1.17	$1.8 \cdot 10^2$	0.97	22
nanopillars	0.99	$6.1 \cdot 10^6$	1.03	$5.3 \cdot 10^6$
dense + nanopillars	1.17 + 0.99	$2.3 \cdot 10^2$	0.97 + 1.03 (nid)	39

6.3 Front Contact in CIGS Cells

6.3.1 Motivation

Chalcopyrite thin-film solar cells are the only technology able to still keep its share of the global market after the strong cost reduction of crystalline silicon technology [Green, 2016]. CIGS solar cells have demonstrated efficiencies larger than 22% on flat substrates [Frontier, 2015] and an impressive 20.4% on flexible substrates [Chirilă et al., 2013]. The parameters that still need to be improved in order to bridge the gap with the maximum theoretical values are V_{OC} and J_{SC} [Jäger et al., 2015]. CIGS solar cells can also be combined with perovskite cells, to achieve high-efficiency tandem devices [Kranz et al., 2015]. To improve J_{SC} in single-junction CIGS cells as well as in tandem devices, the parasitic absorption of the front TCO should be reduced. Here we tackle this task by substituting the ZnO:Al deposited via magnetron sputtering with the more transparent ZnO:B deposited by LP-MOCVD. The main challenges of this approach are the degradation of the CIGS layer at the temperature typically used for ZnO:B deposition (above 150°C) and possibly the lower workfunction of ZnO:B with respect to CIGS material [Jäger et al., 2015].

6.3.2 Experimental Details

CIGS layers were grown at (EMPA, Switzerland) on 1-mm-thick 5x5 cm^2 glass coated with molybdenum (acting as back contact) by a three-stage co-evaporation process, allowing the fabrication of absorbers with graded concentration of the different elements. Co-evaporation from elemental effusion cells in a high-vacuum chamber (base pressure $1 \cdot 10^{-8}$ mbar). The average [Ga]/([In]+[Ga]) and [Cu]/([Ga]+[In]) ratios were respectively 0.35 and 0.8 and the film thickness was around 2.7 μm. The cadmium sulfide (CdS) layer was deposited using chemical bath deposition. The baseline front contact was composed of a 150-nm-thick ZnO:Al on top of a 50-nm-thick non-intentionally doped ZnO, both deposited using RF magnetron sputtering. The ZnO:B layers were deposited by LP-MOCVD at different B$_2$H$_6$/DEZ ratios (0 - 0.02), H$_2$O/DEZ ratios (1.0 - 1.5) and hotplate temperatures (150 - 180 °C). The optoelectronic properties of the TCO layers were characterized by means of Hall effect setup, profilometer and UV-VIS-NIR spectrometer. The *EQE* of solar cells was measured with a lock-in amplifier. A

TCO properties				
	d μm	N_e cm^{-3}	μ_d cm^2/Vs	R_{sh} Ω_{sq}
ref	0.15	$3.5 \cdot 10^{20}$	17	67
cvd$_{180}$	2.27	$1.0 \cdot 10^{19}$	36	65
sp/cvd$_{180}$	2.10	$1.0 \cdot 10^{19}$	33	70
sp/cvd$_{150}$	2.20	$2.2 \cdot 10^{19}$	24	57

chopped white halogen light source and a dual-grating monochromator generated the probing beam. The beam size was adjusted such that the illumination area was smaller than the device area. Cell temperature was controlled at 25°C with a Peltier while applying white light bias. I-V characteristics of solar cells were measured under simulated standard-test conditions (25 °C, 1000 W/m^2, AM1.5G). A Keithley 2400 source meter with four-terminal sensing was used to acquire J-V characteristics. Additional details regarding the used deposition and characterization techniques can be found elsewhere [Chirilă et al., 2013]. The CIGS cell depositions and characterizations were performed by Thomas Feurer (EMPA).
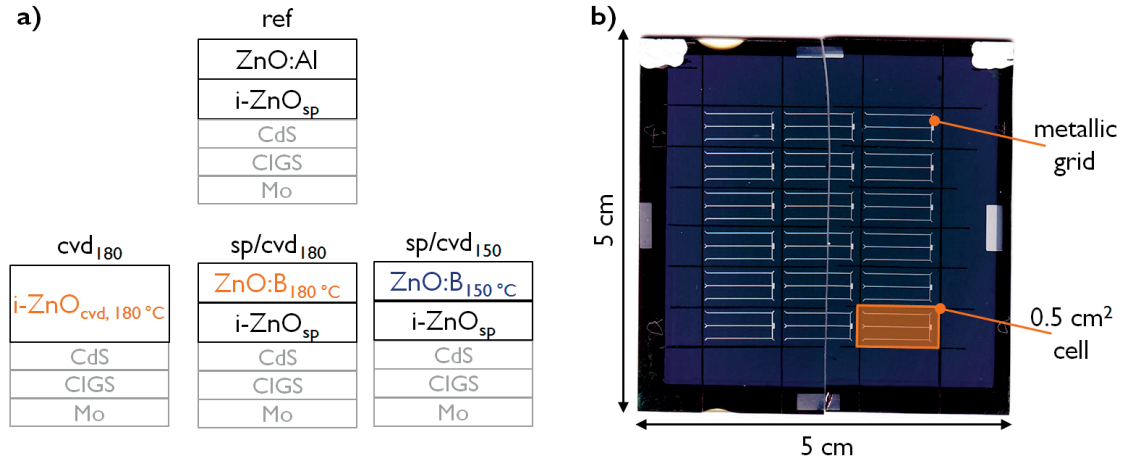
*Figure 6.10: **(a)** Schematics showing the four TCOs applied as front electrodes to CIGS cells: ref sputtered intrinisc ZnO and sputtered ZnO:Al; cvd$_{180}$ intrinsic ZnO deposited using LP-MOCVD at 180°C; sp/cvd$_{180}$ sputtered intrinsic ZnO and ZnO:B deposited using LP-MOCVD at 180 °C; and sp/cvd$_{150}$ sputtered intrinsic ZnO and ZnO:B deposited using LP-MOCVD at 150 °C. **(b)** Picture of the front surface of CIGS cells. The front metallic grid allowsfor the use of moderately resistive front TCOs without increasing the ohmic losses.*

6.3.3 Results

The baseline CIGS cell developed at EMPA was deposited on a soda-lime glass (1 mm thick) and constituted by a rear metallic electrode (molybdenum layer), the p-type absorber of light (CIGS film), a buffer layer (CdS), a resistive and transparent layer (intrinsic ZnO layer), the n-type front transparent electrode (ZnO:Al) and a metallic grid reducing the ohmic losses. The
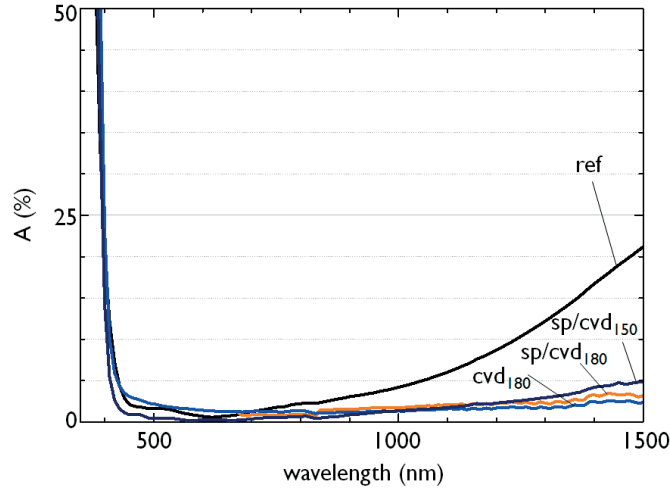
Figure 6.11: Comparison of the electrical and optical (absorptance, A*) properties of the four window layers used for the CIGS cells: ref, cvd$_{180}$, sp/cvd$_{180}$ and sp/cvd$_{150}$.*

schematic of this cell, indicated in the following as *ref,* is shown in Figure 6.10. The presence of the front metallic grid, whose shape is dictated by the compromise between ohmic losses and shadowing, allows for the use of TCOs with moderate R_{sh} (60-70 Ω_{sq}) relaxing the trade-off between absorptance and conductivity. In this section we compare three window layers that are more transparent than the ZnO:Al baseline with the aim of increasing the cell J_{SC} without decreasing V_{OC} or FF. The lower absorptance of these three window layers arises because they are partially or totally composed of ZnO deposited by LP-MOCVD, as shown in Figure 6.10. Two of the window layers, sp/cvd$_{150}$ and sp/cvd$_{180}$, have the first 50 nm of the window layers deposited by sputtering and the conductive layer is deposited by LP-MOCVD at a hotplate temperature of 150°C and 180°C, respectively. The third window layer, cvd$_{180}$, is fully deposited by LP-MOCVD. We chose these three configurations in order to investigate the effect of the resistive ZnO layer and of the deposition temperature on the known decrease of V_{OC} and FF related to the use of LP-MOCVD ZnO.

As shown in Figure 6.11 the window layers based on LP-MOCVD ZnO are more transparent especially in the IR due to the reduced free carrier absorption, their N_e being one order of magnitude lower than the one of the ref sample. The R_{sh} varies between 57 and 70 Ω_{sq} for the different layers. These values are reached without the addition of B for the samples deposited at 180 °C ($N_e = 1.0 \cdot 10^{19}$ cm^{-3}) while a small addition of B was necessary for the sample deposited at 150 °C ($N_e = 2.2 \cdot 10^{19}$ cm^{-3}) due to its lower μ_d.

The lower absorptance of the window layers based on LP-MOCVD ZnO is reflected in a larger J_{SC}, up to 1 mA/cm^2, with respect to the ref sample, as shown in Figure 6.12 . Nevertheless they all show a lower V_{OC} and lower FF which reduces the cell efficiency below the value of the ref cell. Among the CVD-based cells, the cvd$_{180}$ cell shows the higher $V_{OC} \cdot FF$ value leading to a higher η. This cell does not feature the resistive ZnO(i) layer deposited by sputtering that is considered necessary to obtain high-efficiency cells [Luque and Hegedus, 2003, Jing

Cell properties				
front TCO	V_{OC} mV	J_{SC} mA/cm^2	FF %	η %
ref	706	32.3	76.1	17.3
cvd_{180}	689	32.6	74.4	16.8
sp/cvd_{180}	657	32.5	72.4	15.5
sp/cvd_{150}	673	33.3	73.7	16.5
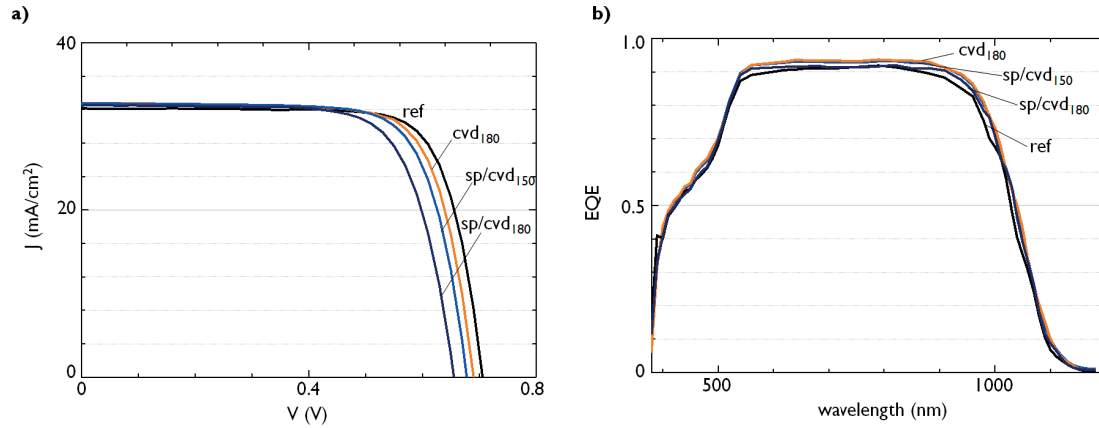
Figure 6.12: Comparison of electrical parameters of CIGS cells for different front electrodes: ref, cvd$_{180}$, sp/cvd$_{180}$ and sp/cvd$_{150}$. The values refer to the best five cells. (a) I-V curves and (b) external quantum efficiency curves of the CIGS cells.

and Zhan, 2008]. The reason could be probably found in the difference between CVD and sputtering techniques in terms of film growth. ZnO:Al films deposited by sputtering are composed of columnar and straight grains featuring the *c*-axis as preferential orientation. The nucleation (and disordered) layer is thin, and therefore the vertical conductivity is determined mainly by the in-grain material. In order to obtain a resistive layer, it is therefore necessary to deposit an intrinsic ZnO layer with high O content in the deposition gas in order to reduce the conductivity within the grain. The case of intrinsic LP-MOCVD ZnO films is different. As discussed in Section 3.4 the *a*-textured films (the ones incorporated into the CIGS cell) have a selection layer of several hundreds of nanometers. This selection layer contains a high concentration of grain boundaries and is resistive when non-intentionally doped. After this selection layer the faster-growing grains take over providing a lower lateral resistivity. In this way the non-intentionally-doped LP-MOCVD film is composed by two layers a first, thinner and resistive and a second thicker and conductive. This observation explains why for full LP-MOCVD window layers the ZnO(i) layer deposited by sputtering is not necessary. Furthermore when the LP-MOCVD ZnO film is deposited onto the sputtered ZnO(i) film we observe a detrimental effect that decreases both *FF* and V_{OC}. The *FF* and V_{OC} values of the sp/cvd$_{150}$ sample are higher than those of the sp/cvd$_{180}$ sample. We attribute this difference to the lower deposition temperature of sp/cvd$_{150}$ that limits the degradation of the CIGS [Kushiya, 2004].

We substituted the state-of-the-art sputtered-deposited ZnO:Al window layer of CIGS cells with a more transparent LP-MOCVD ZnO:B. We observed a reproducible increase in J_{SC} and a decrease of V_{OC} and FF. We demonstrated that removing the resistive ZnO(i) layer and depositing at a lower temperature partially recovers the losses in V_{OC} and FF.

6.4 a-Si(p)/ZnO:B Interface in Silicon Heterojunction Cells

6.4.1 Motivation

Silicon heterojunction (SHJ) solar cells are fabricated by passivating the surfaces of the crystalline silicon (c-Si) wafer with a thin layer of intrinsic hydrogenated amorphous silicon (a-Si:H(i)). This layer saturates the dangling bond of the Si atoms at the wafer surface reducing the recombination velocity of the minority carriers. The two semi-permeable membranes necessary to separate the photogenerated charge carriers are obtained by depositing on one side a thin layer of p-type a-Si:H (*hole collector*, built-in electric field repels the electrons) and on the other side a layer of n-type a-Si:H (*electron collector*, repelling the holes). The electronic band alignment of the device is shown in Figure 6.13. Note that, the presence of the *ip* layer induce the formation of a thin p-region (called the *inversion layer*) within the c-Si wafer. The presence of this layer, crucial for high-performance devices, induces the formation of a *p-n* junction close to the c-Si wafer surface [Ghannam et al., 2015]. These devices have proven to be very effective in converting solar energy into electricity with efficiencies of up to 25.6% [Panasonic, 2014].
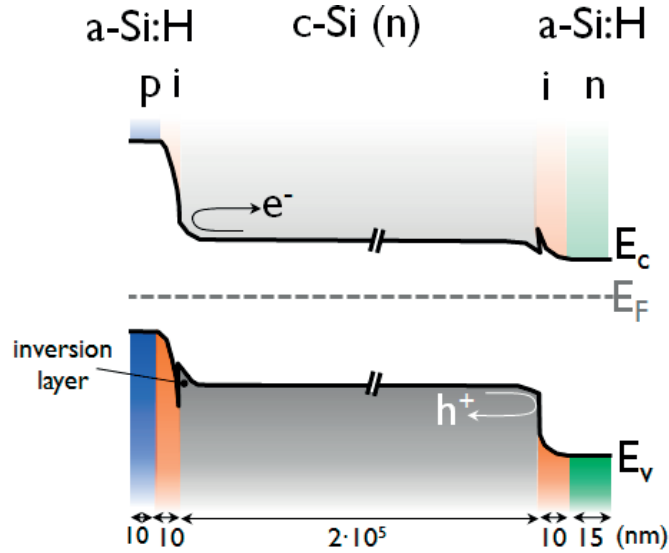
Figure 6.13: Band alignment of the core of a silicon heterojunction cell. A weakly n-doped 200-µm-thick crystalline silicon wafer (c-Si(n)) is covered by intrinsic hydrogenated amorphous silicon (a-Si:H(i)), that reduces the recombination velocity. p- and n-doped a-Si:H are deposited on the two extremities acting as semipermeable membranes for holes and electrons. Adapted from [Descoeudres et al., 2013].

A limited understanding of the transport mechanisms involved at the heterocontacts of SHJ solar cells makes the achievement of high *FF* values, as the one reported in [Panasonic, 2014], an extremely challenging task. The effect of resistive losses at the SHJ front contact is a relevant topic due to its direct impact on the cell efficiency. Although, it has been shown that in SHJ solar cells the increase of the TCO carrier concentration favors the V_{OC} and the *FF* of the cell [Kirner et al., 2015], simulations showed that N_e of the TCO should negatively impact the surface passivation [Rößler et al., 2013, Bivour et al., 2013]. The reason for these opposed effects could be related to the formation of the interface between the a-Si:H(p) and the TCO, and its influence on the inversion layer and on the tunnel recombination junction. In this section we investigate this controversial issue by means of simulations and direct measurements.

6.4.2 Experimental Details

c-Si wafers (4-in float-zone, n-type, nominal resistivity of 2.8 Ωcm) were textured and cleaned by a wet-chemical process. Subsequently, they were dipped in a diluted hydrofluoric solution to strip off the chemical oxide. Thin blanket intrinsic/doped a-Si:H layer stacks were deposited on both wafer surfaces in a PECVD reactor, at 200°C. More details on the a-Si:H stacks used for hole and electron collection can be found elsewhere [Descoeudres et al., 2011]. The thickness of the standard a-Si:H layers, measured by spectroscopic ellipsometry on a planar glass substrate, were 10 nm for the a-Si:H(i) layer and 15 and 10 nm for the a-Si:H(n) and a-Si:H(p) layer, respectively. a-Si:H depositions were performed by Silvia Martin de Nicolas Agut (PVLAB). Indium tin oxide (ITO) films were sputtered from an In$_2$O$_3$:Sn target (10% SnO$_2$), nominally at room temperature. ZnO:B layers were deposited at a hotplate temperature of 180°C. TCO layer thickness, measured on glass, range between 180–250 nm, which are typical TCO thicknesses used in our IBC-SHJ device back contacts [Tomasi et al., 2014]. The effective minority-carrier lifetime of the passivated c-Si wafers, was assessed in the excess minority-charge-carrier density range 10^{14} - 10^{16} cm^{-3}, by transient photoconductance decay measurements [Sinton and Cuevas, 1996]. TCO depositions and carrier lifetime assessment were performed by Florent Sahli (PVLAB).

6.4.3 Results

An a n-type TCO is commonly used as electrode in SHJ cells for both the p- and the n- sides. We investigate the effect of varying the N_e of ZnO:B on both sides (n- and p-type). We assess this effect by measuring the lifetime of the minority carriers (τ_{eff}) within the wafer. The effect of the N_e increase on the n-side is a slight improvement of τ_{eff} (cf.6.14a). This improvement is probably due to higher electric field at the c-Si/a-Si:H(i) interface preventing the holes from recombining at the wafer surface. At the p-side, the increase in N_e of the ZnO:B induce a strong decrease of the carrier lifetime especially at low injection levels. A similar dependence on TCO N_e has been also observed when using ITO instead of ZnO:B [Tomasi et al., 2016].
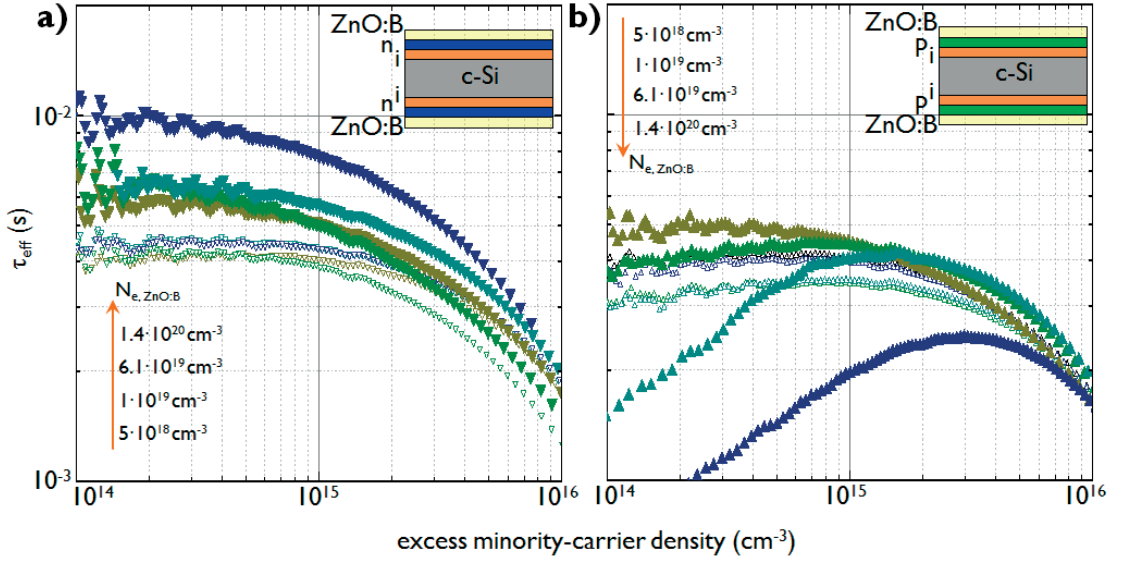
*Figure 6.14: Dependence of the effective minority-carrier lifetime τ in the silicon wafer on the ZnO:B carrier concentration ($N_{e,ZnO:B}$) deposited either on the **(a)** n- or **(b)** p- type a-Si:H. The empty triangles serve as references and represent the carrier lifetime of each sample just before the ZnO:B deposition.*

It is expected that at injection values higher than $\Delta n = 2 \cdot 10^{15}$ cm^{-3}, a decrease in τ_{eff} may translate into a reduced *FF*. Since the a-Si:H(p)/ZnO:B interface is the one presenting the controversial effect we focus our attention on it. By means of the AforsHet software, developed at Helmholtz Zentrum Berlin [Varache et al., 2015], we simulated the electronic band alignment in the stack ZnO:B/a-Si:H(p)/a-Si:H(i)/c-Si(n). The outcomes of the simulations are shown in Figure 6.15. The simulations indicate that the N_e of ZnO:B has two major effects on the band alignment of the stack. First, a decrease of the inversion layer when increasing N_e of the TCO (reducing its ability to prevent electrons coming from c-Si(n) from recombining at the wafer surface); we believe this effect is responsible for the decrease in τ_{eff} observed in Figure 6.14b. The second effect is less evident but nonetheless important. The increase in N_e reduces the depletion region within the TCO at the interface with a-Si:H(p) (cf. Figure 6.15b), therefore increasing the tunneling probability of holes to recombine with electrons. It is known that the tunnelling probability strongly depends on the width of the depletion region to be crossed [Simmons, 1963]. Since it is observed that in real devices an increase in the TCO N_e leads to an increase in FF, it is inferred that the effect of a decreased depletion region is the most important with respect to the device efficiency.

A possible way to circumvent the detrimental effect of the inversion layer reduction would be to increase the thickness of the a-Si:H(p) layer. Its thickness, which does not impact the depletion region at the ZnO/a-Si:H(p) interface, should be at least as large as the region depleted from holes. This would restore the flat-band condition at the p-type a-Si:H/a-Si:H(i) interface and in turn the full height of the inversion layer. In order to avoid the additional parasitic absorption due to the thicker a-Si:H(p), this solution should be implemented in

117

rear-emitter SHJ cells (p-contact at the back) that were demonstrated to be as efficient as standard front-emitter cells [Descoeudres et al., 2013].
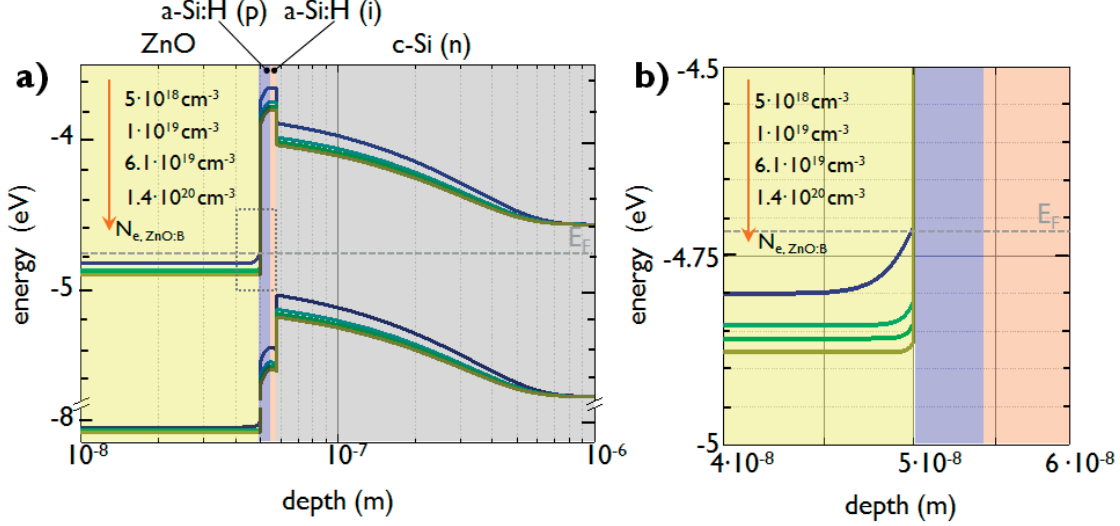
Figure 6.15: Simulation of the effect of the ZnO:B carrier concentration ($N_{e,ZnO:B}$) on the band alignment of the stack ZnO:B/a-Si:H(p)/a-Si:H(i)/c-Si(n). (a) Reduction of the inversion layer in the c-Si(n) and (b) magnified view to underline the narrowing of the depletion region in the ZnO:B at the tunnel junction with a-Si:H(p).

Both these effects come from the fact a-Si:H(p) has a larger WF than non-intentionally doped ZnO. The increase of the ZnO:B N_e further increases the difference in WF underlining the induced effects. In order to clarify this point we analyzed how the band alignment varies with the N_e of the TCO using the X-ray photoemission spectroscopy (XPS) technique. In order to provide reliable values coming from both the substrate and the film, one of the requirements of this technique is a thin (< 5 nm) but continuous film, i.e. no islands or pinholes cf. Figure 6.16. As shown in Figure 6.16 the ZnO film nucleates on a-Si:H forming islands, that will coalesce at a thickness of around 10 nm (cf. Section 3.3). Such layer is too thick for the electrons emitted by the a-Si:H to escape, making impossible the simultaneous measurement of electrons coming from ZnO:B and a-Si:H and in turn the valence band offset. Therefore we decided to run the experiment using ITO deposited by sputtering, that -as shown in Figure 6.16c - starts forming a continuous film after only a couple of nanometers. We chose ITO because, as explained previously, we observed a similar effect of the N_e variation on the τ_{eff} within the Si-wafer [Tomasi et al., 2016].

XPS measurements were performed on two ITO/a-Si:H(p)/a-Si:H(i)/c-Si(n) samples on an ITO layer (thickness around 2-4 nm) with different N_e $1 \cdot 10^{19}$ and $5 \cdot 10^{20}$. The results are presented in Figure 6.17. Both samples clearly show the valence band edge of ITO and of amorphous silicon, meaning that the ITO layer is thick enough to produce a defined valence band onset and simultaneously not too thick to absorb the electrons emitted by the underlying a-Si:H. The Fermi edge (i.e. energy difference between the Fermi level and the maximum of the valence
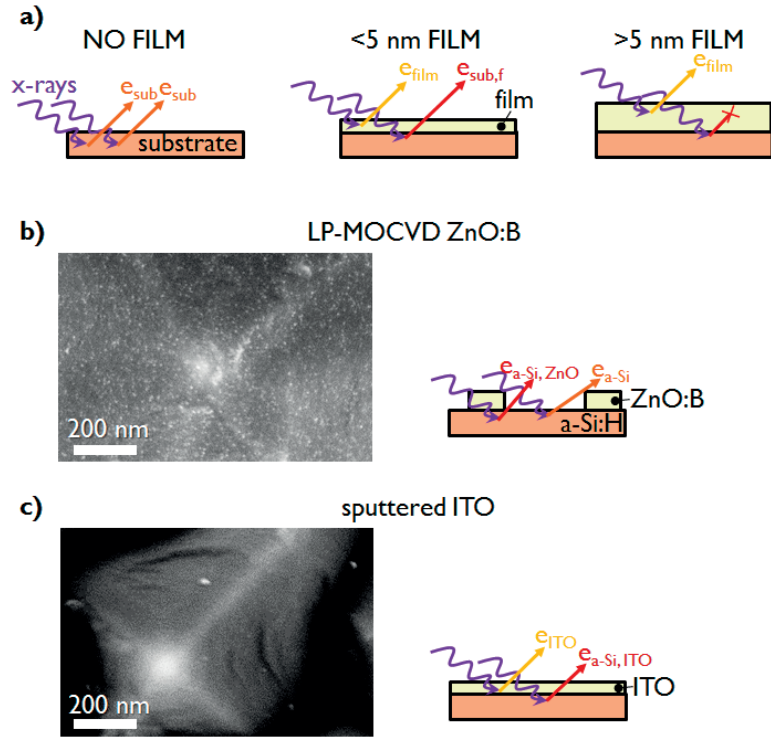
*Figure 6.16: Schematics showing the source of the electrons emitted by XPS analysis depending on the film thickness. **(a)** Effect of the film thickness on the secondary electrons types. SEM micrograph of the nucleation on textured silicon wafer covered by a thin layer of a-Si:H of **(b)** LP-MOCVD ZnO:B, showing island nucleation and **(c)** sputtered ITO, showing continuous film nucleation.*

band, cf. Figure 6.17) of amorphous silicon is measured to be close to 0.95 eV. The Fermi edge of ITO is larger for the sample with a lower N_e (3.5 eV) than for the sample with a higher carrier concentration (3.65 eV). This is an unexpected result. Indeed, the Fermi edge is the energy difference between the valence band offset and the Fermi energy (cf. Figure 6.17c), and therefore ITO with a larger N_e should show a higher Fermi level and in turn a larger Fermi edge, i.e. the opposite of what we observed. This discrepancy can be likely explained by referring to the adsorbed species at the ITO surface. As shown in the inset of Figure 6.17 the O atoms are bonded differently in the two samples, pointing towards different species adsorbed at the surface. Part of this difference could likely be attributed to the higher O flow during the deposition on the low-N_e ITO layer. The presence of adsorbed species affects the alignment of the electronic bands at the surface; this alters the XPS signal, as XPS probes a few nm. In order to get rid of the influence of adsorbed species, this measurement should be performed within an XPS setup equipped with in-situ deposition avoiding a break in the vacuum between the deposition and the measurements [Klein, 2012]. This would allow measurement of a sample having a pristine surface to which the energy level can be referred.

It is known that a high TCO N_e is beneficial for the performance of SHJ cells. Using carrier

lifetime measurements and simulations, we demonstrated that the performance improvement originates from the trade-off of two opposed effects: reduction of the inversion layer and reduction of the depletion region around the TCO/a-Si:H(p) tunnel junction. The intensity of the inversion layer was simulated to depend on the WF mismatch between TCO and a-Si:H(p). To directly verify this dependence we used XPS to measure the band alignment at the TCO/a-Si:H(p) interface. The measurements were not conclusive, likely due to pollutants adsorbed on the surfaces of the samples.

| | FE a-Si:H(p) | FE a-Si:H(p) |
	eV	eV
ITO high N_e	0.92	3.5
ITO low N_e	0.95	3.65
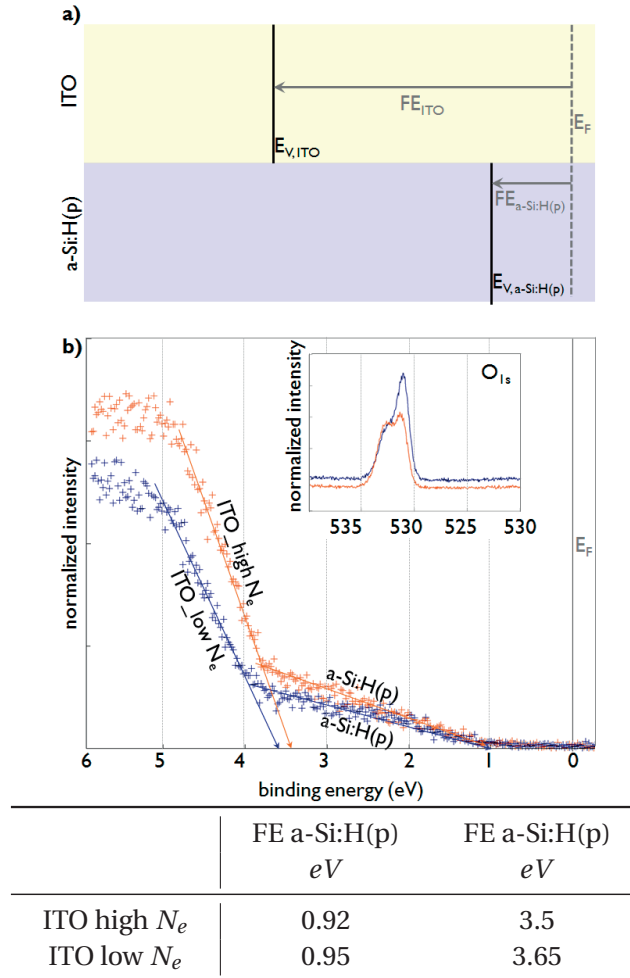
*Figure 6.17: **(a)** Schematics of the band alignment showing the Fermi edge for both the materials. **(b)** XPS curves of the valence band of the system ITO/a-Si:H(p), for low and high ITO carrier concentrations. The arrows show the onset of the Fermi edge for ITO and a-Si:H(p). The inset shows the difference in the O bindings for the two systems. The table indicates the values for the Fermi edge of a-Si:H(p) and ITO extracted from (b).*

6.5 Summary and Conclusions

LP-MOCVD ZnO:B was successfully applied in four different types of solar cells, with the results of simplifying the fabrication process, improving the performances or explaining the working mechanisms. The main outcomes of this work are:

- *Micromorph Cells.* We demonstrated the fabrication of **ZnO bilayers, with a single process**. The layers provide high conductivity, high haze and rounded valleys allowing the growth of high-quality a-Si.

- *Amorphous Silicon Cells.* We **lowered the refractive index of ZnO** from $n = 1.9$ to $n = 1.65$ and by applying this on cells, we reduced the total reflectance of the cells.

- *CIGS Cells.* Using the low-absorptance ZnO:B window layers, we **increased the J_{SC} of the cell**, but V_{OC} and FF remained lower than the ZnO:Al-based baseline. We partially bridged this gap by removing the resistive sputtered ZnO(i) by depositing at a lower deposition temperature (150°C).

- *Silicon Heterojunction Cells.* We **explained that the beneficial effect generated by an increased TCO carrier concentration** (at the p- and n-side) is due to the reduction of the depletion width at the tunnelling recombination junction present at TCO/a-Si:H(p) interface.

7 Conclusions and Perspectives

The general goal of the present thesis was to better describe the mechanisms of film formation and dopant incorporation in LP-MOCVD ZnO:B in order to control film evolution and tailor film properties. We reached this goal through a systematic investigation of many types of films at their different growth stages and applying specialized techniques to accurately measure their optoelectrical and structural properties. Our results demonstrate that a systematic investigation of well-known materials such as ZnO can lead to new findings which have both theoretical significance and straight-forward practical application.

The first section of this chapter summarizes the theoretical and empirical contributions of this thesis. Many topics investigated lead to new interesting questions some of which are presented in the last section.

7.1 Conclusions

7.1.1 Extension of the Space of Deposition Parameters

We performed a systematic study of the combined effect of temperature, H_2O/DEZ and total gas flow on the morphology and preferential orientation of non-intentionally doped films, presented in Chapter 3. We showed that an increase in film crystallinity and a shift of the preferential orientation from c- to a-textured films can be obtained by increasing deposition temperature, increasing H_2O/DEZ and decreasing the total gas flow. The control over these two properties is important since film preferential orientation defines the film morphology and the film crystallinity can be related to the carrier mobility within the film.

Our investigation of the extended space of deposition parameters produced two practical results. First, we developed the ZnO film with a new type of porous morphology and successfully applied it in a-Si:H solar cell. Second, we demostrated that it is possible to maintain certain film properties over a wide range of values of a single deposition parameter if the two other parameters are properly adjusted. For example, we deposited a a-textured rough film at

temperatures close to 120 °C while this type of films are normally deposited only above 180 °C.

7.1.2 Control of Film Preferential Orientation

The data collected through the experimentation with a large space of deposition parameters set the basis for the model describing the evolution of ZnO film crystallinity and film preferential orientation. Our model, presented in Chapter 3, describes the effect of the deposition parameters on the mean free path of the adsorbed atoms and allows to control the film preferential orientation. According to the model, the increase in temperature and H_2O/DEZ ratio increases the adatom mean free path, while an increase in gas flow reduces it. We applied a two-step deposition process alternating film preferential orientation between *a*- and *c*- and based on the developed model and the survival-of-the-fastest principle to grow a film with the grain 25% larger than that of the reference film.

7.1.3 H_2O/DEZ Ratio Favors B Incorporation

We measured the concentration of B atoms that are actually incorporated into the ZnO:B films. We showed that at high B_2H_6/DEZ ratio ($\approx 3.5\%$) the B atomic concentration is $\approx$ 1.5%. By varying the H_2O/DEZ ratio we demonstrated that high H_2O content in the gas phase favors the B incorporation and results in higher carrier concentration. The maximum carrier concentration we obtained at H_2O/DEZ = 0.5 was $1.5 \cdot 10^{20}$ cm^{-3} increasing up to $3.0 \cdot 10^{20}$ cm^{-3} for H_2O/DEZ ratio of 1.5. These new empirical data are presented in Chapter 4.

7.1.4 Same Doping Level, Different Sources of Electron Scattering

In Chapter 4, we investigated the effect of the interplay between intrinsic and extrinsic defects on the sources of electron scattering. We determined the dependence of the carrier mobility on the simultaneous variation of H_2O/DEZ and B_2H_6/DEZ. The results show that the main contribution to electron scattering is not always defined by the doping level, as commonly reported in literature, but that it depends also on the intrinsic defect concentration. For a high H_2O/DEZ (i.e. low intrinsic defect concentration), the main source of electron scattering are the grain boundaries, even for carrier concentration as high as $1 \cdot 10^{20}$ cm^{-3}. For low H_2O/DEZ ratio (i.e. high intrinsic defect concentration) the electron scattering from ionized impurities is the main limitation to the carrier mobility already for non-intentionally doped films (carrier concentration of $2 \cdot 10^{19}$ cm^{-3}).

7.1.5 Boron Segregation in the Film: the Bimodal Distribution

In Chapter 5, we demonstrated that B atoms segregate in the film in a strictly bimodal distribution. The B atoms incorporate only in one side of each grain leading to alternation of doped and non-intentionally doped regions. We attributed this segregation to the different

polarity of the two lateral surfaces of the grain. We measured the contact potential difference at sample surface and demonstrated that the dopant atom segregation leads to a non-uniform carrier concentration distribution within the film. We simulated the effect of the non-uniform distribution and uniform distribution of dopant atoms on the charge carrier transport. We showed that for high doping level (carrier concentration larger than $1 \cdot 10^{20}$ cm^{-3}) the contact resistivity of the film with non-uniform distribution is lower than the resistivity of a film with uniform distribution.

The discovery of bimodal dopant distribution is of theoretical importance for works on TCOs and should be pursued further to confirm and clarify our hypothesis that the polarity affects spatial and optoelectrical properties of materials.

7.1.6   Application in Photovoltaic Cells

In Chapter 6, we presented the implementation of ZnO:B films with some particular properties for four different types of solar cells: micromorph, a-Si:H, CIGS and SHJ.

In Section 6.1, we simplified the fabrication process of micromorph cell by developing an as-deposited bilayer that have the same properties of the state-of-the-art front contact. Our film has the advantage that it does not require the post-deposition treatment to smooth the film surface. The bilayer is obtained by depositing a thin *c*-textured film on top of the *a*-textured film which partially reduces the surface roughness. This technique allows to decouple the optical properties of the layer from its electrical properties. Cells using this front contact demonstrated as-deposited efficiency higher than 12%.

In Section 6.2, we demonstrated the control over the film refractive index by tuning the film porosity. By appropriately varying the deposition parameters we decreased the film refractive index from $n = 1.9$ to $n = 1.65$. We applied the film with the lowest refractive index to a *n-i-p* a-Si:H as antireflection coating, reducing its reflectance to 5% in the visible range, corresponding to a potential gain in short-circuit current of 1%.

In Section 6.3, we substituted the baseline front contact ZnO:Al of CIGS cells with ZnO:B layers. The ZnO:B layers proved to be effective in reducing the parasitic absorption: we measured an increase in J_{SC}, but FF and V_{OC} of the cells with ZnO:B were lower. We partially bridged the gap with the baseline by reducing the deposition temperature and removing the sputtered intrinsic ZnO layer. The best cell with ZnO:B showed the efficiency of 16.8%, slightly lower than the 17.3% of the baseline.

In Section 6.4 we investigated the causes of the known beneficial effect of increasing the carrier concentration of the TCO film on the performance of the SHJ solar cells. We applied the ZnO:B films with increasing carrier concentration on the p contact and measured the variation of the carrier lifetime within the wafer. Combining this data with simulations we explained beneficial effect for the cell efficiency due to the reduction of the depletion region around the tunnel recombination junction (a-Si:H(p)/ZnO:B interface).

7.2 New Characterization Techniques to Analyze Polycrystalline Thin Films

The novelty of this thesis does not simply lie in the experimental observations and proposed models, but also in the specific techniques adopted for film characterization.

The collaboration with the CIME-EPFL allowed for the development of the automated crystallographic orientation mapping technique. This work has also benefited from the complementary measurements (XRD, AFM) performed to validate the technique. The combination of the ACOM with the double wedge preparation method set-up by A.Brian Aebersold (EPFL) provided a way to collect statistically significant number of observations of grains with sizes as small as 20-30 nm. This technical achievement, impossible with a traditional EBSD technique, made it possible to analyze the film preferential orientation within the first hundreds of nanometers and opened a way for an informed deposition control of the preferential orientation.

We demonstrated the importance of NanoSIMS measurements when assessing the distribution of the dopant in polycrystalline films with grain sizes of some hundreds of nanometres.

B atoms are usually difficult to detect because of their low atomic weight and few electronic shells available for X-ray emission. The nuclear reaction analysis proved to be able to quantify bulk concentration of boron atoms as low as $5 \cdot 10^{18}$ cm^{-3} (i.e. $\approx 0.01\%$ atomic concentration).

The assessment of the relative density using the Kanaya-Okayama method, non-destructive technique based on EDS measurements, is normally used for non-homogeneous and compact films. Within this thesis its reliability for porous films was verified by means of complementary optical measurements and simulations.

The successful application of these characterization techniques in ZnO films suggest that they can be also applied to other polycrystalline films and provide new interesting observations about the film properties.

7.3 Perspectives

The results of this thesis give rise to many new interesting theoretical and empirical questions regarding the properties of ZnO deposited by LP-MOCVD and other TCOs and their possible applications in solar cells and other devices. We discuss in more detail three future research avenues.

7.3.1 Grain Boundaries

Grain boundaries are challenging to investigate because they are disordered regions at the atomic scale. In ZnO films by LP-MOCVD the small size of grains and the presence of other

defects within the crystalline regions (i.e. stacking faults and dislocations) often complicate the measurement design and the data interpretation. Nonetheless, grain boundaries play a major role in defining the electrical properties of a polycrystalline film and a better understanding of their electrical and compositional properties is required.

Two useful techniques to probe the electrical behavior of grain boundaries are the capacitance-voltage measurements and the impedance spectroscopy, both reported to be successful for various polycrystalline films [Suresh et al., 1991, Lee et al., 1995, Gerstl et al., 2011, Li et al., 2015]. The recently developed micro-Hall-effect measurement [Petersen et al., 2008] can be also interesting to apply since it could provide direct measurements of the local resistivity across the boundary.

Atom probe tomography is probably the most suitable technique to determine which are the atomic elements present in the surroundings of the boundary [Herbig et al., 2014]. We should note, however, that the tip preparation for the atom probe requires various stages in the transmission electron microscope. A long film exposition to energetic electron beam could partially deplete the sample from the lighter elements (e.g. B-atoms).

7.3.2   Improving the Doping Efficiency

Doping is the single most important parameter to tune the optoelectronic properties in the film. A deep understanding of the dopant incorporation and segregation mechanisms can lead to substantial improvements of the film performance. In this thesis, we showed that only 30 to 60% of the B atoms which are incorporated into the film release a free electron. To improve the doping efficiency we need to investigate the chemical state of the active and non-active B atoms in the film. A useful technique to assess the ionization state of the impurity atoms could be the near edge X-ray absorption [Kochubey et al., 2013].

We attributed the B segregation in the film to a difference in the polarity of the ZnO surfaces, but the reason why the molecules containing B should be attracted by one polar surface and not by the other is still unclear. An investigation of the molecules composing the gas phase would be shed light on this phenomenon. A suitable method to investigate how the gas molecules are dissociated in the gas phase would be the FTIR. An alternative method providing a complementary information would be to analyze the exhaust gases by mass spectroscopy.

The role of hydrogen in the film needs a detailed investigation. We measured the H concentration between 4% and 6% but we could not prove its correlation with the increase in carrier concentration. On the one hand, the addition of H_2 gas in the gas phase did not affect the carrier concentration. On the other hand H-plasma-post-deposition treatment showed to be effective in increasing the carrier concentration of non-intentionally doped films [Ding et al., 2013]. A remote source of ionized H atoms could probably improve the optoelectrical properties of the film and enrich our understanding of the role of H in LP-MOCVD ZnO films.

We pointed out that the maximum carrier concentration achievable in ZnO:B films limits their

use in applications requiring thin layers (e.g. flexible devices). For films deposited using RF magnetron sputtering, the use of Ga and Al dopants in ZnO proved to be more effective than the use of B [Minami et al., 1985, Kohiki et al., 1994]. Typical gas precursors for Ga and Al used in CVD are trimethylgallium (TMG) and trimethylaluminium (TMA). The decomposition temperature of the TMGa-molecule is too high (> 350 °C [Riihelä et al., 1996, Garcia-Alonso et al., 2015, Yamada et al., 2007]) to be compatible with the fabrication of solar cells such as SHJ and CIGS. A supply of ionized atoms from a remote source could be again a solution to the problem. Yet, TMA looks as a more promising solution since it was successfully employed to deposit ZnO:Al films by LP-MOCVD at 140 °C [Kim et al., 2011].

7.3.3 Applications

In Chapter 4, we demonstrated that LP-MOCVD ZnO films deposited at high H_2O/DEZ ratio have very low absorptance and high optical mobility. Reducing the detrimental influence of the grain boundaries on the drift mobility would allow for films with absorptance below 2% and carrier mobility between 60–70 cm^2/Vs at carrier concentration below $5 \cdot 10^{19}$ cm^{-3}. Such films could be potentially applied as front contacts in PV cells.

In Chapter 5, we showed that B atoms segregate in the ZnO:B film, forming an alternation of doped and undoped regions. The ability of controlling the in-plane grain orientation of ZnO:B would open the way to the realization of arrays of doped and non-intentionally doped regions. The realization of such array would be of interest for optoelectronic applications [Shinada et al., 2005]. In this direction, the control of polarity demonstrated by Williams *et al.*[Williams et al., 2013] for sputtered polycrystalline *c*-textured ZnO films deposition represents a promising starting point.

In Chapter 3, we showed the simplicity of tuning the ZnO:B film morphology. In Chapter 6, we demonstrated the application of some of these layers, or a combination of them, in photovoltaic cells. LP-MOCVD ZnO layer can be also applied for other devices that photovoltaic cells. For example, it would be interesting to apply the porous layer (such as the one used in the amorphous silicon cells, Chapter 6) in gas sensing devices as well as scaffolds for batteries.

A Appendix

In Chapter 5 we presented simulation of the potential barrier at grain boundaries by using the AFORS Het software [Varache et al., 2015]. We simulated the two grains which create the grain boundaries by using five layers: two sides for each grain and the grain boundary between them. The schematic of the stack is shown in Figure A.1.

The values of the input parameters used to simulate the "grain layer" and the "grain-boundary layer" are reported in Table A.1.
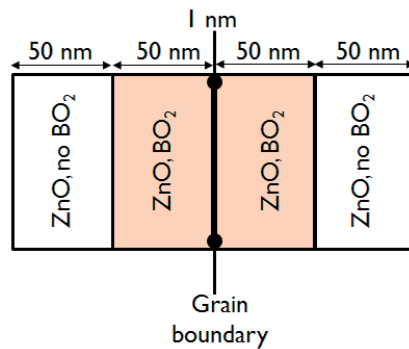
Figure A.1: Schematic illustrating the two grains forming a grain boundary. This stack was used to simulate the potential barrier at grain boundary. The illustrated example is referred to grain boundary of type I.

Table A.1: *Parameters values used in the AFORSHet software to simulate the potential barrier at grain boundary. The table reports the values used for the "grain layer" and the "grain-boundary layer". Some of the parameters were varied to account for the different doping levels.*

parameter		grain	grain boundary
ϵ		8.12	8.12
χ	eV	4.8	4.8
E_g	eV	3.28	3.28
$E_{g,opt}$	eV	variable: 3.29, 3.35, 3.50	3.28
N_c	cm^{-3}	$7.6 \cdot 10^{18}$	$7.6 \cdot 10^{18}$
N_v	cm^{-3}	$7.6 \cdot 10^{18}$	$7.6 \cdot 10^{18}$
μ_n	$cm^2 V^1 s^{-1}$	variable: 40,30,20	1
μ_p	$cm^2 V^1 s^{-1}$	7	0.3
N_a	cm^{-3}	0	0
N_d	cm^{-3}	variable $(1, 6.9, 28 \cdot 10^{19})$	0
ν_e	cms^{-1}	$1 \cdot 10^7$	$1 \cdot 10^7$
ν_h	cms^{-1}	$1 \cdot 10^7$	$1 \cdot 10^7$
ρ	gcm^{-3}	5.52	5.52
r_{ae}	$cm^6 s^{-1}$	0	0
r_{ah}	$cm^6 s^{-1}$	0	0
r_{bb}	$cm^6 s^{-1}$	0	0
d	cm	$5 \cdot 10^{-6}$	$5 \cdot 10^{-6}$
type			Single
charge			acceptor
m*			0.28
$N_{def} = N_t L$	cm^{-3}		$5 \cdot 10^{19}$
$E_{def} = E_t$	eV		3

Bibliography

[Adachi et al., 2013] Adachi, Y., Ohashi, N., Sakaguchi, I., and Haneda, H. (2013). Influence of crystal polarity on Mg incorporation in ZnO: Influence of crystal polarity on Mg incorporation in ZnO. *physica status solidi (b)*, pages 2122 – 2125.

[Adachi et al., 2015] Adachi, Y., Sakaguchi, I., Watanabe, K., Saito, N., and Suzuki, T. (2015). Effects of Impurity Doping on Gas Sensing Properties of ZnO Films Grown by Pulsed Laser Deposition. Tsukuba, Japan.

[Addonizio and Antonaia, 2009] Addonizio, M. and Antonaia, A. (2009). Surface morphology and light scattering properties of plasma etched ZnO:B films grown by LP-MOCVD for silicon thin film solar cells. *Thin Solid Films*, 518(4):1026–1031.

[Addonizio and Diletto, 2008] Addonizio, M. and Diletto, C. (2008). Doping influence on intrinsic stress and carrier mobility of LP-MOCVD-deposited ZnO:B thin films. *Solar Energy Materials and Solar Cells*, 92(11):1488–1494.

[Aebersold et al., 2015] Aebersold, A. B., Alexander, D. T., and Hébert, C. (2015). Height-resolved quantification of microstructure and texture in polycrystalline thin films using TEM orientation mapping. *Ultramicroscopy*, 159:112–123.

[Anno et al., 1998] Anno, H., Hatada, K., Shimizu, H., Matsubara, K., Notohara, Y., Sakakibara, T., Tashiro, H., and Motoya, K. (1998). Structural and electronic transport properties of polycrystalline p-type CoSb[sub 3]. *Journal of Applied Physics*, 83(10):5270.

[Avasthi et al., 1995] Avasthi, D., Acharya, M., Tarey, R., Malhotra, L., and Mehta, G. (1995). Hydrogen profiling and stoichiometry of an a-Six:H film. *Vacuum*, 46(3):265 – 267.

[Baccarani et al., 1978] Baccarani, G., Ricco, B., and Spadini, G. (1978). Transport properties of polycrystalline silicon films. *Journal of Applied Physics*, 49(11):5565 – 5570.

[Baer, 1967] Baer, W. S. (1967). Faraday rotation in ZnO: Determination of the electron effective mass. *Physical Review*, 154(3):785.

[Baji et al., 2012] Baji, Z., Lábadi, Z., Horváth, Z. E., Molnár, G., Volk, J., Bársony, I., and Barna, P. (2012). Nucleation and Growth Modes of ALD ZnO. *Crystal Growth & Design*, 12(11):5615–5620.

Bibliography

[Barna and Adamik, 1998] Barna, P. B. and Adamik, M. (1998). Fundamental structure forming phenomena of polycrystalline films and the structure zone models. *Thin Solid Films*, 317(1):27–33.

[Battaglia et al., 2012] Battaglia, C., Hsu, C.-M., Söderström, K., Escarré, J., Haug, F.-J., Charrière, M., Boccard, M., Despeisse, M., Alexander, D. T. L., Cantoni, M., Cui, Y., and Ballif, C. (2012). Light Trapping in Solar Cells: Can Periodic Beat Random? *ACS Nano*, 6(3):2790–2797.

[Batzill et al., 2005] Batzill, M., Katsiev, K., Burst, J. M., Diebold, U., Chaka, A. M., and Delley, B. (2005). Gas-phase-dependent properties of Sn O 2 (110), (100), and (101) single-crystal surfaces: Structure, composition, and electronic properties. *Physical Review B*, 72(16).

[Bikowski and Ellmer, 2014] Bikowski, A. and Ellmer, K. (2014). Analytical model of electron transport in polycrystalline, degenerately doped ZnO films. *Journal of Applied Physics*, 116(14):143704.

[Bikowski et al., 2015] Bikowski, A., Rengachari, M., Nie, M., Wanderka, N., Stender, P., Schmitz, G., and Ellmer, K. (2015). Research Update: Inhomogeneous aluminium dopant distribution in magnetron sputtered ZnO:Al thin films and its influence on their electrical properties. *APL Materials*, 3(6):060701.

[Birajdar et al., 2007] Birajdar, B., Peranio, N., and Eibl, O. (2007). Quantitative Boron-Analysis Using EDX in SEM and TEM. *Microscopy and Microanalysis*, 13(S03).

[Biron et al., 2013] Biron, R., Hänni, S., Boccard, M., Pahud, C., Söderström, K., Duchamp, M., Dunin-Borkowski, R., Bugnon, G., Ding, L., Nicolay, S., Parascandolo, G., Meillaud, F., Despeisse, M., Haug, F.-J., and Ballif, C. (2013). New progress in the fabrication of n–i–p micromorph solar cells for opaque substrates. *Solar Energy Materials and Solar Cells*, 114:147–155.

[Bish and Post, 1989] Bish, D. L. and Post, J. E. (1989). *Modern Powder Diffraction*, volume 20 of *Reviews in Mineralogy*. Mineralogic Society of America, Washington DC, USA.

[Bivour et al., 2013] Bivour, M., Schröer, S., and Hermle, M. (2013). Numerical Analysis of Electrical TCO / a-Si:H(p) Contact Properties for Silicon Heterojunction Solar Cells. *Energy Procedia*, 38:658–669.

[Blackwell et al., 2013] Blackwell, S., Smith, R., Kenny, S. D., Walls, J. M., and Sanz-Navarro, C. F. (2013). Modelling the growth of ZnO thin films by PVD methods and the effects of post-annealing. *Journal of Physics: Condensed Matter*, 25(13):135002.

[Bleiwas, 2010] Bleiwas, D. I. (2010). Byproduct mineral commodities used for the production of photovoltaic cells. Technical report, US Department of the Interior, US Geological Survey.

[Blood and Orton, 1992] Blood, P. and Orton, J. W. (1992). *The Electrical Characterization of Semiconductors: Majority Carriers and Electron States.* Techniques of Physics. Academic Press.

[Boccard et al., 2012] Boccard, M., Söderström, T., Cuony, P., Battaglia, C., Hänni, S., Nicolay, S., Ding, L., Benkhaira, M., Bugnon, G., Billet, A., Charrière, M., Meillaud, F., Despeisse, M., and Ballif, C. (2012). Optimization of ZnO Front Electrodes for High-Efficiency Micromorph Thin-Film Si Solar Cells. *IEEE Journal of Photovoltaics*, 2(3):229–235.

[Brehme et al., 1999] Brehme, S., Fenske, F., Fuhs, W., Neuber, E., Poschenrieder, M., Selle, B., and Sieber, I. (1999). Free-carrier plasama resonance effects and electron transport in rectively sputtered degenerate ZnO:Al films. *Thin Solid Films*, 342:167 – 173.

[Bright, 2007] Bright, D. M. (2007). *Review of Transparent Conductive Oxides (TCO)*. 50 years of vacuum coating technology and the growth of the society of vacuum coaters. Society of Vacuum Coaters.

[Brune et al., 1999] Brune, H., Bales, G. S., Jacobsen, J., Boragno, C., and Kern, K. (1999). Measuring surface diffusion from nucleation island densities. *Physical Review B*, 60(8):5991–6006.

[Bruneaux et al., 1991] Bruneaux, J., Cachet, H., Froment, M., and Messad, A. (1991). Correlation Between Structural and Electrical Properties of Sprayed Tin Oxide Films With and Without Flourine Doping. *Thin Solid Films*, 197:129 – 142.

[Bugnon et al., 2012] Bugnon, G., Parascandolo, G., Söderström, T., Cuony, P., Despeisse, M., Hänni, S., Holovský, J., Meillaud, F., and Ballif, C. (2012). A New View of Microcrystalline Silicon: The Role of Plasma Processing in Achieving a Dense and Stable Absorber Material for Photovoltaic Applications. *Advanced Functional Materials*, 22(17):3665–3671.

[Carlsson and Martin, 2010] Carlsson, J.-O. and Martin, P. M. (2010). Chapter 7 - Chemical Vapor Deposition. In Martin, P. M., editor, *Handbook of Deposition Technologies for Films and Coatings (Third Edition)*, pages 314–363. William Andrew Publishing, Boston.

[Chang et al., 2010] Chang, H., Wang, F., Wu, J., Kung, C., and Liu, H. (2010). Enhanced conductivity of aluminum doped ZnO films by hydrogen plasma treatment. *Thin Solid Films*, 518(24):7445–7449.

[Chen et al., 2015] Chen, S., Wilson, R. M., and Binions, R. (2015). Synthesis of highly surface-textured ZnO thin films by aerosol assisted chemical vapour deposition. *J. Mater. Chem. A*, 3(11):5794–5797.

[Chirilă et al., 2013] Chirilă, A., Reinhard, P., Pianezzi, F., Bloesch, P., Uhl, A. R., Fella, C., Kranz, L., Keller, D., Gretener, C., Hagendorfer, H., Jaeger, D., Erni, R., Nishiwaki, S., Buecheler, S., and Tiwari, A. N. (2013). Potassium-induced surface modification of Cu(In,Ga)Se2 thin films for high-efficiency solar cells. *Nature Materials*, 12(12):1107–1111.

[Chopra et al., 1983] Chopra, K. L., Major, S., and Pandya, D. (1983). Transparent Conductors - a Status Review. *Thin Solid Films*, 102:1–46.

Bibliography

[Collazo et al., 2007] Collazo, R., Mita, S., Rice, A., Dalmau, R. F., and Sitar, Z. (2007). Simultaneous growth of a GaN pn lateral polarity junction by polar selective doping. *Applied Physics Letters*, 91(21):212103.

[Consonni et al., 2012] Consonni, V., Rey, G., Roussel, H., and Bellet, D. (2012). Thickness effects on the texture development of fluorine-doped SnO2 thin films: The role of surface and strain energy. *Journal of Applied Physics*, 111(3):033523.

[Cullity, 2001] Cullity, B. (2001). *Elements Of X Ray Diffraction*. Prentice-Hall, 3rd edition.

[Cuony, 2011] Cuony, P. (2011). *Optical layers for thin-film silicon solar cells*. PhD thesis, Ecole Polytechnique Fédérale de Lausanne, Lausanne.

[De Wolf et al., 2012] De Wolf, S., Descoeudres, A., Holman, Z. C., and Ballif, C. (2012). High-efficiency Silicon Heterojunction Solar Cells: A Review. *green*, 2(1).

[Delgado et al., 2011] Delgado, J., Vilarigues, M., Ruivo, A., Corregidor, V., Silva, R. d., and Alves, L. (2011). Characterisation of medieval yellow silver stained glass from Convento de Cristo in Tomar, Portugal. *Nuclear Instruments and Methods in Physics Research Section B: Beam Interactions with Materials and Atoms*, 269(20):2383–2388.

[Descoeudres et al., 2011] Descoeudres, A., Barraud, L., De Wolf, S., Strahm, B., Lachenal, D., Guérin, C., Holman, Z. C., Zicarelli, F., Demaurex, B., Seif, J., Holovsky, J., and Ballif, C. (2011). Improved amorphous/crystalline silicon interface passivation by hydrogen plasma treatment. *Applied Physics Letters*, 99(12):123506.

[Descoeudres et al., 2013] Descoeudres, A., Holman, Z. C., Barraud, L., Morel, S., De Wolf, S., and Ballif, C. (2013). > 21% efficient silicon heterojunction solar cells on n-and p-type wafers compared. *Photovoltaics, IEEE Journal of*, 3(1):83–89.

[Despeisse et al., 2011] Despeisse, M., Battaglia, C., Boccard, M., Bugnon, G., Charrière, M., Cuony, P., Hänni, S., Löfgren, L., Meillaud, F., Parascandolo, G., Söderström, T., and Ballif, C. (2011). Optimization of thin film silicon solar cells on highly textured substrates. *physica status solidi (a)*, 208(8):1863–1868.

[Dieterle et al., 2011] Dieterle, L., Butz, B., and Müller, E. (2011). Optimized Ar+-ion milling procedure for TEM cross-section sample preparation. *Ultramicroscopy*, 111(11):1636–1644.

[Ding, 2013] Ding, L. (2013). *Low-Pressure Chemical Vapor Deposited Zinc Oxide Fimls: Towards Decoupled Opto-Electrical and Morphological Properties for More Efficient Electrodes*. PhD thesis, Ecole Polytechnique Fédérale de Lausanne.

[Ding et al., 2012] Ding, L., Boccard, M., Bugnon, G., Benkhaira, M., Nicolay, S., Despeisse, M., Meillaud, F., and Ballif, C. (2012). Highly transparent ZnO bilayers by LP-MOCVD as front electrodes for thin-film micromorph silicon solar cells. *Solar Energy Materials and Solar Cells*, 98:331–336.

[Ding et al., 2014] Ding, L., Fanni, L., Messerschmidt, D., Zabihzadeh, S., Masis, M. M., Nicolay, S., and Ballif, C. (2014). Tailoring the surface morphology of zinc oxide films for high-performance micromorph solar cells. *Solar Energy Materials and Solar Cells*, 128:378–385.

[Ding et al., 2013] Ding, L., Nicolay, S., Steinhauser, J., Kroll, U., and Ballif, C. (2013). Relaxing the Conductivity/Transparency Trade-Off in MOCVD ZnO Thin Films by Hydrogen Plasma. *Advanced Functional Materials*, 23(41):5177–5182.

[Dominé et al., 2008] Dominé, D., Buehlmann, P., Bailat, J., Billet, A., Feltrin, A., and Ballif, C. (2008). Optical management in high-efficiency thin-film silicon micromorph solar cells with a silicon oxide based intermediate reflector. *physica status solidi (RRL) - Rapid Research Letters*, 2(4):163–165.

[Drouin et al., 2007] Drouin, D., Couture, A. R., Joly, D., Tastet, X., Aimez, V., and Gauvin, R. (2007). CASINO V2. 42—A Fast and Easy-to-use Modeling Tool for Scanning Electron Microscopy and Microanalysis Users. *Scanning*, 29(3):92–101.

[Dziewior and Schmid, 1977] Dziewior, J. and Schmid, W. (1977). Auger coefficients for highly doped and highly excited silicon. *Applied Physics Letters*, 31(5):346.

[Earnshaw and Greenwood, 1997] Earnshaw, A. and Greenwood, N. N. (1997). *Chemistry of the Elements*. Elsevier Butterworth-Heinemann, 2nd edition edition.

[Ellmer, 2001] Ellmer, K. (2001). Resistivity of polycrystalline zinc oxide films: current status and physical limit. *Journal of Physics D: Applied Physics*, 34(21):3097.

[Ellmer, 2012] Ellmer, K. (2012). Past achievements and future challenges in the development of optically transparent electrodes. *Nature Photonics*, 6(12):809–817.

[Ellmer et al., 1996] Ellmer, K., Diesner, K., Wendt, R., and Fiechter, S. (1996). Relations between Texture and Electrical Parameters of Thin Polycrystalline Zinc Oxide Films. *Solid State Phenomena*, 51-52:541–546.

[Ellmer et al., 2008] Ellmer, K., Klein, A., and Rech, B. (2008). *Transparent Conductive Zinc Oxide*. Number 104 in Springer Series in Material Science. Springer, 1 edition.

[Faÿ, 2003] Faÿ, S. (2003). *L" oxyde de zinc par dépôt chimique en phase vapeur comme contact électrique transparent et diffuseur de lumière pour les cellules solaires*. PhD thesis, Ecole Polytechnique Fédérale de Lausanne, Lausanne.

[Faÿ et al., 2005] Faÿ, S., Kroll, U., Bucher, C., Vallat-Sauvain, E., and Shah, A. (2005). Low pressure chemical vapour deposition of ZnO layers for thin-film solar cells: temperature-induced morphological changes. *Solar Energy Materials and Solar Cells*, 86(3):385–397.

[Faÿ et al., 2007] Faÿ, S., Steinhauser, J., Oliveira, N., Vallat-Sauvain, E., and Ballif, C. (2007). Opto-electronic properties of rough LP-CVD ZnO:B for use as TCO in thin-film silicon solar cells. *Thin Solid Films*, 515(24):8558–8561.

Bibliography

[Fang et al., 2005] Fang, X.-S., Ye, C.-H., Zhang, L.-D., and Xie, T. (2005). Twinning-Mediated Growth of Al2o3 Nanobelts and Their Enhanced Dielectric Responses. *Advanced Materials*, 17(13):1661–1665.

[Fanni et al., 2015a] Fanni, L., Aebersold, A. B., Morales-Masis, M., Alexander, D. T. L., Hessler-Wyser, A., Nicolay, S., Hébert, C., and Ballif, C. (2015a). Increasing Polycrystalline Zinc Oxide Grain Size by Control of Film Preferential Orientation. *Crystal Growth & Design*, 15(12):5886–5891.

[Fanni et al., 2014] Fanni, L., Aebersold, B., Alexander, D., Ding, L., Morales Masis, M., Nicolay, S., and Ballif, C. (2014). c-texture versus a-texture low pressure metalorganic chemical vapor deposition ZnO films: Lower resistivity despite smaller grain size. *Thin Solid Films*, 565:1–6.

[Fanni et al., 2015b] Fanni, L., Delaup, B., Niesen, B., Milstein, Y., Shachal, D., Morales-Masis, M., Nicolay, S., and Ballif, C. (2015b). Tuning the porosity of zinc oxide electrodes: from dense to nanopillar films. *Materials Research Express*, 2(7):075006.

[Favier et al., 2011] Favier, A., Muñoz, D., Martín de Nicolás, S., and Ribeyron, P.-J. (2011). Boron-doped zinc oxide layers grown by metal-organic CVD for silicon heterojunction solar cells applications. *Solar Energy Materials and Solar Cells*, 95(4):1057–1061.

[Fox, 2010] Fox, M. (2010). *Optical properties of solids*. Oxford University Press, second edition.

[Fraser and Cook, 1972] Fraser, D. B. and Cook, H. D. (1972). Highly Conductive, Transparent Films of Sputtered In2- x Sn x O 3- y. *Journal of the Electrochemical Society*, 119(10):1368–1374.

[Freeman et al., 2000] Freeman, A. J., Poeppelmeier, K. R., Mason, T. O., Chang, R. P. H., and Marks, T. J. (2000). Chemical and thin-film strategies for new transparent conducting oxides. *MRS Bulletin*, 25(8):45–51.

[Frijnts et al., 2015] Frijnts, T., Kühnapfel, S., Ring, S., Gabriel, O., Calnan, S., Haschke, J., Stannowski, B., Rech, B., and Schlatmann, R. (2015). Analysis of photo-current potentials and losses in thin film crystalline silicon solar cells. *Solar Energy Materials and Solar Cells*, 143:457–466.

[Frontier, 2015] Frontier, S. (2015). Solar Frontier hits 22.3% on CIGS cell: pv-magazine.

[Fujimura et al., 1993] Fujimura, N., Nishihara, T., Goto, S., Xu, J., and Ito, T. (1993). Control of preferred orientation for ZnOx films: control of self-texture. *Journal of Crystal Growth*, 130:269 – 279.

[Fujiwara and Kondo, 2005] Fujiwara, H. and Kondo, M. (2005). Effects of carrier concentration on the dielectric function of ZnO:Ga and In 2 O 3 : Sn studied by spectroscopic ellipsometry: Analysis of free-carrier and band-edge absorption. *Physical Review B*, 71(7).

[Furubayashi et al., 2005] Furubayashi, Y., Hitosugi, T., Yamamoto, Y., Inaba, K., Kinoda, G., Hirose, Y., Shimada, T., and Hasegawa, T. (2005). A transparent metal: Nb-doped anatase TiO[sub 2]. *Applied Physics Letters*, 86(25):252101.

[Garcia-Alonso et al., 2015] Garcia-Alonso, D., Potts, S. E., van Helvoirt, C. A. A., Verheijen, M. A., and Kessels, W. M. M. (2015). Atomic layer deposition of B-doped ZnO using triiso-propyl borate as the boron precursor and comparison with Al-doped ZnO. *J. Mater. Chem. C*, 3(13):3095–3107.

[Garrido et al., 2012] Garrido, S., Kong, X., Gotschke, T., Calarco, R., Geelhaar, L., Trampert, A., and Brandt, O. (2012). Spontaneous Nucleation and Growth of GaN Nanowires: The Fundamental Role of Crystal Polarity. *Nano Letters*, 12(12):6119–6125.

[Gatos and Lavine, 1960] Gatos, H. C. and Lavine, M. C. (1960). Characteristic of the {111} surfaces of the III-V intermetallic compounds. *Journal of Electrochemical Society*, 163(4):427 – 433.

[Gavrilov et al., 2003] Gavrilov, G., Krivchitch, A., and Lebedev, V. (2003). Application of nuclear reaction analysis for aging investigations of detectors. *Nuclear Instruments and Methods in Physics Research Section A: Accelerators, Spectrometers, Detectors and Associated Equipment*, 515(1):108–117.

[Germain et al., 2003] Germain, V., Li, J., Ingert, D., Wang, Z. L., and Pileni, M. P. (2003). Stacking Faults in Formation of Silver Nanodisks. *The Journal of Physical Chemistry B*, 107(34):8717–8720.

[Gerstl et al., 2011] Gerstl, M., Navickas, E., Friedbacher, G., Kubel, F., Ahrens, M., and Fleig, J. (2011). The separation of grain and grain boundary impedance in thin yttria stabilized zirconia (YSZ) layers. *Solid State Ionics*, 185(1):32–41.

[Gerthsen et al., 2002] Gerthsen, D., Litvinov, D., Gruber, T., Kirchner, C., and Waag, A. (2002). Origin and consequences of a high stacking fault density in epitaxial ZnO layers. *Applied Physics Letters*, 81(21):3972.

[Ghandhi et al., 1980] Ghandhi, S. K., Field, R. J., and Shealy, J. R. (1980). Highly oriented zinc oxide films grown by the oxidation of diethylzinc. *Applied Physics Letters*, 37(5):449.

[Ghannam et al., 2015] Ghannam, M., Shehadah, G., Abdulraheem, Y., and Poortmans, J. (2015). On the possible role of the interfacial inversion layer in the improvement of the performance of hydrogenated amorphous silicon/crystalline silicon heterojunction solar cells [HIT]. *Solar Energy Materials and Solar Cells*, 132:320–328.

[Glass, 2013a] Glass, S. (2013a). AF32 Eco Thin Glass.

[Glass, 2013b] Glass, S. (2013b). D263t eco Thin Glass.

[Gordon, 2000] Gordon, R. G. (2000). Criteria for choosing transparent conductors. *MRS bulletin*, 25(08):52–57.

Bibliography

[Green, 2016] Green, M. A. (2016). Commercial progress and challenges for photovoltaics. *Nature Energy*, 1(1):15015.

[Green et al., 2015] Green, M. A., Emery, K., Hishikawa, Y., Warta, W., and Dunlop, E. D. (2015). Solar cell efficiency tables (version 46): Solar cell efficiency tables (version 46). *Progress in Photovoltaics: Research and Applications*, 23(7):805–812.

[Grundmann, 2015] Grundmann, M. (2015). Karl Bädeker (1877-1914) and the discovery of transparent conductive materials: Karl Bädeker. *physica status solidi (a)*, 212(7):1409–1426.

[Hagemark, 1976] Hagemark, K. (1976). Defect structure of Zn-doped ZnO. *Journal of Solid State Chemistry*, 16:293 –299.

[Hagendorfer et al., 2014] Hagendorfer, H., Lienau, K., Nishiwaki, S., Fella, C. M., Kranz, L., Uhl, A. R., Jaeger, D., Luo, L., Gretener, C., Buecheler, S., Romanyuk, Y. E., and Tiwari, A. N. (2014). Highly Transparent and Conductive ZnO: Al Thin Films from a Low Temperature Aqueous Solution Approach. *Advanced Materials*, 26(4):632–636.

[Han and Kim, 1995] Han, J.-H. and Kim, D.-Y. (1995). Analysis of the proportionality constant correlating the mean intercept length to the average grain size. *Acta Metallurgica et Materialia*, 43(8):3185–3188.

[Hanada, 2009] Hanada, T. (2009). *Oxide and nitride semiconductors. Processing, properties and applications*, volume 12 of *Advances in Material Research*.

[Harding, 2006] Harding, F. (2006). *Breast Cancer: Cause - Prevention - Cure*. Tekline Publishing.

[Harris, 1952] Harris, G. (1952). Quantitative measurement of preferred orientation in rolled uranium bars. *Philos. Mag. Ser.*, 7(43):336.

[Harrison, 1954] Harrison, S. E. (1954). Conductivity and Hall effect of ZnO at low temperatures. *Physical review*, 93(1):52.

[Haxel et al., 2005] Haxel, G. B., Hedrick, J. B., and Orris, G. J. (2005). Rare Earth Elements—Critical Resources for High Technology. Technical report, U.S. Geological Survey.

[Herbig et al., 2014] Herbig, M., Raabe, D., Li, Y., Choi, P., Zaefferer, S., and Goto, S. (2014). Atomic-Scale Quantification of Grain Boundary Segregation in Nanocrystalline Material. *Physical Review Letters*, 112(12).

[Hänni et al., 2013] Hänni, S., Alexander, D. T. L., Ding, L., Bugnon, G., Boccard, M., Battaglia, C., Cuony, P., Escarré, J., Parascandolo, G., Nicolay, S., Cantoni, M., Despeisse, M., Meillaud, F., and Ballif, C. (2013). On the Interplay Between Microstructure and Interfaces in High-Efficiency Microcrystalline Silicon Solar Cells. *IEEE Journal of Photovoltaics*, 3(1):11–16.

[Holman et al., 2012] Holman, Z. C., Descoeudres, A., Barraud, L., Fernandez, F. Z., Seif, J. P., De Wolf, S., and Ballif, C. (2012). Current Losses at the Front of Silicon Heterojunction Solar Cells. *IEEE Journal of Photovoltaics*, 2(1):7–15.

[Hongsingthong et al., 2013] Hongsingthong, A., Krajangsang, T., Limmanee, A., Sriprapha, K., Sritharathikhun, J., and Konagai, M. (2013). Development of textured ZnO-coated low-cost glass substrate with very high haze ratio for silicon-based thin film solar cells. *Thin Solid Films*, 537:291–295.

[Hoppe et al., 2013] Hoppe, P., Cohen, S., and Meibom, A. (2013). NanoSIMS: Technical Aspects and Applications in Cosmochemistry and Biological Geochemistry. *Geostandards and Geoanalytical Research*, 37(2):111–154.

[Hosono et al., 1996] Hosono, H., Yamashita, Y., Ueda, N., Kawazoe, H., and Shimidzu, K.-i. (1996). New amorphous semiconductor: 2cdo PbOx. *Applied Physics Letters*, 68(5):661.

[Hu et al., 2013] Hu, Z., Zhang, J., and Zhu, Y. (2013). Inverted polymer solar cells with a boron-doped zinc oxide layer deposited by metal organic chemical vapor deposition. *Solar Energy Materials and Solar Cells*, 117:610–616.

[Humphreys, 2001] Humphreys, F. J. (2001). Review grain and subgrain characterisation by electron backscatter diffraction. *Journal of materials science*, 36(16):3833–3854.

[Ingle et al., 1996] Ingle, N., Theodoropolus, C., Mountziaris, T., Wexler, R., and Smith, F. (1996). Reaction kinetics and transport phenomena underlying the low-pressure metalorganic chemical vapor deposition of GaAs. *Journal of Crystal Growth*, 167(3-4):543–556.

[Ingram et al., 2004] Ingram, B. J., Gonzalez, G. B., Kammler, D. R., Bertoni, M. I., and Mason, T. O. (2004). Chemical and structural factors governing transparent conductivity in oxides. *Journal of Electroceramics*, 13(1-3):167–175.

[Jacobs et al., 1998] Jacobs, H. O., Leuchtmann, P., Homan, O. J., and Stemmer, A. (1998). Resolution and contrast in Kelvin probe force microscopy. *Journal of Applied Physics*, 84(3):1168.

[Janotti and Van de Walle, 2005] Janotti, A. and Van de Walle, C. G. (2005). Oxygen vacancies in ZnO. *Applied Physics Letters*, 87(12):122102.

[Janotti and Van de Walle, 2009] Janotti, A. and Van de Walle, C. G. (2009). Fundamentals of zinc oxide as a semiconductor. *Reports on Progress in Physics*, 72(12):126501.

[Jäger et al., 2015] Jäger, T., Romanyuk, Y. E., Bissig, B., Pianezzi, F., Nishiwaki, S., Reinhard, P., Steinhauser, J., Schwenk, J., and Tiwari, A. N. (2015). Improved open-circuit voltage in Cu(In,Ga)Se2 solar cells with high work function transparent electrodes. *Journal of Applied Physics*, 117(22):225303.

[Jing and Zhan, 2008] Jing, Z. and Zhan, J. (2008). Fabrication and Gas-Sensing Properties of Porous ZnO Nanoplates. *Advanced Materials*, 20(23):4547–4551.

Bibliography

[Jo et al., 2005] Jo, W., Kim, S.-J., and Kim, D.-Y. (2005). Analysis of the etching behavior of ZnO ceramics. *Acta Materialia*, 53(15):4185–4188.

[Kajikawa, 2006] Kajikawa, Y. (2006). Texture development of non-epitaxial polycrystalline ZnO films. *Journal of Crystal Growth*, 289(1):387–394.

[Kajikawa, 2012] Kajikawa, Y. (2012). Conduction model covering non-degenerate through degenerate polycrystalline semiconductors with non-uniform grain-boundary potential heights based on an energy filtering model. *Journal of Applied Physics*, 112(12):123713.

[Kajikawa et al., 2003] Kajikawa, Y., Noda, S., and Komiyama, H. (2003). Comprehensive perspective on the mechanism of preferred orientation in reactive-sputter-deposited nitrides. *Journal of Vacuum Science & Technology A: Vacuum, Surfaces, and Films*, 21(6):1943.

[Kanaya and Okayama, 1972] Kanaya, K. and Okayama, S. (1972). Penetration and energy-loss theory of electrons in solid targets. *Journal of Physics D: Applied Physics*, 5(1):43.

[Karen and Woodward, 1998] Karen, P. and Woodward, P. M. (1998). Liquid-mix disorder in crystalline solids: ScMnO 3. *Journal of Solid State Chemistry*, 141(1):78–88.

[Kato et al., 2004] Kato, H., Sano, M., Miyamoto, K., and Yao, T. (2004). High-quality ZnO epilayers grown on Zn-face ZnO substrates by plasma-assisted molecular beam epitaxy. *Journal of Crystal Growth*, 265(3-4):375–381.

[Kawazoe et al., 1997] Kawazoe, H., Yasukawa, M., Hyodo, H., Kurita, M., Yanagi, H., and Hosono, H. (1997). p-type electrical conduction in transparent thin films of CuAlO2. *Nature*, 389:939 – 942.

[Kihara and Donnay, 1985] Kihara, K. and Donnay, G. (1985). Anharmonic thermal vibrations in ZnO. *Canadian Mineralogist*, 23:647 –654.

[Kim et al., 2000] Kim, H., Gilmore, C. M., Horwitz, J. S., Piqué, A., Murata, H., Kushto, G. P., Schlaf, R., Kafafi, Z. H., and Chrisey, D. B. (2000). Transparent conducting aluminum-doped zinc oxide thin films for organic light-emitting devices. *Applied Physics Letters*, 76(3):259.

[Kim et al., 2011] Kim, W.-H., Maeng, W. J., Kim, M.-K., and Kim, H. (2011). Low pressure chemical vapor deposition of aluminum-doped zinc oxide for transparent conducting electrodes. *Journal of The Electrochemical Society*, 158(8):D495–D499.

[Kim et al., 2008] Kim, W. M., Kim, I. H., Ko, J. H., Cheong, B., Lee, T. S., Lee, K. S., Kim, D., and Seong, T.-Y. (2008). Density-of-state effective mass and non-parabolicity parameter of impurity doped ZnO thin films. *Journal of Physics D: Applied Physics*, 41(19):195409.

[Kinemuchi et al., 2011] Kinemuchi, Y., Nakano, H., Kaga, H., Tanaka, S., Uematsu, K., and Watari, K. (2011). Microstructural Evidence of Hall Mobility Anisotropy in c-Axis Textured Al-Doped ZnO: Microstructural Evidence of Hall Mobility Anisotropy in C-Axis Textured Al-Doped ZnO. *Journal of the American Ceramic Society*, 94(8):2339–2343.

[Kirner et al., 2015] Kirner, S., Hartig, M., Mazzarella, L., Korte, L., Frijnts, T., Scherg-Kurmes, H., Ring, S., Stannowski, B., Rech, B., and Schlatmann, R. (2015). The Influence of ITO Dopant Density on J-V Characteristics of Silicon Heterojunction Solar Cells: Experiments and Simulations. *Energy Procedia*, 77:725–732.

[Klein, 2012] Klein, A. (2012). Transparent Conducting Oxides: Electronic Structure-Property Relationship from Photoelectron Spectroscopy with *in situ* Sample Preparation. *Journal of the American Ceramic Society*, pages n/a–n/a.

[Klingshirn et al., 2010] Klingshirn, C. F., Meyer, B. K., Waag, A., Hoffmann, A., and Gertus, J. (2010). *Zinc Oxide. From Fundamental Properties Towards Novel Applications.* Number 120 in Springer Series in Material Science. Springer-Verlag.

[Kluth et al., 2003] Kluth, O., Schöpe, G., Hüpkes, J., Agashe, C., Müller, J., and Rech, B. (2003). Modified Thornton model for magnetron sputtered zinc oxide: film structure and etching behaviour. *Thin Solid Films*, 442(1-2):80–85.

[Knoops et al., 2015] Knoops, H. C. M., van de Loo, B. W. H., Smit, S., Ponomarev, M. V., Weber, J.-W., Sharma, K., Kessels, W. M. M., and Creatore, M. (2015). Optical modeling of plasma-deposited ZnO films: Electron scattering at different length scales. *Journal of Vacuum Science & Technology A: Vacuum, Surfaces, and Films*, 33(2):021509.

[Kobayashi and Nakada, 2014] Kobayashi, T. and Nakada, T. (2014). Effects of post-deposition treatments on transparent conducting ZnO:B thin films grown by MOCVD. *Japanese Journal of Applied Physics*, 53(5S1):05FA03.

[Koch et al., 1997] Koch, M. H., Hartmann, A. J., Lamb, R. N., Neuber, M., and Grunze, M. (1997). Self-texture in the initial stages of ZnO film growth. *The Journal of Physical Chemistry B*, 101(41):8231–8236.

[Kochubey et al., 2013] Kochubey, D., Kaichev, V., Saraev, A., Tomyn, S., Belov, A., and Voloshin, Y. (2013). Combined X-ray Absorption Near-Edge Structure and X-ray Photoelectron Study of the Electrocatalytically Active Cobalt(I) Cage Complexes and the Clathrochelate Cobalt(II)- and Cobalt(III)-Containing Precursors and Analogs. *The Journal of Physical Chemistry C*, 117(6):2753–2759.

[Kohiki et al., 1994] Kohiki, S., Nishitani, M., and Wada, T. (1994). Enhanced electrical conductivity of zinc oxide thin films by ion implantation of gallium, aluminum, and boron atoms. *Journal of Applied Physics*, 75(4):2069.

[Koida et al., 2016] Koida, T., Nishinaga, J., Higuchi, H., Kurokawa, A., Iioka, M., Kamikawa-Shimizu, Y., Yamada, A., Shibata, H., and Niki, S. (2016). Comparison of ZnO:B and ZnO:Al layers for Cu(In,Ga)Se2 submodules. *Thin Solid Films*.

[Kolmogorov, 1937] Kolmogorov, A. (1937). On the statistical theory of crystallization in metals. *Bull. Acad. Sci. USSR, Phys Ser.*, 3:367 – 368.

Bibliography

[Konar et al., 2011] Konar, A., Fang, T., Sun, N., and Jena, D. (2011). Charged basal stacking fault scattering in nitride semiconductors. *Applied Physics Letters*, 98(2):022109.

[Kontis et al., 2016] Kontis, P., Yusof, H. M., Pedrazzini, S., Danaie, M., Moore, K., Bagot, P., Moody, M., Grovenor, C., and Reed, R. (2016). On the effect of boron on grain boundary character in a new polycrystalline superalloy. *Acta Materialia*, 103:688–699.

[Koren et al., 2010] Koren, E., Berkovitch, N., and Rosenwaks, Y. (2010). Measurement of Active Dopant Distribution and Diffusion in Individual Silicon Nanowires. *Nano Letters*, 10(4):1163–1167.

[Kranz et al., 2015] Kranz, L., Abate, A., Feurer, T., Fu, F., Avancini, E., Löckinger, J., Reinhard, P., Zakeeruddin, S. M., Grätzel, M., Buecheler, S., and Tiwari, A. N. (2015). High-Efficiency Polycrystalline Thin Film Tandem Solar Cells. *The Journal of Physical Chemistry Letters*, 6(14):2676–2681.

[Körber et al., 2010] Körber, C., Suffner, J., and Klein, A. (2010). Surface energy controlled preferential orientation of thin films. *Journal of Physics D: Applied Physics*, 43(5):055301.

[Krc et al., 2010] Krc, J., Lipovsek, B., Bokalic, M., Campa, A., Oyama, T., Kambe, M., Matsui, T., Sai, H., Kondo, M., and Topic, M. (2010). Potential of thin-film silicon solar cells by using high haze TCO superstrates. *Thin Solid Films*, 518(11):3054–3058.

[Krc et al., 2003] Krc, J., Smole, F., and Topič, M. (2003). Potential of light trapping in microcrystalline silicon solar cells with textured substrates. *Progress in Photovoltaics: Research and Applications*, 11:429 – 436.

[Kresse et al., 2003] Kresse, G., Dulub, O., and Diebold, U. (2003). Competing stabilization mechanism for the polar ZnO(0001)-Zn surface. *Physical Review B*, 68(24).

[Kudo et al., 1999] Kudo, A., Yanagi, H., Ueda, K., Hosono, H., Kawazoe, H., and Yano, Y. (1999). Fabrication of transparent p–n heterojunction thin film diodes based entirely on oxide semiconductors. *Applied Physics Letters*, 75(18):2851.

[Kumar and Zhou, 2010] Kumar, A. and Zhou, C. (2010). The Race To Replace Tin-Doped Indium Oxide: Which Material Will Win? *ACS Nano*, 4(1):11–14.

[Kunat et al., 2002] Kunat, M., Gil Girol, S., Becker, T., Burghaus, U., and Wöll, C. (2002). Stability of the polar surfaces of ZnO: A reinvestigation using He-atom scattering. *Physical Review B*, 66(8).

[Kushiya, 2004] Kushiya, K. (2004). Development of Cu(InGa)Se2-based thin-film PV modules with a Zn(O,S,OH)x buffer layer. *Solar Energy*, 77(6):717–724.

[Lau et al., 1980] Lau, C. K., Tiku, S. K., and Lakin, K. M. (1980). Growth of epitaxial ZnO thin films by organometallic chemical vapor deposition. *Journal of The Electrochemical Society*, 127(8):1843–1847.

142

[Lee et al., 1995] Lee, J., Hwang, J.-H., Mashek, J. J., Mason, T. O., Miller, A. E., and Siegel, R. W. (1995). Impedance spectroscopy of grain boundaries in nanophase ZnO. *Journal of materials research*, 10(09):2295–2300.

[Levy et al., 1985] Levy, Y., Jurich, M., and Swalen, J. D. (1985). Optical properties of thin layers of SiOx. *Journal of Applied Physics*, 57(7):2601.

[Lewis and Anderson, 1979] Lewis, B. and Anderson, J. (1979). *Nucleation and Growth of Thin Films*, volume 4. Academic Press, New Yor, San Francisco, London.

[Li et al., 2010] Li, J., Fan, H., and Jia, X. (2010). Multilayered ZnO Nanosheets with 3d Porous Architectures: Synthesis and Gas Sensing Application. *The Journal of Physical Chemistry C*, 114(35):14684–14691.

[Li et al., 2015] Li, J., Li, F., Li, C., Yang, G., Xu, Z., and Zhang, S. (2015). Evidences of grain boundary capacitance effect on the colossal dielectric permittivity in (Nb + In) co-doped TiO2 ceramics. *Scientific Reports*, 5:8295.

[Li et al., 2000] Li, L. K., Jurkovic, M. J., Wang, W. I., Van Hove, J. M., and Chow, P. P. (2000). Surface polarity dependence of Mg doping in GaN grown by molecular-beam epitaxy. *Applied Physics Letters*, 76(13):1740.

[Ligeon and Bontemps, 1972] Ligeon, E. and Bontemps, A. (1972). Nuclear reaction analysis of boron and oxygen in silicon. *Journal of Radioanalytical and Nuclear Chemistry*, 12(2):335–351.

[Littleton, 1938] Littleton, J. T. (1938). Insulator.

[Liu et al., 2002] Liu, J., Lu, X., Wang, X., and Chu, W.-K. (2002). Cross section of 11b(p,a)8be reaction for boron analysis. *Nuclear Instruments and Methods in Physics Research B*, 190:107 – 111.

[Llopis and Tobías, 2005] Llopis, F. and Tobías, I. (2005). Influence of texture feature size on the optical performance of silicon solar cells: texture feature size and optical performance. *Progress in Photovoltaics: Research and Applications*, 13(1):27–36.

[Look et al., 2013] Look, D. C., Leedy, K. D., Kiefer, A., Claflin, B., Itagaki, N., Matsushima, K., and Surhariadi, I. (2013). Model for thickness dependence of mobility and concentration in highly conductive zinc oxide. *Optical Engineering*, 52(3):033801–033801.

[Lounis, 2014] Lounis, S. D. (2014). *The influence of dopant distribution on the optoelectronic properties of tin-doped indium oxide nanocrystals and nanocrystal films*. PhD thesis, University of California, Berkeley.

[Lounis et al., 2014] Lounis, S. D., Runnerstrom, E. L., Bergerud, A., Nordlund, D., and Milliron, D. J. (2014). Influence of Dopant Distribution on the Plasmonic Properties of Indium Tin Oxide Nanocrystals. *Journal of the American Chemical Society*, 136(19):7110–7116.

143

Bibliography

[Luque and Hegedus, 2003] Luque, A. and Hegedus, S. (2003). *Photovoltaic Science and Engineering*. John Wiley and Sons, Chichester, UK.

[Macco et al., 2015] Macco, B., Knoops, H. C. M., and Kessels, W. M. M. (2015). Electron Scattering and Doping Mechanisms in Solid-Phase-Crystallized In_2O_3:H Prepared by Atomic Layer Deposition. *ACS Applied Materials & Interfaces*, 7(30):16723–16729.

[Macco et al., 2014] Macco, B., Wu, Y., Vanhemel, D., and Kessels, W. M. M. (2014). High mobility In_2O_3:H transparent conductive oxides prepared by atomic layer deposition and solid phase crystallization: High mobility In_2O_3:H transparent conductive oxides prepared by atomic layer deposition and solid phase crystallization. *physica status solidi (RRL) - Rapid Research Letters*, 8(12):987–990.

[Maejima et al., 2014] Maejima, K., Koida, T., Sai, H., Matsui, T., Saito, K., Kondo, M., and Takagawa, T. (2014). Influences of deposition temperature on characteristics of B-doped ZnO films deposited by metal–organic chemical vapor deposition. *Thin Solid Films*, 559:83–87.

[Mahmood and Park, 2013] Mahmood, K. and Park, S. B. (2013). Highly efficient dye-sensitized solar cell with an electrostatic spray deposited upright-standing boron-doped ZnO (BZO) nanoporous nanosheet-based photoanode. *Journal of Materials Chemistry A*, 1(15):4826.

[Major et al., 1986] Major, S., Banerjee, A., and Chopra, K. L. (1986). Electrical and optical transport in undoped and indium-doped zinc oxide films. *Journal of Materials Research*, 1(02):300–310.

[Makino et al., 2001] Makino, T., Segawa, Y., Kawasaki, M., Ohtomo, A., Shiroki, R., Tamura, K., Yasuda, T., and Koinuma, H. (2001). Band gap engineering based on MgZnO and CdZnO ternary alloy films. *Applied Physics Letters*, 78(9):1237.

[Mang et al., 1995] Mang, A., Reimann, K., and Rübenacke, S. (1995). Band gaps, crystal-field splitting, spin-orbit coupling, and exciton binding energies in ZnO under hydrostatic pressure. *Solid State Communications*, 94(4):251 –254.

[Manley et al., 2014] Manley, P., Yin, G., and Schmid, M. (2014). A method for calculating the complex refractive index of inhomogeneous thin films. *Journal of Physics D: Applied Physics*, 47(20):205301.

[Mao et al., 2016] Mao, C., Fang, L., Zhang, H., Li, W., Wu, F., Qin, G., Ruan, H., and Kong, C. (2016). Effect of B doping on optical, electrical properties and defects of ZnO films. *Journal of Alloys and Compounds*, 676:135–141.

[Mar et al., 1995] Mar, G. L., Timbrell, P. Y., and Lamb, R. N. (1995). Factors influencing the chemical vapor deposition of oriented ZnO films using zinc acetate. *Chemistry of materials*, 7(10):1890–1896.

144

[Maragliano et al., 2014] Maragliano, C., Lilliu, S., Dahlem, M. S., Chiesa, M., Souier, T., and Stefancich, M. (2014). Quantifying charge carrier concentration in ZnO thin films by Scanning Kelvin Probe Microscopy. *Scientific Reports*, 4.

[Mariano and Hanneman, 1963] Mariano, A. N. and Hanneman, R. E. (1963). Crystallographic Polarity of ZnO Crystals. *Journal of Applied Physics*, 34(2):384.

[Martin De Nicolas, 2012] Martin De Nicolas, S. (2012). *a-Si:H/c-Si heterojunction solar cells: back side assessment and improvement.* PhD thesis, Université Paris Sud.

[Martinez and Piqueras, 1979] Martinez, J. and Piqueras, J. (1979). On the mobility of poly-crystalline semiconductors. *Solid State Electronics*, 23:297 – 303.

[Masetti et al., 1983] Masetti, G., Severi, M., and Solmi, S. (1983). Modeling of carrier mobility against carrier concentration in arsenic-, phosphorus-, and boron-doped silicon. *IEEE Transactions on electronic devices*, 30(7):764 –769.

[Matos, 2006] Matos, G. R. (2006). Effects of regulation and technology on end uses of nonfuel mineral commodities in the United States. Technical Report 2006-5194, U.S. Geological Survey.

[Matsuoka, 1971] Matsuoka, M. (1971). Nonohmic properties of zinc oxide ceramics. *Japanese Journal of Applied Physics*, 10(6):736 – 746.

[Matthiessen and Vogt, 1864] Matthiessen, A. and Vogt, C. (1864). On the influence of temperature on the electric conducting-power of alloys. *Philosophical Transactions of the Royal Society of London*, 83:167 – 200.

[McNutt, 2013] McNutt, M. K. (2013). Metal Prices in the United States Through 2010. Technical report, U.S. Geological Survey, Reston, Virginia.

[Melitz et al., 2011] Melitz, W., Shen, J., Kummel, A. C., and Lee, S. (2011). Kelvin probe force microscopy and its application. *Surface Science Reports*, 66(1):1–27.

[Melitz et al., 2010] Melitz, W., Shen, J., Lee, S., Lee, J. S., Kummel, A. C., Droopad, R., and Yu, E. T. (2010). Scanning tunneling spectroscopy and Kelvin probe force microscopy investigation of Fermi energy level pinning mechanism on InAs and InGaAs clean surfaces. *Journal of Applied Physics*, 108(2):023711.

[Messerschmidt et al., 2014] Messerschmidt, D., Bratz, K., Gnehr, W.-M., Romanus, H., Eber-hardt, J., Nicolay, S., and Ballif, C. (2014). Optical properties of anodically degraded ZnO. *Journal of Applied Physics*, 115(9):094902.

[Meyer, 2004] Meyer, B. (2004). First-principles study of the polar O-terminated ZnO surface in thermodynamic equilibrium with oxygen and hydrogen. *Physical Review B*, 69(4).

Bibliography

[Miao et al., 2006] Miao, W.-n., Li, X.-f., Zhang, Q., Huang, L., Zhang, Z.-j., Zhang, L., and Yan, X.-j. (2006). Transparent conductive In2o3:Mo thin films prepared by reactive direct current magnetron sputtering at room temperature. *Thin Solid Films*, 500(1-2):70–73.

[Minami, 2000] Minami, T. (2000). New n-type transparent conducting oxides. *Mrs Bulletin*, 25(08):38–44.

[Minami, 2005] Minami, T. (2005). Transparent conducting oxide semiconductors for transparent electrodes. *Semiconductor Science and Technology*, 20(4):S35–S44.

[Minami et al., 1985] Minami, T., Sato, H., Nanto, H., and Takata, S. (1985). Group III Impurity Doped Zinc Oxide THin Fimls Prepared by RF Magnetron Sputtering. *Japanese Journal of Applied Physics*, 24(10):L781 – L784.

[Minami et al., 1995] Minami, T., Sonohara, H., Kakumu, T., and Takata, S. (1995). Highly transparent and conductive Zn2in2o5 thin films prepared by magnetron sputtering. *Japanese Journal of Applied Physics*, 34(8A):L971 –L974.

[Mirica et al., 2004] Mirica, E., Kowach, G., Evans, P., and Du, H. (2004). Morphological Evolution of ZnO Thin Films Deposited by Reactive Sputtering. *Crystal Growth & Design*, 4(1):147–156.

[Morales-Masis et al., 2015] Morales-Masis, M., Martin De Nicolas, S., Holovsky, J., De Wolf, S., and Ballif, C. (2015). Low-Temperature High-Mobility Amorphous IZO for Silicon Heterojunction Solar Cells. *IEEE Journal of Photovoltaics*, 5(5):1340–1347.

[Morkoç and Özgür, 2009] Morkoç, H. and Özgür, m. (2009). *Zinc oxide: fundamentals, materials and device technology*. Electrical and Electronics Engineering. Wiley-VCH.

[Morosanu, 1990] Morosanu, C. (1990). *Thin Films by Chemical Vapour Deposition*. Number 7 in Thin Film Science and Technology. Elsevier.

[Moulin et al., 2013] Moulin, E., Paetzold, U., Bittkau, K., Ermes, M., Ding, L., Fanni, L., Nicolay, S., Kirchhoff, J., Weigand, D., Bauer, A., Lambertz, A., Ballif, C., and Carius, R. (2013). Thin-film silicon solar cells applying optically decoupled back reflectors. *Materials Science and Engineering: B*, 178(9):645–650.

[Moutinho, 1995] Moutinho, H. R. (1995). Investigation of polycrystalline CdTe thin films deposited by physical vapor deposition, close-spaced sublimation, and sputtering. *Journal of Vacuum Science & Technology A: Vacuum, Surfaces, and Films*, 13(6):2877.

[Myong et al., 2007] Myong, S., Steinhauser, J., Schluchter, R., Fay, S., Vallatsauvain, E., Shah, A., Ballif, C., and Rufenacht, A. (2007). Temperature dependence of the conductivity in large-grained boron-doped ZnO films. *Solar Energy Materials and Solar Cells*, 91(14):1269–1274.

146

[Nanto et al., 1984] Nanto, H., Minami, T., Shooji, S., and Takata, S. (1984). Electrical and optical properties of zinc oxide thin films prepared by rf magnetron sputtering for transparent electrode applications. *Journal of Applied Physics*, 55(4):1029.

[Nečas and Klapetek, 2012] Nečas, D. and Klapetek, P. (2012). Gwyddion: an open-source software for SPM data analysis. *Open Physics*, 10(1).

[Nicolay et al., 2012] Nicolay, S., Benkhaira, M., Ding, L., Escarre, J., Bugnon, G., Meillaud, F., and Ballif, C. (2012). Control of CVD-deposited ZnO films properties through water/DEZ ratio: Decoupling of electrode morphology and electrical characteristics. *Solar Energy Materials and Solar Cells*, 105:46–52.

[Nicolay et al., 2009] Nicolay, S., Faÿ, S., and Ballif, C. (2009). Growth Model of MOCVD Polycrystalline ZnO. *Crystal Growth & Design*, 9(11):4957–4962.

[Nilsson et al., 2011] Nilsson, A., Jonsson, A., Jonsson, J., and Roos, A. (2011). Method for more accurate transmittance measurements of low-angle scattering samples using an integrating sphere with an entry port beam diffuser. *Applied Optics*, 50(7):999–1006.

[Nomoto et al., 2011] Nomoto, J.-i., Miyata, T., and Minami, T. (2011). Optical and electrical properties of transparent conducting B-doped ZnO thin films prepared by various deposition methods. *Journal of Vacuum Science & Technology A: Vacuum, Surfaces, and Films*, 29(4):041504.

[Nonnenmacher et al., 1991] Nonnenmacher, M., O'Boyle, M. P., and Wickramasinghe, H. K. (1991). Kelvin probe force microscopy. *Applied Physics Letters*, 58(25):2921.

[Norris and Watson, 2007] Norris, S. A. and Watson, S. J. (2007). Geometric simulation and surface statistics of coarsening faceted surfaces. *Acta Materialia*, 55(19):6444–6452.

[Oda et al., 1985] Oda, S., Tokunaga, H., Kitajima, N., Hanna, J.-i., Shimizu, I., and Kokado, H. (1985). Highly oriented ZnO films prepared by MOCVD from diethylzinc and alcohols. *Japanese Journal of Applied Physics*, 24(12):1607 – 1610.

[Ogino et al., 2014] Ogino, T., Williams, J. R., Watanabe, K., Sakaguchi, I., Hishita, S., Haneda, H., Adachi, Y., Ohgaki, T., and Ohashi, N. (2014). Effect of crystalline polarity on microstructure and optoelectronic properties of gallium-doped zinc oxide films deposited onto glass substrates. *Thin Solid Films*, 552:56–61.

[Oh et al., 2007] Oh, B.-Y., Jeong, M.-C., and Myoung, J.-M. (2007). Stabilization in electrical characteristics of hydrogen-annealed ZnO:Al films. *Applied Surface Science*, 253(17):7157–7161.

[Ohring, 2002a] Ohring, M. (2002a). Chapter 2 - Vacuum science and technology. In Ohring, M., editor, *Materials Science of Thin Films (Second Edition)*, pages 57–93. Academic Press, San Diego.

Bibliography

[Ohring, 2002b] Ohring, M. (2002b). Chapter 6 - Chemical vapor deposition. In Ohring, M., editor, *Materials Science of Thin Films (Second Edition)*, pages 277–355. Academic Press, San Diego.

[Ohtomo et al., 1998] Ohtomo, A., Kawasaki, M., Koida, T., Masubuchi, K., Koinuma, H., Sakurai, Y., Yoshida, Y., Yasuda, T., and Segawa, Y. (1998). MgZnO as a II VI widegap semiconductor alloy. *Applied Physics Letters*, 72(19):2466.

[Oleson, 2008] Oleson, J. P. (2008). *The Oxford Handbook of Engineering and Technology in the Classical World*. Oxford University Press.

[Ophus et al., 2010a] Ophus, C., Ewalds, T., Luber, E. J., and Mitlin, D. (2010a). The role of self-shadowing on growth and scaling laws of faceted polycrystalline thin films. *Acta Materialia*, 58(15):5150–5159.

[Ophus et al., 2009] Ophus, C., Luber, E., and Mitlin, D. (2009). Simulations of faceted polycrystalline thin films: Asymptotic analysis. *Acta Materialia*, 57(5):1327–1336.

[Ophus et al., 2010b] Ophus, C., Luber, E. J., and Mitlin, D. (2010b). Analytic description of competitive grain growth. *Physical Review E*, 81(1).

[Oriel, 2000] Oriel (2000). FTIR Spectroscopy.

[Orita et al., 2001] Orita, M., Ohta, H., Hirano, M., Narushima, S., and Hosono, H. (2001). Amorphous transparent conductive oxide InGaO3 ZnO: a Zn4s conductor. *Philosophical Magazine Part B*, 81(5):501–515.

[Orton and Powell, 1980] Orton, J. W. and Powell, M. J. (1980). The Hall effect in polycrystalline and powdered semiconductors. *Rep. Prog. Phys.*, 43:1263.

[Pan et al., 2006] Pan, M., Fenwick, W., Strassburg, M., Li, N., Kang, H., Kane, M., Asghar, A., Gupta, S., Varatharajan, R., Nause, J., El-Zein, N., Fabiano, P., Steiner, T., and Ferguson, I. (2006). Metal-organic chemical vapor deposition of ZnO. *Journal of Crystal Growth*, 287(2):688–693.

[Panasonic, 2014] Panasonic (2014). Panasonic HIT(R) Solar Cell Achieves World's Highest Energy Conversion Efficiency of 25.6% at Research Level | Panasonic Key Technologies | Panasonic Newsroom Global.

[Park et al., 2011] Park, S. M., Gu, G. H., and Park, C. G. (2011). Effects of Mg doping to optimize properties ZnO:Al for the transparent conductive oxide (TCO). *physica status solidi (a)*, 208(11):2688–2691.

[Patterson, 1939] Patterson, A. (1939). The Scherrer Formula for X-Ray Particle Size Determination. *Physical Review*, 56:978.

148

[Pawar et al., 2005] Pawar, B., Jadkar, S., and Takwale, M. (2005). Deposition and characterization of transparent and conductive sprayed ZnO:B thin films. *Journal of Physics and Chemistry of Solids*, 66(10):1779–1782.

[Perea et al., 2009] Perea, D. E., Hemesath, E. R., Schwalbach, E. J., Lensch-Falk, J. L., Voorhees, P. W., and Lauhon, L. J. (2009). Direct measurement of dopant distribution in an individual vapour–liquid–solid nanowire. *Nature Nanotechnology*, 4(5):315–319.

[Petersen et al., 2008] Petersen, D. H., Hansen, O., Lin, R., and Nielsen, P. F. (2008). Micro-four-point probe Hall effect measurement method. *Journal of Applied Physics*, 104(1):013710.

[Petritz, 1956] Petritz, R. L. (1956). Theory of photoconductivity in semiconductor films. *Physical Review*, 104(6):1508 – 1516.

[Pisarkiewicz et al., 1989] Pisarkiewicz, T., Zakrzewska, K., and Leja, E. (1989). Scattering of charge carriers in transparent and conducting thin oxide films with a non-parabolic conduction band. *Thin Solid Films*, 174(1):217 – 233.

[Polley and Carter, 2001] Polley, T. A. and Carter, W. B. (2001). Zone model for zinc oxide deposited by combustion chemical vapor deposition. *Thin Solid Films*, 384(2):177–184.

[Preissler et al., 2013] Preissler, N., Bierwagen, O., Ramu, A. T., and Speck, J. S. (2013). Electrical transport, electrothermal transport, and effective electron mass in single-crystalline In 2 O 3 films. *Physical Review B*, 88(8).

[Prunici et al., 2013] Prunici, P., Hamelmann, F. U., Beyer, W., Kurz, H., and Stiebig, H. (2013). Modelling of infrared optical constants for polycrystalline low pressure chemical vapour deposition ZnO:B films. *Journal of Applied Physics*, 113(12):123104.

[Pung et al., 2008] Pung, S.-Y., Choy, K.-L., Hou, X., and Shan, C. (2008). Preferential growth of ZnO thin films by the atomic layer deposition technique. *Nanotechnology*, 19(43):435609.

[Python et al., 2009] Python, M., Madani, O., Dominé, D., Meillaud, F., Vallat-Sauvain, E., and Ballif, C. (2009). Influence of the substrate geometrical parameters on microcrystalline silicon growth for thin-film solar cells. *Solar Energy Materials and Solar Cells*, 93(10):1714–1720.

[Rauch and Dupuy, 2005] Rauch, E. F. and Dupuy, L. (2005). Rapid spot diffraction patterns identification through template matching. *Archives of Metallurgy and Materials*, 50(1):87 – 99.

[Rauch et al., 2008] Rauch, E. F., Véron, M., Portillo, J., Bultreys, D., Maniette, Y., and Nicolopoulos, S. (2008). Automatic crystal orientation and phase mapping in TEM by precession diffraction. *Microscopy and Analysis-UK*, (128):S5 –S8.

[Reibold et al., 2006] Reibold, M., Paufler, P., Levin, A. A., Kochmann, W., Pätzke, N., and Meyer, D. C. (2006). Materials: Carbon nanotubes in an ancient Damascus sabre. *Nature*, 444(7117):286–286.

Bibliography

[Reichelt, 1988] Reichelt, K. (1988). Nucleation and growth of thin films. *Vacuum*, 38(12):1083–1099.

[Rey et al., 2013] Rey, G., Ternon, C., Modreanu, M., Mescot, X., Consonni, V., and Bellet, D. (2013). Electron scattering mechanisms in fluorine-doped SnO2 thin films. *Journal of Applied Physics*, 114(18):183713.

[Reynolds et al., 1999] Reynolds, D. C., Look, D. C., Jogai, B., Litton, C. W., Cantwell, G., and Harsch, W. C. (1999). Valence-band ordering in ZnO. *Physical Review B*, 60(4):2340.

[Riihelä et al., 1996] Riihelä, D., Ritala, M., Matero, R., Leskelä, M., Jokinen, J., and Haussalo, P. (1996). Low temperature deposition of ain films by an alternate supply of trimethyl aluminum and ammonia. *Chemical Vapor Deposition*, 2(6):277–283.

[Rößler et al., 2013] Rößler, R., Leendertz, C., Korte, L., Mingirulli, N., and Rech, B. (2013). Impact of the transparent conductive oxide work function on injection-dependent a-Si:H/c-Si band bending and solar cell parameters. *Journal of Applied Physics*, 113(14):144513.

[Rodnyi and Khodyuk, 2011] Rodnyi, P. A. and Khodyuk, I. V. (2011). Optical and luminescence properties of zinc oxide (Review). *Optics and Spectroscopy*, 111(5):776–785.

[Roth, 1981] Roth, A. P. (1981). Properties of zinc oxide films prepared by the oxidation of diethyl zinc. *Journal of Applied Physics*, 52(11):6685 – 6692.

[Sagalowicz and Fox, 1999] Sagalowicz, L. and Fox, G. R. (1999). Planar defects in ZnO thin films deposited on optical fibers and flat substrates. *Journal of materials research*, 14(05):1876–1885.

[Schirone et al., 1997] Schirone, L., Sotgiu, G., and Califano, F. P. (1997). Chemically etched porous silicon as an anti-reflection coating for high efficiency solar cells. *Thin Solid Films*, 297(1):296–298.

[SchottGlass, 2012] SchottGlass (2012). Borosilicate glass, borofloat 33.

[Schreuder, 2014] Schreuder, N. (2014). Glass windows for energy efficient buildings.

[Schuttauf et al., 2014] Schuttauf, J.-W., Bugnon, G., Stuckelberger, M., Hanni, S., Boccard, M., Despeisse, M., Haug, F.-J., Meillaud, F., and Ballif, C. (2014). Thin-Film Silicon Triple-Junction Solar Cells on Highly Transparent Front Electrodes With Stabilized Efficiencies up to 12.8&#x0025;. *IEEE Journal of Photovoltaics*, 4(3):757–762.

[Seel et al., 2000] Seel, S. C., Thompson, C. V., Hearne, S. J., and Floro, J. A. (2000). Tensile stress evolution during deposition of Volmer–Weber thin films. *Journal of Applied Physics*, 88(12):7079.

[Seto, 1975] Seto, J. Y. W. (1975). The electrical properties of polycrystalline silicon films. *Journal of Applied Physics*, 46(12):5247.

150

[Shah et al., 1999] Shah, A., Torres, P., Tscharner, R., Wyrsch, N., and Keppner, H. (1999). Photovoltaic Technology: The Case for Thin-Film Solar Cells. *Science*, 285(5428):692–698.

[Shealy et al., 1981] Shealy, J. R., Baliga, B. J., Field, R. J., and Ghandhi, S. K. (1981). Preparation and Properties of Zinc Oxide Films Grown by the Oxidation of Diethylzinc. *Journal of The Electrochemical Society*, 128(3):558–561.

[Shinada et al., 2005] Shinada, T., Okamoto, S., Kobayashi, T., and Ohdomari, I. (2005). Enhancing semiconductor device performance using ordered dopant arrays. *Nature*, 437(7062):1128–1131.

[Simmons, 1963] Simmons, J. G. (1963). Generalized Formula for the Electric Tunnel Effect between Similar Electrodes Separated by a Thin Insulating Film. *Journal of Applied Physics*, 34(6):1793.

[Simpson and Cordaro, 1988] Simpson, J. C. and Cordaro, J. F. (1988). Characterization of deep levels in zinc oxide. *Journal of Applied Physics*, 63(5):1781.

[Singh et al., 2001] Singh, A. V., Mehra, R. M., Buthrath, N., Wakahara, A., and Yoshida, A. (2001). Highly conductive and transparent aluminum-doped zinc oxide thin films prepared by pulsed laser deposition in oxygen ambient. *Journal of Applied Physics*, 90(11):5661.

[Singh et al., 2008] Singh, S., Ganguli, T., Kumar, R., Srinivasa, R., and Major, S. (2008). Substrate temperature dependence of growth mode, microstructure and optical properties of highly oriented zinc oxide films deposited by reactive sputtering. *Thin Solid Films*, 517(2):661–669.

[Sinton and Cuevas, 1996] Sinton, R. A. and Cuevas, A. (1996). Contactless determination of current–voltage characteristics and minority-carrier lifetimes in semiconductors from quasi-steady-state photoconductance data. *Applied Physics Letters*, 69(17):2510.

[Smereka et al., 2005] Smereka, P., Li, X., Russo, G., and Srolovitz, D. (2005). Simulation of faceted film growth in three dimensions: microstructure, morphology and texture. *Acta Materialia*, 53(4):1191–1204.

[Smith and Schlegel, 2003] Smith, S. M. and Schlegel, H. B. (2003). Molecular Orbital Studies of Zinc Oxide Chemical Vapor Deposition: Gas-Phase Hydrolysis of Diethyl Zinc, Elimination Reactions, and Formation of Dimers and Tetramers. *Chemistry of Materials*, 15(1):162–166.

[Sommerhalter et al., 2000] Sommerhalter, C., Glatzel, T., Matthes, T., Jäger-Waldau, A., and Lux-Steiner, M. (2000). Kelvin probe force microscopy in ultra high vacuum using amplitude modulation detection of the electrostatic forces. *Applied Surface Science*, 157:263 – 268.

[Spaepen, 2000] Spaepen, F. (2000). Interfaces and stresses in thin films. *Acta Materialia*, 48(1):31–42.

[Stannowski et al., 2013] Stannowski, B., Gabriel, O., Calnan, S., Frijnts, T., Heidelberg, A., Neubert, S., Kirner, S., Ring, S., Zelt, M., Rau, B., Zollondz, J.-H., Bloess, H., Schlatmann, R., and Rech, B. (2013). Achievements and challenges in thin film silicon module production. *Solar Energy Materials and Solar Cells*, 119:196–203.

[Steinhauser, 2008] Steinhauser, J. (2008). *Low pressure chemical vapour deposited Zinc Oxide for thin film silicon solar cells. Optical and electrical properties.* PhD Thesis, University of Neuchâtel.

[Steinhauser et al., 2007] Steinhauser, J., Faÿ, S., Oliveira, N., Vallat-Sauvain, E., and Ballif, C. (2007). Transition between grain boundary and intragrain scattering transport mechanisms in boron-doped zinc oxide thin films. *Applied Physics Letters*, 90(14):142107.

[Suresh et al., 1991] Suresh, P. R., Ramkumar, K., and Satyam, M. (1991). Capacitance-voltage characteristics of grain boundaries in cast polycrystalline silicon. *Journal of Applied Physics*, 69(12):8217.

[Tabuchi et al., 1993] Tabuchi, K., Wenas, W. W., Yamada, A., Konagai, M., and Takahashi, K. (1993). Optimization of ZnO films for amorphous silicon solar cells. *Jpn. J. Appl. Phys.*, 32:3764 – 3769.

[Tasker, 1979] Tasker, P. W. (1979). The stability of ionic crystal surfaces. *Journal of Physics C: Solid State Physics*, 12(22):4977.

[TELSolar, 2014] TELSolar (2014). Press release, July 9th, 2014.

[Thijssen et al., 1992] Thijssen, J. M., Knops, H. J. F., and Dammers, A. J. (1992). Dynamic scaling in polycrystalline growth. *Physical Review B*, 45(15):8650.

[Thompson, 2000] Thompson, C. V. (2000). Structure evolution during processing of polycrystalline films. *Annual review of materials science*, 30(1):159–190.

[Thompson and Carel, 1996] Thompson, C. V. and Carel, R. (1996). Stress and grain growth in thin films. *J. Mech. Phys. Solids*, 44(5):657 – 673.

[Thornton, 1977] Thornton, J. A. (1977). High rate thick film growth. *Annual review of materials science*, 7(1):239–260.

[Tomasi et al., 2014] Tomasi, A., Paviet-Salomon, B., Lachenal, D., Martin de Nicolas, S., Descoeudres, A., Geissbuhler, J., De Wolf, S., and Ballif, C. (2014). Back-Contacted Silicon Heterojunction Solar Cells With Efficiency largere than 21%. *IEEE Journal of Photovoltaics*, 4(4):1046–1054.

[Tomasi et al., 2016] Tomasi, A., Sahli, F., Seif, J. P., Fanni, L., de Nicolas Agut, S. M., Geissbuhler, J., Paviet-Salomon, B., Nicolay, S., Barraud, L., Niesen, B., De Wolf, S., and Ballif, C. (2016). Transparent Electrodes in Silicon Heterojunction Solar Cells: Influence on Contact Passivation. *IEEE Journal of Photovoltaics*, 6(1):17–27.

[Tuna et al., 2010] Tuna, O., Selamet, Y., Aygun, G., and Ozyuzer, L. (2010). High quality ITO thin films grown by dc and RF sputtering without oxygen. *Journal of Physics D: Applied Physics*, 43(5):055402.

[Tyagi and Van Overstraeten, 1983] Tyagi, M. S. and Van Overstraeten, R. (1983). Minority carrier recombination in heavily-doped silicon. *Solid-State Electronics*, 26(6):577–597.

[Van de Walle, 2000] Van de Walle, C. G. (2000). Hydrogen as a cause of doping in zinc oxide. *Physical Review Letters*, 85(5):1012.

[van der Drift, 1967] van der Drift, A. (1967). Evolutionary selection, a principle governing growth orientation in vapour-deposited layers. *Philips Research Reports*, 22:267–288.

[van der Pauw, 1958] van der Pauw, L. (1958). A method of measuring specific resistivity and Hall effect of discs of arbitrary shape. *Philips Research Reports*, 13:1–9.

[Varache et al., 2015] Varache, R., Leendertz, C., Gueunier-Farret, M., Haschke, J., Muñoz, D., and Korte, L. (2015). Investigation of selective junctions using a newly developed tunnel current model for solar cell applications. *Solar Energy Materials and Solar Cells*, 141:14–23.

[Verghese and Clarke, 1999] Verghese, P. M. and Clarke, D. R. (1999). Surface textured zinc oxide films. *Journal of materials research*, 14(03):1039–1045.

[Völz, 2006] Völz, H. G. (2006). *Ullmann's Encyclopdia of Industrial Chemistry*. Wiley-VCH.

[Volger, 1950] Volger, J. (1950). Note on the Hall potential across an inhomogeneous conductor. *Physical Review*, 79(6):1023.

[Vossen, 1976] Vossen, J. (1976). *Physics of Thin Films*, volume 9. Academic Press, New York.

[Wan et al., 2004] Wan, Q., Li, Q. H., Chen, Y. J., Wang, T. H., He, X. L., Li, J. P., and Lin, C. L. (2004). Fabrication and ethanol sensing characteristics of ZnO nanowire gas sensors. *Applied Physics Letters*, 84(18):3654.

[Wang et al., 2012] Wang, J., Wang, Z., Huang, B., Ma, Y., Liu, Y., Qin, X., Zhang, X., and Dai, Y. (2012). Oxygen Vacancy Induced Band-Gap Narrowing and Enhanced Visible Light Photocatalytic Activity of ZnO. *ACS Applied Materials & Interfaces*, 4(8):4024–4030.

[Wang et al., 2006] Wang, L., Yang, Y., Jin, S., and Marks, T. J. (2006). MgO(100) template layer for CdO thin film growth: Strategies to enhance microstructural crystallinity and charge carrier mobility. *Applied Physics Letters*, 88(16):162115.

[Wang et al., 2015] Wang, M., Jiang, L., Wang, Y., Kim, E. J., and Hahn, S. H. (2015). Growth Mechanism of Preferred Crystallite Orientation in Transparent Conducting ZnO:In Thin Films. *Journal of the American Ceramic Society*, pages 1–7.

[Wang et al., 1996] Wang, R., King, L. L., and Sleight, A. W. (1996). Highly conducting transparent thin films based on zinc oxide. *Journal of materials research*, 11(07):1659–1664.

Bibliography

[Wang et al., 2014] Wang, Y., Zhu, J., and Tang, W. (2014). Extracting the effective mass of electrons in transparent conductive oxide thin films using Seebeck coefficient. *Applied Physics Letters*, 104(21):212103.

[Wang et al., 2003] Wang, Z. L., Kong, X. Y., and Zuo, J. M. (2003). Induced Growth of Asymmetric Nanocantilever Arrays on Polar Surfaces. *Physical Review Letters*, 91(18).

[Wasa and Hayakawa, 1971] Wasa, K. and Hayakawa, S. (1971). Electrical and optical properties of sputtered n-p ZnO-Si heterojunctions. *Japanese Journal of Applied Physics*, 10(12):1732.

[Watanabe et al., 2004] Watanabe, H., Yamada, N., and Okaji, M. (2004). Linear thermal expansion coefficient of silicon from 293 to 1000 K. *International journal of thermophysics*, 25(1):221–236.

[Weiss and Shapiro, 1953] Weiss, H. G. and Shapiro, I. (1953). Mechanism of the Hydrolysis of Diborane in the Vapor Phase1. *Journal of the American Chemical Society*, 75(5):1221–1224.

[Wenas et al., 1991a] Wenas, W. W., Yamada, A., Konagai, M., and Takahashi, K. (1991a). Textured ZnO Thin Films for Solar Cells Grown by Metalorganic Chemical Vapor Deposition. *Japanese Journal of Applied Physics*, 30:L441.

[Wenas et al., 1991b] Wenas, W. W., Yamada, A., Takahashi, K., Yoshino, M., and Konagai, M. (1991b). Electrical and optical properties of boron-doped ZnO thin films for solar cells grown by metalorganic chemical vapor deposition. *Journal of Applied Physics*, 70(11):7119 –7123.

[Wiberg and Holleman, 2001] Wiberg, N. and Holleman, A. (2001). *Inorganic Chemistry*. Academic Press.

[Williams et al., 2013] Williams, J. R., Furukawa, H., Adachi, Y., Grachev, S., Sondergard, E., and Ohashi, N. (2013). Polarity control of intrinsic ZnO films using substrate bias. *Applied Physics Letters*, 103(4):042107.

[Wulff, 1895] Wulff, Yuri, G. (1895). *On the question of the velocity of growth and dissolution of crystal faces.* Master Thesis, Warsaw University, Warsaw.

[Yamada et al., 2010] Yamada, T., Makino, H., Yamamoto, N., and Yamamoto, T. (2010). In-grain and grain boundary scattering effects on electron mobility of transparent conducting polycrystalline Ga-doped ZnO films. *Journal of Applied Physics*, 107(12):123534.

[Yamada et al., 2007] Yamada, T., Miyake, A., Kishimoto, S., Makino, H., Yamamoto, N., and Yamamoto, T. (2007). Low resistivity Ga-doped ZnO thin films of less than 100 nm thickness prepared by ion plating with direct current arc discharge. *Applied Physics Letters*, 91(5):051915.

[Yan et al., 2004] Yan, Y., Dalpian, G. M., Al-Jassim, M. M., and Wei, S.-H. (2004). Energetics and electronic structure of stacking faults in ZnO. *Physical Review B*, 70(19).

154

[Yasukawa et al., 1995] Yasukawa, M., Hosono, H., Ueda, N., and Kawazoe, H. (1995). Novel transparent and electroconductive amorphous semiconductor: amorphous AgSbO3 film. *Japanese Journal of Applied Physics*, 34(3A):L281 – L284.

[Yoldas and Partlow, 1985] Yoldas, B. and Partlow, P. (1985). Formation of broad band ARC on fused silica for high power laser applications. *Thin Solid Films*, 129:1–14.

[Young et al., 2000] Young, D. L., Coutts, T. J., Kaydanov, V. I., Gilmore, A. S., and Mulligan, W. P. (2000). Direct measurement of density-of-states effective mass and scattering parameter in transparent conducting oxides using second-order transport phenomena. *Journal of Vacuum Science & Technology A: Vacuum, Surfaces, and Films*, 18(6):2978.

[Zerweck et al., 2005] Zerweck, U., Loppacher, C., Otto, T., Grafström, S., and Eng, L. M. (2005). Accuracy and resolution limits of Kelvin probe force microscopy. *Physical Review B*, 71(12).

[Zhang and Ma, 1996] Zhang, D. and Ma, H. (1996). Scattering mechanisms of charge carriers in transparent conducting oxide films. *Applied Physics A*, 62(5):487 – 492.

[Zunick, 1950] Zunick, M. J. (1950). Conductive coating on glass.

Lorenzo Fanni

Chemin de Epinettes 36,

1007 Lausanne

+41 (0)76 263 83 93

lorenzo.p.fanni@gmail.com

33, single, Italian citizenship

LANGUAGES

Italian	Native
English	Fluent
French	Fluent
German	Intermediate

EDUCATION

10.2012 - present	**PhD** Photovoltaics	*EPFL, Lausanne (CH)*
09.2005 - 02.2008	**Master** Condensed Matter Physics	*University of Genova (IT)* *Fraunhofer ISE, Freiburg (DE)*
09.2002 – 11.2005	**Bachelor** Physics	*University of Genova (IT)*

WORK EXPERIENCE

01.2012 – 09.2012	**Research Engineer** Photovoltaics	*EPFL, Lausanne (CH)*
01.2011 – 12.2011	**Researcher** Photovoltaics	*EURAC, Bolzano (IT)*
07.2008 – 12.2010	**Researcher** Photovoltaics	*SUPSI, Lugano (CH)*

TECHNICAL SKILLS

Material Synthesis Processes

Low Pressure Chemical Vapor Deposition, RF-Magnetron Sputtering

Characterization Techniques

Scanning Electron Microscopy, X-ray diffraction, UV/VIS/NIR Spectroscopy, Fourier Transform Infrared Spectroscopy, Atomic Force Microscopy, Sun Simulator

Informatics

Origin, Latex, RefDex, AforsHet, Gwyddion, Matlab, Office suite

MAIN PUBLICATIONS

- *A detailed analysis of gains and losses of a fully-integrated flat roof amorphous silicon photovoltaic plant* Solar Energy 85 9 (2011) 2360-2373

- *Seasonal power fluctuations of amorphous silicon thin-film solar modules: distinguishing between different contributions* Progress in Photovoltaics: Research and Applications 22 2 (2014) 208-217

- *How accurate is a commercial monitoring system for photovoltaic plant?* Progress in Photovoltaics: Research and Applications 22 8 (2014) 910-922

- *Increasing polycrystalline zinc oxide grain size by control of film preferential orientation* Crystal Growth & Design 15 12 (2015) 5886-5891